



DUAL FINE TRACKING CONTROL  
OF A  
SATELLITE LASER COMMUNICATION UPLINK  
  
THESIS

Louis A. Noble, Major, USAF

AFIT/GSS/ENG/06-02

DEPARTMENT OF THE AIR FORCE  
AIR UNIVERSITY

**AIR FORCE INSTITUTE OF TECHNOLOGY**

Wright-Patterson Air Force Base, Ohio

APPROVED FOR PUBLIC RELEASE; DISTRIBUTION UNLIMITED.

The views expressed in this thesis are those of the author and do not reflect the official policy or position of the United States Air Force, Department of Defense, or the United States Government.

AFIT/GSS/ENG/06-02

DUAL FINE TRACKING CONTROL  
OF A  
SATELLITE LASER COMMUNICATION UPLINK

THESIS

Presented to the Faculty  
Department of Aeronautics and Astronautics  
Graduate School of Engineering and Management  
Air Force Institute of Technology  
Air University  
Air Education and Training Command  
In Partial Fulfillment of the Requirements for the  
Degree of Master of Science (Space Systems)

Louis A. Noble, B.S.M.E., M.S.M.E.  
Major, USAF

September 2006

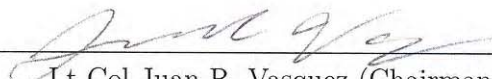
APPROVED FOR PUBLIC RELEASE; DISTRIBUTION UNLIMITED.

AFIT/GSS/ENG/06-02


DUAL FINE TRACKING CONTROL  
OF A  
SATELLITE LASER COMMUNICATION UPLINK

Louis A. Noble, B.S.M.E., M.S.M.E.  
Major, USAF

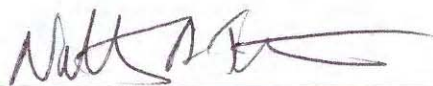
Approved:

  
Lt Col Juan R. Vasquez (Chairman)

25 Aug 06  
date

  
Dr. Richard G. Cobb (Member)

25 Aug 06  
date

  
Lt Col Nathan A. Titus (Member)

25 Aug 06  
date

*Abstract*

A dual fine tracking control system (FTCS) is developed for a single aperture optical communication receiver to compensate for high frequency disturbances affecting tracking of two incident laser communication beams. The optical communication receiver resides within a payload module aboard a geosynchronous satellite, while each laser communication transmitter is housed within a module aboard a high altitude unmanned aerial vehicle (UAV). In addition to platform specific disturbances, the impact of atmospheric optical disturbances affecting tracking error are investigated. The system dynamics and FTCS are modeled and evaluated in MATLAB and SIMULINK. An optimal controller is developed to mitigate these disturbances and provide tracking errors commensurate with a bit error rate (BER) that does not exceed  $10^{-6}$ .

Based on the respective optimal state estimates of each beam, the dual control technique regulates the fine tracking error for each beam by switching in time between each state estimate and applying linear quadratic regulator (LQR) control to a single fast steering mirror (FSM). Optical turbulence induced random beam wander effects revealed limited impact to tracking error due to spatial separation between transmitters, due to the defined communication architecture geometry. Moreover, simulation results indicated that dual control did not achieve the tracking error limit; however, single control of one beam at the cost of tracking error on the other beam, achieved a sufficient temporal mean tracking error to meet the required BER.

## *Acknowledgements*

I would like to thank my faculty advisor, Lt Col Juan Vasquez, for his continued guidance and support throughout the course of this thesis effort. The time, recommendations, and consideration were truly invaluable. My appreciation goes to my other committee members as well.

Louis A. Noble

## *Table of Contents*

	Page
Abstract . . . . .	iv
Acknowledgements . . . . .	v
List of Figures . . . . .	x
List of Tables . . . . .	xv
I. Introduction . . . . .	1
1.1 Dual Fine Tracking Control System . . . . .	1
1.1.1 Internal Disturbances . . . . .	3
1.1.2 External Disturbances . . . . .	4
1.1.3 Fine Tracking Error Budget . . . . .	5
1.2 Summary . . . . .	6
II. Literature Review . . . . .	7
2.1 Platform Vibration Disturbance Rejection . . . . .	7
2.2 Acoustic Beam Steering . . . . .	8
2.3 Nonlinear Optics . . . . .	10
2.4 Antenna Gain Optimization . . . . .	10
2.4.1 Received Signal Power . . . . .	10
2.4.2 Bit Error Rate Performance . . . . .	11
2.4.3 Transmitter and Receiver Gain Optimization . .	13
2.5 Summary . . . . .	15
III. Dual Fine Tracking Control System . . . . .	16
3.1 Transmitter . . . . .	17
3.1.1 Aircraft Dynamics . . . . .	17
3.1.2 Laser Source . . . . .	17
3.1.3 Transmission Effects . . . . .	19
3.2 Channel . . . . .	21
3.3 Receiver . . . . .	23
3.3.1 Satellite Dynamics . . . . .	23
3.3.2 Optical Communication System . . . . .	24
3.3.3 Receiver Effects . . . . .	28
3.4 Dual Fine Tracking Control System Model . . . . .	29
3.4.1 Plant Disturbance . . . . .	31
3.4.2 Measurement Noise . . . . .	32

	Page
3.4.3 Plant . . . . .	33
3.4.4 Kalman Filter . . . . .	37
3.4.5 Controller . . . . .	40
3.5 Summary . . . . .	42
IV. Analysis and Results . . . . .	43
4.1 Noise Effects . . . . .	44
4.1.1 Measurement Noise . . . . .	44
4.1.2 Plant Disturbance . . . . .	44
4.2 No Control . . . . .	50
4.3 Single Fine Tracking Control . . . . .	52
4.3.1 Time Response . . . . .	52
4.3.2 Frequency Response . . . . .	54
4.3.3 Disturbance Rejection . . . . .	54
4.4 Dual Fine Tracking Control . . . . .	56
4.4.1 Time Response . . . . .	56
4.4.2 Frequency Response . . . . .	58
4.4.3 Disturbance Rejection . . . . .	58
4.5 Bit Error Rate Performance . . . . .	59
4.6 Summary . . . . .	62
V. Conclusions . . . . .	63
5.1 Thesis Summary . . . . .	63
5.2 Contributions . . . . .	65
5.3 Recommendations and Future Work . . . . .	65
Appendix A. Optical Communication System . . . . .	67
A.1 Data Transmission . . . . .	67
A.1.1 NRZ-L PCM Baseband Waveform Statistics . . . . .	67
A.1.2 NRZ-L PCM Baseband Waveform Power Spectral Density . . . . .	71
A.2 Optical Receiver . . . . .	73
A.2.1 Received Current . . . . .	73
A.2.2 Matched Filter . . . . .	74
A.2.3 Symbol Detection . . . . .	74
A.3 Probability of Bit Error . . . . .	75
A.3.1 Gaussian Communication Channel . . . . .	76
A.3.2 Fading Communication Channel: Non-Ideal Tracking . . . . .	78
A.4 Link Margin . . . . .	82
A.4.1 Received Optical Power . . . . .	82



	Page
A.4.2 Receiver Sensitivity . . . . .	82
A.4.3 Link Margin . . . . .	83
A.5 Summary . . . . .	85
Appendix B. Satellite Dynamics . . . . .	86
B.1 Satellite Position . . . . .	86
B.1.1 Orbit Location . . . . .	86
B.1.2 Satellite Location . . . . .	88
B.2 Satellite Attitude Dynamics . . . . .	89
B.2.1 Attitude Kinematics . . . . .	91
B.2.2 Satellite Field of View . . . . .	95
B.3 Disturbance Environment . . . . .	97
B.4 Summary . . . . .	98
Appendix C. Aircraft Dynamics . . . . .	99
C.1 Aircraft Position . . . . .	99
C.2 Aircraft Attitude Dynamics . . . . .	99
C.2.1 Attitude Dynamics . . . . .	99
C.2.2 Attitude Kinematics . . . . .	101
C.3 Transmitter Module . . . . .	104
C.3.1 Transmitter Position . . . . .	104
C.3.2 Transmitter Attitude Dynamics . . . . .	104
C.3.3 Transmitter Attitude Kinematics . . . . .	106
C.3.4 Transmitter Attitude Equations of Motion . . . . .	107
C.4 Disturbance Environment . . . . .	107
C.4.1 Pointing Loss . . . . .	108
C.4.2 Aerodynamic-Optical Loss . . . . .	109
C.5 Summary . . . . .	109
Appendix D. Optical Components . . . . .	111
D.1 Transmitter . . . . .	111
D.1.1 Laser Source . . . . .	111
D.1.2 Optical Modulation . . . . .	115
D.1.3 Transmitter Antenna Gain . . . . .	120
D.2 Receiver . . . . .	121
D.2.1 Optical Signal Processing . . . . .	121
D.2.2 Receiver Antenna Gain . . . . .	124
D.2.3 Optical Signal Detection . . . . .	124
D.3 Summary . . . . .	135

	Page
Appendix E.      Communication Channel . . . . .	136
E.1    Atmospheric Loss . . . . .	136
E.1.1    Attenuation . . . . .	136
E.1.2    Optical Turbulence . . . . .	137
E.1.3    Atmospheric Loss . . . . .	145
E.2    Path Loss . . . . .	147
E.3    Optical Background Radiation . . . . .	147
E.4    Summary . . . . .	149
Appendix F.      Controller Characterization . . . . .	150
F.1    Weighting Matrices . . . . .	150
F.1.1    State Weighting Matrix Response . . . . .	152
F.1.2    Control Weighting Matrix Response . . . . .	153
F.2    Switching Time . . . . .	156
F.2.1    Ensemble Average Tracking Error Response . .	160
F.2.2    Ensemble Average Control Input Response . .	160
F.2.3    Temporal Average Response . . . . .	160
F.3    Summary . . . . .	167
Appendix G.      Dual Fine Tracking Control System Simulation Model .	168
Bibliography . . . . .	171

## *List of Figures*

Figure		Page
1.1.	Laser Communication System Architecture . . . . .	2
1.2.	Dual Fine Tracking Control System . . . . .	3
1.3.	Uplink Communication Block Diagram . . . . .	4
1.4.	Fine Tracking Error Budget Tree . . . . .	6
2.1.	Bragg Diffraction . . . . .	9
2.2.	Coordinate Transformation . . . . .	12
3.1.	Beam Propagation . . . . .	19
3.2.	Propagation Distance vs. Elevation Angle . . . . .	19
3.3.	Uplink Beam Diffractive Beam Radius . . . . .	20
3.4.	Uplink Beam Free-Space Peak Irradiance . . . . .	20
3.5.	Atmospheric Loss . . . . .	22
3.6.	Path Loss . . . . .	22
3.7.	Random Beam Wander . . . . .	23
3.8.	Satellite and Receiver Field of View . . . . .	25
3.9.	$E_b/N_o$ Performance due to Radial Tracking Error . . . . .	27
3.10.	Probability of Bit Error Performance Curve due to Radial Tracking Error . . . . .	28
3.11.	Dual Fine Tracking Control System Closed Loop Diagram . . .	30
3.12.	Fast Steering Mirror Step Response . . . . .	35
3.13.	Tip/Tilt Axis Frequency Response . . . . .	35
4.1.	Measurement Noise Time Response . . . . .	45
4.2.	Measurement Noise Power Spectral Density . . . . .	45
4.3.	Elevation Angle Affects on Spatial Separation and Beam Wander	46
4.4.	Beam Wander Ensemble Average Mean Tracking Error Response for 13 Elevation Angles . . . . .	47

Figure		Page
4.5.	Beam Wander Ensemble Average Tracking Error Standard Deviation Response for 13 Elevation Angles . . . . .	48
4.6.	Beam Wander Ensemble Average Control Input Response for 13 Elevation Angles . . . . .	48
4.7.	Beam Wander Temporal Average Mean Tracking Error Response	49
4.8.	Beam Wander Temporal Average Tracking Error Standard Deviation Response . . . . .	49
4.9.	Beam Wander Temporal Average Control Input Response . . .	50
4.10.	Plant Disturbance Time Response . . . . .	51
4.11.	Plant Disturbance Noise Power Spectral Density . . . . .	51
4.12.	No Control Ensemble Average Mean Tracking Error Time Response . . . . .	52
4.13.	No Control Ensemble Average Tracking Error Standard Deviation Time Response . . . . .	53
4.14.	No Control Ensemble Average Radial Tracking Error Time Response . . . . .	53
4.15.	Beam A Control Only: Ensemble Average Radial Tracking Error Time Response . . . . .	54
4.16.	Beam B Control Only: Ensemble Average Radial Tracking Error Time Response . . . . .	55
4.17.	Beam A Control Only: Fast Steering Mirror Frequency Response Function . . . . .	55
4.18.	Beam B Control Only: Fast Steering Mirror Frequency Response Function . . . . .	56
4.19.	Beam A Control Only: Disturbance Rejection . . . . .	57
4.20.	Beam B Control Only: Disturbance Rejection . . . . .	57
4.21.	Dual Fine Tracking Control Ensemble Average Radial Tracking Error Time Response . . . . .	58
4.22.	Dual Fine Tracking Control Fast Steering Mirror Frequency Response Function . . . . .	59
4.23.	Dual Fine Tracking Control Disturbance Rejection . . . . .	60

Figure		Page
4.24.	Temporal Average of Ensemble Radial Tracking Error Performance . . . . .	61
A.1.	PCM Baseband Waveform . . . . .	68
A.2.	NRZ-L PCM Baseband Waveform PSD . . . . .	72
A.3.	OOK Optical Receiver . . . . .	73
A.4.	Gaussian Conditional Probability Density Functions . . . . .	76
A.5.	Complementary Error Function Curve . . . . .	78
A.6.	OOK Modulation Theoretical BER Curve . . . . .	79
A.7.	Theoretical Detected Received Optical Signal Power . . . . .	83
A.8.	Receiver Sensitivity vs . . . . .	84
A.9.	Link Margin . . . . .	84
B.1.	GCI Frame Satellite Orbit . . . . .	87
B.2.	ECF Frame Satellite Orbit . . . . .	88
B.3.	Satellite Attitude . . . . .	90
B.4.	Orbit Reference Frame Rate of Change . . . . .	93
B.5.	Satellite Field of View Geometry . . . . .	95
C.1.	Aircraft Attitude . . . . .	100
C.2.	Transmitter Platform . . . . .	105
D.1.	Propagation Distance vs Elevation Angle . . . . .	114
D.2.	Diffraction Beam Waist Radius vs Elevation Angle . . . . .	114
D.3.	Transmitted Peak Irradiance vs Elevation Angle . . . . .	115
D.4.	OOK Digital Bandpass Modulation . . . . .	116
D.5.	Transmitted Optical Signal PSD . . . . .	120
D.6.	Transmitter Antenna Gain vs Wavelength . . . . .	121
D.7.	Receiver Field of View Geometry . . . . .	123
D.8.	Theoretical Received Optical Signal Power . . . . .	128
D.9.	Theoretical Received DC Current . . . . .	128
D.10.	Quadrant Cell Detector . . . . .	129

Figure		Page
D.11.	Maximum Quantum Shot Noise Power . . . . .	134
D.12.	Maximum Photodetector Noise Equivalent Current Power . . .	134
E.1.	Refractive Index Structure Constant Profile . . . . .	138
E.2.	Relative Refractive Index Structure Constant Profile . . . . .	139
E.3.	Irradiance Fluctuation Condition . . . . .	141
E.4.	Effective Beam Radius . . . . .	142
E.5.	Mean Peak Irradiance . . . . .	142
E.6.	Beam Spreading Loss . . . . .	143
E.7.	Root Mean Square Beam Wander . . . . .	144
E.8.	Beam Wander Loss . . . . .	144
E.9.	Tracked On-Axis Scintillation Index . . . . .	146
E.10.	Atmospheric Loss . . . . .	146
E.11.	Path Loss . . . . .	147
F.1.	State Weighting Matrix Ensemble Average Mean Tracking Error Response . . . . .	153
F.2.	State Weighting Matrix Ensemble Average Tracking Error Stan- dard Deviation Response . . . . .	154
F.3.	State Weighting Matrix Ensemble Average Control Response .	154
F.4.	State Weighting Matrix Temporal Mean Tracking Error Response	155
F.5.	State Weighting Matrix Temporal Tracking Error Standard De- viation Response . . . . .	155
F.6.	State Weighting Matrix Temporal Control Response . . . . .	156
F.7.	Control Weighting Matrix Ensemble Average Mean Tracking Er- ror Response . . . . .	157
F.8.	Control Weighting Matrix Ensemble Average Tracking Error Stan- dard Deviation Response . . . . .	157
F.9.	Control Weighting Matrix Ensemble Average Control Response	158
F.10.	Control Weighting Matrix Temporal Mean Tracking Error Re- sponse . . . . .	158

Figure		Page
F.11.	Control Weighting Matrix Temporal Tracking Error Standard Deviation Response . . . . .	159
F.12.	Control Weighting Matrix Temporal Control Response . . . . .	159
F.13.	Tracking Error Time Response, $t \in (0, 0.01s)$ . . . . .	161
F.14.	Tracking Error Time Response, $t \in (0.02, 0.03s)$ . . . . .	161
F.15.	Tracking Error Time Response, $t \in (0.20, 0.21s)$ . . . . .	162
F.16.	Tracking Error Time Response, $t \in (1.00, 1.01s)$ . . . . .	162
F.17.	Control Input Time Response, $t \in (0, 0.01s)$ . . . . .	163
F.18.	Control Input Time Response, $t \in (0.02, 0.03s)$ . . . . .	163
F.19.	Control Input Time Response, $t \in (0.20, 0.21s)$ . . . . .	164
F.20.	Control Input Time Response, $t \in (1.00, 1.01s)$ . . . . .	164
F.21.	Switching Time Temporal Average Mean Tracking Error . . . . .	165
F.22.	Switching Time Temporal Average Tracking Error Standard Deviation . . . . .	166
F.23.	Switching Time Temporal Average Control Input . . . . .	166
G.1.	Dual Fine Tracking Control System Simulation Model . . . . .	168
G.2.	Optical Signal Processing Block . . . . .	169
G.3.	Plant Disturbance Noise Block . . . . .	169
G.4.	Measurement Noise Block . . . . .	170
G.5.	Kalman Filter Block . . . . .	170
G.6.	Controller Block . . . . .	170

*List of Tables*

Table		Page
F.1.	Weighting Matrix Variables . . . . .	152
F.2.	Candidate Switching Time Variables . . . . .	160



# DUAL FINE TRACKING CONTROL OF A SATELLITE LASER COMMUNICATION UPLINK

## I. Introduction

Satellite communication systems predominately operate within the radio frequency (RF) and microwave frequency regions of the electromagnetic spectrum. Laser communication systems operate at higher frequency regions, infrared (IR) to ultraviolet (UV), which are capable of providing more bandwidth. On the other hand, due to narrow beamwidth, laser communication systems are more sensitive to propagation disturbances. Propagation disturbances cause degradation of incident beam energy at the optical receiver, which adversely affects communication link bit error rate (BER) performance.

The fundamental objective of this work is to design an optical communication receiver fine tracking control system to compensate for disturbances affecting line of sight (LOS) uplink beam propagation from two spatially separated aircraft terminals, as shown in Figure 1.1. The design methodology encompasses four steps: define the physical system and control requirements, develop a system model, design a controller, and simulate the design. If successful, this method would provide a possible solution as a multiple access scheme for satellite laser communications.

### ***1.1 Dual Fine Tracking Control System***

The receiver dual fine tracking control system (FTCS) is shown in Figure 1.2. Each incident beam passes through a single telescope aperture and is transferred by a fast steering mirror (FSM), denoted by  $F(t)$  subject to plant disturbance  $w_d(t)$ , to signal and position photodetector sensors. The position sensor, known as a quadrant cell detector (QD), converts the received optical power into azimuth and elevation

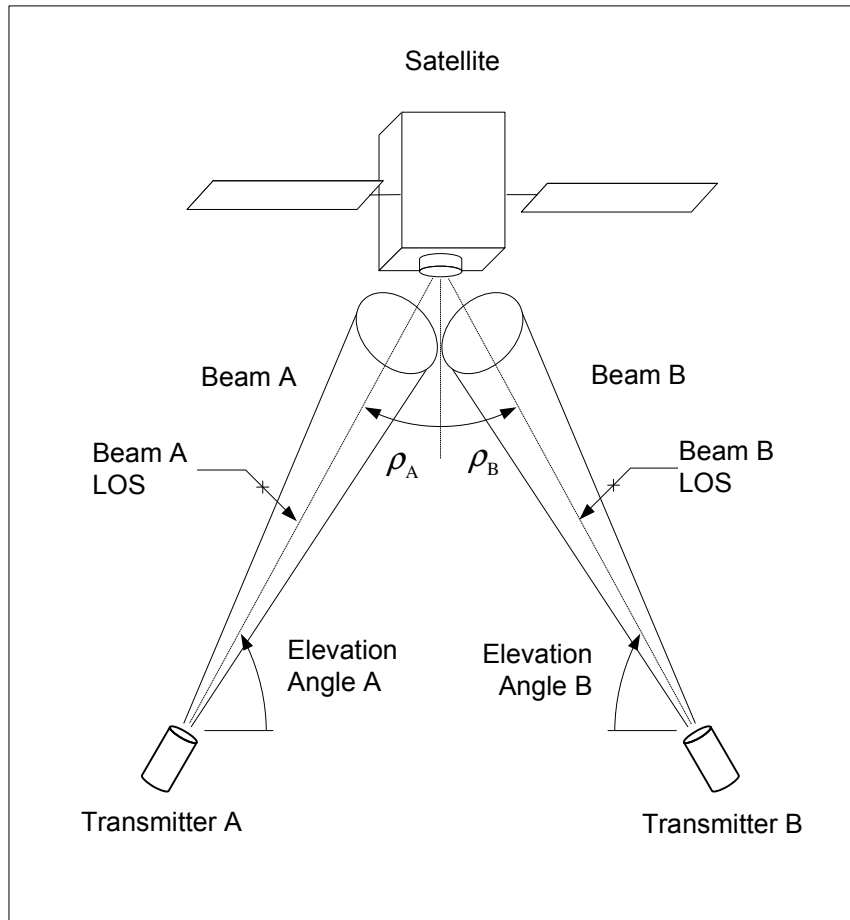


Figure 1.1: Laser Communication System Architecture

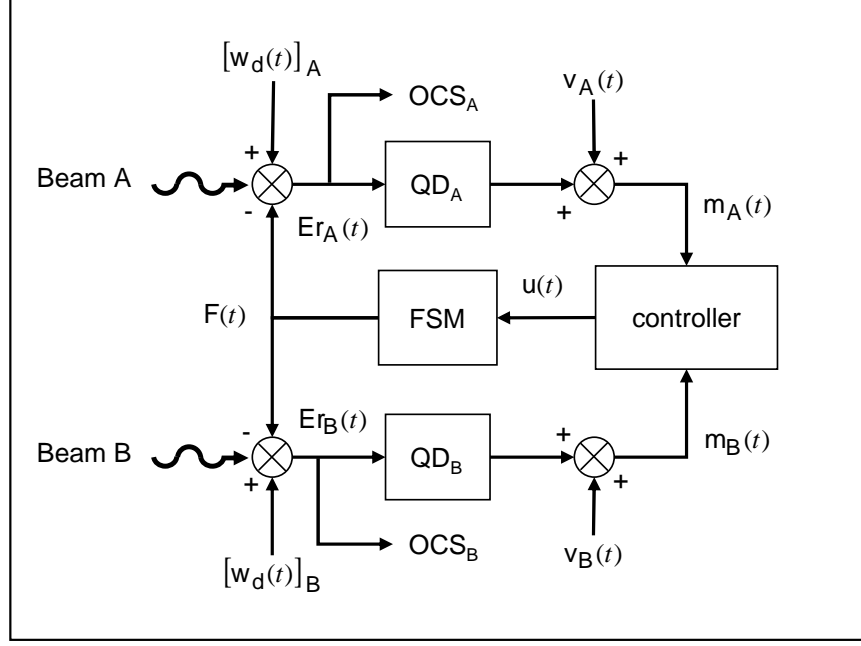


Figure 1.2: Dual Fine Tracking Control System

tracking error signals, and is subject to sensor noise  $v(t)$ . Within the optical communication system (OCS), a signal sensor converts received optical power into electrical signals for signal processing. Based on the measured states for each beam,  $m_A(t)$  and  $m_B(t)$  respectively, the dual control technique regulates the tracking error for each beam by switching in time between optimal estimates of each system state and commands, via  $u(t)$ , a single FSM to center the incident beam on the position detector for maximum available received signal power. Tracking performance, depending on internal and external disturbance rejection, is quantified by maintaining the residual tracking error,  $E_r(t)$ , within the fine tracking error budget.

*1.1.1 Internal Disturbances.* Control system internal disturbances are caused by sensor noise, sensor bias, actuator nonlinearities, and satellite plant disturbances. Sensor noise is caused by uncertainties in measured states due to quantum shot noise,  $N_q$ , and thermal noise,  $N_o$ . Sensor bias, unique to each sensor, is a constant error between the actual and measured state. In particular, dark current,  $N_d$ , is a bias inherent to a photodetection devices. Plant disturbances are vibrations caused by

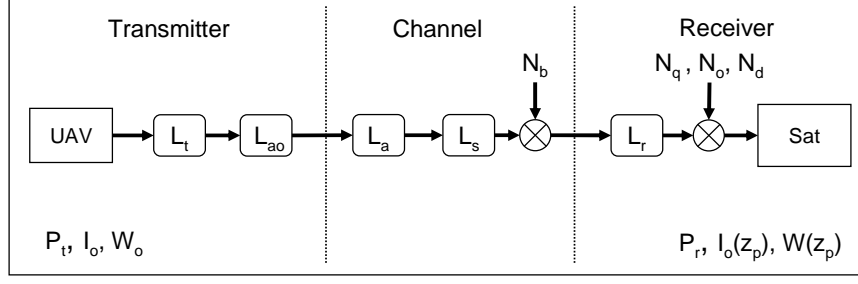


Figure 1.3: Uplink Communication Block Diagram

platform structural loads. These internal disturbances, categorized as receiver effects as shown in Figure 1.3, induce beam tracking loss, denoted as  $L_r$ .

*1.1.2 External Disturbances.* Uplink propagation of each beam is adversely affected by external disturbances, which attenuate the transmitted power,  $P_t$ . Subsequent to propagation, the observed received power,  $P_r$ , determines link margin and BER performance, which are fundamental performance measures in digital communication systems. These external disturbances can be categorized as transmitter and channel effects, as shown in Figure 1.3, and described below.

*1.1.2.1 Transmitter Effects.* Transmission of a signal through a channel, the propagation medium, requires an antenna sized to the signal wavelength [29, page 168]. Wavelength is inversely proportional to frequency; hence, laser communication yields a small antenna size and narrow beamwidth. Although a narrow beamwidth, on the order of  $10 \mu\text{rad}$ , may reduce interference effects, any mechanical disturbance adversely affects pointing accuracy [15, page 137]. Typical pointing loss sources,  $L_t$ , are aircraft flight structural loads arising from control hardware, turbulence, and unsteady aerodynamics. Unlike RF systems, laser communication systems encounter additional signal degradation due to aerodynamic-optical loss,  $L_{ao}$ . Aerodynamic-optical loss is caused by beam phase distortion, due to turbulent boundary layer effects, during transmission from an airborne platform.

*1.1.2.2 Channel Effects.* The communication channel consists of the Earth's atmosphere and free space. Propagation through the atmospheric portion produces three main disturbances: absorption, scattering, and optical turbulence [2, page 1]. The atmosphere is a nonhomogenous medium in which atoms interact with an incident electromagnetic wave, depending upon its wavelength, by either dissipative absorption or scattering [13, pages 86-87]. Optical turbulence produces index of refraction fluctuations which induce beam spreading, random beam wander, and beam scintillation upon a propagating optical wave. Based on relative atmospheric conditions, these disturbances yield an overall atmospheric loss,  $L_a$ .

As a function of propagation distance,  $z_p$ , and wavelength, free-space diffraction affects an electromagnetic wave by increasing its initial beam waist radius,  $W_o$ , to a final waist radius,  $W(z_p)$ . In turn, the initial beam peak irradiance,  $I_o$  is dispersed about the final waist radius to a decreased final peak irradiance,  $I_o(z_p)$ . As a consequence, the attenuation in transmitted power is defined as a path loss,  $L_s$ . In addition, optical background radiation,  $N_b$ , affects photodetection sensitivity as an independent parameter in quantum shot noise power.

*1.1.3 Fine Tracking Error Budget.* The fine tracking error budget is comprised of error sources arranged in a hierarchical relationship, as shown in Figure 1.4. Disturbance error contributors are external and internal disturbance sources, as defined above. Hardware error contributors are manufacture and assembly of system components, which are assumed to be corrected or minimized during analysis, alignment, and calibration. Software error contributors are digital communication jitter, estimation error, and control system sampling jitter. Sources of software error are assumed to be corrected or minimized during real-time or off-line calculations applied to the closed-loop control algorithm. Unforeseen error sources, arising during modeling, simulation, or experimentation, will be analyzed and added to the appropriate category.

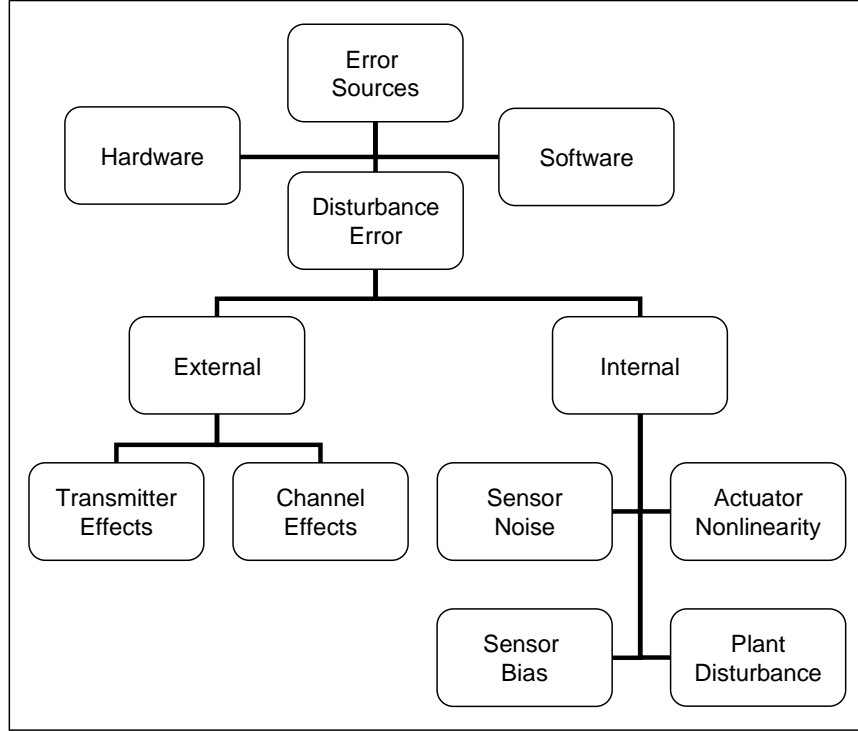


Figure 1.4: Fine Tracking Error Budget Tree

## 1.2 Summary

This chapter presented the dual fine tracking control problem, which investigates the feasibility of a single FSM to regulate tracking errors for two uplink beams. Chapter II provides a literature review of common methods for laser beam pointing and tracking control. Chapter III presents the underlying physics of laser beam uplink propagation and development of the dual FTCS model. Chapter IV provides simulation data analysis and performance results. Lastly, Chapter V summarizes the research and contributions, and provides recommendations for future work.

## II. Literature Review

Maintaining accurate beam pointing in the presence of disturbances has been a fundamental goal in satellite laser communication systems. Typically there are three types of pointing: acquisition, coarse tracking, and fine tracking. Acquisition, utilizing satellite ephemeris, beacons, or navigation data, establishes the initial line of sight (LOS) communication link between the transmitter and receiver. Coarse tracking compensates for large angular deviations and low frequency disturbances, while fine tracking compensates for high frequency disturbances. These functions are incorporated into a pointing, acquisition, and tracking (PAT) control system to maintain LOS communications.

Much of the fine tracking control research focused primarily on high frequency disturbance rejection, also known as jitter. The limiting factor is closed-loop control bandwidth versus disturbance bandwidth [30, page 569]. Closed-loop bandwidth is determined by the cutoff frequency, which is determined by the -3 dB point of the control system frequency response [21, page 572]. Ideally, 2 to 3 KHz control bandwidth is desired [20, page 72]; with a tracking accuracy of 1  $\mu$ rad, due to the narrow beamwidth of an optical link [8, page 252]. Several methods have been investigated for high frequency disturbance rejection: platform vibration disturbance rejection, acoustic beam steering, nonlinear optics, and antenna gain optimization. A discussion of each method will be presented.

### *2.1 Platform Vibration Disturbance Rejection*

Tracking errors are normally caused by sensor noise, estimation error, noisy actuators, and platform vibrations; however, platform vibrations are the dominant error source [8, pages 252-253]. Platform vibrations, at either the transmitter or receiver, produce beam position fluctuations on the receiver position detector. On-orbit spacecraft platform vibrations, characterized by measurement data from the European Space Agency (ESA) OLYMPUS satellite, revealed high frequency disturbances above 100 Hz affecting an optical communication payload [36, pages 207-212]. In particular,

power in the frequency responses are observed approximately up to 500 Hz from solar array actuators, 1 KHz from microwave switches, and up to 450 Hz from thruster firings.

Through various studies, comparison of linear versus nonlinear tracking control methods yielded varied low frequency performance; however, nonlinear methods achieved better high frequency performance. Assuming disturbances are zero mean white Gaussian noise, adaptive direct feedforward control achieved approximately 9 dB greater jitter disturbance rejection than linear quadratic Gaussian (LQG) control, at the cost of computation resources [25, pages 191-194]. An alternate design, incorporating a self-tuning feedforward control loop with linear feedback control, achieved at least a 25 dB disturbance rejection, and without self-tuning, linear feedback control dropped to below 10 dB of disturbance rejection at frequencies above 300 Hz [31, pages 572-574]. Investigation of frequency dependent noise, commonly referred to as colored noise, disturbance effects revealed similar high frequency disturbance rejection results for LQG control compared with adaptive least mean squares (LMS) and gradient adaptive lattice (GAL) algorithms, however, both adaptive control methods resulted in added noise to the system response [33, page 16].

## ***2.2 Acoustic Beam Steering***

Acoustic beam steering relies on the acoustic optic phenomenon using sound waves to change the index of refraction of the propagation medium. The simplest form of this acoustic optical effect is Bragg diffraction: an incident optical beam is diffracted by constructive interference based on [26, pages 801-806]

$$\sin(\theta_B) = \left( \frac{\lambda_c}{2\lambda_s} \right) \quad (2.1)$$



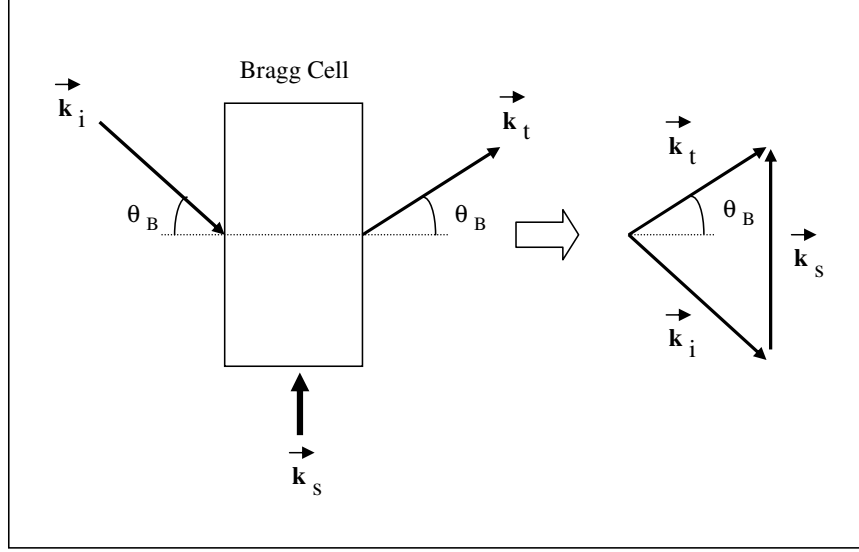


Figure 2.1: Bragg Diffraction

where  $\lambda_c$  is the carrier wavelength,  $\lambda_s$  is the sound wavelength, and  $\theta_B$  is the Bragg angle. This condition is equivalent to the following vector relationship,

$$\vec{k}_t = \vec{k}_i + \vec{k}_s \quad (2.2)$$

where  $\vec{k}_t$  is the transmitted optical wave,  $\vec{k}_i$  is the incident optical wave, and  $\vec{k}_s$  is the sound wave. The vector magnitudes are determined by wave numbers  $k_c = 2\pi/\lambda_c$  and  $k_s = 2\pi/\lambda_s$ , for optical and sound wave vectors respectively. An optimum amplitude reflectance occurs when  $k_s = 2k_c \sin(\theta_B)$  [26, page 805].

A common device used to implement acoustic beam steering is a Bragg Cell, as shown in Figure 2.1 [26, page 801]. Utilizing a Bragg Cell and a position sensing photodetector, a deflection angle can be calculated as [19, page 2209]

$$\theta_D = \left( \frac{\lambda_c}{\lambda_s n_i} \right) - 2\theta_B \quad (2.3)$$

where  $n_i$  is the index of refraction. Based on the measured deflection angle, used as an error source, the sound frequency input to the Bragg Cell is adjusted, which steers the optical beam in the desired direction for zero deflection.

### 2.3 *Nonlinear Optics*

Linear or nonlinear behavior of an optical wave is dependent upon the propagation medium [26, page 738]. Free-space exhibits properties of a linear medium, while a nonlinear medium affects the propagation of light due to a nonlinear relationship between the polarization density and electric field [26, page 739]. Based on the optical phase conjugation principle, wavefront aberrations can be removed from an incident beam [26, page 761]. Using nonlinear optical receiver components, an adaptive laser beam tracking scheme reduced incident beam angular deflection, resulting in better performance than classical tracking systems against milli-radian amplitude disturbances at frequencies  $\geq 100$  Hz [9, page 72].

### 2.4 *Antenna Gain Optimization*

Disturbances on an incident beam degrade the received signal power, which affects the communication system's bit error rate (BER) performance. Depending upon the tracking error statistics, transmitter or receiver antenna gain can be optimized to improve system performance [8, page 252]. Following the approach of Chen and Gardner, antenna gain optimization method relies on initial determination of the theoretical received signal power and corresponding system BER.

*2.4.1 Received Signal Power.* Received signal power,  $P_r$ , is generally determined by the Friis transmission equation [23, page 110].

$$P_r = P_t G_t L_s G_r \quad (2.4)$$

where  $P_t$  is the transmitted signal power,  $G_t$  is the transmitter gain,  $L_s$  is the path loss, and  $G_r$  is the receiver gain. Path loss, depending upon carrier wavelength,  $\lambda_c$ , results from divergence of an electromagnetic wave as it propagates, which is denoted by [29, page 254]

$$L_s = \left( \frac{\lambda_c}{4\pi z_p} \right)^2 \quad (2.5)$$

where  $z_p$  is the propagation distance. Accounting for additional loss factors, similar to RF communications, the transmission equation, also known as the link equation, can be modified as [15, pages 94-105]

$$P_r = (\eta_t P_t G_t L_t L_{ao})(L_s L_a)(L_r G_r \eta_r) \quad (2.6)$$

where  $\eta_t$  is transmitter efficiency loss,  $L_t$  is transmitter pointing loss,  $L_{ao}$  is aerodynamic-optical loss,  $L_a$  is atmospheric loss,  $L_r$  is receiver tracking loss, and  $\eta_r$  is the receiver efficiency loss.

*2.4.2 Bit Error Rate Performance.* Elevation and azimuth angular errors, denoted by  $x$  and  $y$  respectively, are assumed to be statistically independent Gaussian random variables [15, page 100]. The probability density functions of these errors can be used to determine signal loss and corresponding BER performance statistics [27, page 296]. The angular error joint probability density function is expressed as [10, pages 101, 208]

$$f_{XY}(x, y) = \frac{1}{2\pi\sigma_x\sigma_y} \exp\left[\frac{-(x - m_x)^2}{2\sigma_x^2}\right] \exp\left[\frac{-(y - m_y)^2}{2\sigma_y^2}\right] \quad (2.7)$$

where  $m_i$  and  $\sigma_i^2$  are respectively the corresponding mean and variance statistics of the errors. Assuming the azimuth and elevation errors are caused by combined disturbance effects, which yield similar behavior in either direction, error variances are assumed to be equivalent [27, page 297].

In addition, the control system regulates error about a zero set point, thus mean error is assumed to be zero. Based on both assumptions, the joint probability density function can be modified as,

$$f_{XY}(x, y) = \left(\frac{1}{2\pi\sigma^2}\right) \exp\left[\frac{-(x^2 + y^2)}{2\sigma^2}\right] \quad (2.8)$$

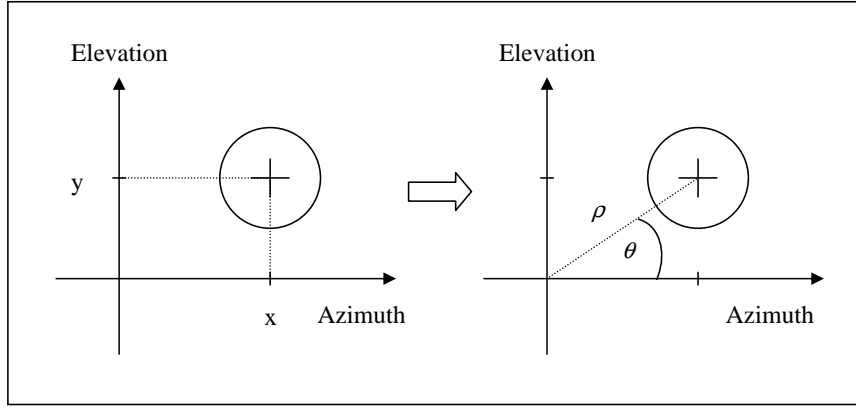


Figure 2.2: Coordinate Transformation

Performing a transformation into polar coordinates, as shown in Figure 2.2, a radial error probability density function can be determined, since the transformed probability is approximately equivalent to the original [10, pages 227-230]. Hence the probability density functions are related by,

$$f_{XY}(x, y)dx dy = f_{R\Theta}(\rho, \theta)dA \quad (2.9)$$

where

$$x = \rho \cos(\theta)$$

$$y = \rho \sin(\theta)$$

$$\rho^2 = x^2 + y^2$$

$$A = \text{area}$$

Matching the derivatives to the transformation variables, a relation is given by the

transformation Jacobian [10, page 229]

$$\begin{aligned}
\left| \frac{dxdy}{dA} \right| &= J(\rho, \theta) = \det \begin{pmatrix} \frac{\partial x}{\partial \rho} & \frac{\partial x}{\partial \theta} \\ \frac{\partial y}{\partial \rho} & \frac{\partial y}{\partial \theta} \end{pmatrix} = \det \begin{bmatrix} \cos(\theta) & -\rho \sin(\theta) \\ \sin(\theta) & \rho \cos(\theta) \end{bmatrix} \\
&= \rho [\cos^2(\theta) + \sin^2(\theta)] \\
&= \rho
\end{aligned} \tag{2.10}$$

Substituting Equations 2.8 and 2.10 into Equation 2.9, the polar coordinate joint probability density function is expressed as,

$$\begin{aligned}
f_{R\Theta}(\rho, \theta) &= f_{XY}(x, y) J(\rho, \theta) \\
&= \left( \frac{\rho}{2\pi\sigma^2} \right) \exp \left( -\frac{\rho^2}{2\sigma^2} \right)
\end{aligned} \tag{2.11}$$

Assuming  $\theta$  is equally likely to be any value within  $[0, 2\pi]$ , the polar coordinate joint probability density function can be converted to a marginal probability density function over  $\rho$ , which has Rayleigh statistics defined as [10, page 230]

$$f_R(\rho) = \int_0^{2\pi} f_{R\Theta}(\rho, \theta) d\theta = \left( \frac{\rho}{\sigma^2} \right) \exp \left( -\frac{\rho^2}{2\sigma^2} \right) \tag{2.12}$$

A general expression for the average BER for a communication system is a function of the signal modulation probability of bit error,  $P_{mod}$  defined in Appendix A, and an arbitrary radial error probability density function defined as [27, page 298]

$$BER = \int_0^\infty [P_{mod} f_R(\rho)] d\rho \tag{2.13}$$

The domain of integration assumes the radial tracking error resides within  $[0, \infty]$ , based on the Rayleigh statistics. However, receiver physical dimensions can limit the domain to reside within the receiver aperture radius.

*2.4.3 Transmitter and Receiver Gain Optimization.* Minimizing BER as the cost function, optimum gain can be determined by evaluating  $P_{mod}$  as a function of

received signal power,  $P_r$ . Assuming the incident beam behaves as a Gaussian beam, transmitter gain, receiver gain, and corresponding transmitter pointing and receiver tracking losses are defined as [8, page 253]

$$G_t = \left[ \frac{2\pi W_o}{\lambda_c} \right]^2 \quad (2.14)$$

$$G_r = \left( \frac{\pi D_{ap}}{\lambda_c} \right)^2 \quad (2.15)$$

$$L_t = \exp(-G_t \rho_t^2) \quad (2.16)$$

$$L_r = \exp(-G_r \rho_r^2) \quad (2.17)$$

where  $W_o$  is the initial beam waist radius,  $D_{ap}$  is the receiver aperture diameter,  $\rho_t$  is the transmitter radial pointing error, and  $\rho_r$  is the receiver radial tracking error. The radial pointing and tracking errors, subject to the previously derived Rayleigh statistics, are defined respectively as

$$f_R(\rho_t) = \left( \frac{\rho_t}{\sigma_t^2} \right) \exp\left(-\frac{\rho_t^2}{2\sigma_t^2}\right) \quad (2.18)$$

$$f_R(\rho_r) = \left( \frac{\rho_r}{\sigma_r^2} \right) \exp\left(-\frac{\rho_r^2}{2\sigma_r^2}\right) \quad (2.19)$$

Incorporating Equations 2.6 and 2.18 into Equation 2.13, an optimal transmitter gain is determined by [8, page 255]

$$\frac{dBER}{dG_t} = 0 = \int_0^\infty \frac{\partial P_{mod}}{\partial G_t} f_R(\rho_t) d\rho_t \quad (2.20)$$

Solving Equations 2.6, 2.18, and 2.20 simultaneously for  $G_t$  and  $P_r$  results in pointing error variance being inversely proportional to maximum transmitter gain but proportional to minimum received power [8, page 255]. Utilizing a similar method, an optimum receiver gain can be determined by solving Equations 2.6, 2.19, and 2.20 simultaneously for  $G_r$  and  $P_r$ .

## **2.5   *Summary***

Several fine tracking control methods have been presented for an incident laser beam. For the purposes of this study, the fine tracking control methodology will incorporate techniques from platform vibration disturbance rejection and the underlying theory in antenna gain optimization. These methods were chosen to limit implementation complexity and take advantage of using a single fast steering mirror (FSM) within the dual fine tracking control system (FTCS) described in Chapter I. Chapter III will develop the dual FTCS model, based on LQG control, and apply received signal power, radial tracking error, receiver tracking loss, and BER performance as constraints on performance.

### III. Dual Fine Tracking Control System

The laser communication system architecture, illustrated in Figure 1.1, consists of two communication links, one from each aircraft transmitter to the satellite receiver, commonly referred to as a terminal-to-satellite communication uplink. The proposed method developed for this work investigates the performance of the receiver terminal, using a single fast steering mirror (FSM) providing fine tracking control, to maintain line of sight (LOS) with two spatially separated transmitting terminals. The control concept relies on quadrant detectors measuring relative tracking errors for each incident beam, while the FSM corrects for these errors depending on controller commands. Control requirements are driven by the maximum allowed radial tracking error to maintain a communication bit error rate (BER) of  $10^{-6}$ , which is a commonly used performance limit in satellite communications [1, page 25].

The satellite is assumed to be a three-axis stabilized rigid-body platform, derived in Appendix B, located in a geosynchronous orbit at 35,786 km altitude [16, page 117]. The receiver terminal module, mounted on the nadir panel and aligned with the yaw axis, utilizes a Cassegrain telescope antenna with an assumed aperture efficiency,  $\eta_r$ , of 0.8 [23, page 110]. The telescope, with arbitrarily selected specifications of 300 mm primary mirror, 15 focal ratio, and 10 magnitude ratio, collects all incident optical sources within its field of view (FOV) [13, pages 174, 221]. A 1.0 nm optical bandpass filter is used to limit the amount of incident optical background radiation [5, page 680]. All receiver electronic components are maintained at a noise temperature of 400 K [23, page 118].

Each aircraft platform is a high altitude unmanned aerial vehicle (UAV) loitering within the satellite receiver field of view ( $\text{FOV}_R$ ) at 60,000 ft (18.3 km) altitude above mean sea level under clear-sky conditions. The transmitting terminal is assumed to be mounted above the aircraft center of mass (cm) within a dorsal module aligned with the yaw axis, with a minimum 20 degree elevation angle. For the purposes of this study, each UAV is assumed to be a three-axis stabilized rigid-body platform subject to platform disturbances which induce pointing errors and aerodynamic-optical effects



on the uplink beam. The transmitter antenna aperture efficiency,  $\eta_t$ , is assumed to be 0.8 [23, page 110].

### 3.1 Transmitter

*3.1.1 Aircraft Dynamics.* Based on the geocentric latitude and longitude of each aircraft,  $(\phi_i, \lambda_i)$ , relative to the GCI frame as derived in Appendix C, the respective position and velocity vectors, are determined by

$$\vec{r}_i = r_a \left[ \cos(\lambda_i) \cos(\phi_i) \hat{i} + \sin(\lambda_i) \cos(\phi_i) \hat{j} + \sin(\phi_i) \hat{k} \right] \quad (3.1)$$

$$\vec{v}_i = \frac{d\vec{r}_i}{dt} = \vec{\omega}_i \times \vec{r}_i \quad (3.2)$$

where  $r_a = 18.3 + R_E = 6,396$  km is the aircraft position magnitude,  $R_E = 6,378$  km is the Earth equatorial radius, and  $\omega_i$  is the angular velocity vector. Attitude dynamics for each aircraft, as derived in Appendix C, are denoted by

$$\dot{\vec{\omega}}_i = -\mathbf{I}_i^{-1} \boldsymbol{\Omega}_i \mathbf{I}_i \vec{\omega}_i + \mathbf{I}_i^{-1} \vec{T}_i \quad (3.3)$$

where  $\mathbf{I}_i$  is the aircraft moment of inertia matrix,  $\boldsymbol{\Omega}_i$  is the angular velocity vector skew symmetric matrix, and  $\vec{T}_i$  is the total torque vector.

*3.1.2 Laser Source.* Each aircraft transmits an On-Off Keying (OOK) band-pass modulated 100 mW near infrared (Near IR) laser beam, as derived in Appendices A and D, with an initial beam radius of 40 mm, at wavelengths of 1510 nm and 1550 nm respectively. The data rate from each transmitter is 100 Kbps, which equates to a signal bandwidth of 200 KHz. Based upon theoretical uplink beam propagation characteristics, derived in Appendices D and E, the initial beam radius and transmission wavelengths were chosen to maximize transmission gain and minimize the adverse effects of atmospheric loss. Assuming a lowest order transverse electromagnetic (TEM<sub>00</sub>) collimated Gaussian beam, as derived in Appendices A and D, each transmitted beam can be described by its optical field equation, diffractive beam

radius, and irradiance profile respectively as

$$s(t) = E_o \left[ 1 + \frac{g(t)}{V} \right] \cos(\omega_c t + \phi_c) \quad (3.4)$$

$$W(z_p) = W_o \sqrt{1 + \left( \frac{2z_p}{k_c W_o^2} \right)^2} \quad [\text{m}] \quad (3.5)$$

$$I(\rho_z, z_p) = \left[ \frac{2P_t}{\pi W^2(z_p)} \right] \exp \left[ -\frac{2\rho_z^2}{W^2(z_p)} \right] \quad [\text{W/m}^2] \quad (3.6)$$

where

$E_o$  = signal amplitude

$g(t)$  = modulation baseband waveform

$V$  = modulation voltage amplitude

$\omega_c$  = carrier frequency

$\phi_c$  = carrier phase

$W_o$  = initial beam radius

$z_p$  = propagation distance

$k_c$  = wave number

$\rho_z$  = radial distance from propagation axis

$P_t$  = transmitted power

As the beam propagates, its irradiance profile expands based on the diffractive beam radius,  $W(z_p)$ . Hence, the received power,  $P_r$ , is calculated from the received peak irradiance,  $I_0(z_p)$ , as illustrated in Figure 3.1. Based on the FOV<sub>R</sub> geometry defined in Appendix D, the transmitter elevation angle is limited from 77.3° to 90°. Thus, as shown in Figure 3.2, the propagation distance decreases as elevation angle increases [16, page 111]. Given the predefined laser source parameters and elevation angle range, the theoretical uplink beam propagation characteristics are shown in Fig-

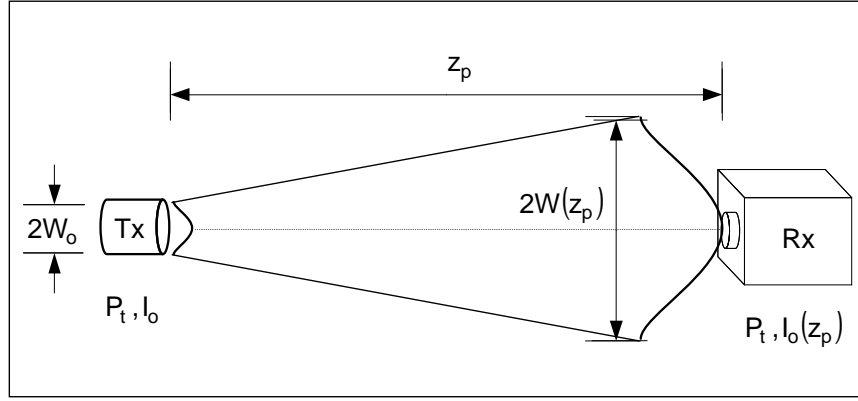


Figure 3.1: Beam Propagation

ures 3.3 and 3.4. In particular, an increasing elevation angle results in less diffraction and higher irradiance, due to less propagation through the atmosphere.

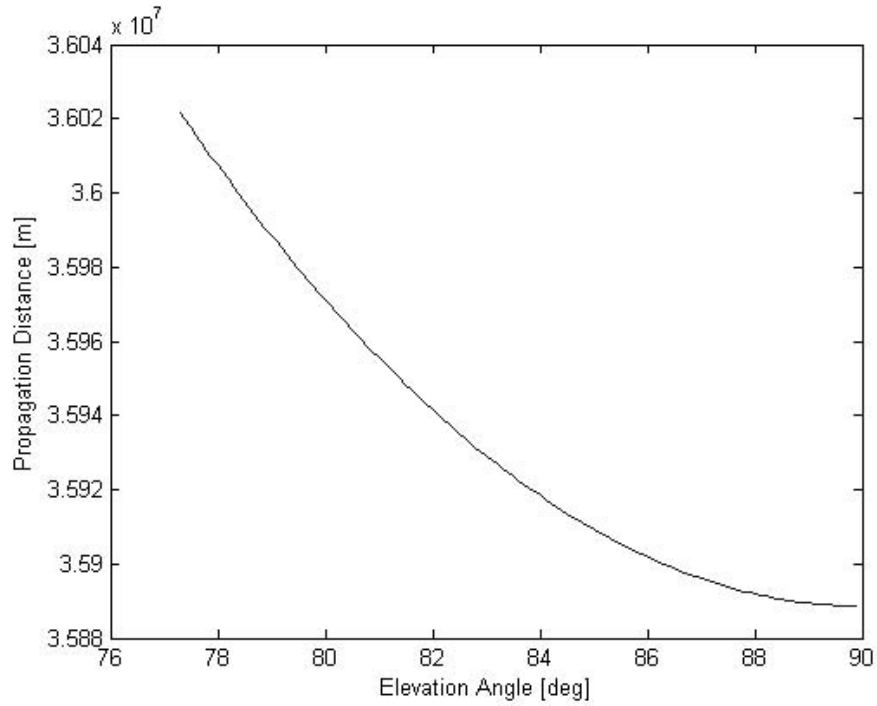


Figure 3.2: Propagation Distance vs. Elevation Angle

*3.1.3 Transmission Effects.* For the purposes of this study, emphasis is placed on the receiver tracking performance and it is assumed each UAV is a rigid body in the steady flight regime and loitering within  $FOV_R$ . Hence, attitude stabiliza-

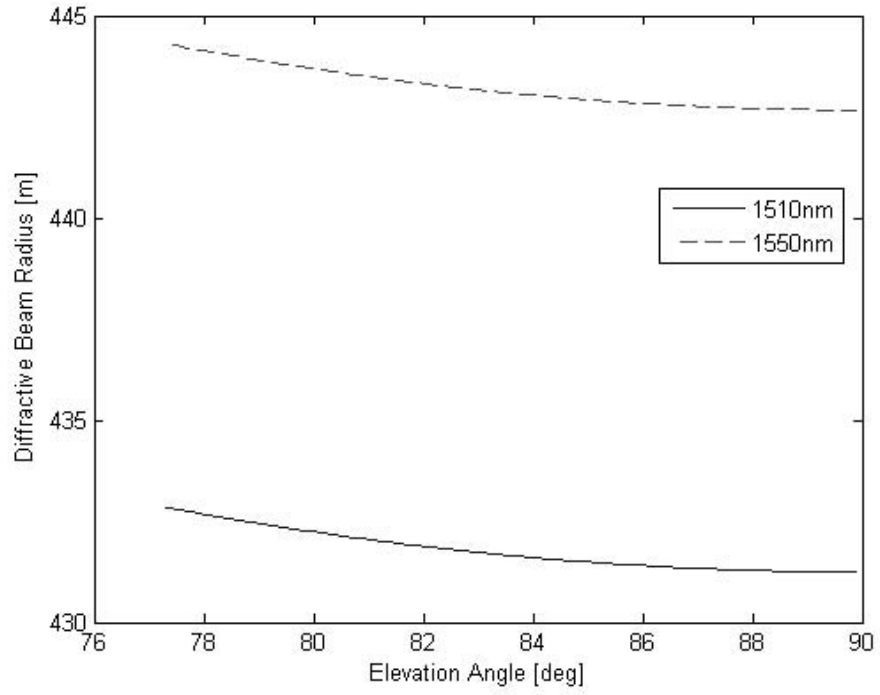


Figure 3.3: Uplink Beam Diffractive Beam Radius

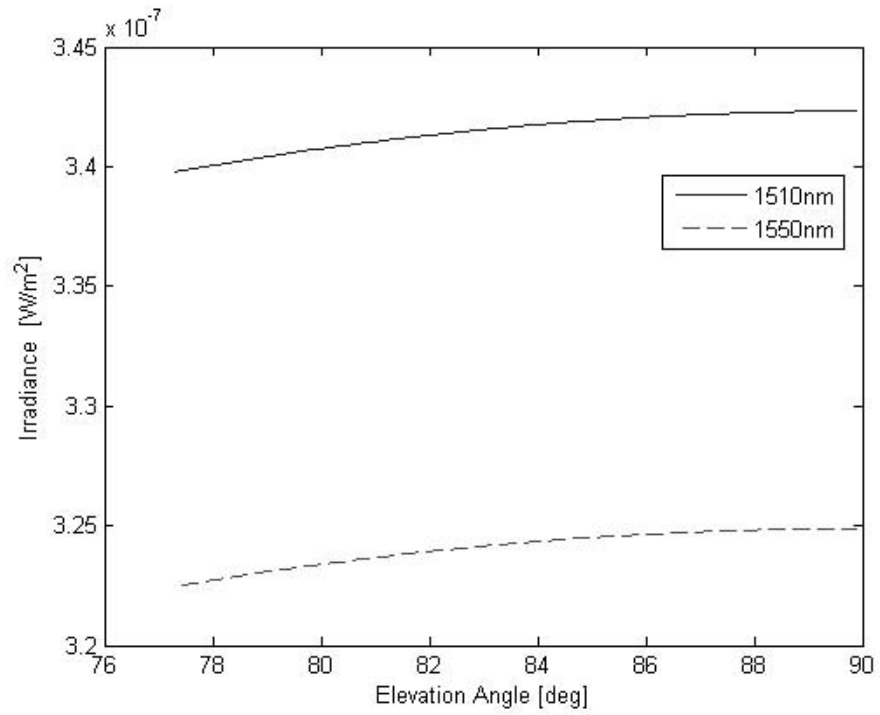


Figure 3.4: Uplink Beam Free-Space Peak Irradiance

tion and constant flight parameters are controlled by an autopilot [39, page 307]. In addition, since the transmitting terminal is aboard an aircraft, aerodynamic-optical effect is an additional phenomenon which degrades the initial beam propagation. These adverse transmission effects, defined in Appendix C, are quantified by the transmitter pointing loss,  $L_t = -0.969$  dB, and aerodynamic-optical loss,  $L_{ao} = -1.549$  dB. Based on the associated transmitter antenna gain, this pointing loss creates independent random azimuth and elevation pointing error, each assumed to have zero-mean white Gaussian statistics, with a variance calculated in Appendix C respectively for each beam as

$$(\sigma_t^2)_A = 4.0274 \times 10^{-12} \text{ [rad}^2\text{]} \quad (3.7)$$

$$(\sigma_t^2)_B = 4.2436 \times 10^{-12} \text{ [rad}^2\text{]} \quad (3.8)$$

### 3.2 Channel

As illustrated in Figure 1.3, the propagation channel, comprised of the Earth's atmosphere and free-space, produces three adverse effects: atmospheric loss, path loss, and optical background radiation. As defined and modeled in Appendix E, theoretical atmospheric loss and path loss for the given laser source parameters are illustrated in Figures 3.5 and 3.6. A longer wavelength is inherently less susceptible to optical turbulence; however, as shown in Figure 3.7, optical turbulence induces random beam wander about the propagation axis, which is independent of wavelength but dependent on elevation angle. Optical background radiation, as derived in Appendices D and E, is modeled as additive white gaussian noise (AWGN) which adversely impacts optical signal detection.

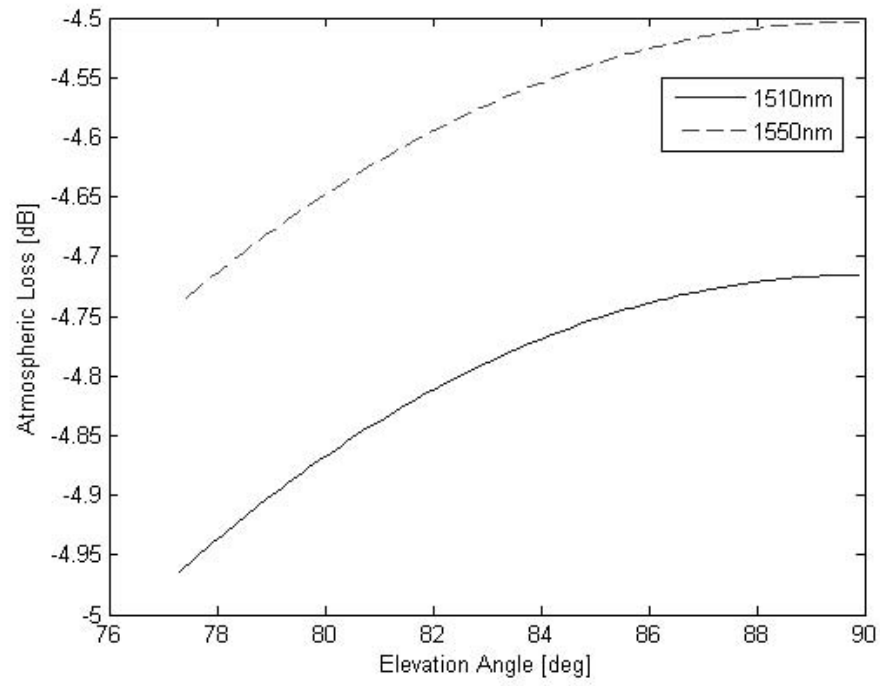


Figure 3.5: Atmospheric Loss

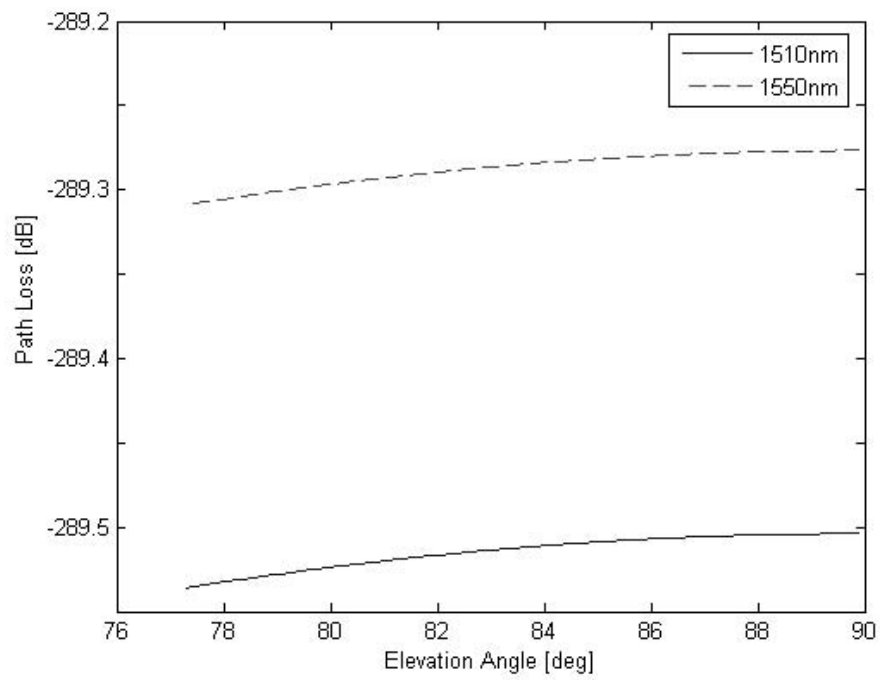


Figure 3.6: Path Loss

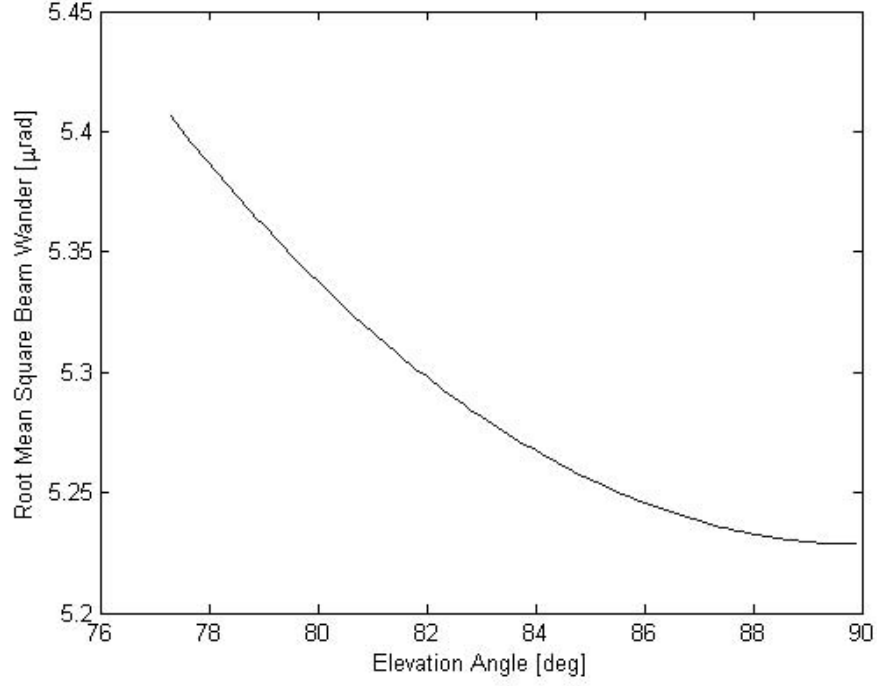


Figure 3.7: Random Beam Wander

### 3.3 Receiver

*3.3.1 Satellite Dynamics.* As shown in Appendix B, the geocentric inertial frame (GCI) satellite position and velocity vectors are determined as

$$\vec{r}_s = R^{GE} \vec{r}_{xyz} \quad (3.9)$$

$$\vec{v}_s = \frac{d\vec{r}_s}{dt} = \vec{\omega}_s \times \vec{r}_s \quad (3.10)$$

where  $\vec{r}_{xyz}$  is the Earth centered fixed (ECF) frame satellite position,  $R^{GE}$  is the ECF to GCI rotational transformation, and  $\vec{\omega}_s$  is the satellite's angular velocity vector. Based on the predefined operational parameters, the position vector magnitude is  $r_s = R_E + R_h = 42,164$  km, where  $R_h$  is the satellite altitude.

*3.3.1.1 Field of View.* The satellite FOV, assuming a spherical Earth, is the visible circular area about the subsatellite point (SSP) [16, page 161]. Based on the operational parameters for satellite location and aircraft transmitter mini-

imum elevation angle, as calculated in Appendix B, the satellite FOV is determined to be  $\text{FOV}_S = 16.34^\circ$  [0.285 rad], which covers a circular area  $\pm 61.82^\circ$  [ $\pm 1.078$  rad] along the Earth's surface about the SSP. The receiver FOV, as calculated in Appendix D, is determined to be  $\text{FOV}_R = 3.82^\circ$  [0.066 rad], which covers a circular area  $\pm 10.81^\circ$  [ $\pm 0.189$  rad]. The relationship between satellite FOV and receiver FOV is depicted in Figure 3.8.

*3.3.1.2 Satellite Attitude Dynamics.* Assuming small attitude motion, as shown in Appendix B, satellite orientation is defined by Euler angles: roll angle,  $\phi_s$ , pitch angle,  $\theta_s$ , and yaw angle,  $\psi_s$ . Applying attitude kinematics, the satellite angular velocity vector is defined by

$$\vec{\omega}_s = \begin{pmatrix} \omega_x \\ \omega_y \\ \omega_z \end{pmatrix} = \begin{pmatrix} \dot{\phi}_s - \omega_o \psi_s \\ \dot{\theta}_s - \omega_o \\ \dot{\psi}_s + \omega_o \phi_s \end{pmatrix} \quad (3.11)$$

where  $\omega_o$  is the orbital angular velocity. However, due to the geosynchronous orbit, the orbital period is equivalent to the Earth's rotational period, which is  $\omega_E = 7.289 \times 10^{-5}$  rad/s. Hence, satellite attitude dynamics is defined by linearized Euler's equations of rotational motion as,

$$\begin{aligned} \ddot{\phi}_s &= \omega_o \left[ 1 + \frac{(I_z - I_x)}{I_x} \right] \dot{\psi}_s + \omega_o^2 \left[ \frac{(I_z - I_x)}{I_x} \right] \phi_s + \frac{T_x}{I_x} \\ \ddot{\theta}_s &= \frac{T_y}{I_x} \\ \ddot{\psi}_s &= -\omega_o \dot{\phi}_s + \frac{T_z}{I_z} \end{aligned} \quad (3.12)$$

where  $I_x$  and  $I_z$  are the mass moments of inertia of the axisymmetric satellite body and  $T_x$ ,  $T_y$ , and  $T_z$  are the total torques about each principal axis.

*3.3.2 Optical Communication System.* The optical communication system (OCS), as derived in Appendix A, performs OOK demodulation by direct detection



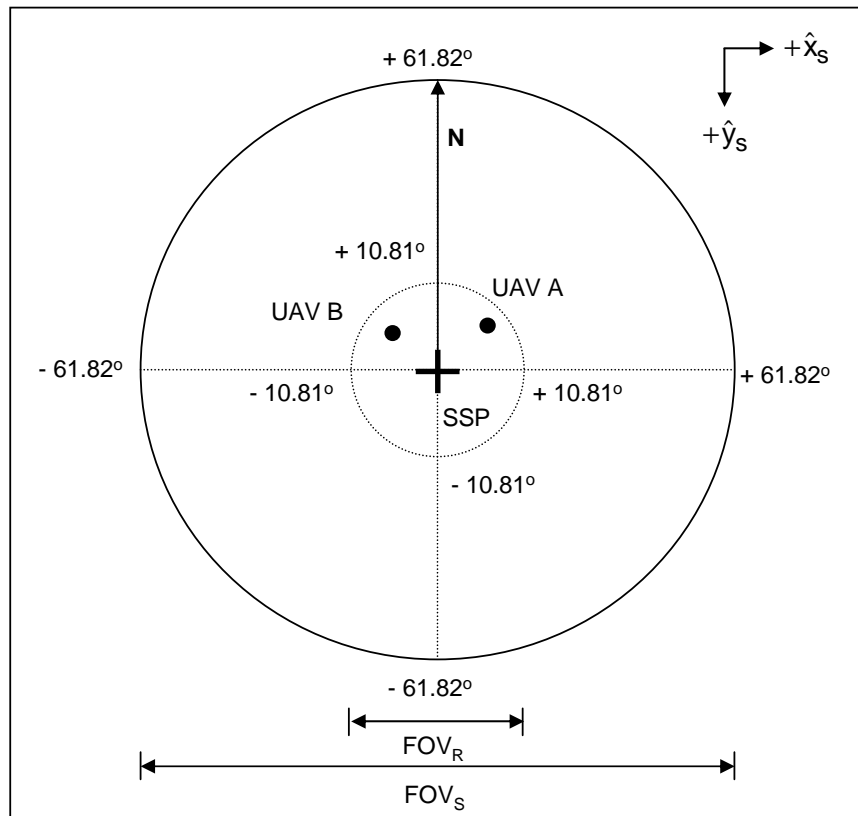


Figure 3.8: Satellite and Receiver Field of View

of the received optical signal power,  $P_r$ . Received power is used to determine communication link BER, a fundamental performance measure for digital communication systems. As a function of radial tracking error,  $P_r$  is defined as

$$P_r(\rho_r) = (\alpha_r G_r) L_r = (\alpha_r G_r) \exp(-G_r \rho_r^2) \quad (3.13)$$

where  $\rho_r$  is the radial tracking error,  $\alpha_r$  incorporates a priori known parameters of the Friis transmission equation,  $G_r$  is the receiver gain, and  $L_r$  is the tracking loss. The received optical signal power is converted by an avalanche photodiode (APD), with a multiplicative gain of 20, into a received current signal, defined as

$$\begin{aligned} i_r &= i_{dc} + i_n \\ &= R_{ph} P_r + i_n \quad [\text{A}] \end{aligned} \quad (3.14)$$

where  $i_{dc}$  is the detector DC current,  $R_{ph}$  is the detector responsivity, and  $i_n$  is the detector noise. After filtering, the received bit energy to average noise power spectral density ratio  $E_b/N_o$ , as derived in Appendix A, is determined as

$$\frac{E_b}{N_o} = [K_r \alpha_r G_r \exp(-G_r \rho_r^2)]^2 \quad (3.15)$$

where  $K_r$  is a function of  $R_{ph}$  and noise power. Based on the previously defined transmitter, channel, and receiver parameters, the relationship between  $E_b/N_o$  and  $\rho_r$  is shown in Figure 3.9. In particular, the longer wavelength, less affected by atmospheric loss, has a slower attenuation rate as  $\rho_r$  increases.

The associated probability of bit error, as defined in Chapter II, is determined by [27, page 298]

$$P_B = BER = \int_0^\infty [P_{mod} f_R(\rho_r)] d\rho_r \quad (3.16)$$

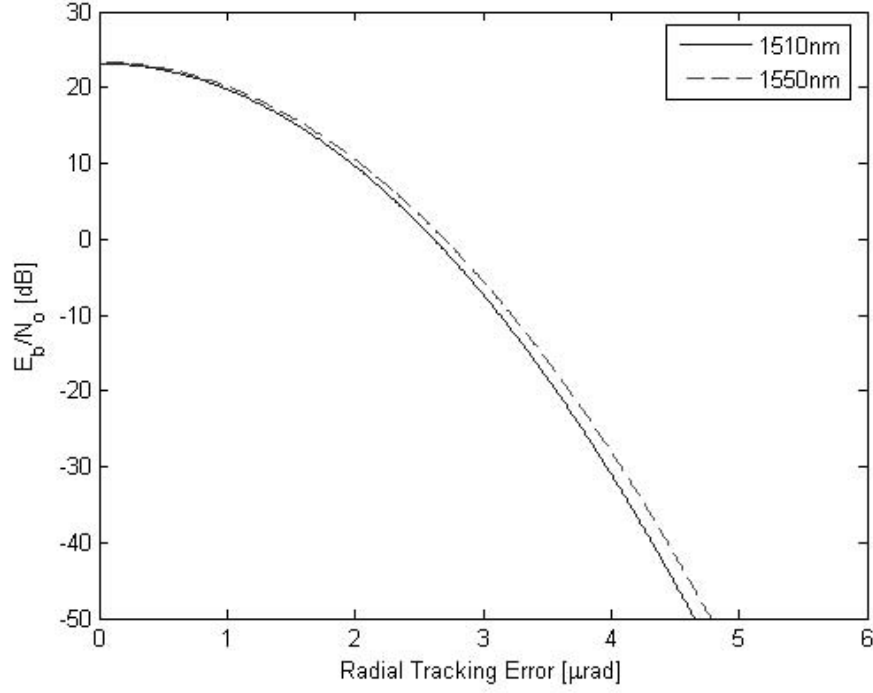


Figure 3.9:  $E_b/N_o$  Performance due to Radial Tracking Error

where  $P_{mod}$  is the modulation BER and  $f_R(\rho_r)$  is the radial tracking error probability distribution function, defined in Chapter II by Equation 2.19. After incorporation of the OOK modulation BER, defined in Appendix A by Equation A.38, the probability of bit error becomes

$$P_B = \int_0^\infty Q [K_r \alpha_r G_r \exp(-G_r \rho_r^2)] f_R(\rho_r) d\rho_r \quad (3.17)$$

where  $Q[x]$  is the complementary error function. Based on the previously defined transmitter, channel, and receiver parameters, the theoretical probability of bit error as a function of radial tracking error is shown in Figure 3.10. In particular, in order to maintain a  $BER = 10^{-6}$  the maximum radial tracking error for Beam A (1510 nm) is approximately 1.68  $\mu\text{rad}$  and Beam B (1550 nm) is approximately 1.74  $\mu\text{rad}$ . Thus, for the purposes of this study, 1.68  $\mu\text{rad}$  will be the tracking error performance limit.

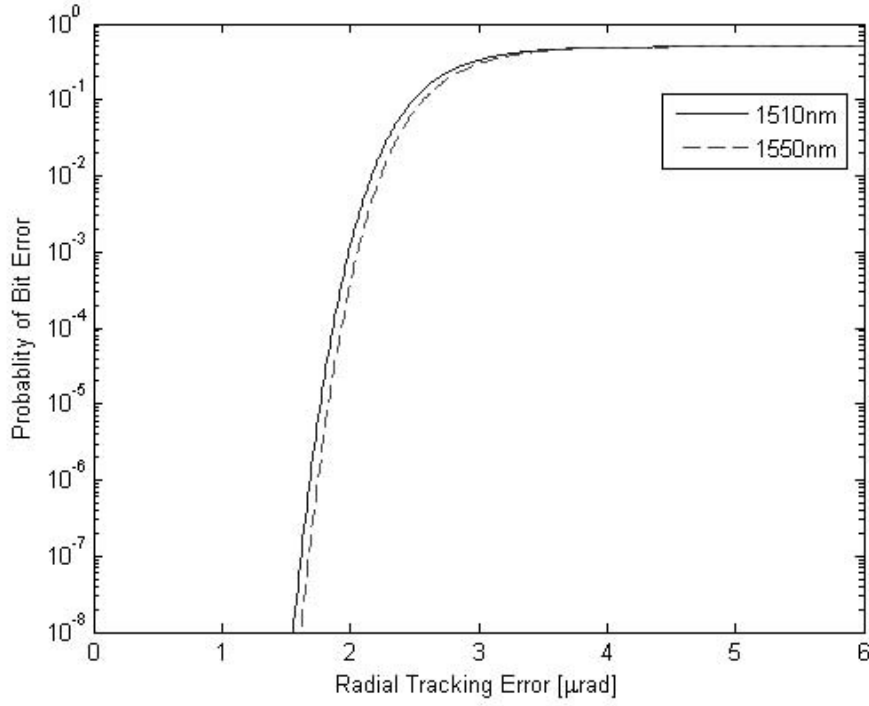


Figure 3.10: Probability of Bit Error Performance Curve due to Radial Tracking Error

### 3.3.3 Receiver Effects.

**3.3.3.1 Platform Disturbances.** Since attitude disturbances are the primary concern, it is assumed the satellite structure and associated ADCS adequately compensates for expected environmental disturbances. To account for common on-orbit internal disturbances, as described in Appendix B, a zero mean Gaussian noise power spectral density (PSD) model was developed by the European Space Agency (ESA) OLYMPUS satellite experiment as [36, page 206]

$$S_S(f) = \frac{160}{1 + f^2} \text{ } [\mu\text{rad}^2/\text{Hz}] \quad (3.18)$$

**3.3.3.2 Detector Noise.** As derived in Appendix D, photodetector noise is comprised of three independent noise sources: quantum shot noise, thermal noise, and dark current. As such, the equivalent current noise power within a pho-

to detector is defined as [1, page 154]

$$i_n^2 = i_{qsh}^2 + i_{th}^2 + 2q_e i_{du} BW_d \text{ [A}^2\text{]} \quad (3.19)$$

where  $i_{qsh}^2$  is quantum shot noise current power,  $i_{th}^2$  is thermal noise current power,  $q_e$  is the electronic charge,  $i_{du}$  is unmultiplied dark current.  $BW_d$  is the detection bandwidth, which is a function of the null-to-null signal bandwidth,  $BW_{NN} = 200$  KHz, determined as [17, pages 943-944]

$$\begin{aligned} BW_d &\approx 0.886 BW_{NN} = (0.886)(200) \\ &\approx 177.2 \text{ [KHz]} \end{aligned} \quad (3.20)$$

Thus, as shown in Appendix D, the the maximum theoretical detector equivalent noise power occurs within a range of  $3.9162 \times 10^{-18} \text{ A}^2$  to  $3.9164 \times 10^{-18} \text{ A}^2$ , based on wavelength and elevation angle.

### 3.4 Dual Fine Tracking Control System Model

Derived from Figure 1.2, the dual fine tracking control system (FTCS) model is presented in the closed loop diagram shown in Figure 3.11. Plant disturbance signals,  $wd_A(t)$  and  $wd_B(t)$ , are caused by transmitter, channel, and receiver effects.  $F(t)$  is the FSM output x-axis and y-axis angle used to steer the incident beams. Residual tracking error, for each beam, is determined respectively by

$$Er_A(t) = wd_A(t) - F(t) = \begin{bmatrix} wd_{Ax}(t) - F_x(t) \\ wd_{Ay}(t) - F_y(t) \end{bmatrix} \quad (3.21)$$

$$Er_B(t) = wd_B(t) - F(t) = \begin{bmatrix} wd_{Bx}(t) - F_x(t) \\ wd_{By}(t) - F_y(t) \end{bmatrix} \quad (3.22)$$

Each quadrant detector (QD), assumed to have an identity gain matrix transfer function, measures the respective beam centroid azimuth (x-axis) and elevation (y-axis)

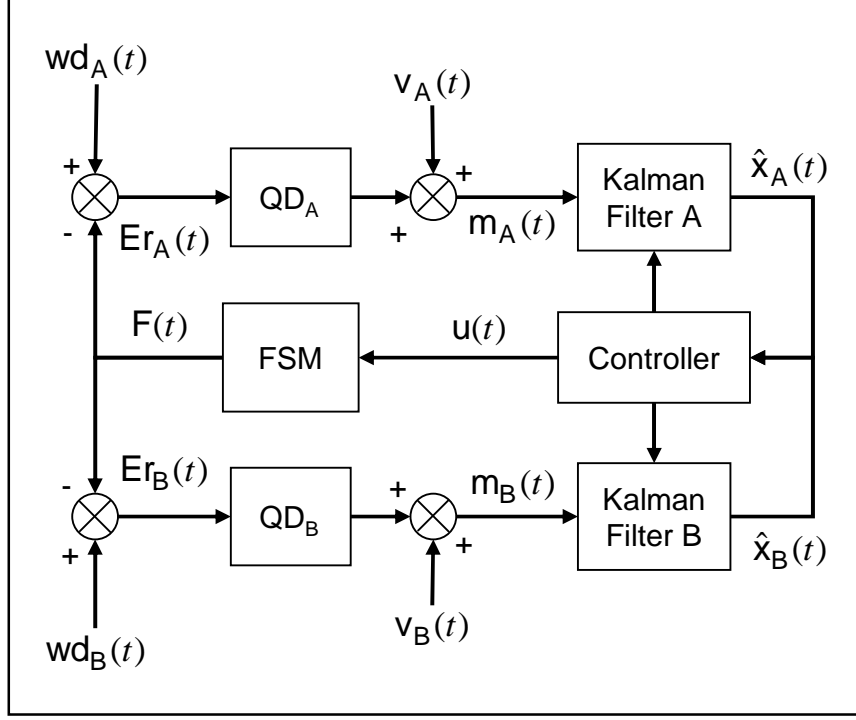


Figure 3.11: Dual Fine Tracking Control System Closed Loop Diagram

tracking error. After corruption by zero-mean white Gaussian noise, denoted by  $v_A(t)$  and  $v_B(t)$  respectively, the measured states are determined by

$$m_A(t) = Er_A(t) + v_A(t) = \begin{bmatrix} Er_{Ax}(t) + v_{Ax}(t) \\ Er_{Ay}(t) + v_{Ay}(t) \end{bmatrix} \quad (3.23)$$

$$m_B(t) = Er_B(t) + v_B(t) = \begin{bmatrix} Er_{Bx}(t) + v_{Bx}(t) \\ Er_{By}(t) + v_{By}(t) \end{bmatrix} \quad (3.24)$$

A Kalman filter is used to estimate the system states,  $\hat{x}_A(t)$  and  $\hat{x}_B(t)$  respectively for each beam, based on the noise corrupted measured states and control signal,  $u(t)$ . Based on an as yet to be determined switching time,  $T_{sw}$ , the controller switches between the estimated system states and generates the control signal based on the linear quadratic regulator (LQR) algorithm, which commands the FSM.

*3.4.1 Plant Disturbance.* Plant disturbance is comprised of the transmitter pointing error, satellite internal disturbances, and optical turbulence induced random beam wander. Transmitter point error and beam wander are assumed to be zero-mean white Gaussian noise inputs. However, satellite disturbance is a frequency dependent zero-mean Gaussian distribution, hence nonwhite noise, also known as colored noise.

*3.4.1.1 Colored Noise Source.* A shaping filter, combined with a unit spectral density white noise source, is used to model colored noise, defined as [7, pages 78-79]

$$G_{SF}(s) = \frac{b_F}{s + a_F} \quad (3.25)$$

where the filter parameters,  $a_F$  and  $b_F$ , are determined from the filter output power spectral density as [25, page 190]

$$\begin{aligned} S_{SF}(\omega) &= \frac{b_F^2}{\omega^2 + a_F^2} = \left( \frac{1}{1 + f^2} \right) \left( \frac{2\pi}{2\pi} \right)^2 \\ &= \frac{(2\pi)^2}{\omega^2 + (2\pi)^2} \end{aligned} \quad (3.26)$$

Thus, the shaping filter transfer function is defined as

$$G_{SF}(s) = \frac{2\pi}{s + 2\pi} \quad (3.27)$$

The associated satellite disturbance white noise source, defined by zero mean Gaussian statistics, has a power spectral density defined by [25, page 190]

$$S_S(f) = \frac{160}{2} = 80 \times 10^{-12} \text{ [rad}^2/\text{Hz}] \quad (3.28)$$

*3.4.1.2 White Noise Sources.* Transmitter pointing errors and optical turbulence induced random beam wander, are assumed to be frequency independent. Thus, an equivalent white noise power spectral density for each noise source is deter-

mined respectively as

$$[S_t(f)]_A = (\sigma_t^2)_A = 4.0274 \times 10^{-12} \text{ [rad}^2/\text{Hz}] \quad (3.29)$$

$$[S_t(f)]_B = (\sigma_t^2)_B = 4.2436 \times 10^{-12} \text{ [rad}^2/\text{Hz}] \quad (3.30)$$

$$S_{bw}(f) = [rms(bw)]^2 \text{ [rad}^2/\text{Hz}] \quad (3.31)$$

*3.4.1.3 Total Plant Disturbance.* The total plant disturbance white power spectral density, for azimuth and elevation tracking error, is defined respectively for each incident beam as

$$\begin{aligned} [S_w(f)]_A &= S_S(f) + [S_t(f)]_A + [S_{bw}(f)]_A \\ &= (80 + 4.0274) \times 10^{-12} + [rms(bw)_A]^2 \text{ [rad}^2/\text{Hz}] \end{aligned} \quad (3.32)$$

$$\begin{aligned} [S_w(f)]_B &= S_S(f)(f) + [S_t(f)]_B + [S_{bw}(f)]_B \\ &= (80 + 4.2436) \times 10^{-12} + [rms(bw)_B]^2 \text{ [rad}^2/\text{Hz}] \end{aligned} \quad (3.33)$$

where  $rms(bw)$  for each beam is determined by its spatial location within the receiver FOV. Thus, based on the previously determined random beam wander profile, the satellite disturbance is the dominant plant disturbance source.

*3.4.2 Measurement Noise.* Measurement noise is caused by the QD noise, assumed to be zero-mean white Gaussian noise. However, QD SNR is inversely proportional to the azimuth and elevation error variance, as derived in Appendix D [15, page 182]. Thus, based on the predetermined maximum theoretical detector noise power and assuming a unit signal power, the measurement noise power spectral den-



sity, is defined respectively for each incident beam as

$$[S_v(f)]_A \approx 3.9163 \times 10^{-18} \text{ [rad}^2/\text{Hz}] \quad (3.34)$$

$$[S_v(f)]_B \approx 3.9164 \times 10^{-18} \text{ [rad}^2/\text{Hz}] \quad (3.35)$$

*3.4.3 Plant.* The FSM is a linear mechanical device subject to rotational motion about two orthogonal axes, commonly referred to as tip (x-axis) and tilt (y-axis) axes. Assuming uncoupled dynamics, motion about either axis is modeled by a second order transfer function as [21, page 226]

$$G_{xx} = G_{yy} = \frac{\omega_n^2}{s^2 + 2\zeta\omega_n s + \omega_n^2} \quad (3.36)$$

where  $\omega_n$  is the natural frequency and  $\zeta$  is the damping ratio. For the purposes of this study, each axis is assumed to have the same natural frequency and damping ratio, defined respectively as  $\omega_n = 5000 \text{ rad/s}$  and  $\zeta = 0.5$ , based on experiment and analysis of a Newport Corporation FSM [33, page 3]. Thus, the FSM transfer function is defined as

$$G_{FSM} = \begin{bmatrix} G_{xx} & 0 \\ 0 & G_{yy} \end{bmatrix} \quad (3.37)$$

Since  $\zeta < 1$ , each axis behaves like a single-input to single-output (SISO) underdamped system. Hence, the FSM poles are complex conjugates and lie in the left-half s-plane, calculated as [21, pages 225-226]

$$p_1, p_2 = -2.5 \pm 4.3301i \quad (3.38)$$

$$p_3, p_4 = -2.5 \pm 4.3301i \quad (3.39)$$

Thus, each FSM axis is a stable SISO system with an initial oscillatory transient response. The associated damped natural frequency is determined as [21, page 227]

$$\omega_d = \omega_n \sqrt{1 - \zeta^2} \quad (3.40)$$

$$= (5000) \sqrt{1 - (0.5)^2} = 4330.1 \text{ [rad/s]} \quad (3.41)$$

*3.4.3.1 Time Response.* Applying the MATLAB Control System toolbox step response algorithm, the FSM step response is shown in Figure 3.12. Transient response characteristics for each FSM axis, rise time, maximum percent overshoot, and 2% settling time, were calculated respectively as [21, pages 231-233]

$$t_r = \left( \frac{1}{\omega_d} \right) \tan^{-1} \left( \frac{\omega_d}{\zeta \omega_n} \right) = 0.0003 \text{ [sec]} \quad (3.42)$$

$$\text{MP\%} = \exp[-\pi(\zeta \omega_n)/\omega_d] \times 100\% = 16.3 \% \quad (3.43)$$

$$t_s = \frac{4}{\zeta \omega_n} = 0.0016 \text{ [sec]} \quad (3.44)$$

*3.4.3.2 Frequency Response.* Since the tip and tilt axes are uncoupled and have the same response behavior, applying the MATLAB Control System toolbox Bode algorithm, the FSM frequency response for one axis is shown in Figure 3.13. The FSM bandwidth, based on the  $-3$  dB cutoff frequency, is determined approximately as

$$FSM_c = 6.36 \times 10^3 \text{ [rad/sec]} \quad (3.45)$$

$$= 1.012 \text{ [KHz]} \quad (3.46)$$

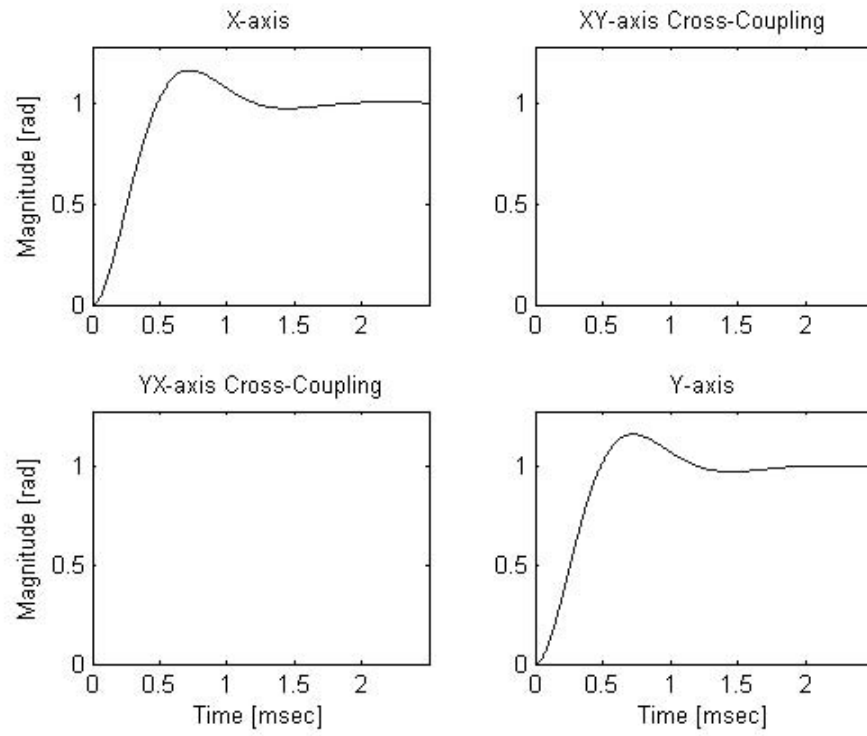


Figure 3.12: Fast Steering Mirror Step Response

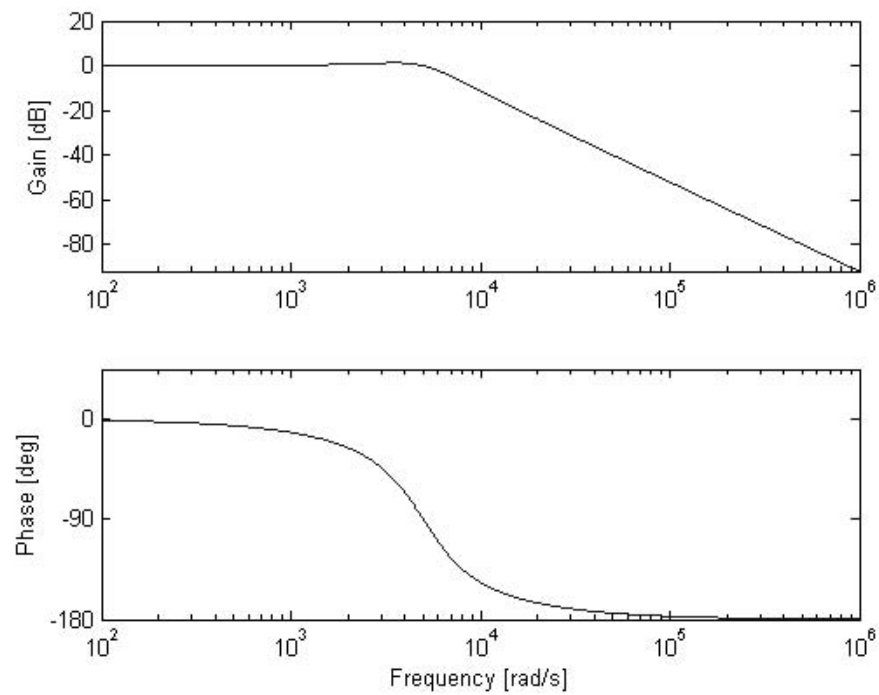


Figure 3.13: Tip/Tilt Axis Frequency Response

3.4.3.3 *State Space Model.* The plant state space representation is

defined as

$$\dot{X}(t) = \mathbf{A}X(t) + \mathbf{B}_u u(t) + \mathbf{B}_w w(t) \quad (3.47)$$

$$m(t) = \mathbf{C}_m X(t) + v(t) \quad (3.48)$$

where the state vector is defined as

$$X(t) = \begin{bmatrix} F_x(t) & \dot{F}_x(t) & F_y(t) & \dot{F}_y(t) \end{bmatrix}^T \quad (3.49)$$

Thus, the control, plant disturbance, and measurement noise input vectors are defined respectively as

$$u(t) = \begin{bmatrix} u_x(t) & u_y(t) \end{bmatrix}^T \quad (3.50)$$

$$wd(t) = \begin{bmatrix} wd_x(t) & wd_y(t) \end{bmatrix}^T \quad (3.51)$$

$$v(t) = \begin{bmatrix} v_x(t) & v_y(t) \end{bmatrix}^T \quad (3.52)$$

Based on the system state vector, input vectors, and FSM transfer function, the linear time-invariant state matrices are defined as

$$\mathbf{A} = \begin{pmatrix} 0 & 1 & 0 & 0 \\ -2.5 \times 10^7 & -5000 & 0 & 0 \\ 0 & 0 & 0 & 1 \\ 0 & 0 & -2.5 \times 10^7 & -5000 \end{pmatrix}$$

$$\mathbf{B}_u = \begin{pmatrix} 0 & 0 \\ 2.5 \times 10^7 & 0 \\ 0 & 0 \\ 0 & 2.5 \times 10^7 \end{pmatrix}; \quad \mathbf{B}_w = \begin{pmatrix} 0 & 0 \\ 1 & 0 \\ 0 & 0 \\ 0 & 1 \end{pmatrix}$$

$$\mathbf{C}_m = \begin{pmatrix} 1 & 0 & 0 & 0 \\ 0 & 0 & 1 & 0 \end{pmatrix}$$

*3.4.4 Kalman Filter.* Since the LQR algorithm requires full state feedback, an estimator is required to estimate the tip and tilt slew rate,  $\dot{F}_x(t)$  and  $\dot{F}_y(t)$  respectively. Based on the measured states, subject to independent plant noise and measurement noise being white, a Kalman filter is the optimal estimator [7, page 231]. However, the plant disturbance is nonwhite noise, thus the plant model must be augmented with a shaping filter state model [7, page 266]. The Kalman filter is designed based on the augmented plant model, with the filter gain being determined using algorithms available in MATLAB.

*3.4.4.1 Augmented Plant State Model.* The shaping filter state space model is defined as

$$\dot{X}_F(t) = \mathbf{A}_F X_F(t) + \mathbf{B}_F w_1(t) \quad (3.53)$$

$$wd(t) = \mathbf{C}_F X_F(t) \quad (3.54)$$

where  $w_1(t)$  is a unit spectral density two input matrix, and the shaping filter state vector is defined as

$$X_F(t) = \begin{bmatrix} wd_x(t) & wd_y(t) \end{bmatrix}^T \quad (3.55)$$

The resulting shaping filter matrices are defined as

$$\mathbf{A}_F = -a_F \begin{pmatrix} 1 & 0 \\ 0 & 1 \end{pmatrix}; \mathbf{B}_F = b_F \begin{pmatrix} 1 & 0 \\ 0 & 1 \end{pmatrix}; \mathbf{C}_F = \begin{pmatrix} 1 & 0 \\ 0 & 1 \end{pmatrix}$$

Thus, the augmented plant model is defined as

$$\dot{X}_G(t) = \mathbf{A}_G X_G(t) + \mathbf{B}_G u(t) + \mathbf{B}_w w_1(t) \quad (3.56)$$

$$m(t) = \mathbf{C}_m X_G(t) + v(t) \quad (3.57)$$

where the augmented state vector is defined as

$$X_G(t) = \begin{bmatrix} X(t) & \vdots & X_F(t) \end{bmatrix}^T \quad (3.58)$$

Based on the augmented state vector and input vectors, the time-invariant state matrices are defined as

$$\mathbf{A}_G = \begin{bmatrix} \mathbf{A} & \vdots & \mathbf{B}_w \mathbf{C}_F \\ \dots & & \dots \\ 0_{2 \times 4} & \vdots & \mathbf{A}_F \end{bmatrix}; \quad \mathbf{B}_G = \begin{bmatrix} \mathbf{B}_u \\ \dots \\ 0_{2 \times 2} \end{bmatrix}; \quad \mathbf{B}_w = \begin{bmatrix} 0_{4 \times 2} \\ \dots \\ \mathbf{B}_F \end{bmatrix}$$

$$\mathbf{C}_m = \begin{pmatrix} -\mathbf{C}_m & \vdots & \mathbf{C}_F \end{pmatrix}$$

The augmented output matrix is chosen to yield a tracking error, defined as

$$\begin{aligned} Er(t) &= \begin{pmatrix} -\mathbf{C}_m & \vdots & \mathbf{C}_F \end{pmatrix} \begin{bmatrix} X(t) \\ \dots \\ X_F(t) \end{bmatrix} = -\mathbf{C}_m X(t) + \mathbf{C}_F X_F(t) \\ &= \begin{bmatrix} wd_x(t) - F_x(t) \\ wd_y(t) - F_y(t) \end{bmatrix} \end{aligned} \quad (3.59)$$

*3.4.4.2 Steady-State Kalman Filter.* Although the plant 2% settling time is 0.0016 seconds, the fine tracking control system (FTCS) is envisioned to operate over a longer time period. Thus, the Kalman filter is designed to operate over a time period longer than the plant settling time. Hence, a steady-state Kalman

filter will be used to estimate the states for each beam, which is nearly optimal when estimating states over a long time period [7, page 256]. The steady-state Kalman filter, defined by the predictor/corrector form, is implemented for each beam respectively as [7, page 257]

$$\dot{\hat{X}}_A(t) = \mathbf{A}_G \hat{X}_A(t) + \mathbf{B} \mathbf{u}_G u(t) + \mathbf{L}_A \left[ m_A(t) - \mathbf{C} \mathbf{m}_G \hat{X}_A(t) \right] \quad (3.60)$$

$$\dot{\hat{X}}_B(t) = \mathbf{A}_G \hat{X}_B(t) + \mathbf{B} \mathbf{u}_G u(t) + \mathbf{L}_B \left[ m_B(t) - \mathbf{C} \mathbf{m}_G \hat{X}_B(t) \right] \quad (3.61)$$

where the state estimate vectors are defined respectively as

$$\hat{X}_A(t) = \left[ \hat{X}(t) \quad \hat{w}d_{Ax}(t) \quad \hat{w}d_{Ay}(t) \right]^T \quad (3.62)$$

$$\hat{X}_B(t) = \left[ \hat{X}(t) \quad \hat{w}d_{Bx}(t) \quad \hat{w}d_{By}(t) \right]^T \quad (3.63)$$

$\mathbf{L}_A$  and  $\mathbf{L}_B$  are the steady-state Kalman gains, defined respectively by [7, page 242]

$$\mathbf{L}_A = [\Sigma_e(\infty)]_A \mathbf{C} \mathbf{m}_G^T (\mathbf{S}_v)_A^{-1} \quad (3.64)$$

$$\mathbf{L}_B = [\Sigma_e(\infty)]_B \mathbf{C} \mathbf{m}_G^T (\mathbf{S}_v)_B^{-1} \quad (3.65)$$

where  $[\Sigma_e(\infty)]_A$  and  $[\Sigma_e(\infty)]_B$  are the steady-state estimation error covariance matrices respectively for each beam and  $(\mathbf{S}_v)_A$  and  $(\mathbf{S}_v)_B$  are the respective positive definite diagonal measurement noise spectral density matrices. Each steady-state estimation error covariance matrix is computed by solving for the steady-state solution of the algebraic Riccati equation defined as [7, pages 243]

$$\begin{aligned} 0 &= \Sigma_e(\infty) \mathbf{A}_G^T + \mathbf{A}_G \Sigma_e(\infty) + [\mathbf{B} \mathbf{w}_G] [\mathbf{S}_w] [\mathbf{B} \mathbf{w}_G^T] \\ &\quad - \Sigma_e(\infty) [\mathbf{C} \mathbf{m}_G^T] [\mathbf{S}_v^{-1}] [\mathbf{C} \mathbf{m}_G] \Sigma_e(\infty) \end{aligned} \quad (3.66)$$

where  $\mathbf{S}_w$  is the associated positive definite diagonal plant disturbance noise spectral density matrix.

*3.4.5 Controller.* As determined for the Kalman filter, the dual FTCS is designed to operate over a longer time period than the transient response; hence, the LQR controller is designed as a steady-state controller [7, page 196]. However, the control system must regulate the tracking error occurring from both beams. Thus, with only a single FSM, the controller is designed to switch between the estimated states from each filter.

*3.4.5.1 Linear Quadratic Regulator Control.* Since the linear plant is driven by random conditions and random disturbance inputs, a stochastic regulator is the optimal controller, which is designed to minimize a cost function defined as [7, pages 218, 221]

$$J_{SR} = \frac{1}{2}E \left[ \int_0^\infty \hat{E}r^T(t) \mathbf{Z} \hat{E}r(t) + u^T(t) \mathbf{R} u(t) \right] \quad (3.67)$$

where  $\mathbf{Z}$  is the tracking error weighting matrix and  $\mathbf{R}$  is the control weighting matrix, in which both are initially assumed to be identity matrices. However, due to being in steady-state, the stochastic regulator gain equals the steady-state LQR gain [7, page 221]. Thus, in terms of the state estimates, the controller cost function is defined as

$$\begin{aligned} J &= \frac{1}{2}E \left[ \int_0^\infty \hat{E}r^T(t) \mathbf{Z} \hat{E}r(t) + u^T(t) \mathbf{R} u(t) \right] \\ &= \frac{1}{2}E \left\{ \int_0^\infty \left[ \mathbf{C} \mathbf{m}_G \hat{\mathbf{X}}_G(t) \right]^T \mathbf{Z} \left[ \mathbf{C} \mathbf{m}_G \hat{\mathbf{X}}_G(t) \right] + u^T(t) \mathbf{R} u(t) \right\} \\ &= \frac{1}{2}E \left\{ \int_0^\infty \hat{\mathbf{X}}_G^T(t) \left[ \mathbf{C} \mathbf{m}_G^T \mathbf{Z} \mathbf{C} \mathbf{m}_G \right] \hat{\mathbf{X}}_G(t) + u^T(t) \mathbf{R} u(t) \right\} \\ &= \frac{1}{2}E \left[ \int_0^\infty \hat{\mathbf{X}}_G^T(t) \mathbf{Q} \hat{\mathbf{X}}_G(t) + u^T(t) \mathbf{R} u(t) \right] \end{aligned} \quad (3.68)$$

where  $\mathbf{Q}$  is the state weighting matrix. Based on the chosen state and control weighting matrices, the optimal steady-state feedback gain is determined by [7, page 206]

$$\mathbf{K} = (\mathbf{R}^{-1}) (\mathbf{B} \mathbf{u}_G^T) (\mathbf{P}) \quad (3.69)$$



where  $\mathbf{P}$  is the steady-state solution of the algebraic Riccati equation, which is defined as [7, pages 206]

$$\mathbf{P}\mathbf{A}_G + \mathbf{A}_G^T\mathbf{P} - \mathbf{P}[\mathbf{B}\mathbf{u}_G] [\mathbf{R}^{-1}] [\mathbf{B}\mathbf{u}_G^T] \mathbf{P} + \mathbf{Q} = 0 \quad (3.70)$$

Thus, the control input to the FSM is defined as [7, page 187]

$$u(t) = -\mathbf{K} \cdot \hat{\mathbf{X}}(t) \quad (3.71)$$

*3.4.5.2 Switching Time.* Since the dual FTCS regulates the tracking error for each beam by switching in time between each state estimate, the system can be considered a switched system. Assuming a time period defined by an arbitrary number,  $T_f$ , the full-state feedback estimate is varied based on a time interval defined by

$$t \in [nT_{sw}, (n+1)T_{sw}] \subset [0, T_f] \quad (3.72)$$

where  $n$  is an arbitrary nonnegative integer and  $T_{sw}$  is the switching time. Thus, the control input is defined as

$$u(t) = \begin{cases} -\mathbf{K} \cdot \hat{\mathbf{X}}_A(t) & : n = 1, 3, 5, \dots \\ -\mathbf{K} \cdot \hat{\mathbf{X}}_B(t) & : n = 0, 2, 4, \dots \end{cases} \quad (3.73)$$

Although, both subsystems are linear with quadratic cost functions, a closed-form solution for an optimal switching time is still an open problem [38, page 2]. Ideally, a switched system must not exhibit the Zeno phenomenon, defined by infinitely many switchings in a finite time period [37, page 2684]. It is envisioned during the analysis process to determine if the dual FTCS satisfies this criteria.

### 3.5 *Summary*

This chapter developed the dual fine tracking control problem. Based on the presented theoretical uplink beam propagation characteristics, a maximum residual radial tracking error of  $1.68 \mu\text{rad}$  is the performance requirement to achieve a communication BER of  $10^{-6}$ . Since the plant is envisioned to operate longer than its settling time and is driven by non-white disturbance noise, a steady-state Kalman filter is used to estimate the plant states augmented with the disturbance noise for each incident beam. Based on these estimated augmented states, linear plant, and quadratic cost function, a steady-state LQR based controller is desired. However, due to two sets of state estimates, the controller must incorporate some type of switching time sequence to regulate tracking error on both beams. Appendix G shows the implemented dual FTCS model designed in SIMULINK.

## IV. Analysis and Results

Analysis of FTCS performance is based on applying Monte Carlo analysis, taking samples generated from multiple simulation runs, and computing an ensemble and temporal average of the outputs. In order to perform ensemble averaging, the system model is converted to a fixed-step system using the SIMULINK Runge-Kutta solver solution. After trial and error, a fixed time step of  $T_s = 5 \times 10^{-5}$  sec was used to ensure the solver did not encounter a singularity. Only ten Monte Carlo simulation runs were performed to ensure against creating memory overloads, due to the small fixed time step and final time selection, in processing the data in MATLAB. In addition, a rate transition block, defaulted to act as a unit delay for continuous sample time, is used on all plant disturbance and measurement noise inputs to ensure proper timing of these inputs into the system. Correlation time for the bandlimited white noise blocks, due to SIMULINK requirements, is changed to an integer factor of the fixed time step as  $t_c = 20T_s = 0.001$  sec.

As determined in Appendix F, simulation results reveal optimum regulator performance is achieved with a state weighting scale factor of 10 and control weighting scale factor of 0.1. In general, initial transients occurred at intervals of approximately 0.001 sec, due to the correlation time for the bandlimited white noise blocks. On the other hand, neither candidate switching time case, defined in Appendix F, positively or negatively affected controller performance. Hence, for the purposes of this study, the defined optimum regulator weighting parameters will be implemented with a switching time of 0.02s, which allows the noise correlation time to remain an order of magnitude faster.

In order to determine relative capability, dual FTCS performance was compared to observed tracking error without control compensation and single fine tracking control of either beam. Noise effects are characterized for measurement and plant disturbance inputs. In particular, UAV spatial separation affects upon plant disturbance were analyzed against the observed tracking error. Disturbance rejection analysis was

performed, for either control case, by comparison of each frequency response function (FRF).

#### 4.1 *Noise Effects*

Noise affects on tracking error were observed for each axis, based on a 5 second simulation time. Each noise source was modeled by a SIMULINK bandlimited white noise block with a correlation time of 0.001 sec. Since the satellite plant disturbance is a colored noise source, a shaping filter is applied after the associated equivalent white noise source block. The output variance of each block was scaled to a unit variance and multiplied by a corresponding gain to yield the desired noise variance, as defined in Chapter III. Each block is assigned a unique random seed value which is reset every simulation case. Frequency responses were calculated for the measurement and plant disturbance noise.

*4.1.1 Measurement Noise.* The measurement noise time response, within a 1 second time domain, is shown in Figure 4.1. In particular, the modeled sensor noise, exhibits similar behavior about each axis. Based on the time response, the corresponding power spectral density (PSD) was calculated and illustrated in Figure 4.2. Up until approximately 1 KHz the PSD is relatively flat, which is consistent with the chosen noise block correlation time.

*4.1.2 Plant Disturbance.* As defined in Chapter III, plant disturbance is a function of the transmitter pointing error, satellite disturbance, and optical turbulence induced random beam wander. Satellite disturbance is modeled as colored noise, while pointing error and beam wander effects were modeled by zero-mean white Gaussian statistics. However, as determined in Appendix E, beam wander increases as propagation distance increases, which is a function of decreasing transmitter elevation angle. Elevation angle changes based upon either changing transmitter altitude or Earth central angle (ECA), as shown in Appendices B and D. Since, transmission

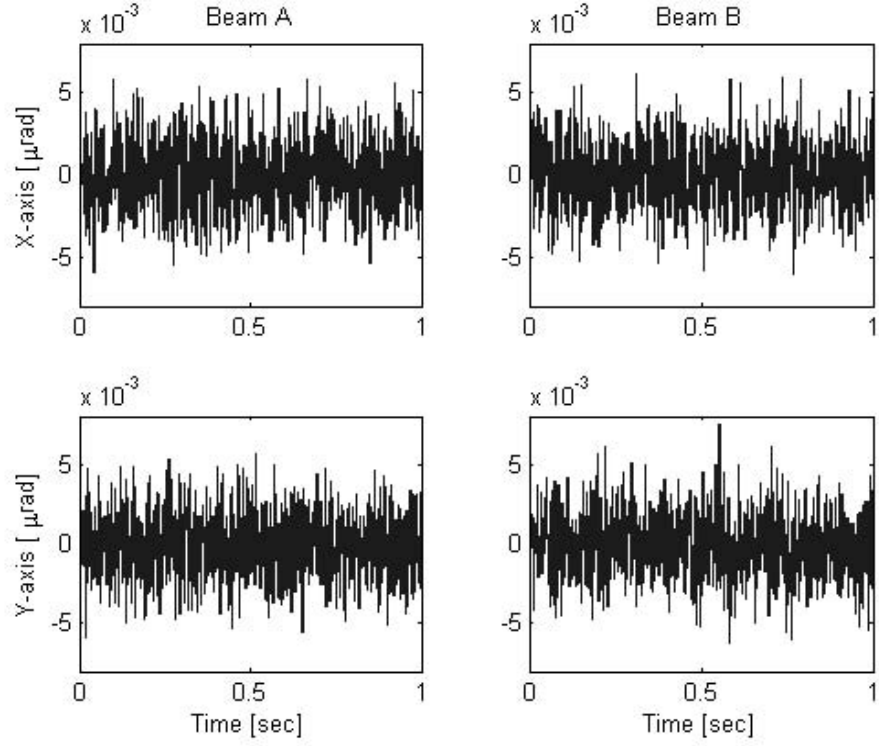


Figure 4.1: Measurement Noise Time Response

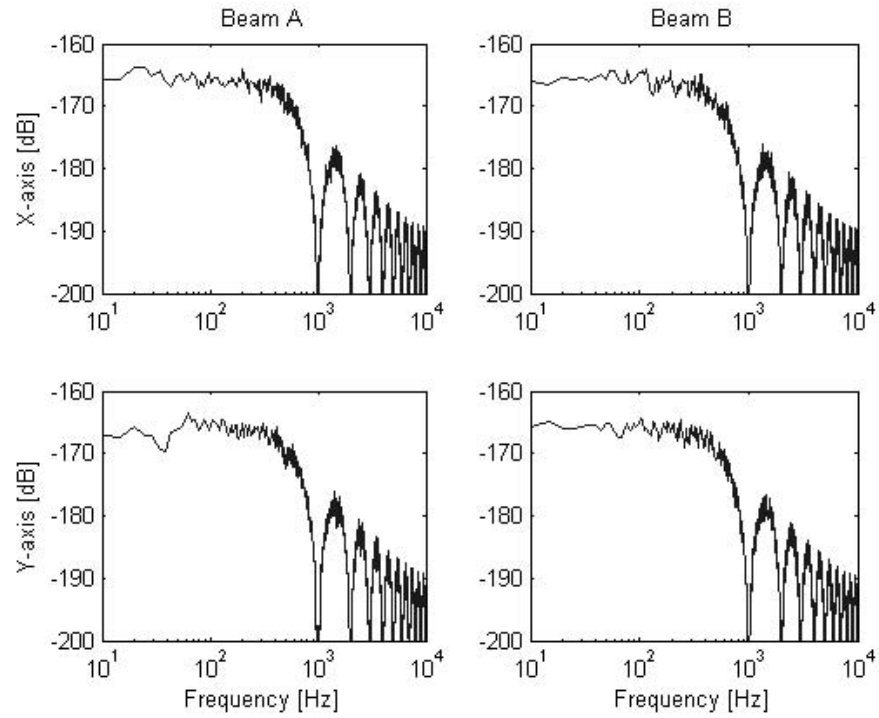


Figure 4.2: Measurement Noise Power Spectral Density

altitude is assumed to be fixed, plant disturbance will vary due to changing ECA, which manifests as a changing spatial separation between aircraft platforms.

*4.1.2.1 Spatial Separation Effects.* Assuming UAV<sub>A</sub> is located at the subsatellite point (SSP), corresponding to an elevation angle of 90°, as UAV<sub>B</sub> closes spatial separation between aircraft, its elevation angle increases, as determined for 13 arbitrarily chosen elevation angles within the receiver field of view (FOV<sub>R</sub>) illustrated in Figure 4.3. In particular, the corresponding rms beam wander decreases as the aircraft elevation angle increases, due to less atmospheric propagation.

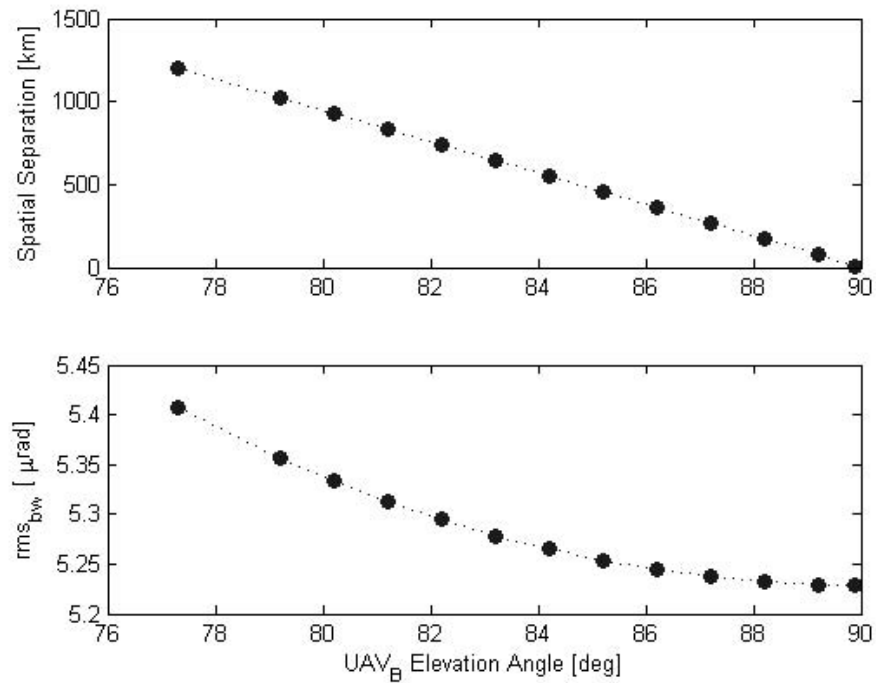


Figure 4.3: Elevation Angle Affects on Spatial Separation and Beam Wander

Based on simulation final time,  $T_f = 1$  second, the ensemble average mean and standard deviation data were calculated over the 10 Monte Carlo runs for tracking error and control input subject to changing rms<sub>bw</sub> resulting from each arbitrarily chosen elevation angle. Figures 4.4 thru 4.6 show a magnified view of the statistics on the time response data for each of the 13 elevation angles. Specifically, Beam

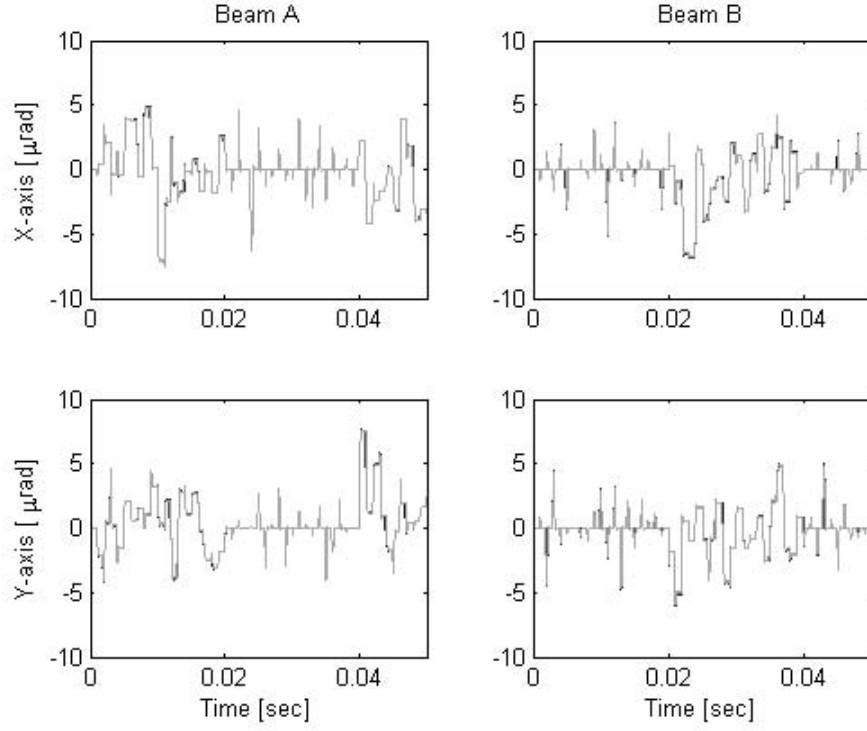


Figure 4.4: Beam Wander Ensemble Average Mean Tracking Error Response for 13 Elevation Angles

B is regulated from 0 to 0.02 sec resulting in reduced mean and standard deviation values. Similarly, Beam A is regulated from 0.02 to 0.04 sec resulting in reduced mean and standard deviation values. Control input response shows similar behavior for each FSM axis, which is due to uncoupled dynamics and each axis modeled by the same SISO system. In particular, both tracking error and control input response data exhibit transients 0.001s, due to noise source correlation time, which behave as random amplitude step inputs. The data indicates similar controlled system performance at all 13 elevation angles. This is clearly illustrated by taking a temporal average of the ensemble averaged mean and standard deviation data for each elevation angle. Figures 4.7 thru 4.9 reveal that each  $\text{rms}_{\text{bw}}$  associated with each elevation angle yields relatively similar temporal mean and standard deviation results for each beam. In addition, temporal mean and standard deviation statistics of control input exhibits a similar trend. Based upon these results for the range in elevation angles within  $\text{FOV}_R$ , spatial separation does not adversely affect FTCS performance.

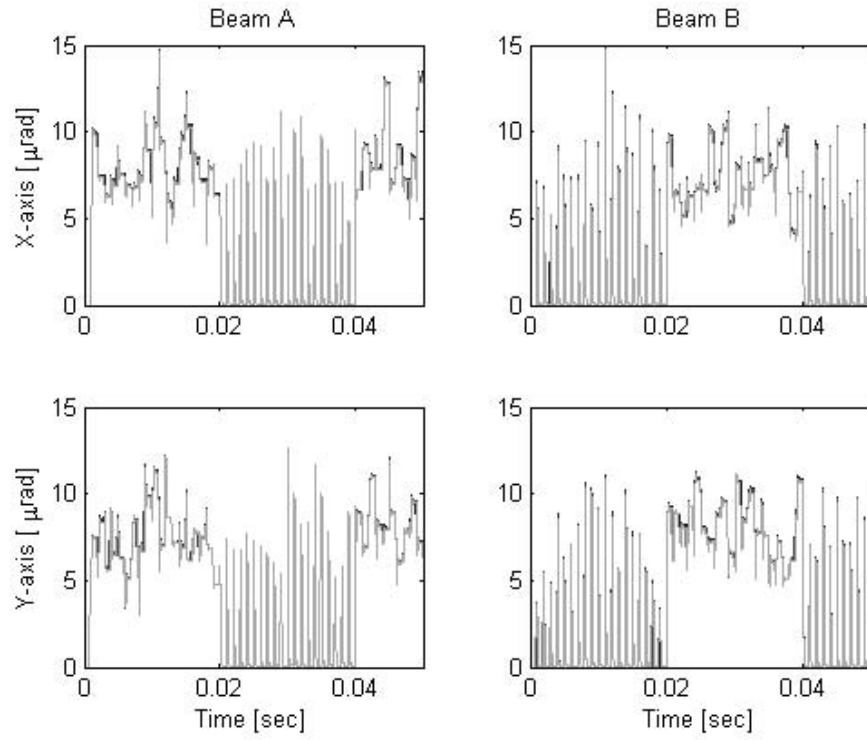


Figure 4.5: Beam Wander Ensemble Average Tracking Error Standard Deviation Response for 13 Elevation Angles

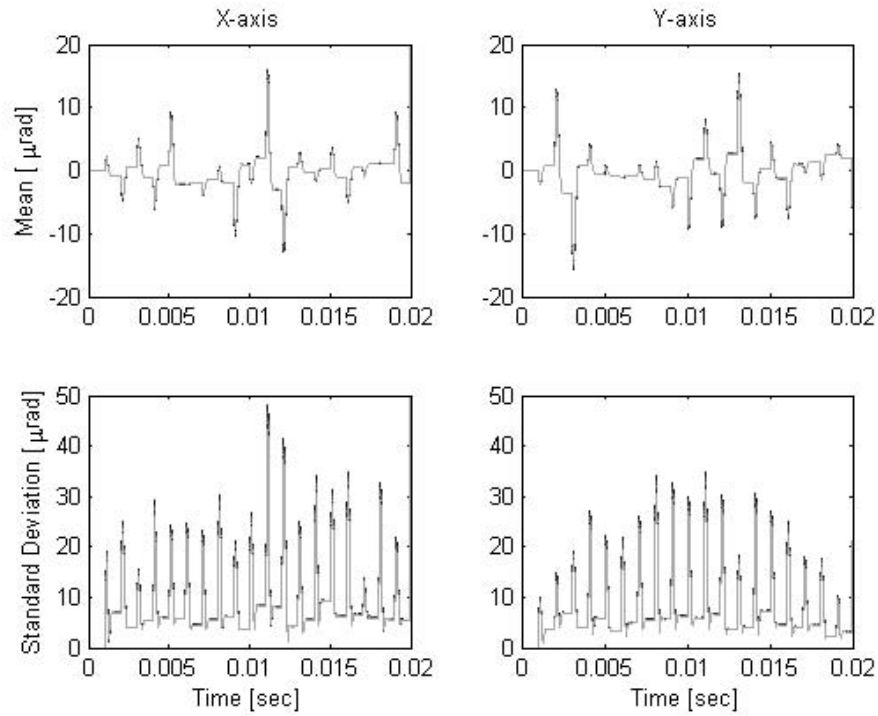


Figure 4.6: Beam Wander Ensemble Average Control Input Response for 13 Elevation Angles



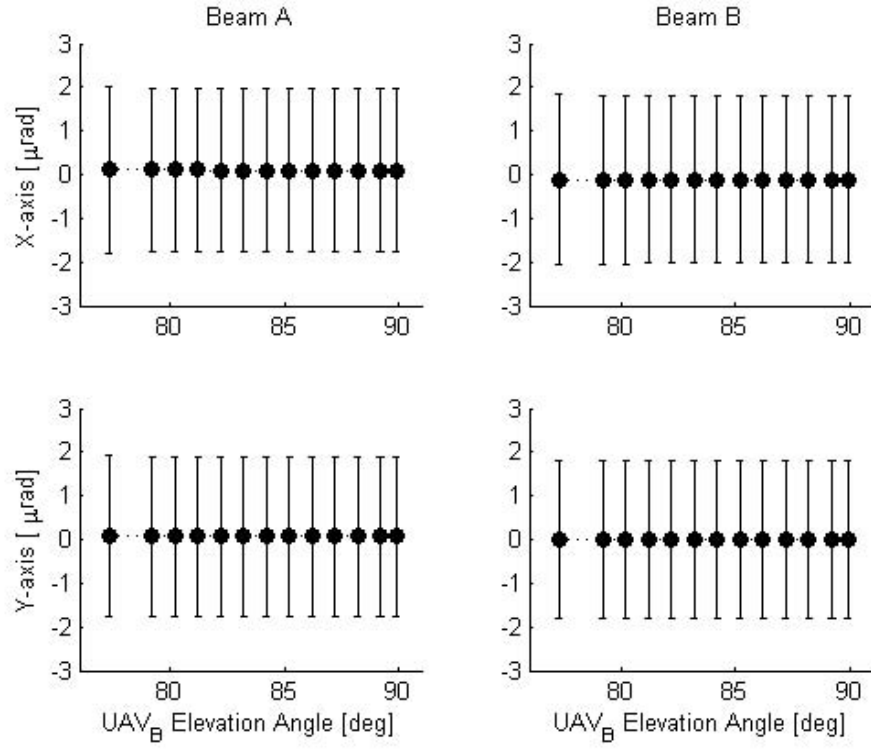


Figure 4.7: Beam Wander Temporal Average Mean Tracking Error Response

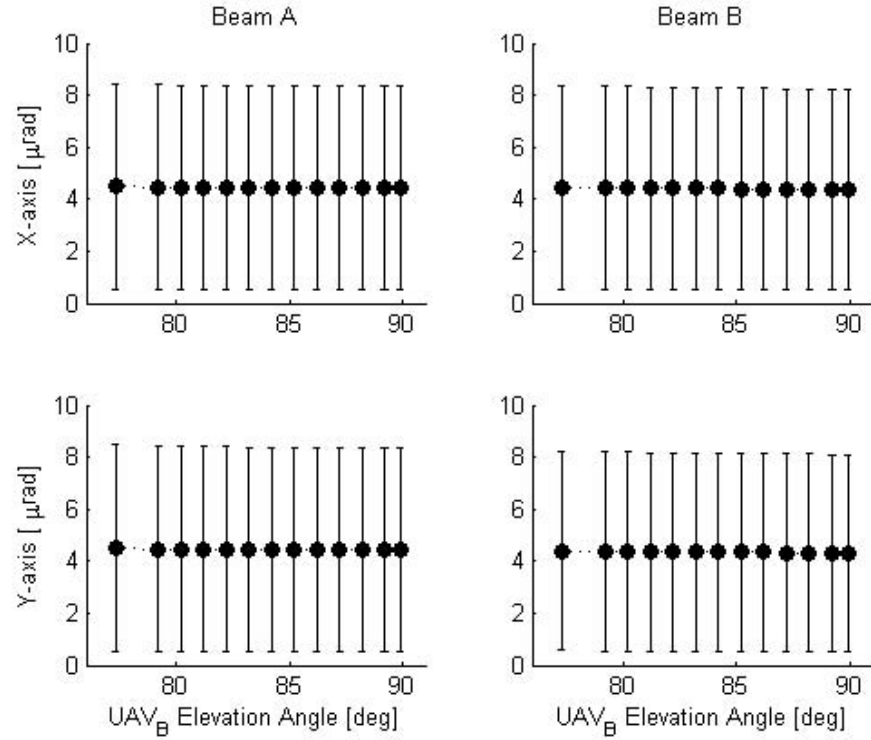


Figure 4.8: Beam Wander Temporal Average Tracking Error Standard Deviation Response

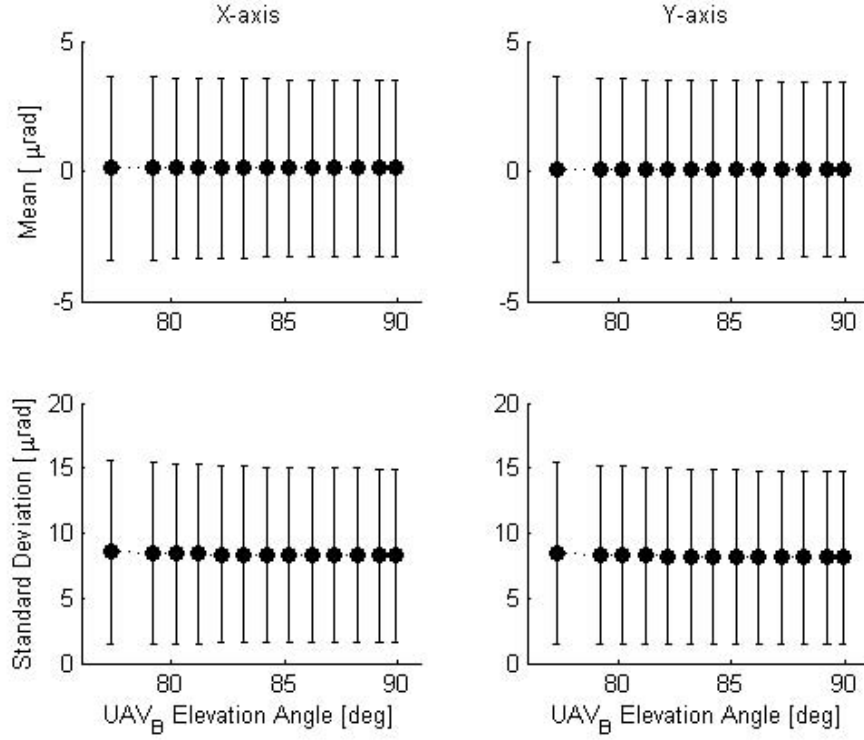


Figure 4.9: Beam Wander Temporal Average Control Input Response

*4.1.2.2 Plant Disturbance Power Spectral Density.* Based on the maximum theoretical beam wander, plant disturbance noise time response over a 1 second time frame is shown in Figure 4.10. In particular, the modeled plant disturbance, exhibits similar behavior about each axis. Based on the time response, the corresponding power spectral density (PSD) was calculated and is illustrated in Figure 4.11. As seen with the measurement noise response, the plant disturbance noise PSD decays above approximately 1 KHz, due to the noise block correlation time.

## 4.2 No Control

Using a 5 second simulation time, tracking error data was observed for each axis and the associated radial tracking error, as derived in Chapter II as  $\rho = \sqrt{x^2 + y^2}$ . Figures 4.12 thru 4.13 illustrate a magnified view of the tracking error time response ensemble average (10 runs) mean and standard deviation data. Clearly, without regulation, the tracking error has a similar time response as the plant disturbance.

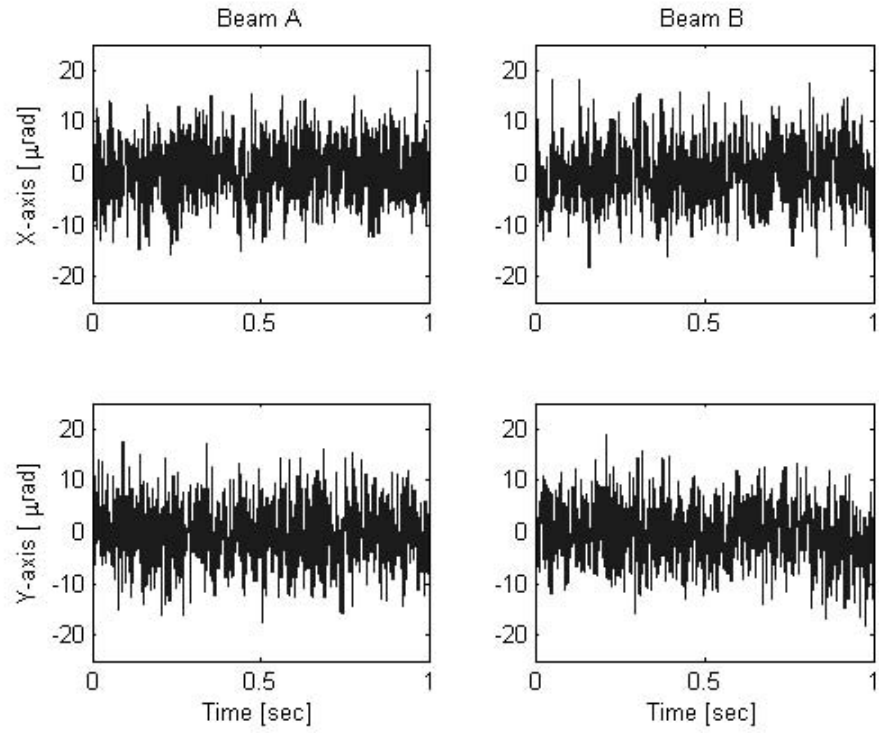


Figure 4.10: Plant Disturbance Time Response

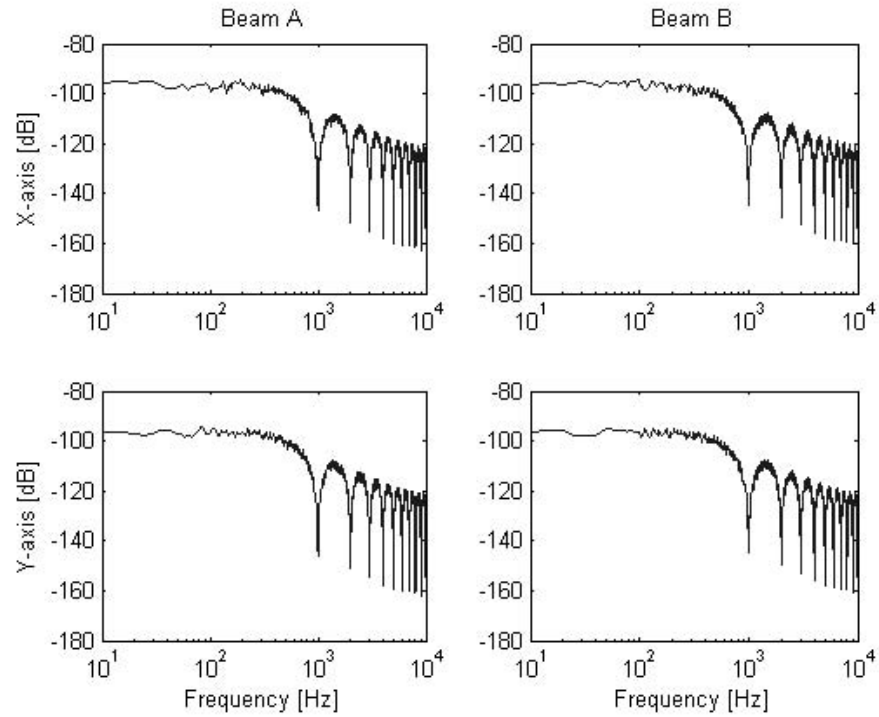


Figure 4.11: Plant Disturbance Power Spectral Density

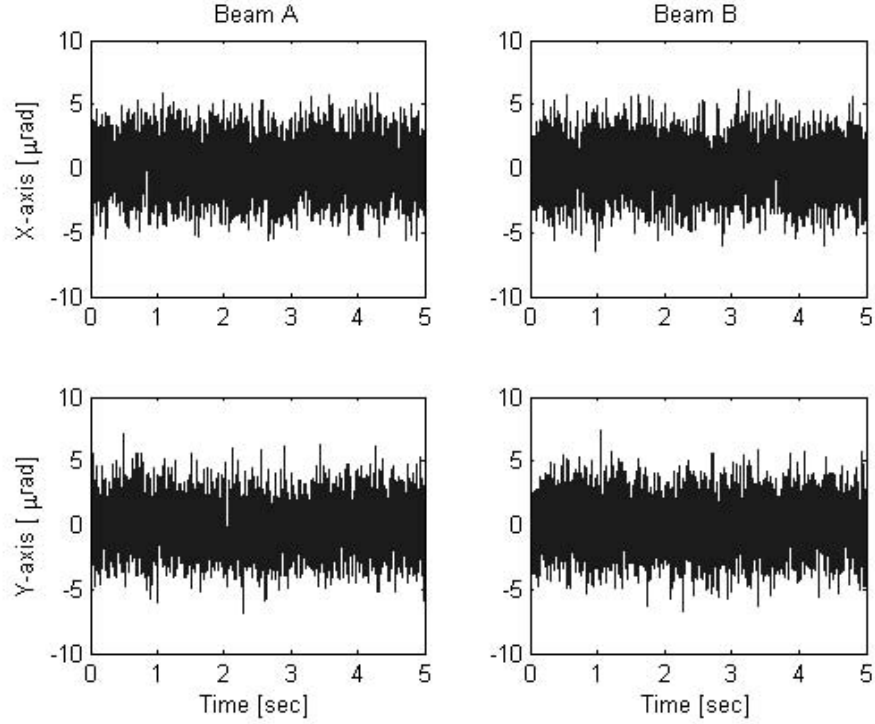


Figure 4.12: No Control Ensemble Average Mean Tracking Error Time Response

In terms of radial tracking error, the associated ensemble average mean and standard deviation is shown in Figures 4.14.

### 4.3 *Single Fine Tracking Control*

As determined in Appendix F, optimum regulator performance was achieved with a state weighting scale factor of 10 and control weighting scale factor of 0.1. Using the same simulation set up as described for the no control case, radial tracking error time response data was observed for single tracking control applied for each beam. In addition, based on the time response, the FSM frequency response was calculated and analyzed for disturbance rejection capability.

*4.3.1 Time Response.* As illustrated in Figures 4.15 and 4.16, the controller regulates beam tracking error, subject to random amplitude noise inputs at intervals of the noise correlation time. In either case, there is no apparent benefit in regulating

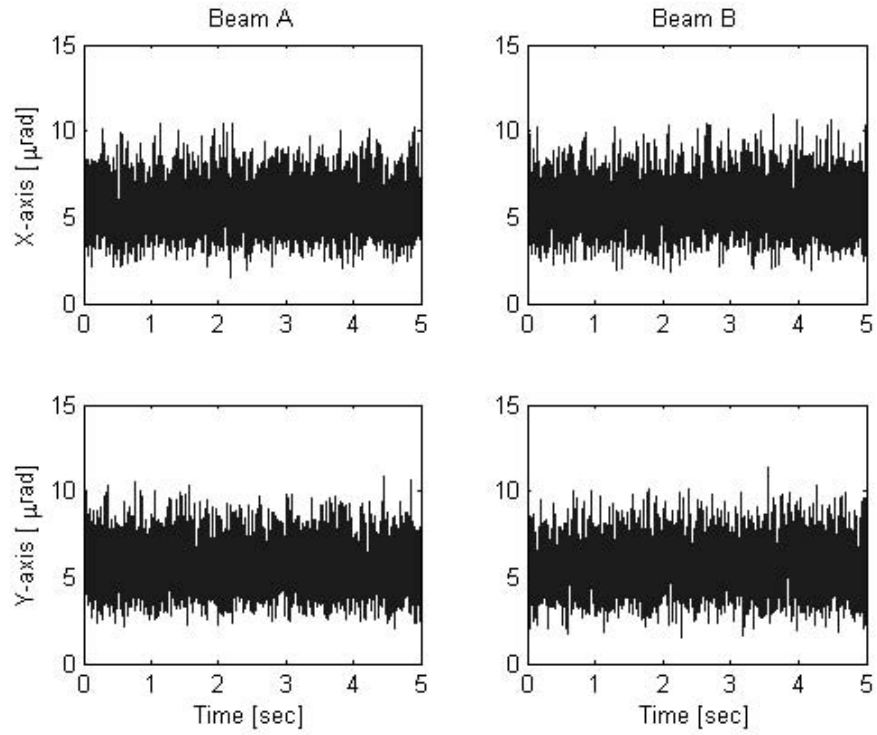


Figure 4.13: No Control Ensemble Average Tracking Error Standard Deviation Time Response

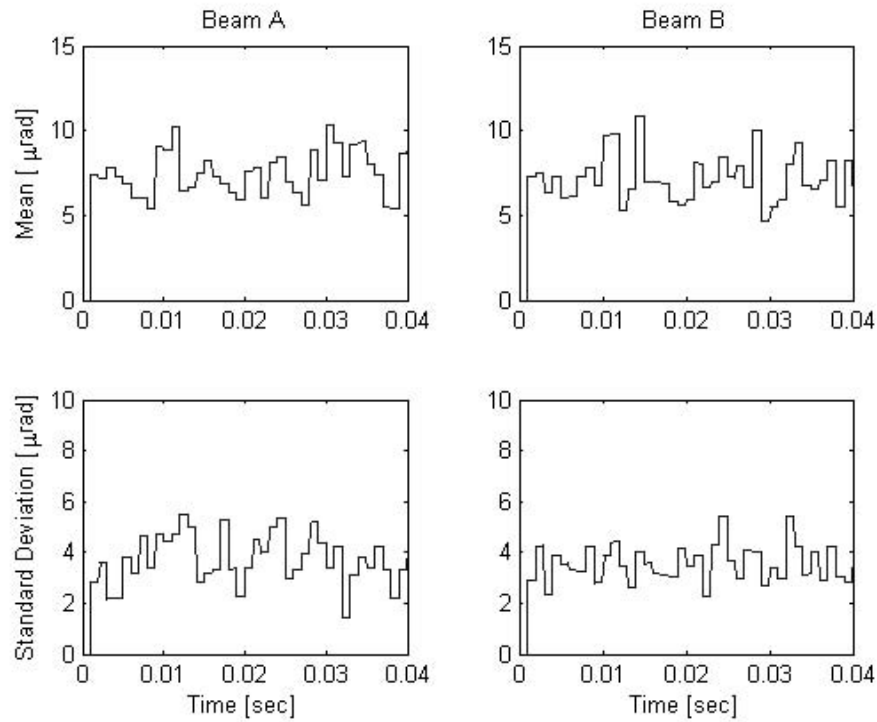


Figure 4.14: No Control Ensemble Average Radial Tracking Error Time Response

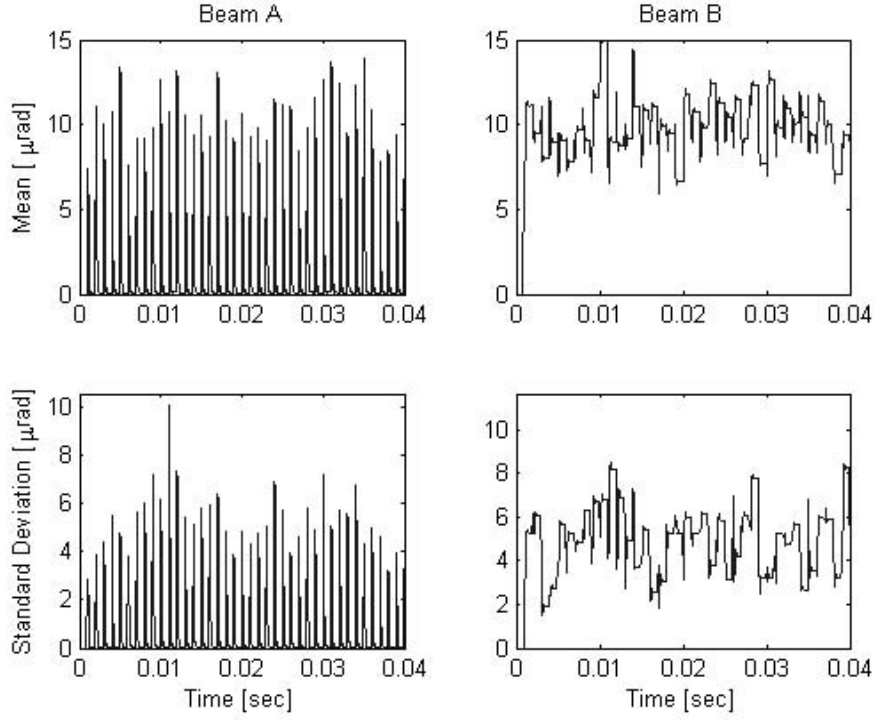


Figure 4.15: Beam A Control Only: Ensemble Average Radial Tracking Error Time Response

tracking error for a single beam over the other. Any variation is simply due to the random noise samples.

*4.3.2 Frequency Response.* Based on the observed simulation time response data, each signal is filtered by a Hann window, processed into a frequency spectrum by Fast Fourier transform (FFT), and averaged 20 times to achieve an adequate linear estimate of the frequency response data. As illustrated in Figures 4.17 and 4.18, the frequency response function (FRF) was calculated for each single fine tracking control scheme based on the single fine tracking control input and corresponding FSM output response. In either case, the FSM achieved similar magnitude and phase distributions. Thus, there is no apparent benefit in regulating tracking error for a single beam over the other.

*4.3.3 Disturbance Rejection.* The corresponding disturbance rejection is calculated and illustrated in Figures 4.19 and 4.20. Although the accuracy of this

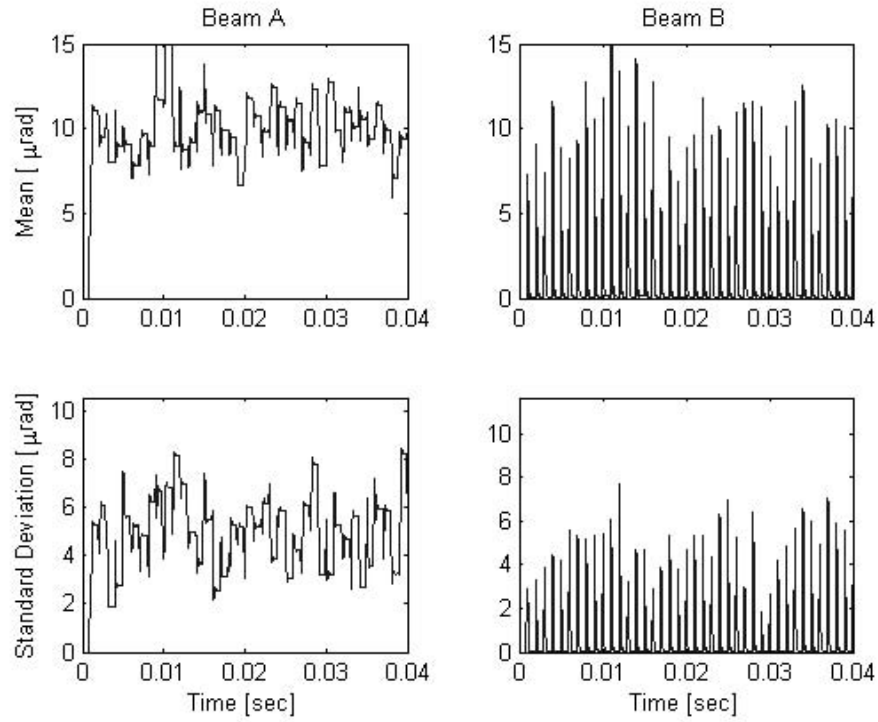


Figure 4.16: Beam B Control Only: Ensemble Average Radial Tracking Error Time Response

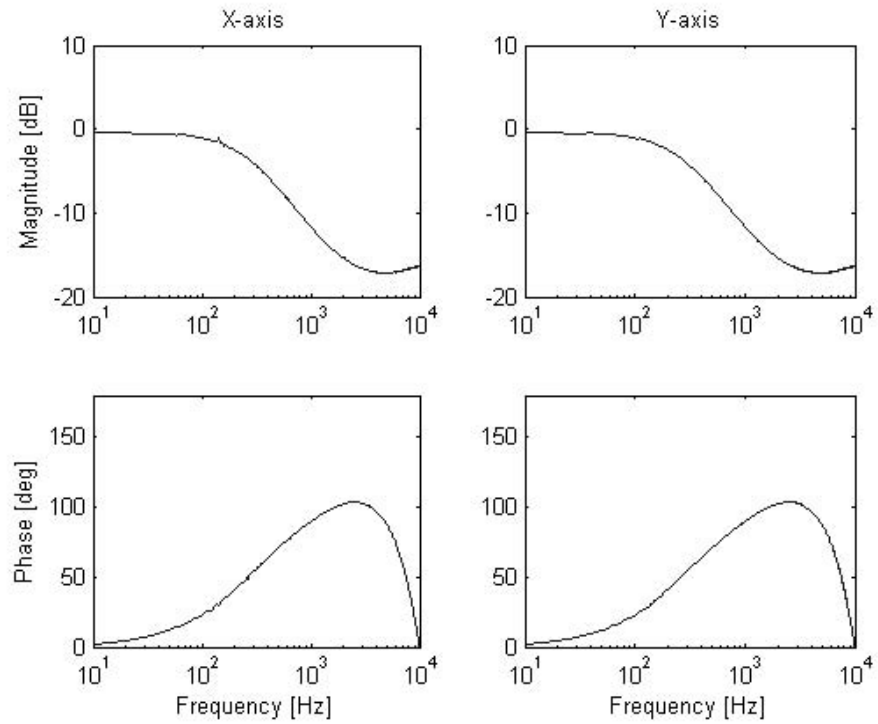


Figure 4.17: Beam A Control Only: Fast Steering Mirror Frequency Response Function

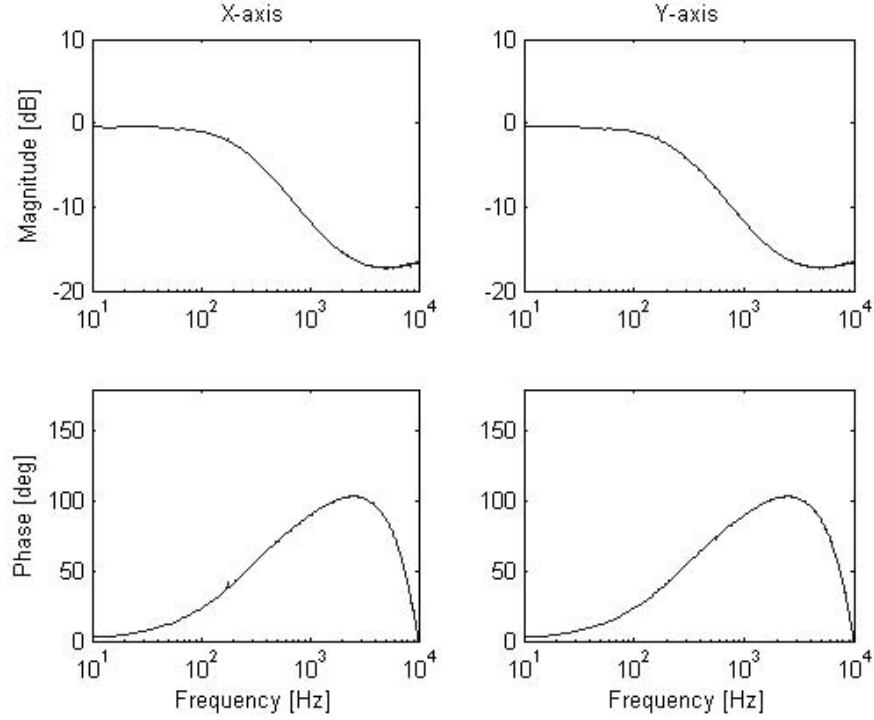


Figure 4.18: Beam B Control Only: Fast Steering Mirror Frequency Response Function

data is suspect do the chosen noise correlation time, approximately 11.15 dB power rejection is observed for either regulated beam tracking error. Thus, fine tracking control does somewhat reduce line of sight beam propagation effects.

#### 4.4 Dual Fine Tracking Control

Using the same simulation set up as described for the single fine tracking control case, a switching time of 0.02s was implemented for dual fine tracking control of both incident beams. The ensemble average tracking error time response data was observed and used to calculate the associated FSM frequency response. Based on the observed plant disturbance frequency response spectrum, disturbance rejection was calculated for each beam.

*4.4.1 Time Response.* As illustrated in Figure 4.21, the controller regulates radial tracking error for both beams, subject to random amplitude noise inputs at



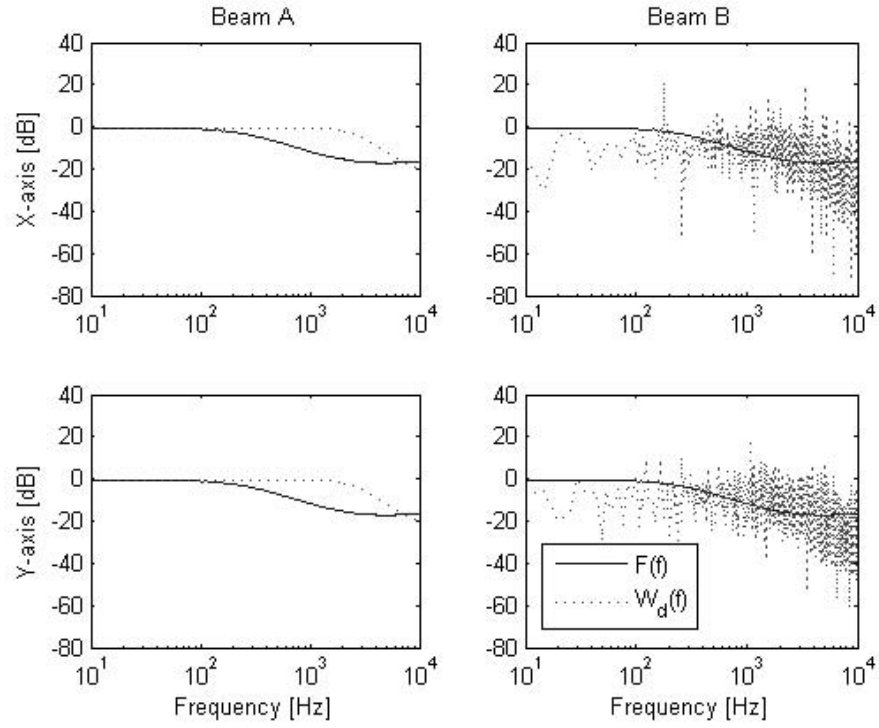


Figure 4.19: Beam A Control Only: Disturbance Rejection

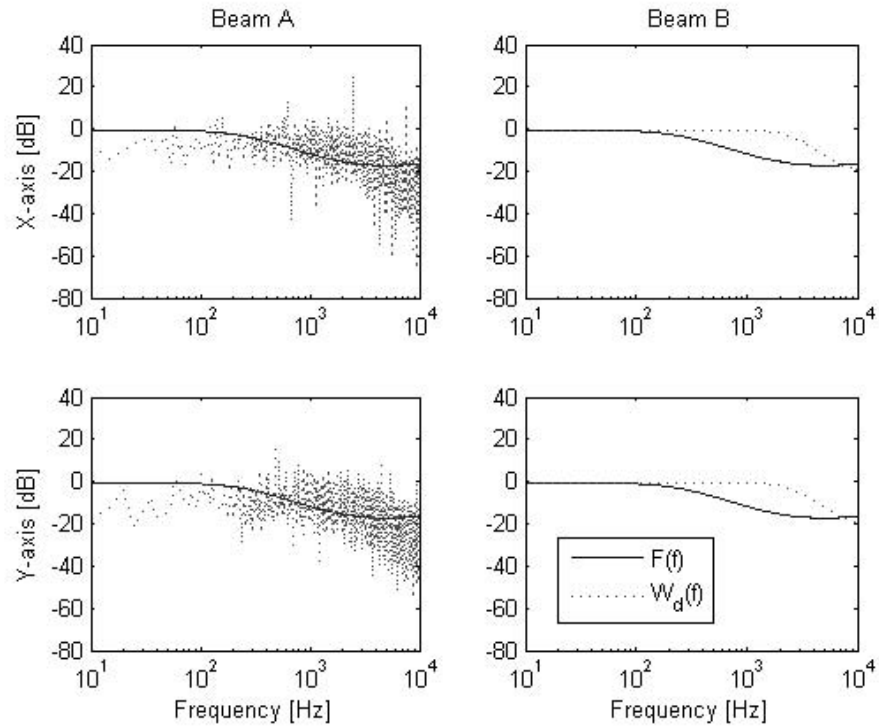


Figure 4.20: Beam B Control Only: Disturbance Rejection

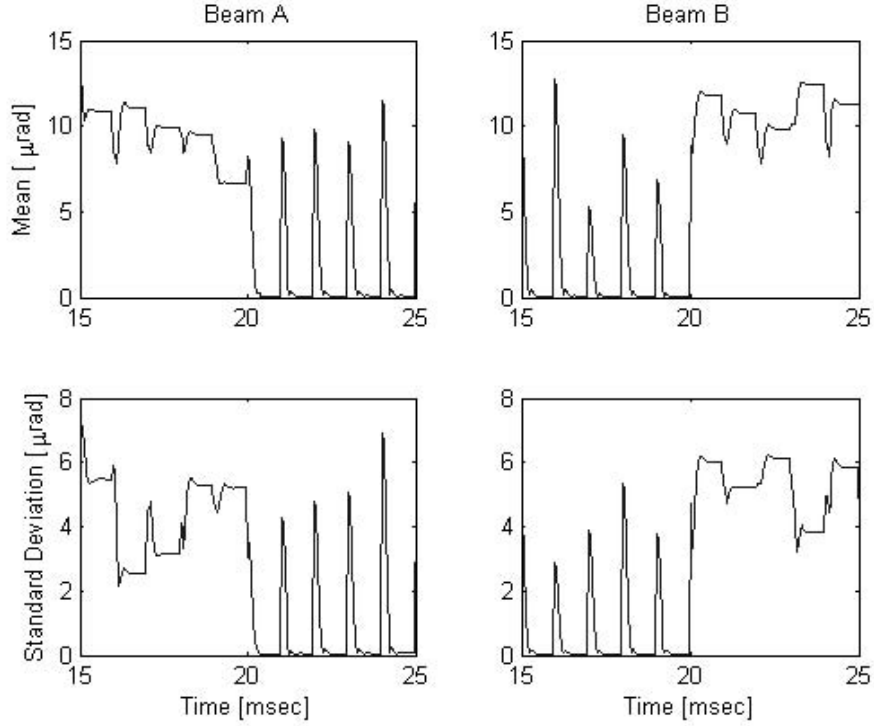


Figure 4.21: Dual Fine Tracking Control Ensemble Average Radial Tracking Error Time Response

intervals of the noise correlation time. Regulation is alternated between each beam, based on the chosen switching time of 0.02s. Comparison with either single tracking control scheme, Figures 4.15 and 4.16 respectively, reveals dual tracking control achieves a similar regulation performance, sharing the negative disturbance effects.

*4.4.2 Frequency Response.* The frequency response function, illustrated in Figure 4.22, was calculated for the dual fine tracking control scheme using the same approach discussed in section 4.3.2. In either case, the FSM achieved similar magnitude and phase distribution. Although highly corrupted by noise at higher frequencies, the dual control FRF exhibits similar behavior as single fine tracking control.

*4.4.3 Disturbance Rejection.* The corresponding disturbance rejection is calculated and illustrated in Figure 4.23. As revealed for single fine tracking control scheme, the accuracy of this data is suspect due to the chosen noise correlation time.

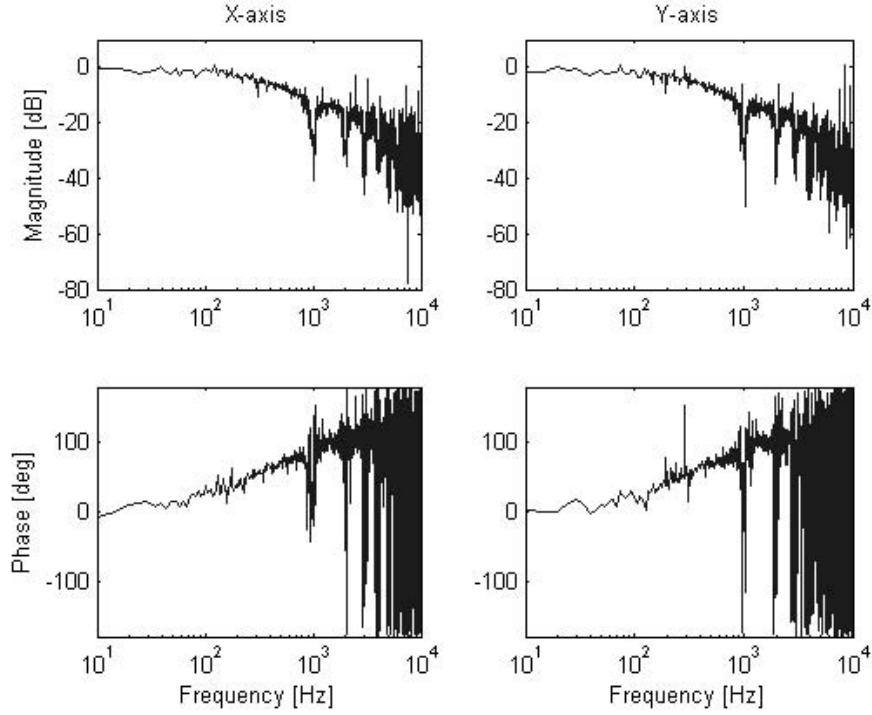


Figure 4.22: Dual Fine Tracking Control Control Fast Steering Mirror Frequency Response Function

Assuming the observed frequency response is accurate up to a 1000 Hz, slight power rejection is observed for each axis.

#### 4.5 Bit Error Rate Performance

Taking a temporal average of the ensemble averaged radial tracking error data for each control scheme, illustrated in Figure 4.24, yields remarkably different results for each scheme. Without regulation compensation, the observed temporal average mean radial tracking error for both beams is approximately  $7.268 \mu\text{rad}$ . While single control of either beam yields mean error of approximately  $1.6 \mu\text{rad}$ , the non-controlled beam suffers a mean error of approximately  $10.11 \mu\text{rad}$ . Dual control yields approximately  $5.85 \mu\text{rad}$  mean tracking error. In addition, standard deviation statistics exhibit the same trend between each control scheme. Both statistics reveal increased dispersion about the respective means for the regulated beams versus the non-regulated beams. As shown in Figure 3.10, a radial tracking error greater than

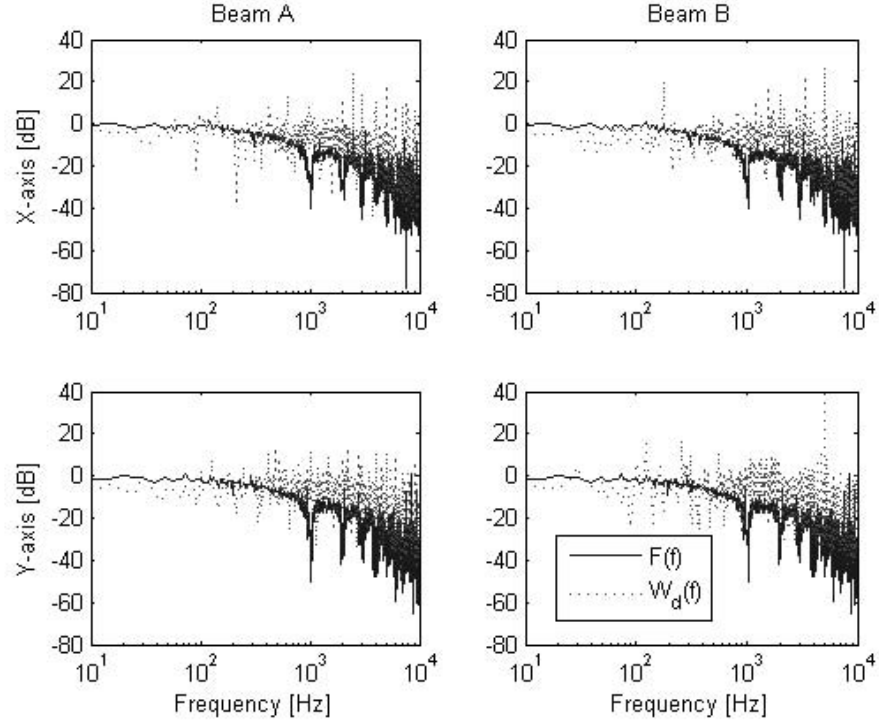


Figure 4.23: Dual Fine Tracking Control Disturbance Rejection

approximately  $4.2 \mu\text{rad}$  yields a BER of 1. Thus, only regulation of a single beam, at the cost of the other beam, satisfies the tracking error requirement of  $1.68 \mu\text{rad}$ . Chapter V will discuss a possible implementation scheme that could still exploit the dual tracking approach.

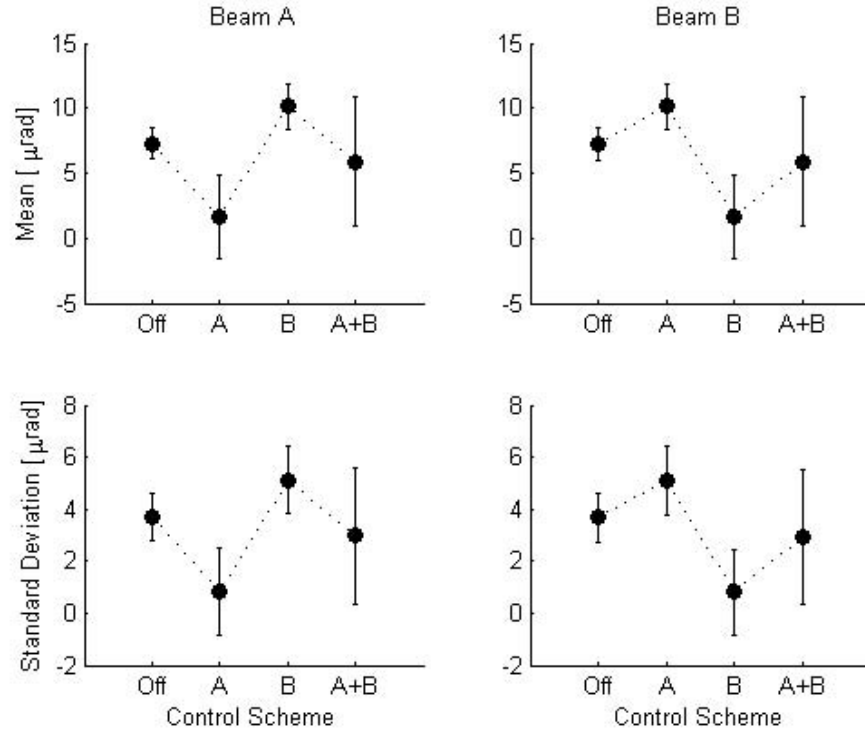


Figure 4.24: Temporal Average of Ensemble Radial Tracking Error Performance  
 Off: No Control, A: Beam A Control Only, B: Beam B Control Only, A+B: Dual Control

#### ***4.6 Summary***

Dual fine tracking control system simulation data was observed and compared to non-control and single fine tracking control simulation data. Based on Monte Carlo analysis, ensemble average mean and standard deviation statistics were computed for the time response and revealed similar tracking error regulation performance between single and dual fine tracking control. In either case, regulation occurred at regular time intervals due to the noise correlation time. However, the chosen time of 0.001s appeared to affect the frequency response of the disturbance inputs. Hence, the control system frequency response accuracy was limited.

## V. Conclusions

### 5.1 Thesis Summary

A conceptual dual fine tracking control system (FTCS) was designed and simulated to evaluate the effectiveness of a single fast steering mirror (FSM) to compensate for disturbances affecting line of sight propagation of two uplink laser communication beams. The optical receiver resided in a satellite in geosynchronous orbit while each incident beam originated from two spatially separated unmanned aerial vehicles (UAVs). Optical frequencies are desired for their low power, high bandwidth, and narrow beamwidth characteristics. On the other hand, compared to radio frequencies, optical frequencies are highly susceptible to propagation disturbances, which attenuates received signal power. Degradation in received signal power adversely affects communication link bit error rate (BER) performance, which is a fundamental performance measure in digital communications. As defined in Chapter I, for the purposes of this study, the primary parameter of interest for disturbances affecting uplink beam propagation is residual tracking error.

Chapter II, provided a review of previous works covering various methods for laser beam pointing and tracking control. In particular, optical power loss can be modeled as a decreasing exponential function of radial tracking error and BER performance is subject to tracking error probability distribution. Given this observation, a dual fine tracking control system was designed in Chapter III based on a residual radial tracking error limit of  $1.68 \mu\text{rad}$ , which yields a BER of approximately  $10^{-6}$ . This error limit was determined from the theoretical propagation characteristics of each uplink beam.

Propagation of each beam was affected by transmitter effects, channel effects, and receiver effects. Other than the power loss subject to propagation distance, the greatest power attenuation occurred from atmospheric loss. To minimize atmospheric loss, each transmitted beam was modeled with a wavelength of 1510 and 1550 nm respectively. In particular, the largest source of atmospheric loss, approximately between -4.5 to -5 dB, was attributed to random beam wander, which is caused

by optical turbulence. Random beam wander varied as a function of propagation distance, which was determined from the elevation angle of the UAV transmitter. However, the defined satellite receiver field of view ( $\text{FOV}_R$ ) and UAV altitudes limited the range of elevation angles between 76 and 90 degrees. This range in elevation angle, corresponded to UAV spatial separation limited to  $\pm 10.81^\circ$  latitude/longitude.

Chapter IV characterized and analyzed dual FTCS performance. Based on the respective Kalman filter state estimates of each beam, a linear quadratic regulator (LQR) controller applied steady state regulator gain and switching time to compensate for tracking errors upon each beam. Initial simulation results of various weighting matrix combinations, revealed an optimum regulator performance achieved with a state weighting factor of 10 and control weighting factor of 0.1. Modeled as zero-mean white Gaussian noise and zero-mean non-white Gaussian noise respectively, measurement noise and plant disturbance noise models were dependent upon their simulation correlation time, which was required to be an integer multiple of the simulation step time, due to simulation restrictions. Since various switching times, chosen as multiples of the FSM 2% settling time of 0.002s, did not yield any noticeable positive or negative effects, a time of 0.02s was chosen for simulation purposes. Although, switching control revealed slight disturbance rejection, the accuracy of the frequency response data was suspect above a 1000 Hz. In addition, based on desired regulation time duration, relatively large to infinitely many switching times can occur.

Temporal averaging of the radial tracking error time response data revealed dual fine tracking control did not achieve the residual radial tracking error limit. Although dual control obtained a better result than no control, on average, single control of one beam achieved a temporal mean of  $1.6 \mu\text{rad}$ , which more than sufficiently meets the required tracking error. However, this performance is achieved at the cost of approximately  $10.11 \mu\text{rad}$  mean radial tracking error on the other beam.

An implementation that could exploit these results is to only utilize communication data from each beam during periods of applied control. This still would



result in a single aperture system with data received in short bursts. In particular, a time division multiple access (TDMA) scheme, a common communication resource allocation method, could be the optimal solution.

## **5.2 Contributions**

A dual fine tracking control methodology has been developed for propagation of two satellite laser communication uplink beams. The concept incorporated common uplink beam propagation disturbance sources with Kalman filtering and LQR control to yield a dual fine tracking control system.

LQR weighting matrix identification methodology was developed based on tracking error performance. The concept entailed calculating the ensemble average and temporal average tracking error statistics and evaluating the associated mean and dispersion for each weighting.

Based on the defined geometry between the satellite receiver and UAV transmitters, the optical turbulence induced random beam wander affects on plant disturbance were investigated and revealed limited impacts to tracking error due to spatial separation between transmitters within the receiver field of view.

## **5.3 Recommendations and Future Work**

Based upon the software used, simulation of the control system required using a fixed-step solver methodology, to analyze response statistics. This required a fixed time step of 0.00005s and required large amounts of memory to collect and process the data. However, this simulation was performed in the continuous-time simulation environment. In addition, modeled noise sources required a correlation time as an integer multiple of the fixed-step time. Although, an arbitrarily chosen correlation time may simplify time response analysis, it may be inadequate for accurate frequency response data. A possible remedy to this would be to simulate the system in a discrete-time environment.

Future work should include developing and implementing a TDMA communication scheme within the simulation environment to determine impacts to system performance. In addition, the simulation model should incorporate modulation and demodulation models to determine corresponding bit error rate performance.

A higher level fidelity model of aircraft attitude dynamics is required to investigate disturbance affects on transmitter pointing error. In particular, this could be applied to a two-way communication link between the satellite and transmitter to incorporate the necessary pointing commands in the transmitter attitude control system.

Experimental level evaluation is recommended in order to validate the adequacy of this approach. This would require optical hardware and software components assembled in a controlled vibration environment. Propagation disturbance could be induced by either filtering, adaptive optics, or fast steering mirrors.

## Appendix A. Optical Communication System

### A.1 Data Transmission

During transmission, all user information (UI) is converted into digital information binary digits (bits), which are formatted into message bits,  $b_i$ . Pulse modulation converts these message bits into a nonreturn-to-zero level (NRZ-L) pulse code modulation (PCM) baseband waveform,  $g(t)$ , as shown in Figure A.1. For a given message bit rate,  $R_b$ , the baseband waveform data rate and symbol duration are determined respectively by

$$R_g = R_b \quad (\text{A.1})$$

$$T_g = \frac{1}{R_b} = T_b \quad (\text{A.2})$$

The message sequence is inherently a random sequence of bits, in which it is assumed the occurrence of a 1 or 0 is equally likely within the symbol interval,  $T_b$ , and independent of all other intervals [12, page 247]. Channel symbols 1 and 0 are denoted by bipolar pulses of amplitudes  $+V$  and  $-V$  respectively, which occur with equal probability,  $P(+V) = P(-V) = 1/2$ . Hence, the NRZ-L PCM baseband waveform,  $g(t)$ , is a sample of a binary random process denoted by

$$G(t) = \begin{cases} +V & : b_i = 1 \\ -V & : b_i = 0 \end{cases} \quad (\text{A.3})$$

$$\text{for } nT_b \leq t \leq (n+1)T_b, \quad n = 0, 1, 2, 3, \dots$$

*A.1.1 NRZ-L PCM Baseband Waveform Statistics.* The mean and autocorrelation functions of a random process are the two moments of interest for a communication system [29, page 23]. The mean is determined by [10, pages 334]

$$m_G(t) = E[G(t)] = \int_{-\infty}^{\infty} g f_G(g) dg \quad (\text{A.4})$$

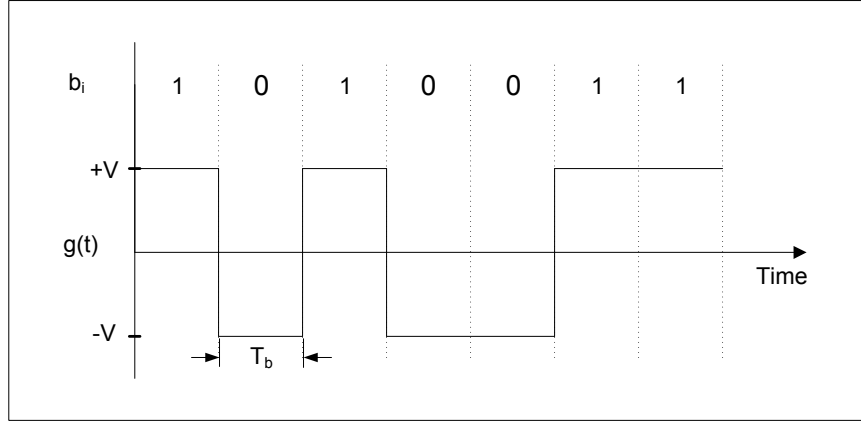


Figure A.1: PCM Baseband Waveform: (a) Channel Symbol Sequence, (b) NRZ-L PCM Waveform.

where  $f_G(g)$  is the probability density function (pdf) of  $G(t)$ . Since  $G(t)$  is either  $+V$  or  $-V$  for all  $t$ , its pdf is determined by the sum of delta functions denoted by [18, pages 58, 195]

$$\begin{aligned} f_G(g) &= P(+V)\delta(g - V) + P(-V)\delta(g + V) \\ &= \left(\frac{1}{2}\right) [\delta(g - V) + \delta(g + V)] \end{aligned} \quad (\text{A.5})$$

Thus, the mean is calculated as

$$\begin{aligned} m_G(t) &= \int_{-\infty}^{\infty} g f_G(g) dg \\ &= \left(\frac{1}{2}\right) \int_{-\infty}^{\infty} g [\delta(g - V) + \delta(g + V)] dg \\ &= \left(\frac{1}{2}\right) [(V) + (-V)] \\ &= 0 \end{aligned} \quad (\text{A.6})$$

The autocorrelation of  $G(t)$  is determined by [10, pages 335]

$$R_G(t_1, t_2) = E[G(t_1)G(t_2)] = \int_{-\infty}^{\infty} \int_{-\infty}^{\infty} g_1 g_2 [f_{G_1, G_2}(g_1, g_2)] dg_1 dg_2 \quad (\text{A.7})$$

where  $f_{G1,G2}(g_1, g_2)$  is the joint pdf of  $G(t_1)$  and  $G(t_2)$ , and  $t_1$  and  $t_2$  are arbitrary time constants. Similar to the pdf derivation, the joint pdf is determined by the sum of delta functions denoted respectively by [18, pages 72, 79, 195]

$$\begin{aligned}
f_{G1,G2}(g_1, g_2) &= f_{G1,G2}(g_1, g_2|t_g) f_{T_b}(t_g) \\
&= [P(g_1 = +V, g_2 = +V)\delta(g_1 - V, g_2 - V) \\
&+ P(g_1 = +V, g_2 = -V)\delta(g_1 - V, g_2 + V) \\
&+ P(g_1 = -V, g_2 = +V)\delta(g_1 + V, g_2 - V) \\
&+ P(g_1 = -V, g_2 = -V)\delta(g_1 + V, g_2 + V)] f_{T_b}(t_g) \quad (\text{A.8})
\end{aligned}$$

where  $t_g$  is a uniform random variable in the interval  $[0, T_b]$ , which accounts for the unsynchronized realizations of  $G(t)$ , and  $f_{T_b}(t_g)$  is the associated pdf defined as [12, page 248]

$$f_{T_b}(t_g) = \begin{cases} 1/T_b & : 0 \leq t_g \leq T_b \\ 0 & : \text{elsewhere} \end{cases} \quad (\text{A.9})$$

If  $|t_2 - t_1| = |\tau|$  and  $|\tau| + t_g \geq T_b$ ,  $G(t_1)$  and  $G(t_2)$  occur in different pulse intervals and are independent. Thus, the joint conditional pdf is determined by [18, page 195]

$$\begin{aligned}
f_{G1,G2}(g_1, g_2|t_g) &= P(g_1 = +V)P(g_2 = +V)\delta(g_1 - V, g_2 - V) \\
&+ P(g_1 = +V)P(g_2 = -V)\delta(g_1 - V, g_2 + V) \\
&+ P(g_1 = -V)P(g_2 = +V)\delta(g_1 + V, g_2 - V) \\
&+ P(g_1 = -V)P(g_2 = -V)\delta(g_1 + V, g_2 + V) \\
&= \left(\frac{1}{4}\right)\delta(g_1 - V, g_2 - V) + \left(\frac{1}{4}\right)\delta(g_1 - V, g_2 + V) \\
&+ \left(\frac{1}{4}\right)\delta(g_1 + V, g_2 - V) + \left(\frac{1}{4}\right)\delta(g_1 + V, g_2 + V) \quad (\text{A.10})
\end{aligned}$$

which implies an autocorrelation function defined as

$$\begin{aligned}
R_G(t_1, t_2) &= \int_{-\infty}^{\infty} \int_{-\infty}^{\infty} \int_{-\infty}^{\infty} g_1 g_2 f_{G1, G2}(g_1, g_2 | t_g) f_{T_b}(t_g) dg_1 dg_2 dt_g \\
&= \left( \frac{1}{T_b} \right) \int_0^{T_b - |\tau|} \int_{-\infty}^{\infty} \int_{-\infty}^{\infty} g_1 g_2 f_{G1, G2}(g_1, g_2 | t_g) dg_1 dg_2 dt_g \\
&= \left( \frac{1}{4} \right) \left( \frac{T_b - |\tau|}{T_b} \right) \left[ \int_{-\infty}^{\infty} \int_{-\infty}^{\infty} g_1 g_2 \delta(g_1 - V, g_2 - V) dg_1 dg_2 \right. \\
&\quad + \int_{-\infty}^{\infty} \int_{-\infty}^{\infty} g_1 g_2 \delta(g_1 - V, g_2 + V) dg_1 dg_2 \\
&\quad + \int_{-\infty}^{\infty} \int_{-\infty}^{\infty} g_1 g_2 \delta(g_1 + V, g_2 - V) dg_1 dg_2 \\
&\quad \left. + \int_{-\infty}^{\infty} \int_{-\infty}^{\infty} g_1 g_2 \delta(g_1 + V, g_2 + V) dg_1 dg_2 \right] \\
&= \left( \frac{1}{4} - \frac{|\tau|}{4T_b} \right) [(V)(V) + (V)(-V) + (-V)(V) + (-V)(-V)] \\
&= \left( \frac{1}{4} \right) \left( 1 - \frac{|\tau|}{T_b} \right) [2V^2 - 2V^2] = 0
\end{aligned} \tag{A.11}$$

However, if  $|\tau| + t_g < T_b$ ,  $G(t_1)$  and  $G(t_2)$  occur within the same pulse interval. Thus, the joint conditional pdf is defined by [18, page 195]

$$\begin{aligned}
f_{G1, G2}(g_1, g_2 | t_g) &= P(g_2 = +V | g_1 = +V) P(g_1 = +V) \delta(g_1 - V, g_2 - V) \\
&\quad + P(g_2 = -V | g_1 = +V) P(g_1 = +V) \delta(g_1 - V, g_2 + V) \\
&\quad + P(g_2 = +V | g_1 = -V) P(g_1 = -V) \delta(g_1 + V, g_2 - V) \\
&\quad + P(g_2 = -V | g_1 = -V) P(g_1 = -V) \delta(g_1 + V, g_2 + V) \\
&= (1) \left( \frac{1}{2} \right) \delta(g_1 - V, g_2 - V) + (0) \left( \frac{1}{2} \right) \delta(g_1 - V, g_2 + V) \\
&\quad + (0) \left( \frac{1}{2} \right) \delta(g_1 + V, g_2 - V) + (1) \left( \frac{1}{2} \right) \delta(g_1 + V, g_2 + V) \\
&= \left( \frac{1}{2} \right) [\delta(g_1 - V, g_2 - V) + \delta(g_1 + V, g_2 + V)]
\end{aligned} \tag{A.12}$$

which implies an autocorrelation function defined as

$$\begin{aligned}
R_G(t_1, t_2) &= \int_{-\infty}^{\infty} \int_{-\infty}^{\infty} \int_{-\infty}^{\infty} g_1 g_2 f_{G1, G2}(g_1, g_2 | t_g) f_{T_b}(t_g) dg_1 dg_2 dt_g \\
&= \left( \frac{1}{T_b} \right) \int_0^{T_b - |\tau|} \int_{-\infty}^{\infty} \int_{-\infty}^{\infty} g_1 g_2 f_{G1, G2}(g_1, g_2 | t_g) dg_1 dg_2 dt_g \\
&= \left( \frac{1}{2} \right) \left( 1 - \frac{|\tau|}{T_b} \right) \left[ \int_{-\infty}^{\infty} \int_{-\infty}^{\infty} g_1 g_2 \delta(g_1 - V, g_2 - V) dg_1 dg_2 \right. \\
&\quad \left. + \int_{-\infty}^{\infty} \int_{-\infty}^{\infty} g_1 g_2 \delta(g_1 + V, g_2 + V) dg_1 dg_2 \right] \\
&= \left( \frac{1}{2} \right) \left( 1 - \frac{|\tau|}{T_b} \right) [(V)(V) + (-V)(-V)] \\
&= \left( \frac{1}{2} \right) \left( 1 - \frac{|\tau|}{T_b} \right) [V^2 + V^2] \\
&= V^2 \left( 1 - \frac{|\tau|}{T_b} \right) \tag{A.13}
\end{aligned}$$

Therefore, the autocorrelation function is

$$R_G(t_1, t_2) = R_G(\tau) = \begin{cases} V^2 (1 - |\tau|/T_b) & : |\tau| < T_b \\ 0 & : |\tau| \geq T_b \end{cases} \tag{A.14}$$

In particular, based on the mean,  $m_G(t) = 0$ , and the autocorrelation function,  $R_G(t_1, t_2) = R_G(\tau)$ , the autocovariance of  $G(t)$  is defined as [10, page 335]

$$\begin{aligned}
C_G(t_1, t_2) &= E [\{G(t_1) - m_G(t_1)\} \{G(t_2) - m_G(t_2)\}] \\
&= E [\{G(t_1) - 0\} \{G(t_2) - 0\}] = E [G(t_1)G(t_2)] \\
&= R_G(t_1, t_2) = R_G(\tau) \tag{A.15}
\end{aligned}$$

Since the mean is constant and the autocovariance is a function of  $\tau = t_2 - t_1$ ,  $G(t)$  is a wide-sense stationary process (WSS) [10, page 359].

*A.1.2 NRZ-L PCM Baseband Waveform Power Spectral Density.* The baseband waveform power spectral density (PSD), determined from the Fourier transform

of  $R_G(\tau)$ , is derived as [10, page 404]

$$\begin{aligned}
S_G(f) &= \mathcal{F}\{R_G(\tau)\} = \int_{-\infty}^{\infty} R_G(\tau) \exp(-j2\pi f\tau) d\tau \\
&= (V^2 T_b) \left[ \frac{\sin(\pi f T_b)}{\pi f T_b} \right]^2 \\
&= (V^2 T_b) \text{sinc}^2(f T_b)
\end{aligned} \tag{A.16}$$

Based on the Chapter III defined data rate,  $R_b = 100$  Kbps, NRZ-L PCM waveform PSD is shown in Figure A.2, scaled for unit amplitude. The average power is determined by [29, page 25]

$$R_G(0) = V^2 \left( 1 - \frac{0}{T_b} \right) = V^2 \tag{A.17}$$

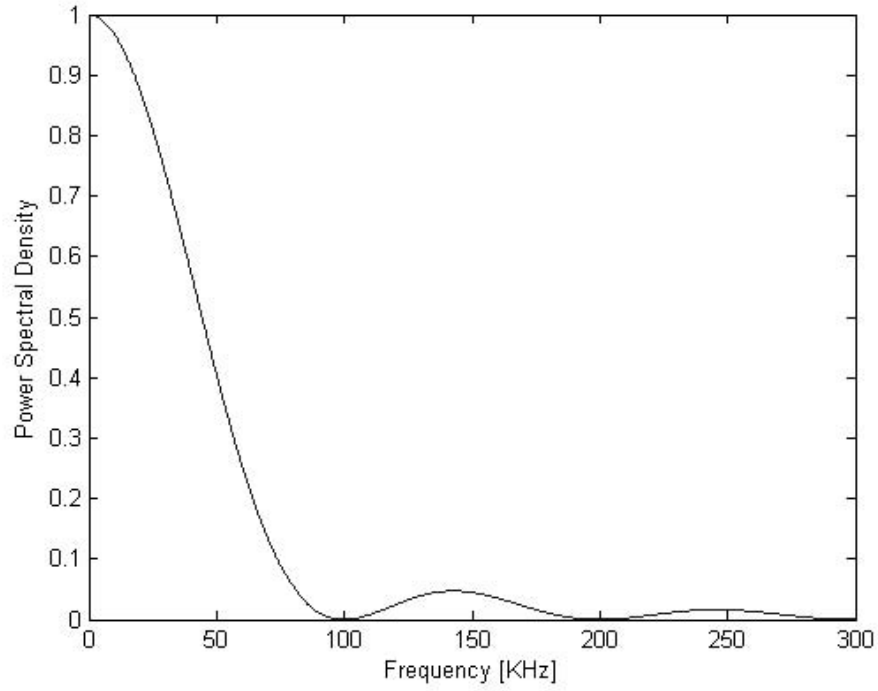


Figure A.2: NRZ-L PCM Baseband Waveform PSD



## A.2 Optical Receiver

A conceptual OOK optical receiver is illustrated in Figure A.3. After optical signal processing as defined in Appendix D, an avalanche photodiode (APD) detects and converts the received optical power into an amplified current signal,  $i_r(t)$ . A matched filter maximizes the signal-to-noise ratio (SNR) prior to sampling a current test statistic,  $z(T_b)$ , for the decision circuit. Due to noise,  $N_o$ , distortion effects inherent within the received signal, the decision circuit observes the received signal and determines whether  $s_1$  is sent, denoted by hypothesis  $H_1$ , or  $s_2$  is sent, denoted by hypothesis  $H_2$  [6, page 534]. After symbol decision, based on the threshold  $\gamma_o$ , the estimated received symbol is assigned to its corresponding estimated message bits,  $\hat{b}_i$ , which in turn are formatted back into user information.

*A.2.1 Received Current.* The received current signals, based on the unipolar transmitted signals within the interval  $t \in [0, T_b]$  defined in Appendix D, are defined respectively as

$$\begin{aligned} i_1(t) &= i_{dc} + i_n(t) \\ &= R_{ph}P_r + i_n(t) \quad [\text{A}] \end{aligned} \tag{A.18}$$

$$\begin{aligned} i_2(t) &= 0 + i_n(t) \\ &= i_n(t) \quad [\text{A}] \end{aligned} \tag{A.19}$$

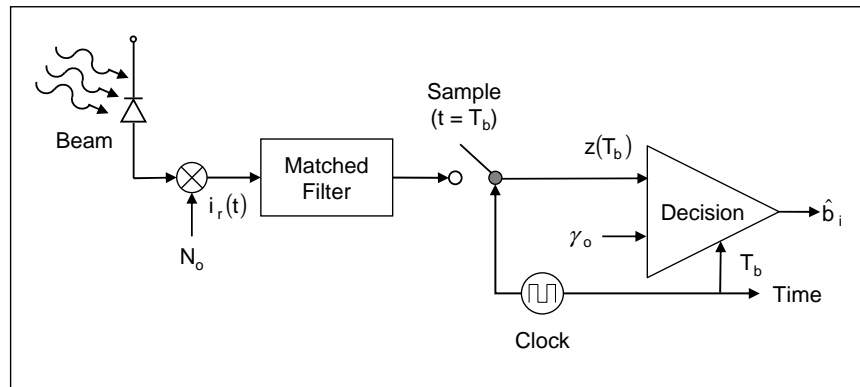


Figure A.3: OOK Optical Receiver

where  $i_{dc}$  is the dc current,  $R_{ph}$  is the photodetector responsivity,  $P_r$  is the received optical power, and  $i_n$  is the current noise.

*A.2.2 Matched Filter.* In order to maximize the SNR for sampling and detection, the received current signal is filtered by a matched filter. The maximum output SNR is defined by the ratio of the input signal energy and noise power spectral density, defined as [29, page 127]

$$SNR_T = \frac{\{E[i_1(t)] - E[i_2(t)]\}^2}{\sigma_o^2} = \frac{2E_d}{N_o} \quad (\text{A.20})$$

where  $E_d$  is the input energy difference signal,  $\sigma_o^2$  is the output noise variance, and  $N_o/2$  is the two-sided power spectral density of the input noise.  $N_o$  is associated with thermal noise and is the dominant photodetector noise source, as determined in Appendix D. Thermal noise is characterized as a zero-mean additive white Gaussian noise (AWGN) and is used to model communication system noise [29, page 33]. Thus, based on the noise statistics, the matched filter output SNR is determined as

$$SNR_T = \frac{i_{dc}^2}{\sigma_o^2} = \frac{2E_d}{N_o} \quad (\text{A.21})$$

The ideal energy difference, based on noiseless unipolar input current signals within the time interval  $[0, T_b]$ , assuming a unit Ohm resistance, is determined as [29, page 128]

$$\begin{aligned} E_d &= \int_0^{T_b} \{ E[i_1(t)] - E[i_2(t)] \}^2 dt = \int_0^{T_b} (R_{ph}P_r)^2 dt \\ &= (R_{ph}P_r)^2 T_b \quad [\text{J}] \end{aligned} \quad (\text{A.22})$$

*A.2.3 Symbol Detection.* Assuming symbol synchronization is maintained for optimum demodulation, the symbol detection goal is to determine whether the sampled current test statistic from the matched filter output,  $z(T_b)$ , satisfies either

hypothesis  $H_1$  or  $H_2$ , determined respectively as

$$H_1 : z(T_b) = i_{dc} + i_n(T_b) \quad (\text{A.23})$$

$$H_2 : z(T_b) = i_n(T_b) \quad (\text{A.24})$$

Since  $z(T_b)$  is a function of  $i_n(T_b)$ , a zero-mean Gaussian random variable, it is also subject to Gaussian statistics. Thus, the corresponding conditional pdfs for either signal being sent are denoted respectively by [10, page 113]

$$p(z|s_1) = \left( \frac{1}{\sigma_o \sqrt{2\pi}} \right) \exp \left\{ -\frac{[z - i_{dc}]^2}{2\sigma_o^2} \right\} \quad (\text{A.25})$$

$$p(z|s_2) = \left( \frac{1}{\sigma_o \sqrt{2\pi}} \right) \exp \left\{ -\frac{z^2}{2\sigma_o^2} \right\} \quad (\text{A.26})$$

Assuming the transmitted unipolar signal waveforms have an equally likely a priori probability,  $P(s_1) = P(s_2) = 1/2$ , the conditional pdfs are symmetric, as shown in Figure A.4. Thus, the decision criterion, to estimate which symbol was sent, is based on the maximum likelihood criterion as [29, page 110]

$$z(T_b) \geq \gamma_o \implies \text{symbol } 1 \quad (\text{A.27})$$

$$z(T_b) < \gamma_o \implies \text{symbol } 0 \quad (\text{A.28})$$

where  $\gamma_o$  is the optimum decision threshold. The optimum threshold is determined from the minimum error criterion, which is a function of the means of each conditional pdf denoted by [29, page 182]

$$\gamma_o = \frac{i_{dc}}{2} \quad (\text{A.29})$$

### **A.3 Probability of Bit Error**

Based on the maximum likelihood criterion, there are two ways a symbol detection and estimation error can occur for a binary system: false detection and missed

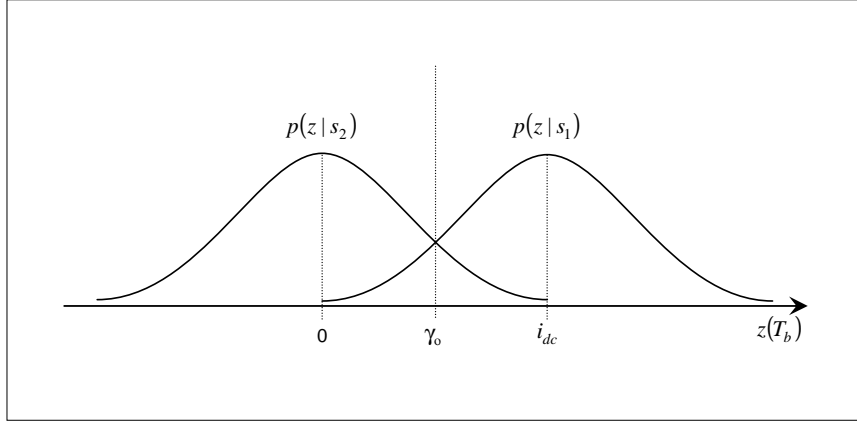


Figure A.4: Gaussian Conditional Probability Density Functions

detection. The probability of error is calculated by the summation of the probabilities of these two occurrences [29, page 1044]. False detection, also referred to as false alarm, occurs when the sampled voltage exceeds the voltage threshold when  $s_2$  is sent. Conversely, missed detection, referred to as probability of fade, occurs when  $s_1$  is sent but the sampled voltage does not exceed the voltage threshold. Thus, the probability of symbol error,  $P_E$ , is defined as [29, page 1044]

$$P_E = P(s_1)P_{Fade} + P(s_2)P_{False} \quad (\text{A.30})$$

Since OOK modulation is an orthogonal binary signaling set, the probability of bit error is equivalent to the probability of symbol error, denoted by [29, page 551]

$$P_B = P_E = P(s_1)P_{Fade} + P(s_2)P_{False} \quad (\text{A.31})$$

*A.3.1 Gaussian Communication Channel.* Assuming the communication channel, defined in Appendix E, behaves as an AWGN channel the corresponding

false alarm and fade probabilities are determined respectively by [29, page 1044]

$$P_{False} = \int_{\gamma_o}^{\infty} p(z|s_2) dz \quad (\text{A.32})$$

$$P_{Fade} = \int_{-\infty}^{\gamma_o} p(z|s_1) dz \quad (\text{A.33})$$

Thus, the probability of bit error is determined as

$$\begin{aligned} P_B &= P(s_1)P_{Fade} + P(s_2)P_{False} \\ &= P(s_1) \left[ \int_{-\infty}^{\gamma_o} p(z|s_1) dz \right] + P(s_2) \left[ \int_{\gamma_o}^{\infty} p(z|s_2) dz \right] \end{aligned} \quad (\text{A.34})$$

Since both symbols are equally likely to have been sent and symmetry of the conditional pdfs, the probability of bit error simplifies to [29, page 121]

$$\begin{aligned} P_B &= \left( \frac{1}{2} \right) \left[ \int_{-\infty}^{\gamma_o} p(z|s_1) dz \right] + \left( \frac{1}{2} \right) \left[ \int_{\gamma_o}^{\infty} p(z|s_2) dz \right] \\ &= \int_{\gamma_o}^{\infty} p(z|s_2) dz \\ &= \int_{\gamma_o}^{\infty} \left( \frac{1}{\sigma_o \sqrt{2\pi}} \right) \exp \left\{ -\frac{z^2}{2\sigma_o^2} \right\} dz \end{aligned} \quad (\text{A.35})$$

Let

$$\begin{aligned} u &= \frac{z}{\sigma_o} \implies \sigma_o du = dz \\ \gamma_o \leq z \leq \infty &\implies \frac{\gamma_o}{\sigma_o} \leq u \leq \infty \\ x &= \frac{\gamma_o}{\sigma_o} = \frac{i_{dc}}{2\sigma_o} \end{aligned}$$

Thus

$$P_B = \int_x^{\infty} \left( \frac{1}{\sqrt{2\pi}} \right) \exp \left[ -\frac{u^2}{2} \right] du = Q(x) \quad (\text{A.36})$$

where  $Q(x)$  is the complementary error function [29, page 1044]. Figure A.5 illustrates the relationship between  $Q(x)$  and an arbitrary  $x \in [0, 6]$ , commonly referred to as the error curve. Substituting in the predetermined matched filter output SNR, the

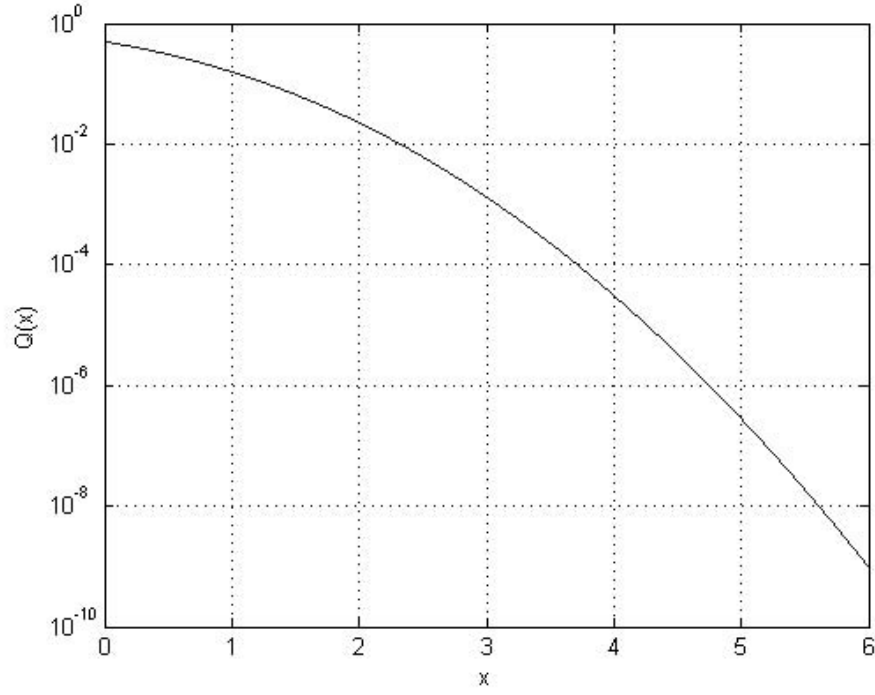


Figure A.5: Complementary Error Function Curve

arbitrary Q-function parameter becomes

$$\begin{aligned}
 x &= \frac{i_{dc}}{2\sigma_o} = \sqrt{\frac{i_{dc}^2}{4\sigma_o^2}} = \sqrt{\left(\frac{1}{4}\right) \left(\frac{2E_d}{N_o}\right)} = \sqrt{\frac{E_d}{2N_o}} \\
 &= \sqrt{\frac{(2E_b)}{(2N_o)}} = \sqrt{\frac{E_b}{N_o}}
 \end{aligned} \tag{A.37}$$

where  $E_b$  is the average energy per bit, defined as  $E_b = E_d/2$  for orthogonal signals [29, page 132]. Thus, the probability of bit error for OOK modulation, shown in Figure A.6, is determined as

$$P_B = P_{mod} = Q\left(\sqrt{\frac{E_b}{N_o}}\right) \tag{A.38}$$

*A.3.2 Fading Communication Channel: Non-Ideal Tracking.* Assuming the incident beam irradiance, defined in Appendix D as  $I(\rho_z, z_p)$ , fluctuates at a slower rate relative to the sample time interval,  $T_b$ , the average received optical power,  $P_r$ , is

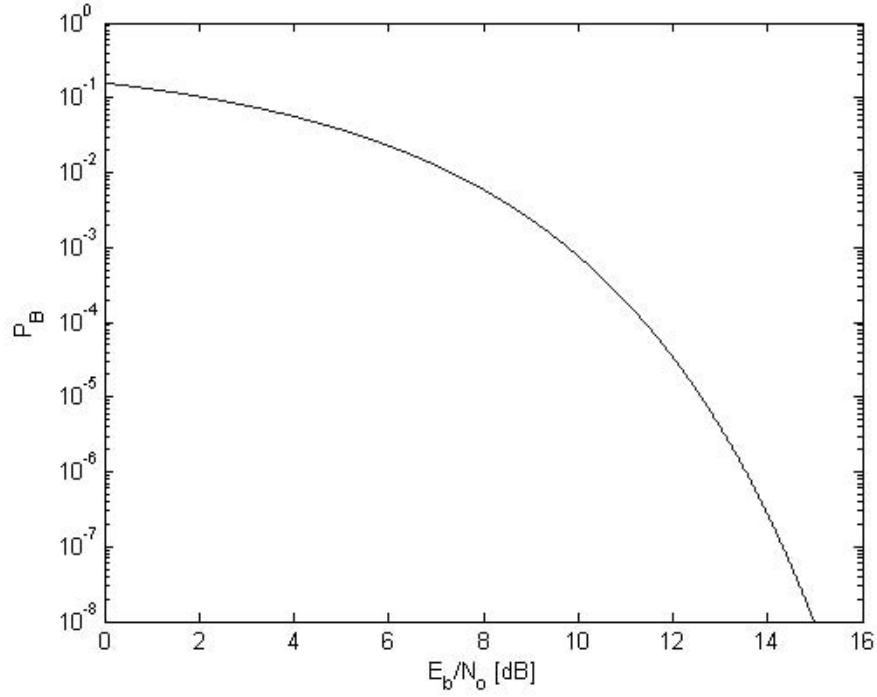


Figure A.6: OOK Modulation Theoretical BER Curve

constant [3, page 268]. However, tracking errors, quantified by the tracking loss  $L_r$ , attenuates the received power. Thus, the random tracking error fluctuates incident beam irradiance about the propagation axis,  $\vec{z}_p$ , creating a fading effect within the communication channel.

As defined previously in Chapter II,  $P_r$  is determined from the Friis transmission equation by [15, pages 94-105]

$$P_r = P_t(\eta_t G_t L_t L_{ao})(L_s L_a)(L_r G_r \eta_r)$$

where  $P_t$  is the transmitted power,  $\eta_t$  is transmitter efficiency,  $G_t$  is the transmitter antenna gain,  $L_t$  is the pointing loss,  $L_{ao}$  is aerodynamic-optical loss,  $L_s$  is the path loss,  $L_a$  is atmospheric loss,  $L_r$  is the tracking loss,  $G_r$  is the receiver antenna gain, and  $\eta_r$  is the receiver efficiency loss. Let

$$\alpha_r = P_t(\eta_t G_t L_t L_{ao})(L_s L_a)(\eta_r) \quad (\text{A.39})$$

Assuming  $\alpha_r$  and  $G_r$  are known a priori,  $P_r$  can be defined as a function of the radial receiver tracking error,  $\rho_r$ , denoted by

$$P_r(\rho_r) = \alpha_r G_r L_r = \alpha_r G_r \exp(-G_r \rho_r^2) \quad (\text{A.40})$$

As defined in Chapter II, the receiver tracking error is subject to Rayleigh probability distribution, denoted by

$$f_R(\rho_r) = \left( \frac{\rho_r}{\sigma_r^2} \right) \exp\left(-\frac{\rho_r^2}{2\sigma_r^2}\right) : \rho_r \geq 0 \quad (\text{A.41})$$

Since  $P_r$  is an exponential function of a Rayleigh random variable, the probability of an event involving  $P_r$ , defined on the interval  $(0, \alpha_r G_r]$ , is equivalent to the corresponding event involving  $\rho_r$ , defined on the interval  $[0, \infty)$  [10, page 120]. Thus

$$P[0 \leq P_r \leq \alpha_r G_r] = P_\Theta = \int_0^\infty f_R(\rho_r) d\rho_r \quad (\text{A.42})$$

Hence, the probability of fade and false detection, assuming  $\rho_r$  and  $i_n(t)$  are independent random variables, are determined respectively by [10, page 209]

$$\begin{aligned} P_{Fade} &= P\{\rho_r \geq 0 \cap [z(T_b) < \gamma_o | s_1]\} \\ &= P[\rho_r \geq 0] P[z(T_b) < \gamma_o | s_1] \\ &= \left\{ \int_0^\infty f_R(\rho_r) d\rho_r \right\} \left\{ \int_{-\infty}^{\gamma_o} p(z | s_1) dz \right\} \\ &= \int_0^\infty \int_{-\infty}^{\gamma_o} [p(z | s_1) f_R(\rho_r)] dz d\rho_r \end{aligned} \quad (\text{A.43})$$

$$\begin{aligned} P_{False} &= P\{\rho_r \geq 0 \cap [z(T_b) > \gamma_o | s_2]\} \\ &= P[\rho_r \geq 0] P[z(T_b) > \gamma_o | s_2] \\ &= \left\{ \int_0^\infty f_R(\rho_r) d\rho_r \right\} \left\{ \int_{\gamma_o}^\infty p(z | s_2) dz \right\} \\ &= \int_0^\infty \int_{\gamma_o}^\infty [p(z | s_2) f_R(\rho_r)] dz d\rho_r \end{aligned} \quad (\text{A.44})$$



The probability of bit error is determined as

$$\begin{aligned}
P_B &= P(s_1)P_{Fade} + P(s_2)P_{False} \\
&= \frac{1}{2} \left\{ \int_0^\infty \int_{-\infty}^{\gamma_o} [p(z|s_1) f_R(\rho_r)] dz d\rho_r + \int_0^\infty \int_{\gamma_o}^\infty [p(z|s_2) f_R(\rho_r)] dz d\rho_r \right\} \\
&= \frac{1}{2} \int_0^\infty \left\{ \int_{-\infty}^{\gamma_o} p(z|s_1) dz + \int_{\gamma_o}^\infty p(z|s_2) dz \right\} f_R(\rho_r) d\rho_r \\
&= \frac{1}{2} \int_0^\infty \left\{ 2 \int_{\gamma_o}^\infty p(z|s_2) dz \right\} f_R(\rho_r) d\rho_r \\
&= \int_0^\infty \left\{ \int_{\gamma_o}^\infty p(z|s_2) dz \right\} f_R(\rho_r) d\rho_r \\
&= \int_0^\infty (P_{mod}) f_R(\rho_r) d\rho_r
\end{aligned} \tag{A.45}$$

where the modulation probability of bit error is determined as

$$\begin{aligned}
P_{mod} &= Q \left( \sqrt{\frac{E_b}{N_o}} \right) = Q \left( \sqrt{\frac{E_d}{2N_o}} \right) = Q \left( \sqrt{\frac{i_{dc}^2 T_b}{2N_o}} \right) \\
&= Q \left( \sqrt{\frac{[R_{ph} P_r(\rho_r)]^2}{2N_o R_b}} \right) = Q \left\{ \left[ \frac{(R_{ph})^2}{(N_o)(2R_b)} \right]^{1/2} P_r(\rho_r) \right\} \\
&= Q \left\{ \left[ \frac{(R_{ph})^2}{\sigma_o^2} \right]^{1/2} P_r(\rho_r) \right\} = Q \{ K_r P_r(\rho_r) \} \\
&= Q [K_r \alpha_r G_r \exp(-G_r \rho_r^2)]
\end{aligned} \tag{A.46}$$

Thus, the probability of bit error for a fading communication channel, due to tracking loss, is defined by

$$P_B = \int_0^\infty Q [K_r \alpha_r G_r \exp(-G_r \rho_r^2)] f_R(\rho_r) d\rho_r \tag{A.47}$$

#### A.4 Link Margin

Comparison of the detected received signal power with receiver sensitivity,  $Rx_s$  determines the system link margin, denoted in dB by

$$\text{Link Margin} = P_r \text{ [dB]} - Rx_s \text{ [dB]} \quad (\text{A.48})$$

*A.4.1 Received Optical Power.* The parameters used to determine the detected received signal power are determined from the Friis transmission equation, and the avalanche photodiode (APD) gain as

$$P_r = (P_t \eta_t G_t L_t L_{ao})(L_s L_a)(L_r G_r \eta_r) G_d \quad (\text{A.49})$$

where  $G_d$  is the APD gain defined in Appendix D. Based on the Chapter III defined operational parameters, the theoretical detected received optical power for each beam is shown in Figure A.7. Although, a larger wavelength is less susceptible to atmospheric loss, at higher elevation angles the shorter wavelength achieves slightly better power performance.

*A.4.2 Receiver Sensitivity.* Since the noise statistics are Gaussian, in addition to the optimum decision threshold, the complementary error function provides an estimate of the receiver performance [1, page 42]. Thus, the receiver sensitivity is determined as the minimum received power required to maintain the desired system BER, for a given message data rate [1, page 43]. For the purposes of this study, the minimum received power which produces a system BER of  $10^{-6}$ , common for free-space communications, will be the receiver sensitivity.

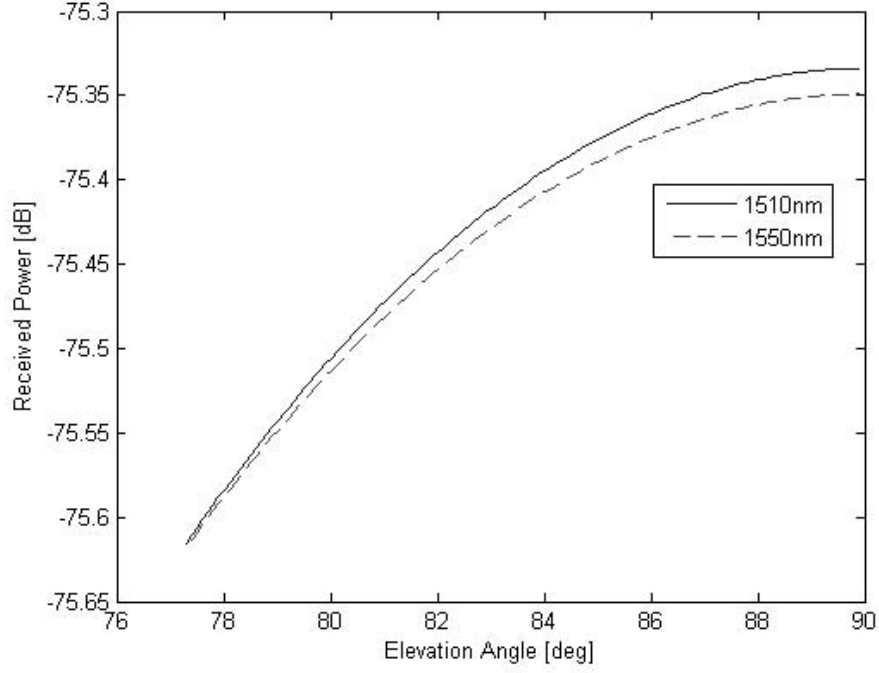


Figure A.7: Theoretical Detected Received Optical Signal Power

Based on the complementary error function curve, as shown in Figure A.5, the receiver sensitivity is determined as [1, page 246]

$$\begin{aligned}
 Q(x) &= 10^{-6} \Rightarrow x \approx 4.753 \\
 Rx_s &= (2x) \left( \frac{1}{R_{ph}} \right) (i_n^2)^{1/2} \text{ [W]}
 \end{aligned} \tag{A.50}$$

where  $i_n^2$  is the total equivalent noise power at the APD. Thus, for each transmitted beam, the receiver sensitivity is shown in Figure A.8.

*A.4.3 Link Margin.* Based on the detected received optical power and receiver sensitivity, for a transmitted symbol 1, the system link margin is shown in Figure A.9. Thus, within the receiver field of view (FOV), the longer wavelength achieves approximately 0.1 dB greater link margin performance. In either case, both beams achieve a positive margin above 1.5 dB, assuming no tracking loss effects, which will satisfy the required system BER performance [29, page 265].

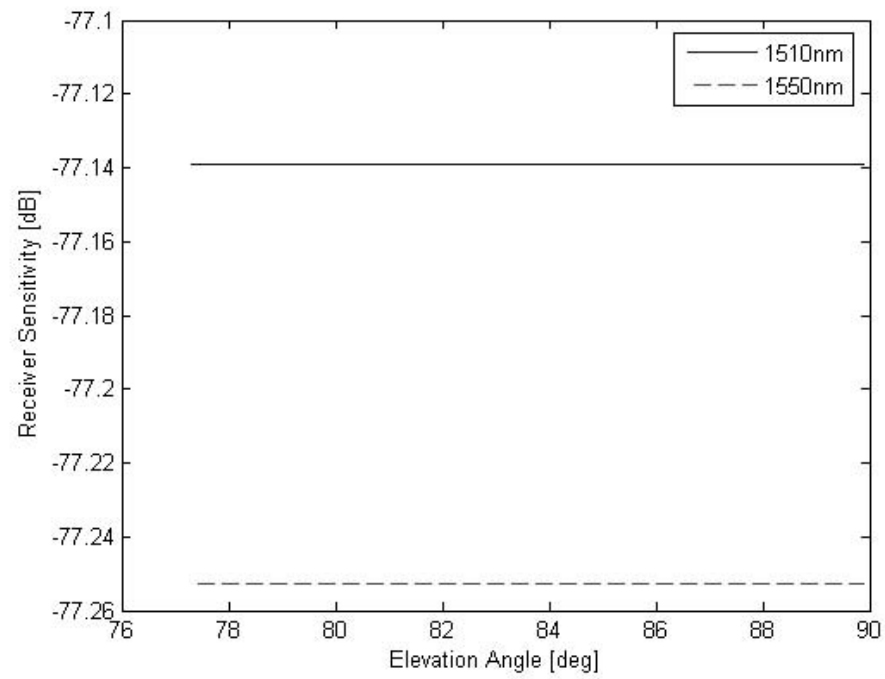


Figure A.8: Receiver Sensitivity

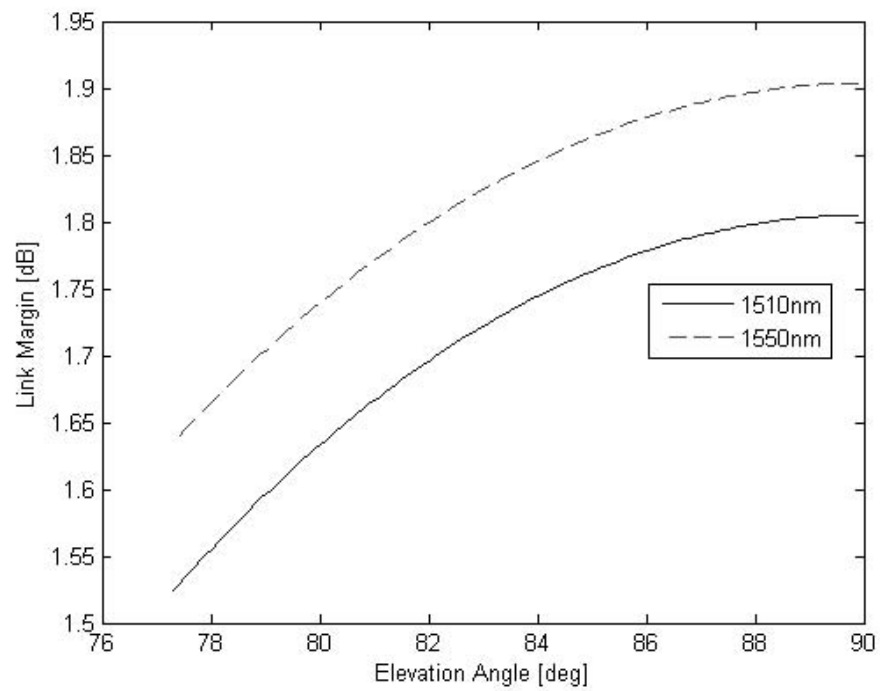


Figure A.9: Link Margin

### ***A.5 Summary***

This appendix presented the fundamental communication theory aspects, probability of bit error and link margin, of the laser communication architecture. Probability of bit error, commonly referred to as bit error rate (BER), provides a measure of communication system performance, which is dependent upon received signal power and radial tracking error statistics. In addition, based on the modulation scheme, the system BER is used to determine the receiver sensitivity and link margin, which determines if adequate signal power is available for communications.

## Appendix B. Satellite Dynamics

### B.1 Satellite Position

The relative satellite orbital motion about Earth can be described by the two body problem equation of motion [34, page 50]

$$\frac{d^2 \vec{r}_s}{dt^2} = - \left( \frac{\mu}{r_s^3} \right) \vec{r}_s \quad (\text{B.1})$$

This relation satisfies both conservation of energy and angular momentum per unit mass denoted by [34, pages 50-52]

$$E = \frac{1}{2} v_s^2 - \frac{\mu}{r_s} \quad (\text{B.2})$$

$$\vec{H} = \vec{r}_s \times \vec{v}_s \quad (\text{B.3})$$

where  $\vec{r}_s$  is the satellite position vector,  $\vec{v}_s$  is the satellite velocity vector,  $E$  is the energy per unit mass,  $\vec{H}$  is the angular momentum vector, and  $\mu = 3.986 \times 10^5 \text{ km}^3/\text{s}^2$  is the Earth's gravitational constant.

*B.1.1 Orbit Location.* Orbit orientation relative to a geocentric inertial (GCI) reference frame, defined by unit vectors  $\hat{i}$ ,  $\hat{j}$ , and  $\hat{k}$  as shown in Figure B.1, and satellite motion within the orbital plane are determined by the following classical orbital elements [34, page 60]:

$e$  = eccentricity

$a$  = semimajor axis

$i$  = inclination

$T_o$  = time since perigee passage

$\Omega$  = right ascension of ascending node

$\omega$  = argument of perigee

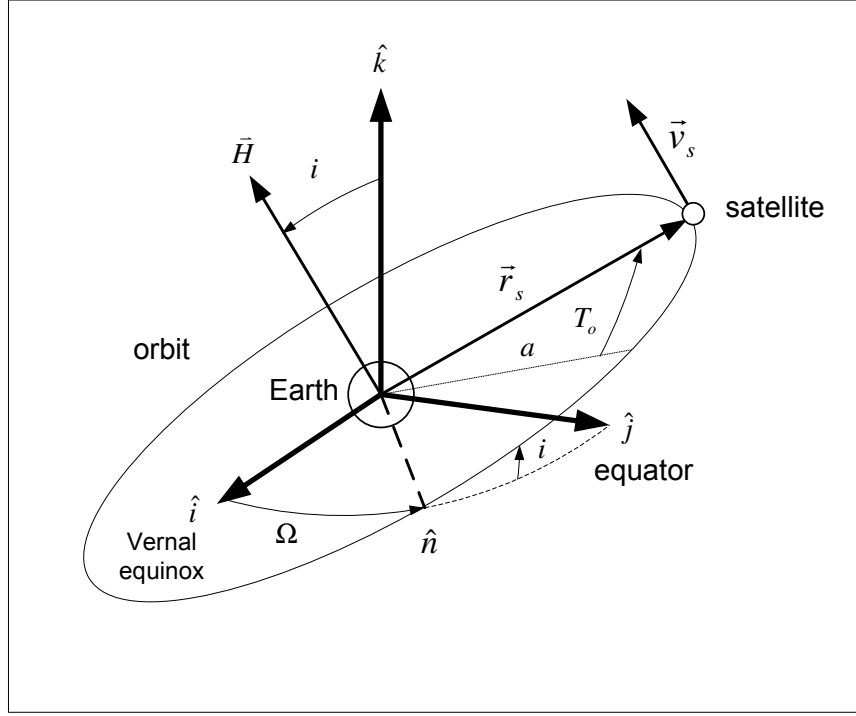


Figure B.1: GCI Frame Satellite Orbit

Orbit energy and angular momentum magnitude are determined by [34, page 56]

$$E = -\frac{\mu}{2a} \quad (\text{B.4})$$

$$H = \sqrt{\mu a (1 - e^2)} \quad (\text{B.5})$$

A circular orbit assumption implies  $e = 0$  and  $\omega$  can not be determined. However, an alternate orbital element, known as the argument of latitude,  $u_o$ , is used to determine relative orbital position from the line of nodes,  $\hat{n}$ , also referred to as the nodal unit vector [16, page 134]. Within the equatorial plane,  $\Omega$  determines the angular position of the nodal vector from the vernal equinox,  $\hat{i}$ , as shown in Figure B.1. Using conic section geometry, based on the GCI frame, the nodal unit vector is [34, page 62]

$$\hat{n} = \frac{\hat{k} \times \vec{H}}{|\hat{k} \times \vec{H}|} = \cos(\Omega)\hat{i} + \sin(\Omega)\hat{j} \quad (\text{B.6})$$

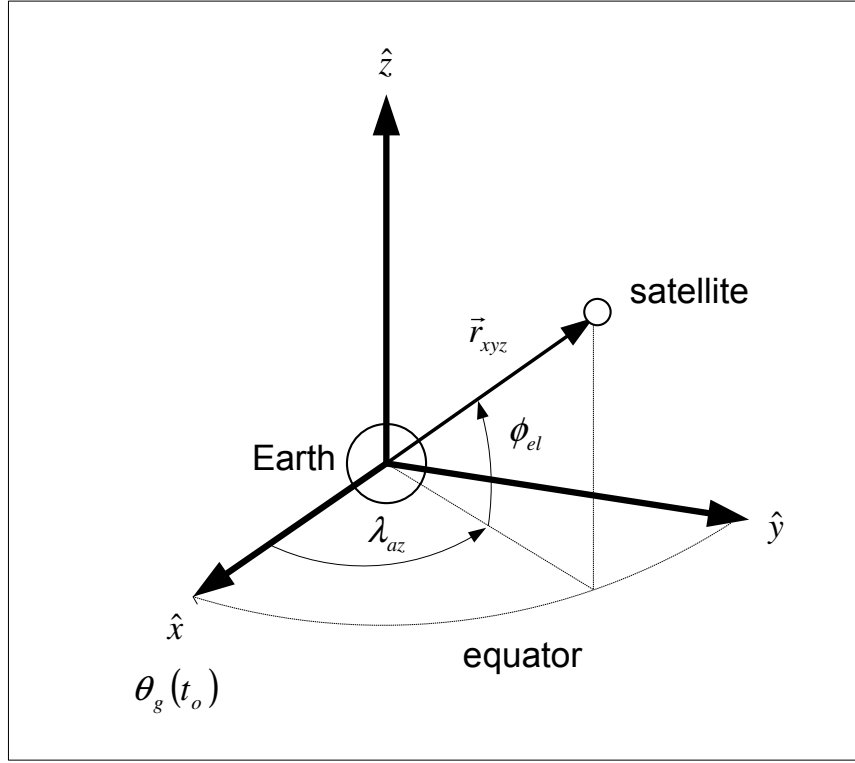


Figure B.2: ECF Frame Satellite Orbit

Accounting for Greenwich sidereal time,  $\theta_G(t_o)$ , angle between vernal equinox and Greenwich meridian at epoch, satellite longitude location,  $\lambda_{az}$ , and the orbital angular velocity,  $\omega_o$ , the argument of latitude over time is determined by [28, page 43]

$$u_o(t) = \omega_o(t - t_o) + \theta_G(t_o) + \lambda_{az} - \Omega \quad (\text{B.7})$$

*B.1.2 Satellite Location.* In terms of the Earth centered fixed (ECF) reference frame, defined by unit vectors  $\hat{x}$ ,  $\hat{y}$ , and  $\hat{z}$  illustrated in Figure B.2, relative position from Greenwich meridian,  $\hat{x} = \theta_G(t_o)$ , is determined by [16, page 100]

$$\vec{r}_{xyz} = a [\cos(\lambda_{az}) \cos(\phi_{el}) \hat{x} + \sin(\lambda_{az}) \cos(\phi_{el}) \hat{y} + \sin(\phi_{el}) \hat{z}] \quad (\text{B.8})$$

where  $\lambda_{az}$  is the azimuth, also referred to as longitude location, and  $\phi_{el}$  is the elevation, also referred to as latitude location. The satellite GCI reference frame position



vector,  $\vec{r}_s$ , is related to the ECF reference frame position vector,  $\vec{r}_{xyz}$ , by the following rotational transformation:

$$\vec{r}_{xyz} = R^{EG} \vec{r}_s \quad (\text{B.9})$$

where

$$R^{EG} = R_3(u_o(t)) R_1(i) R_3(\Omega) = (R^{GE})^T \quad (\text{B.10})$$

The corresponding direction cosine matrices, for positive counter clockwise rotations, are determined by

$$\begin{aligned} R_1(\alpha) &= \begin{pmatrix} 1 & 0 & 0 \\ 0 & \cos(\alpha) & \sin(\alpha) \\ 0 & -\sin(\alpha) & \cos(\alpha) \end{pmatrix} \\ R_2(\alpha) &= \begin{pmatrix} \cos(\alpha) & 0 & \sin(\alpha) \\ 0 & 1 & 0 \\ -\sin(\alpha) & 0 & \cos(\alpha) \end{pmatrix} \\ R_3(\alpha) &= \begin{pmatrix} \cos(\alpha) & \sin(\alpha) & 0 \\ -\sin(\alpha) & \cos(\alpha) & 0 \\ 0 & 0 & 1 \end{pmatrix} \end{aligned}$$

Thus, GCI position and velocity vectors are determined as

$$\vec{r}_s = R^{GE} \vec{r}_{xyz} \quad (\text{B.11})$$

$$\vec{v}_s = \frac{d\vec{r}_s}{dt} = \vec{\omega}_s \times \vec{r}_s \quad (\text{B.12})$$

where  $\vec{\omega}_s$  is the satellite angular velocity vector.

## B.2 Satellite Attitude Dynamics

As illustrated in Figure B.3, satellite attitude within orbit is defined about either the orbit reference frame or satellite body reference frame. Vectors  $\hat{x}_o$ ,  $\hat{y}_o$ ,  $\hat{z}_o$  represent the orbit reference axis frame:  $\hat{z}_o$  is the negative unit vector of  $\vec{r}_s$ ,  $\hat{x}_o$  is the unit vector

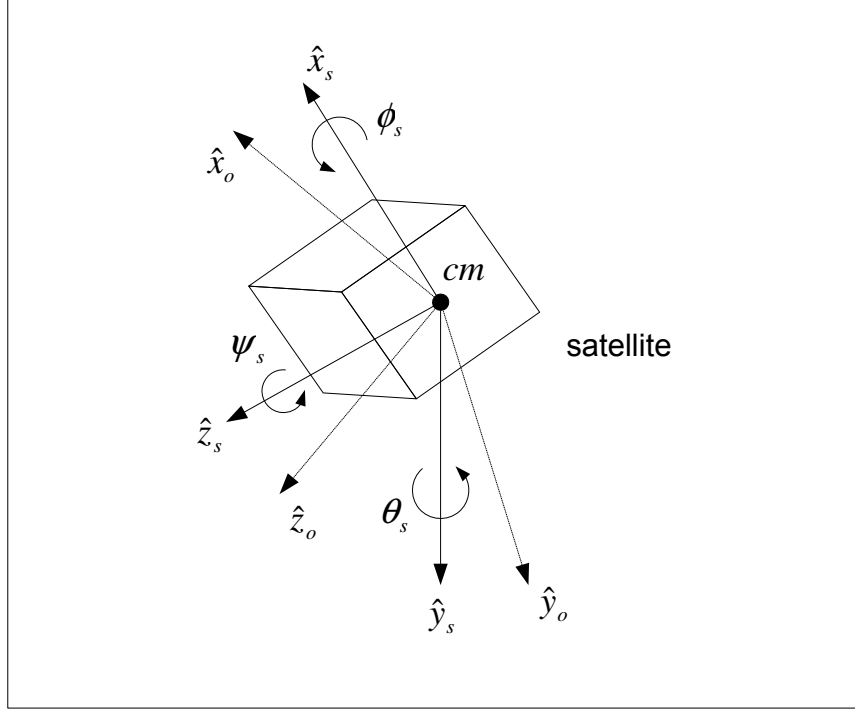


Figure B.3: Satellite Attitude

of  $\vec{v}_s$ , and  $\hat{y}_o$  is normal to the orbit plane. Unit vectors  $\hat{x}_s, \hat{y}_s, \hat{z}_s$  define the satellite body axis frame. Attitude motion of the satellite platform about its center of mass (cm) is defined by Euler's rotational equation of motion as [28, page 95]

$$\dot{\vec{h}}_s + \vec{\omega}_s \times \vec{h}_s = \vec{T}_s \quad (\text{B.13})$$

where  $\vec{h}_s$  is the satellite body angular momentum vector and  $\vec{T}_s$  is the total torque vector acting on the satellite body. Assuming an axisymmetric rigid body about the  $\hat{z}_s$  axis and alignment with the principal axes of inertia, the satellite body angular momentum vector is determined by

$$\vec{h}_s = \mathbf{I}_s \vec{\omega}_s = \begin{pmatrix} I_x & 0 & 0 \\ 0 & I_x & 0 \\ 0 & 0 & I_z \end{pmatrix} \begin{pmatrix} \omega_x \\ \omega_y \\ \omega_z \end{pmatrix} = \begin{pmatrix} I_x \omega_x \\ I_x \omega_y \\ I_z \omega_z \end{pmatrix} \quad (\text{B.14})$$

where  $\mathbf{I}_s$  is the satellite moment of inertia matrix. Thus, attitude equations of motion can be represented by the following nonlinear equations:

$$\begin{aligned}\dot{\omega}_x &= -\left[\frac{(I_z - I_x)}{I_x}\right]\omega_y\omega_z + \frac{T_x}{I_x} \\ \dot{\omega}_y &= -\left[\frac{(I_x - I_z)}{I_x}\right]\omega_x\omega_z + \frac{T_y}{I_x} \\ \dot{\omega}_z &= \frac{T_z}{I_z}\end{aligned}\tag{B.15}$$

*B.2.1 Attitude Kinematics.* Applying attitude kinematics,  $\vec{\omega}_s$  is defined as [28, page 102],

$$\vec{\omega}_s = \vec{\omega}_{so} + \vec{\omega}_{ois}\tag{B.16}$$

where  $\vec{\omega}_{so}$  is the satellite body relative to orbit frame angular velocity vector and  $\vec{\omega}_{ois}$  is the angular velocity vector of the orbit reference frame relative to the GCI frame in satellite body coordinates. Satellite attitude with respect to the body axis reference frame, as shown in Figure B.3, is defined by Euler angles: roll angle,  $\phi_s$ , about the  $\hat{x}_s$  axis, pitch angle,  $\theta_s$ , about the  $\hat{y}_s$  axis, and yaw angle,  $\psi_s$ , about the  $\hat{z}_s$  axis. Assuming a yaw, pitch, and roll order of rotational transformation,  $\vec{\omega}_{so}$  is determined as [28, page 103]

$$\vec{\omega}_{so} = R_1(\phi_s)R_2(\theta_s)R_3(\psi_s)\begin{pmatrix} 0 \\ 0 \\ \dot{\psi}_s \end{pmatrix} + R_1(\phi_s)R_2(\theta_s)\begin{pmatrix} 0 \\ \dot{\theta}_s \\ 0 \end{pmatrix} + R_1(\phi_s)\begin{pmatrix} \dot{\phi}_s \\ 0 \\ 0 \end{pmatrix}\tag{B.17}$$

For small Euler angles, where  $\cos(\alpha) \approx 1$  and  $\sin(\alpha) \approx \alpha$ , the rotational transformation matrices are approximated respectively by

$$R_1(\phi_s)R_2(\theta_s)R_3(\psi_s) = \begin{pmatrix} 1 & \psi_s & -\theta_s \\ \psi_s & 1 & \phi_s \\ \theta_s & -\phi_s & 1 \end{pmatrix} \quad (\text{B.18})$$

$$R_1(\phi_s)R_2(\theta_s) = \begin{pmatrix} 1 & 0 & \theta_s \\ 0 & 1 & \phi_s \\ -\theta_s & -\phi_s & 1 \end{pmatrix} \quad (\text{B.19})$$

$$R_1(\phi_s) = \begin{pmatrix} 1 & 0 & 0 \\ 0 & 1 & \phi_s \\ 0 & -\phi_s & 1 \end{pmatrix} \quad (\text{B.20})$$

Thus,

$$\vec{\omega}_{so} \approx \begin{pmatrix} \dot{\phi}_s \\ \dot{\theta}_s \\ \dot{\psi}_s \end{pmatrix} \quad (\text{B.21})$$

To determine  $\vec{\omega}_{oi}$ , angular rate of change of each orbit reference frame axis, as shown in Figure B.4, respectively is determined by,

$$\begin{aligned} \frac{d\hat{x}_o}{dt} &= \frac{d\hat{x}_o}{d\gamma} \frac{d\gamma}{dt} = \hat{y}_o \omega_3 \\ &= \frac{d\hat{x}_o}{d\beta} \frac{d\beta}{dt} = -\hat{z}_o \omega_2 \\ \frac{d\hat{y}_o}{dt} &= \frac{d\hat{y}_o}{d\alpha} \frac{d\alpha}{dt} = \hat{z}_o \omega_1 \\ &= \frac{d\hat{y}_o}{d\gamma} \frac{d\gamma}{dt} = -\hat{x}_o \omega_3 \\ \frac{d\hat{z}_o}{dt} &= \frac{d\hat{z}_o}{d\beta} \frac{d\beta}{dt} = \hat{x}_o \omega_2 \\ &= \frac{d\hat{z}_o}{d\alpha} \frac{d\alpha}{dt} = -\hat{y}_o \omega_1 \end{aligned}$$

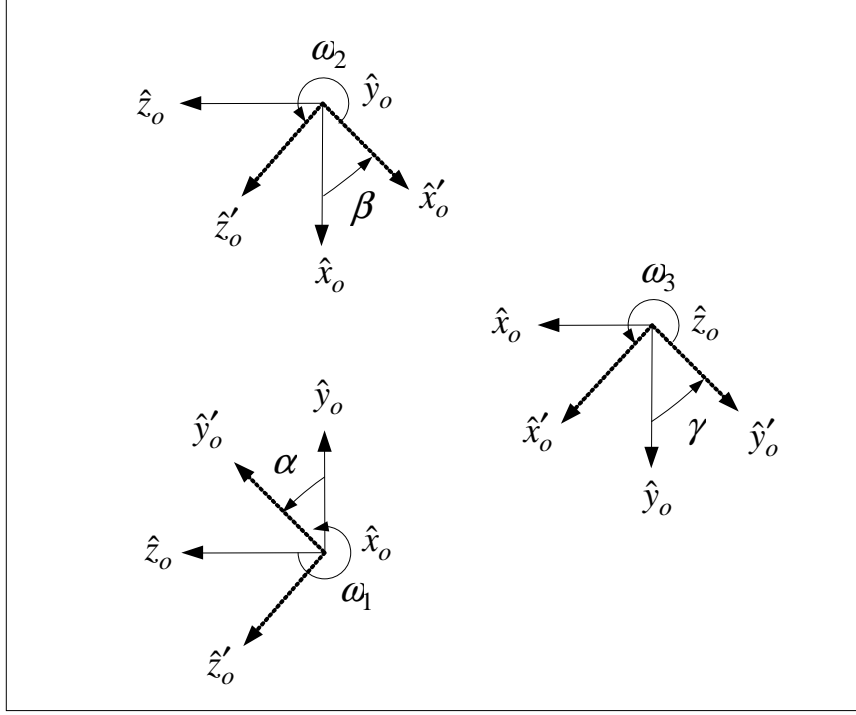


Figure B.4: Orbit Reference Frame Rate of Change

After performing a dot product between each rate of change and associated orbit reference frame axis, the respective angular velocities are [28, page 106]

$$\begin{aligned}
 \frac{d\hat{x}_o}{dt} \cdot \hat{y}_o &= -\frac{d\hat{y}_o}{dt} \cdot \hat{x}_o = |\hat{y}_o\omega_3| |\hat{y}_o| \cos(0) = \omega_3 \\
 \frac{d\hat{y}_o}{dt} \cdot \hat{z}_o &= -\frac{d\hat{z}_o}{dt} \cdot \hat{y}_o = |\hat{z}_o\omega_1| |\hat{z}_o| \cos(0) = \omega_1 \\
 \frac{d\hat{z}_o}{dt} \cdot \hat{x}_o &= -\frac{d\hat{x}_o}{dt} \cdot \hat{z}_o = |\hat{x}_o\omega_2| |\hat{x}_o| \cos(0) = \omega_2
 \end{aligned} \tag{B.22}$$

Substituting in the predetermined GCI coordinates for each respective orbit reference

frame axis

$$\begin{aligned}
\omega_1 &= -\frac{d\hat{z}_o}{dt} \cdot \hat{y}_o = -\frac{d}{dt} \left( \frac{-\vec{r}_s}{|\vec{r}_s|} \right) \cdot \left( \frac{\vec{r}_s \times \vec{v}_s}{|\vec{r}_s \times \vec{v}_s|} \right) = \frac{1}{r_s [r_s v_s \sin(90)]} \frac{d\vec{r}_s}{dt} \cdot (\vec{r}_s \times \vec{v}_s) \\
&= \left( \frac{1}{r_s^2 v_s} \right) (\vec{v}_s) \cdot (\vec{r}_s \times \vec{v}_s) = 0 \\
\omega_2 &= \frac{d\hat{z}_o}{dt} \cdot \hat{x}_o = \left( -\frac{1}{r_s} \right) \frac{d\vec{r}_s}{dt} \cdot \left( \frac{\vec{v}_s}{|\vec{v}_s|} \right) = \frac{-1}{r_s v_s} (\vec{v}_s \cdot \vec{v}_s) = \frac{-v_s}{r_s} \cos(0) = -\omega_o \\
\omega_3 &= \frac{d\hat{x}_o}{dt} \cdot \hat{y}_o = \left( \frac{1}{v_s} \right) \frac{d\vec{v}_s}{dt} \cdot \left( \frac{\vec{r}_s \times \vec{v}_s}{|\vec{r}_s \times \vec{v}_s|} \right) = \frac{1}{v_s [r_s v_s \sin(90)]} \frac{d^2 \vec{r}_s}{dt^2} \cdot (\vec{r}_s \times \vec{v}_s) \\
&= \left( \frac{1}{r_s v_s^2} \right) \left( \frac{-\mu}{r_s^3} \right) \vec{r}_s \cdot (\vec{r}_s \times \vec{v}_s) = \left( \frac{-\mu}{r_s^4 v_s^2} \right) \vec{r}_s \cdot (\vec{r}_s \times \vec{v}_s) = 0
\end{aligned}$$

Thus,

$$\vec{\omega}_{oi} = \begin{pmatrix} \omega_1 \\ \omega_2 \\ \omega_3 \end{pmatrix} = \begin{pmatrix} 0 \\ -\omega_o \\ 0 \end{pmatrix} \quad (\text{B.23})$$

In terms of the satellite body axis reference frame, for small Euler angles,

$$\begin{aligned}
\vec{\omega}_{ois} &= R_1(\phi_s) R_2(\theta_s) R_3(\psi_s) \vec{\omega}_{oi} \\
&= \begin{pmatrix} 1 & \psi_s & -\theta_s \\ \psi_s & 1 & \phi_s \\ \theta_s & -\phi_s & 1 \end{pmatrix} \begin{pmatrix} 0 \\ -\omega_o \\ 0 \end{pmatrix} \\
&= \begin{pmatrix} -\omega_o \psi_s \\ -\omega_o \\ \omega_o \phi_s \end{pmatrix} \quad (\text{B.24})
\end{aligned}$$

Thus, the satellite angular velocity vector is

$$\vec{\omega}_s = \begin{pmatrix} \omega_x \\ \omega_y \\ \omega_z \end{pmatrix} = \begin{pmatrix} \dot{\phi}_s - \omega_o \psi_s \\ \dot{\theta}_s - \omega_o \\ \dot{\psi}_s + \omega_o \phi_s \end{pmatrix} \quad (\text{B.25})$$

Substituting into the nonlinear attitude dynamic equations, accounting for small Euler angles where  $\alpha\dot{\alpha} \approx 0$  and  $\dot{\alpha}\dot{\beta} \approx 0$ , satellite attitude motion is defined by linearized rotational equations of motion as,

$$\begin{aligned}\ddot{\phi}_s &= \omega_o \left[ 1 + \frac{(I_z - I_x)}{I_x} \right] \dot{\psi}_s + \omega_o^2 \left[ \frac{(I_z - I_x)}{I_x} \right] \phi_s + \frac{T_x}{I_x} \\ \ddot{\theta}_s &= \frac{T_y}{I_x} \\ \ddot{\psi}_s &= -\omega_o \dot{\phi}_s + \frac{T_z}{I_z}\end{aligned}\tag{B.26}$$

*B.2.2 Satellite Field of View.* The satellite FOV geometry, as shown in Figure B.5, is determined by [16, page 108]

$$\rho_E = \sin^{-1}(R_E/r_s)\tag{B.27}$$

$$\rho_o = 90^\circ - \rho_E\tag{B.28}$$

$$D_E = R_E \tan(\rho_o)\tag{B.29}$$

where  $\rho_E$  is the radial distance of Earth visible from orbit,  $R_E$  is the Earth's radius,  $\rho_o$  is the radial distance of Earth from the Earth's cm, and  $D_E$  is the Earth horizon distance, also referred to as slant range. Based on the satellite's operational constraints,

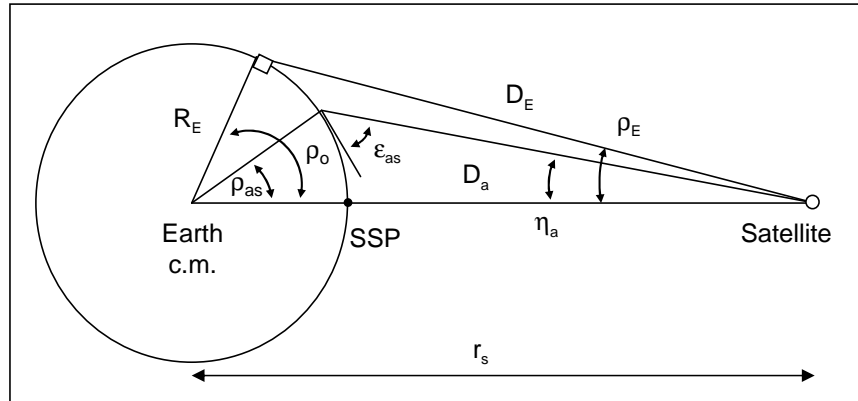


Figure B.5: Satellite Field of View Geometry

defined in Chapter III, these parameters are determined as,

$$\rho_E = \sin^{-1}(6,378/42,164) = 8.7^\circ [0.152 \text{ rad}] \quad (\text{B.30})$$

$$\rho_o = 90^\circ - 8.7^\circ = 81.3^\circ [1.419 \text{ rad}] \quad (\text{B.31})$$

$$D_E = (6,378) \tan(81.3) = 41,679 \text{ km} \quad (\text{B.32})$$

Due to the aircraft's operational constraint on minimum elevation angle, defined in Chapter III as  $20^\circ$ , the actual satellite FOV is determined by,

$$FOV_S = 2\eta_a \quad (\text{B.33})$$

where  $\eta_a$  is the nadir angle, radial distance from SSP to aircraft visible from orbit. The angular relationships between aircraft and satellite longitude and latitude locations,  $(\lambda_{az}, \phi_{el})$  and  $(\lambda_a, \phi_a)$  respectively, are defined as [16, page 111]

$$\begin{aligned} \rho_{as} &= \cos^{-1} [\sin(\phi_{el}) \sin(\phi_a) + \cos(\phi_{el}) \cos(\phi_a) \cos(|\lambda_{az} - \lambda_a|)] \\ \lambda_{as} &= \cos^{-1} [\sin(\phi_a) - \cos(\rho_{as}) \sin(\phi_{el}) / (\sin(\rho_{as}) \cos(\phi_{el}))] \\ \varepsilon_{sa} &= \cos^{-1} \left( \frac{\sin(\eta_a)}{\sin(\rho_e)} \right) \end{aligned} \quad (\text{B.34})$$

where  $\rho_{as}$  is the radial distance from SSP to aircraft along the Earth's surface, defined as the Earth central angle,  $\lambda_{as}$  is the azimuth direction from SSP to aircraft, and  $\varepsilon_{sa}$  elevation angle from aircraft to satellite. The satellite azimuth direction from the aircraft, measured from true north, is determined by

$$0^\circ \leq \lambda_{as} < 180^\circ \implies \lambda_{sa} = 180^\circ + \lambda_{as} \quad (\text{B.35})$$

$$180^\circ \leq \lambda_{as} < 360^\circ \implies \lambda_{sa} = \lambda_{as} - 180^\circ \quad (\text{B.36})$$



For a given aircraft position,  $\vec{r}_a$ , the nadir angle and maximum range are determined by [16, page 111]

$$\eta_a = 90^\circ - \rho_{as} - \varepsilon_{sa} \quad (\text{B.37})$$

$$= \sin^{-1} [\sin(\rho_e) \cos(\varepsilon_{sa})] \quad (\text{B.38})$$

$$D_a = r_a \left[ \frac{\sin(\rho_{as})}{\sin(\eta_a)} \right] \quad (\text{B.39})$$

where  $D_a$  is the maximum range between the satellite and aircraft. Thus, for the predefined operational constraints, the maximum nadir angle, satellite FOV, Earth coverage, and maximum range are determined as

$$\eta_a = \sin^{-1} [\sin(8.7) \cos(20)] = 8.172^\circ [0.143 \text{ rad}] \quad (\text{B.40})$$

$$FOV_S = 2(8.172) = 16.343^\circ [0.285 \text{ rad}] \quad (\text{B.41})$$

$$\begin{aligned} \rho_{as} &= 90^\circ - \eta_a - \varepsilon_{sa} \\ &= 90^\circ - 8.172^\circ - 20^\circ = 61.828^\circ [1.079 \text{ rad}] \end{aligned} \quad (\text{B.42})$$

$$D_a = (6396) \left[ \frac{\sin(61.828)}{\sin(8.172)} \right] = 39,668 \text{ km} \quad (\text{B.43})$$

### ***B.3 Disturbance Environment***

Orbit perturbing forces are considered negligible; hence, attitude disturbances are the primary concern. The satellite structure is the primary load path and designed to compensate for expected minimum stiffness requirements for rigid body purposes [35, page 2]. Due to alignment with the positive yaw axis,  $+z_s$ , platform disturbances creating roll and pitch attitude errors affect receiver pointing. Assuming the attitude determination and control system (ADCS) adequately compensates against expected external environmental platform disturbance torques, maintaining three-axis stabilization, satellite internal disturbances affect pointing error. In particular, common internal disturbances are cm uncertainty, control hardware misalignment or output error, liquid fuel sloshing, rotating machinery, and thermal shock [16, page 355].

Spacecraft structural loads are comprised of structurally transmitted vibration, shock, and thermal stress [11, page 417]. Vibration and shock induced structural loads result from translational and angular accelerations produced by control hardware. Thermal stress, due to differential heating or cooling, results in structural deformations.

Control hardware misalignment or output error and cm uncertainty, produce disturbance torques during both translational and rotational motion [16, page 355]. These disturbances are modeled as constant disturbance torques during thruster firings. Liquid fuel sloshing and rotating machinery effects are modeled as sinusoidal disturbance torques. Thermal shocks arise from thermal stresses on solar arrays when the satellite enters or leaves eclipse [16, page 355]. Assuming each solar array behaves as a cantilever beam, thermal shocks are modeled as impulse disturbance torques.

#### ***B.4 Summary***

This appendix presented the fundamental satellite orbital and attitude dynamics principles which impact the dual FTCS design. Location of the satellite geosynchronous orbit maximizes the field of view (FOV) coverage area over the Earth's surface and determines the relative uplink beam propagation distances. It is assumed the ADCS provides three-axis stabilization against expected environmental disturbances, which limits the platform disturbances to be from internal sources. These internal disturbances are considered to be random torque inputs defined in the linearized rotational equations of motion. Although not explicitly implemented in the simulation, these equations of motion are the basis for the plant disturbance noise affecting motion about the x-axis and y-axis, as shown in Chapter III and Appendix G.

## Appendix C. Aircraft Dynamics

### C.1 Aircraft Position

As illustrated in Figure C.1, aircraft attitude is defined about either a true North reference frame or aircraft body axis reference frame. Based on aircraft location, true North reference frame is defined by unit vectors  $\hat{x}_n, \hat{y}_w, \hat{z}_v$ :  $\hat{x}_n$  aligned with true North,  $\hat{y}_w$  faces due West,  $\hat{z}_v$  local unit vector of  $\vec{r}_a$ . Unit vectors  $\hat{x}_a, \hat{y}_a, \hat{z}_a$ , roll, pitch, and yaw axis respectively, define the aircraft body axis reference frame.

Since the UAV is operating within the satellite receiver field of view, defined in Appendix D as  $\text{FOV}_R$ , and assuming a spherical Earth, the geocentric longitude and latitude over time are

$$\lambda_a(t) = \omega_o(t - t_o) + \theta_G(t_o) + \delta\lambda_a(t) \quad (\text{C.1})$$

$$\phi_a(t) = \phi_{el} + \delta\phi_a(t) \quad (\text{C.2})$$

where  $\delta\lambda_a(t)$  is the longitude displacement and  $\delta\phi_a(t)$  is the latitude displacement. In terms of the GCI frame, defined by unit vectors  $\hat{i}, \hat{j}$ , and  $\hat{k}$ , the relative position and velocity vectors are denoted by

$$\vec{r}_a = r_a \left[ \cos(\lambda_a) \cos(\phi_a) \hat{i} + \sin(\lambda_a) \cos(\phi_a) \hat{j} + \sin(\phi_a) \hat{k} \right] \quad (\text{C.3})$$

$$\vec{v}_a = \frac{d\vec{r}_a}{dt} = \vec{\omega}_a \times \vec{r}_a \quad (\text{C.4})$$

where  $r_a$  is the position vector magnitude and  $\vec{\omega}_a$  is the aircraft angular velocity vector.

### C.2 Aircraft Attitude Dynamics

*C.2.1 Attitude Dynamics.* Attitude dynamics about the aircraft cm is defined from Euler's rotational equation of motion as

$$\dot{\vec{h}}_a + \vec{\omega}_a \times \vec{h}_a = \vec{T}_a \quad (\text{C.5})$$

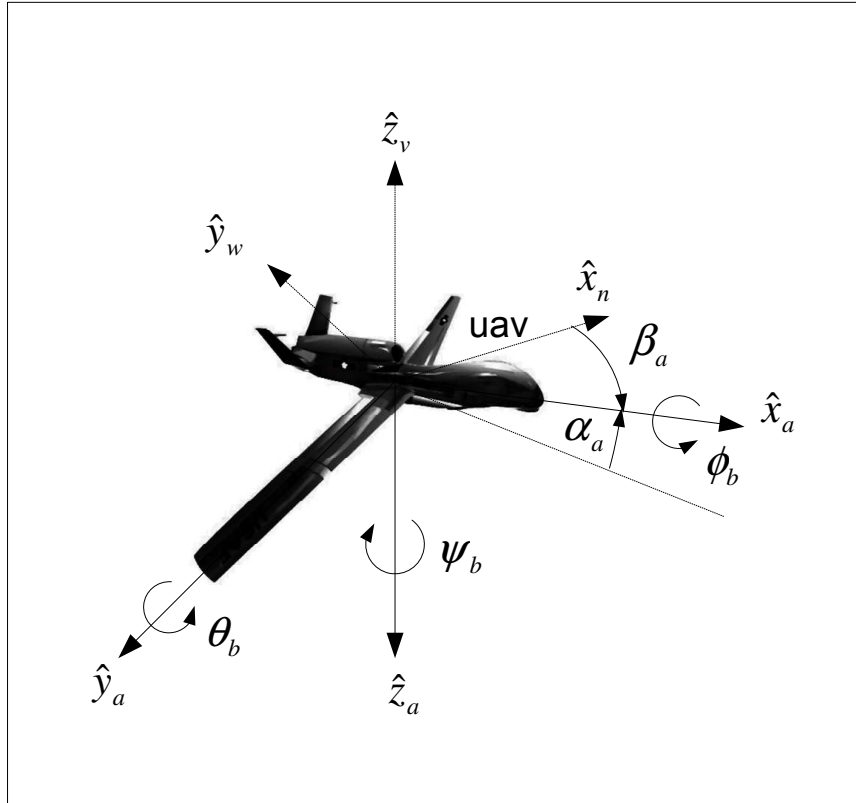


Figure C.1: Aircraft Attitude

where  $\vec{h}_a$  is the aircraft angular momentum vector and  $\vec{T}_a$  is the total aircraft torque vector. Only one aircraft body axis,  $\hat{y}_a$ , is aligned to a principal axis; thus, the aircraft body angular momentum vector is defined by [39, page 374]

$$\vec{h}_a = \mathbf{I}_a \vec{\omega}_a = \begin{pmatrix} I_{11} & 0 & I_{13} \\ 0 & I_{22} & 0 \\ I_{31} & 0 & I_{33} \end{pmatrix} \vec{\omega}_a \quad (\text{C.6})$$

where  $\mathbf{I}_a$  is the aircraft moment of inertia matrix. The aircraft angular velocity vector,  $\vec{\omega}_a$ , is equivalent to the sum of the body axis and true North reference frame angular velocity vectors defined respectively by

$$\vec{\omega}_a = \begin{pmatrix} \omega_{xa} \\ \omega_{ya} \\ \omega_{za} \end{pmatrix} = \vec{\omega}_{ab} + \vec{\omega}_{nb} \quad (\text{C.7})$$

where  $\vec{\omega}_{ab}$  is body axis reference frame angular velocity vector and  $\vec{\omega}_{nb}$  is the true North reference frame angular velocity vector in body axis coordinates.

*C.2.2 Attitude Kinematics.* Heading angle,  $\beta_a$ , and angle of attack,  $\alpha_a$ , determine body axis reference frame orientation relative to true North reference frame. Attitude with respect to the body axis reference frame, as shown in Figure C.1, is defined by Euler angles: roll angle  $\phi_b$ , pitch angle  $\theta_b$ , and yaw angle  $\psi_b$ . Both reference frames are related to the GCI frame by the following rotational transformations

$$\begin{aligned} R^{NA} &= R_1(180)R_2(-\alpha_a)R_3(-\beta_a) \\ R^{NG} &= R_1(\phi_a)R_3(-[90 - \lambda_a]) \\ R^{AG} &= R^{AN}R^{NG} = (R^{NA})^T R^{NG} \end{aligned}$$

where  $R^{NA}$  denotes the rotational transformation from the body axis reference frame to the true North reference frame,  $R^{NG}$  denotes the rotational transformation from

the GCI frame to the true North reference frame, and  $R^{AG}$  denotes the rotational transformation from the GCI frame to the body axis reference frame.

Incorporating the corresponding direction cosine matrices,  $R^{NA}$  and  $R^{NG}$  are determined as

$$\begin{aligned}
R^{NA} &= R_1(180)R_2(-\alpha_a)R_3(-\beta_a) \\
&= \begin{pmatrix} 1 & 0 & 0 \\ 0 & -1 & 0 \\ 0 & 0 & -1 \end{pmatrix} \begin{pmatrix} \cos(\alpha_a) & 0 & -\sin(\alpha_a) \\ 0 & 1 & 0 \\ \sin(\alpha_a) & 0 & \cos(\alpha_a) \end{pmatrix} \begin{pmatrix} \cos(\beta_a) & -\sin(\beta_a) & 0 \\ \sin(\beta_a) & \cos(\beta_a) & 0 \\ 0 & 0 & 1 \end{pmatrix} \\
&= \begin{pmatrix} 1 & 0 & 0 \\ 0 & -1 & 0 \\ 0 & 0 & -1 \end{pmatrix} \begin{pmatrix} \cos(\alpha_a)\cos(\beta_a) & -\cos(\alpha_a)\sin(\beta_a) & -\sin(\alpha_a) \\ \sin(\beta_a) & \cos(\beta_a) & 0 \\ \sin(\alpha_a)\cos(\beta_a) & -\sin(\alpha_a)\sin(\beta_a) & \cos(\alpha_a) \end{pmatrix} \\
&= \begin{pmatrix} \cos(\alpha_a)\cos(\beta_a) & -\cos(\alpha_a)\sin(\beta_a) & -\sin(\alpha_a) \\ -\sin(\beta_a) & -\cos(\beta_a) & 0 \\ -\sin(\alpha_a)\cos(\beta_a) & \sin(\alpha_a)\sin(\beta_a) & -\cos(\alpha_a) \end{pmatrix} \tag{C.8}
\end{aligned}$$

$$\begin{aligned}
R^{NG} &= R_1(\phi_a)R_3(-[90 - \lambda_a]) \\
&= \begin{pmatrix} 1 & 0 & 0 \\ 0 & \cos(\phi_a) & \sin(\phi_a) \\ 0 & -\sin(\phi_a) & \cos(\phi_a) \end{pmatrix} \begin{pmatrix} \cos(\lambda_a - 90) & \sin(\lambda_a - 90) & 0 \\ -\sin(\lambda_a - 90) & \cos(\lambda_a - 90) & 0 \\ 0 & 0 & 1 \end{pmatrix} \\
&= \begin{pmatrix} 1 & 0 & 0 \\ 0 & \cos(\phi_a) & \sin(\phi_a) \\ 0 & -\sin(\phi_a) & \cos(\phi_a) \end{pmatrix} \begin{pmatrix} -\sin(\lambda_a) & \cos(\lambda_a) & 0 \\ -\cos(\lambda_a) & -\sin(\lambda_a) & 0 \\ 0 & 0 & 1 \end{pmatrix} \\
&= \begin{pmatrix} -\sin(\lambda_a) & \cos(\lambda_a) & 0 \\ -\cos(\phi_a)\cos(\lambda_a) & -\cos(\phi_a)\sin(\lambda_a) & \sin(\phi_a) \\ \sin(\phi_a)\cos(\lambda_a) & \sin(\phi_a)\sin(\lambda_a) & \cos(\phi_a) \end{pmatrix} \tag{C.9}
\end{aligned}$$

Assuming a roll, pitch, and yaw, order of rotational transformation, the body axis reference frame angular velocity vector is defined by

$$\vec{\omega}_{ab} = R_3(\psi_b)R_2(\theta_b)R_1(\phi_b) \begin{pmatrix} \dot{\phi}_b \\ 0 \\ 0 \end{pmatrix} + R_3(\psi_b)R_2(\theta_b) \begin{pmatrix} 0 \\ \dot{\theta}_b \\ 0 \end{pmatrix} + R_3(\psi_b) \begin{pmatrix} 0 \\ 0 \\ \dot{\psi}_b \end{pmatrix} \quad (\text{C.10})$$

The true North reference frame angular velocity vector is determined by,

$$\begin{aligned} \vec{\omega}_n &= R^{NG}\vec{\omega}_E \\ &= \begin{pmatrix} -\sin(\lambda_a) & \cos(\lambda_a) & 0 \\ -\cos(\phi_a)\cos(\lambda_a) & -\cos(\phi_a)\sin(\lambda_a) & \sin(\phi_a) \\ \sin(\phi_a)\cos(\lambda_a) & \sin(\phi_a)\sin(\lambda_a) & \cos(\phi_a) \end{pmatrix} \begin{pmatrix} 0 \\ 0 \\ \omega_E \end{pmatrix} \\ &= \begin{pmatrix} 0 \\ \omega_E \sin(\phi_a) \\ \omega_E \cos(\phi_a) \end{pmatrix} \end{aligned} \quad (\text{C.11})$$

where  $\vec{\omega}_E$  is the Earth's angular velocity vector and  $\omega_E = 7.289 \times 10^{-5}$  rad/s. In terms of the aircraft body axis reference frame, the true North angular velocity vector becomes

$$\begin{aligned} \vec{\omega}_{nb} &= R^{AG}\vec{\omega}_E = (R^{NA})^T R^{NG}\vec{\omega}_E = (R^{NA})^T \vec{\omega}_n \\ &= \begin{pmatrix} \cos(\alpha_a)\cos(\beta_a) & -\sin(\beta_a) & -\sin(\alpha_a)\cos(\beta_a) \\ -\cos(\alpha_a)\sin(\beta_a) & -\cos(\beta_a) & \sin(\alpha_a)\sin(\beta_a) \\ -\sin(\alpha_a) & 0 & -\cos(\alpha_a) \end{pmatrix} \begin{pmatrix} 0 \\ \omega_E \sin(\phi_a) \\ \omega_E \cos(\phi_a) \end{pmatrix} \\ &= \omega_E \begin{pmatrix} -\sin(\beta_a)\sin(\phi_a) - \sin(\alpha_a)\cos(\beta_a)\cos(\phi_a) \\ -\cos(\beta_a)\sin(\phi_a) + \sin(\alpha_a)\sin(\beta_a)\cos(\phi_a) \\ -\cos(\alpha_a)\cos(\phi_a) \end{pmatrix} \end{aligned} \quad (\text{C.12})$$

Thus, aircraft attitude equations of motion can be represented as

$$\dot{\vec{\omega}}_a = -\mathbf{I}_a^{-1} \boldsymbol{\Omega}_a \mathbf{I}_a \vec{\omega}_a + \mathbf{I}_a^{-1} \vec{T}_a \quad (\text{C.13})$$

where  $\boldsymbol{\Omega}_a$  is the angular velocity vector skew symmetric matrix defined as,

$$\boldsymbol{\Omega}_a = \begin{pmatrix} 0 & \omega_{za} & -\omega_{ya} \\ -\omega_{za} & 0 & \omega_{xa} \\ \omega_{ya} & -\omega_{xa} & 0 \end{pmatrix} \quad (\text{C.14})$$

### C.3 Transmitter Module

It is assumed that all transmitter components are housed within a telescope mounted on a gimbaled platform, as shown in Figure C.2. The telescope body behaves as a cylindrical axisymmetric rigid body, defined by  $\hat{x}_t$ ,  $\hat{y}_t$ ,  $\hat{z}_t$  principal axes and body rates  $\dot{\theta}_t$ ,  $\dot{\psi}_t$ . The outer gimbal is aligned with the  $\hat{z}_a$  axis for azimuth control, while the inner gimbal is aligned with the  $\hat{y}_t$  axis for elevation control. The transmitted beam is aligned with the  $\hat{x}_t$  axis.

*C.3.1 Transmitter Position.* In terms of the GCI frame, the relative transmitter position and velocity vectors are denoted by

$$\vec{r}_t = R^{GT} \begin{bmatrix} 1 & 0 & 0 \end{bmatrix}^T \quad (\text{C.15})$$

$$\vec{v}_t = \frac{d\vec{r}_t}{dt} = \vec{\omega}_t \times \vec{r}_t \quad (\text{C.16})$$

where  $R^{GT}$  is the rotational transformation from the transmitter principal axis frame to the GCI frame and  $\vec{\omega}_t$  is the transmitter angular velocity vector.

*C.3.2 Transmitter Attitude Dynamics.* Attitude dynamics about the transmitter cm is defined from Euler's rotational equation of motion as

$$\dot{\vec{h}}_t + \vec{\omega}_t \times \vec{h}_t = \vec{T}_t \quad (\text{C.17})$$



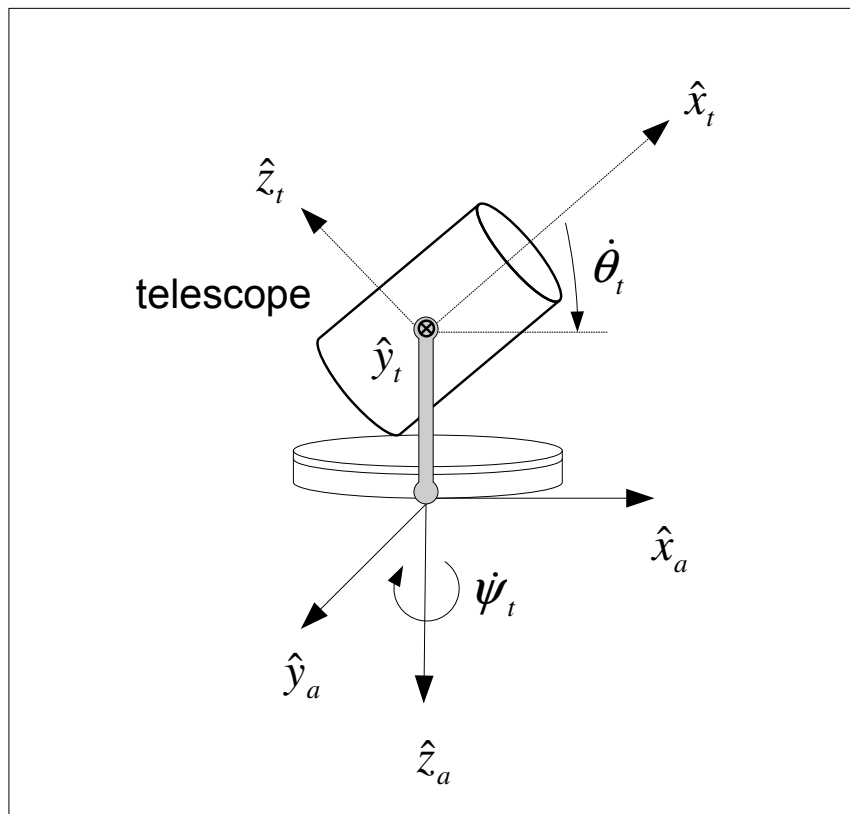


Figure C.2: Transmitter Platform

where  $\vec{h}_t$  is the transmitter angular momentum vector and  $\vec{T}_t$  is the total transmitter torque vector.

*C.3.3 Transmitter Attitude Kinematics.* Transmitter attitude relative to the true North, aircraft body axis, and GCI reference frames are determined respectively by,

$$R^{NT} = R_3(\lambda_{sa})R_2(\varepsilon_{sa}) \quad (C.18)$$

$$R^{AT} = R^{AN}R^{NT} = (R^{NA})^T R^{NT} \quad (C.19)$$

$$R^{TG} = R^{TN}R^{NG} = (R^{NT})^T R^{NG} \quad (C.20)$$

where  $R^{NT}$  denotes the rotational transformation from the transmitter principal axis reference frame to the true North reference frame,  $R^{AT}$  denotes the rotational transformation from the transmitter principal axis reference frame to the aircraft body axis reference frame, and  $R^{TG}$  denotes the rotational transformation from the GCI frame to the transmitter principal axis reference frame.

Incorporating the corresponding direction cosine matrices,  $R^{NT}$  is determined as,

$$\begin{aligned} R^{NT} &= R_3(\lambda_{sa})R_2(\varepsilon_{sa}) \\ &= \begin{pmatrix} \cos(\lambda_{sa}) & \sin(\lambda_{sa}) & 0 \\ -\sin(\lambda_{sa}) & \cos(\lambda_{sa}) & 0 \\ 0 & 0 & 1 \end{pmatrix} \begin{pmatrix} \cos(\varepsilon_{sa}) & 0 & \sin(\varepsilon_{sa}) \\ 0 & 1 & 0 \\ -\sin(\varepsilon_{sa}) & 0 & \cos(\varepsilon_{sa}) \end{pmatrix} \\ &= \begin{pmatrix} \cos(\lambda_{sa})\cos(\varepsilon_{sa}) & \sin(\lambda_{sa}) & \cos(\lambda_{sa})\sin(\varepsilon_{sa}) \\ -\sin(\lambda_{sa})\cos(\varepsilon_{sa}) & \cos(\lambda_{sa}) & -\sin(\lambda_{sa})\sin(\varepsilon_{sa}) \\ -\sin(\varepsilon_{sa}) & 0 & \cos(\varepsilon_{sa}) \end{pmatrix} \end{aligned} \quad (C.21)$$

*C.3.4 Transmitter Attitude Equations of Motion.* Transmitter angular velocity and angular momentum vectors are determined respectively by

$$\begin{aligned}
\vec{\omega}_t &= \begin{bmatrix} \omega_{xt} & \omega_{yt} & \omega_{zt} \end{bmatrix}^T \\
&= \begin{bmatrix} 0 \cdot \hat{x}_t & \dot{\theta}_t \cdot \hat{y}_t & \dot{\psi}_t \cdot \hat{z}_t \end{bmatrix}^T + R^{TA} \vec{\omega}_a + R^{TG} \vec{\omega}_E \\
&= \begin{bmatrix} 0 \cdot \hat{x}_t & \dot{\theta}_t \cdot \hat{y}_t & \dot{\psi}_t \cdot \hat{z}_t \end{bmatrix}^T + (R^{NA})^T R^{NT} \vec{\omega}_a + (R^{NT})^T R^{NG} \vec{\omega}_E \\
&= \begin{bmatrix} 0 \cdot \hat{x}_t & \dot{\theta}_t \cdot \hat{y}_t & \dot{\psi}_t \cdot \hat{z}_t \end{bmatrix}^T + (R^{NA})^T R^{NT} \vec{\omega}_a + (R^{NT})^T \vec{\omega}_n \quad (C.22)
\end{aligned}$$

$$\vec{h}_t = \mathbf{I}_t \vec{\omega}_t = \begin{pmatrix} I_{tx} & 0 & 0 \\ 0 & I_{ty} & 0 \\ 0 & 0 & I_{tz} \end{pmatrix} \vec{\omega}_t \quad (C.23)$$

where  $\mathbf{I}_t$  is the transmitter moment of inertia matrix.

Thus, transmitter attitude equations of motion can be represented as

$$\dot{\vec{\omega}}_t = -\mathbf{I}_t^{-1} \boldsymbol{\Omega}_t \mathbf{I}_t \vec{\omega}_t + \mathbf{I}_t^{-1} \vec{T}_t \quad (C.24)$$

where  $\boldsymbol{\Omega}_t$  is the transmitter angular velocity vector skew symmetric matrix defined as,

$$\boldsymbol{\Omega}_t = \begin{pmatrix} 0 & \omega_{zt} & -\omega_{yt} \\ -\omega_{zt} & 0 & \omega_{xt} \\ \omega_{yt} & -\omega_{xt} & 0 \end{pmatrix} \quad (C.25)$$

#### ***C.4 Disturbance Environment***

Aircraft perturbing forces are defined by external disturbance forces from two flight reference regimes: steady and unsteady flight. Steady flight is classified as nonaccelerated and nonrotating flight dynamics, while unsteady flight is classified as rotational flight dynamics [39, pages 222-223]. For the purposes of this study, emphasis is placed on the receiver fine tracking performance and it is assumed each UAV is a rigid body in the steady flight regime and loitering within  $\text{FOV}_R$ . Hence, aircraft

attitude stabilization and constant flight parameters are controlled by an autopilot [39, page 307].

*C.4.1 Pointing Loss.* Assuming the autopilot compensates for low frequency external disturbances while the transmitter gimbal system maintains coarse pointing, high frequency disturbances, also referred to as jitter, are the primary concern for this study. Previous work has shown, for a direct detection system, pointing jitter induces optical power losses of -1.8 dB [0.66] and -0.1 dB [0.98] respectively for 1  $\mu$ rad and 0.2  $\mu$ rad radial pointing error [8, page 256,259]. Thus, based on the tracking error requirements defined in Chapter III, it is assumed the pointing loss is

$$L_t \approx 0.8 [-0.969 \text{ dB}] \quad (\text{C.26})$$

At the satellite receiver, this pointing loss is assumed to create random beam wander, assumed to have zero-mean white Gaussian statistics, within the receiver field of view (FOV). As such, the variance of the radial pointing error can be determined, from the pointing loss and antenna gain equations in Chapter II, as [8, page 253]

$$\begin{aligned} \sigma_t^2 &= -\frac{\ln(L_t)}{G_t} = -\frac{\ln(0.8)}{G_t} \\ &= -\ln(0.8) \left( \frac{\lambda_c}{2\pi W_o} \right)^2 [\text{rad}^2] \end{aligned} \quad (\text{C.27})$$

Assuming the azimuth and elevation errors have equal variances, the corresponding azimuth and elevation variance respectively is determined as

$$(\sigma_t^2)_x = (\sigma_t^2)_y = \frac{\sigma_t^2}{2} = -\frac{\ln(0.8)}{8\pi^2} \left( \frac{\lambda_c}{W_o} \right)^2 [\text{rad}^2] \quad (\text{C.28})$$

Thus, the corresponding azimuth and elevation pointing error variance, based on the Chapter III defined transmitter parameters, is calculated respectively for each beam

as

$$(\sigma_t^2)_A = -\frac{\ln(0.8)}{8\pi^2} \left( \frac{1510 \times 10^{-9}}{0.04} \right)^2 = 4.0274 \times 10^{-12} \text{ [rad}^2\text{]} \quad (\text{C.29})$$

$$(\sigma_t^2)_B = -\frac{\ln(0.8)}{8\pi^2} \left( \frac{1550 \times 10^{-9}}{0.04} \right)^2 = 4.2436 \times 10^{-12} \text{ [rad}^2\text{]} \quad (\text{C.30})$$

*C.4.2 Aerodynamic-Optical Loss.* Aerodynamic-optical effects are due to turbulent airflow about an aircraft inducing air density fluctuations resulting in phase distortion of the transmitted beam. Phase distortion affects on-axis gain, denoted by the Strehl ratio, which relates the beam irradiance to an ideal Gaussian beam irradiance. Thus, aerodynamic-optical loss can be approximated by the Strehl ratio as [15, page 115]

$$L_{ao} \approx \text{Strehl Ratio} = \exp(-k_c a_e)^2 \quad (\text{C.31})$$

where  $a_e$  is the rms wavefront error.

For wavelengths from visible to infrared (IR), with an aircraft at 35,000 ft and speed Mach 0.85, simulation revealed a severe strehl ratio, approximately 0.3 to 0.6, for the visible spectrum, while IR suffered a minor strehl ratio near unity [32, pages 6, 11]. Based on the chosen laser source wavelengths and UAV operational parameters defined in Chapter III, it is assumed the strehl ratio is 0.7 [32, page 11]. Thus, the aero optical loss is determined as

$$L_{ao} \approx 0.7 \text{ [-1.549 dB]} \quad (\text{C.32})$$

## C.5 Summary

This appendix presented the fundamental flight and attitude dynamics for the UAV platform and transmitter telescope. Assuming the autopilot maintains steady-flight conditions and coarse tracking is maintained by the transmitter gimbal mechanism, attitude disturbances are considered to be random torque inputs defined in the transmitter attitude equations of motion. Although not explicitly implemented

in the simulation, these equations of motion are the basis for the pointing jitter affecting motion about the x-axis and y-axis, as shown in Chapter III and Appendix G. As a result, pointing jitter induces a pointing loss of approximately 0.8, based on zero-mean white Gaussian statistics. In addition, aerodynamic-optical effects impart a power loss of approximately 0.7.

## Appendix D. Optical Components

### D.1 Transmitter

*D.1.1 Laser Source.* Propagation of electromagnetic (EM) energy per unit area per unit time, within a medium based on direction  $\vec{z}_p$ , is described by the Poynting vector as [13, page 48]

$$\vec{S} = c^2 \epsilon \left[ \vec{E}(\vec{z}_p, t) \times \vec{B}(\vec{z}_p, t) \right] \quad (\text{D.1})$$

where

$$\begin{aligned} c &= \text{speed of light} \\ &\approx 3 \times 10^8 \text{ m/s} \\ \epsilon &= \text{electric permittivity} \\ \vec{E} &= \text{electric field vector} \\ \vec{B} &= \text{magnetic field vector} \\ t &= \text{time} \end{aligned}$$

The electric and magnetic field vector functions are related by satisfaction of partial differential equations, known as Maxwell's equations [26, page 159]. In particular,  $\vec{E}$ , commonly referred to as the optical field, is used to define propagation, denoted by [13, page 50]

$$\vec{E}(\vec{z}_p, t) = E_o \cos(\omega_c t + \phi_c) \text{ [V/m]} \quad (\text{D.2})$$

where  $E_o$  is the amplitude,  $\omega_c$  is angular temporal frequency, and  $\phi_c$  is the phase. Angular temporal frequency is defined by

$$\omega_c = \frac{2\pi c}{\lambda_c} = 2\pi f_c \text{ [rad/s]} \quad (\text{D.3})$$

where  $\lambda_c$  is the wavelength and  $f_c$  is the temporal frequency.

Irradiance, equivalent to optical power per unit area, is proportional to the time average of the Poynting vector and commonly denoted as [13, page 50]

$$I = \langle \vec{S} \rangle_T = \frac{\epsilon c E_o^2}{2} \text{ [W/m}^2\text{]} \quad (\text{D.4})$$

As the beam propagates, irradiance is subject to Fraunhofer diffraction as a function of the propagation distance,  $z_p$ , and radial distance,  $\rho_z$ , from the propagation axis,  $\vec{z}_p$ . Based on the defined operational parameters in Chapter III, the laser source is assumed to be a lowest order transverse electromagnetic (TEM<sub>00</sub>) collimated Gaussian beam. Thus, irradiance is defined respectively as [26, pages 85-86]

$$I(\rho_z, z_p) = I_o \left[ \frac{W_o}{W(z_p)} \right]^2 \exp \left[ -\frac{2\rho_z^2}{W^2(z_p)} \right] \quad (\text{D.5})$$

$$W(z_p) = W_o \left[ 1 + \left( \frac{z_p}{z_o} \right)^2 \right]^{1/2} \quad (\text{D.6})$$

$$z_o = \frac{\pi W_o^2}{\lambda_c} \quad (\text{D.7})$$

where  $I_o$  is the peak irradiance,  $W_o$  is the initial beam waist radius,  $W(z_p)$  is the diffractive beam waist radius at  $z_p$ , and  $z_o$  is the half the depth of focus. Irradiance is modeled as a Gaussian function of  $\rho_z$  and has a peak value at  $\rho_z = 0$  [26, pages 83-85]. Hence, the irradiance mean, and variance are determined respectfully as

$$\begin{aligned} E[I(\rho_z, z_p)] &= I_o \left[ \frac{W_o}{W(z_p)} \right]^2 \int_{-\infty}^{\infty} \rho_z \exp \left[ -\frac{2\rho_z^2}{W^2(z_p)} \right] d\rho_z \\ &= I_o \left[ \frac{W_o}{W(z_p)} \right]^2 \left[ -\frac{W^2(z_p)}{4} \right] \left\{ \exp \left[ -\frac{2\rho_z^2}{W^2(z_p)} \right] \right\}_{-\infty}^{\infty} \\ &= \left( -\frac{I_o W_o^2}{4} \right) (0) = 0 \end{aligned} \quad (\text{D.8})$$



$$\begin{aligned}
VAR[I(\rho_z, z_p)] &= E[I(\rho_z, z_p)^2] - E[I(\rho_z, z_p)]^2 \\
&= I_o^2 \left[ \frac{W_o}{W(z_p)} \right]^4 \int_{-\infty}^{\infty} \rho_z \exp \left[ -\frac{4\rho_z^2}{W^2(z_p)} \right] d\rho_z - 0 \\
&= I_o^2 \left[ \frac{W_o}{W(z_p)} \right]^4 \left[ \frac{W(z_p)}{2} \right]^2 = \frac{I_o^2}{4} \left[ \frac{W_o^4}{W^2(z_p)} \right] \\
&= \left[ \frac{I_o^2 W_o^4}{4} \right] \left[ \frac{1}{W^2(z_p)} \right] \tag{D.9}
\end{aligned}$$

Transmitted optical power is determined by [26, page 85]

$$P_t = \frac{1}{2} I_o (\pi W_o^2) \quad [\text{W}] \tag{D.10}$$

Thus, in terms of transmitted optical power, irradiance is defined as

$$\begin{aligned}
I(\rho_z, z_p) &= \left[ \frac{2P_t}{\pi W_o^2} \right] \left[ \frac{W_o}{W(z_p)} \right]^2 \exp \left[ -\frac{2\rho_z^2}{W^2(z_p)} \right] \\
&= \left[ \frac{2P_t}{\pi W^2(z_p)} \right] \exp \left[ -\frac{2\rho_z^2}{W^2(z_p)} \right] \quad [\text{W/m}^2] \tag{D.11}
\end{aligned}$$

As a function of propagation distance, the peak irradiance is denoted by

$$I_o(z_p) = I(0, z_p) = \left[ \frac{2P_t}{\pi W^2(z_p)} \right] \quad [\text{W/m}^2] \tag{D.12}$$

Based on the Chapter III defined operational parameters for the communication uplink, where  $P_t = 100 \text{ mW}$ ,  $W_o = 40 \text{ mm}$ ,  $\varepsilon_{sa} \in [77.3^\circ, 90^\circ]$ , and  $h \in [18.3 \text{ km}, 35786 \text{ km}]$ , Figures D.1 thru D.3 illustrate the theoretical free-space propagation characteristics for a collimated Gaussian beam at arbitrary Near IR carrier wavelengths,  $\lambda_c \in [800 \text{ nm}, 1100 \text{ nm}, 1300 \text{ nm}, 1500 \text{ nm}]$ . Based on the satellite receiver field of view, defined later in this section, as the elevation angle increases the uplink beam propagates through less of the atmosphere. However, shorter wavelengths suffer less diffraction and achieve a higher free space peak irradiance.

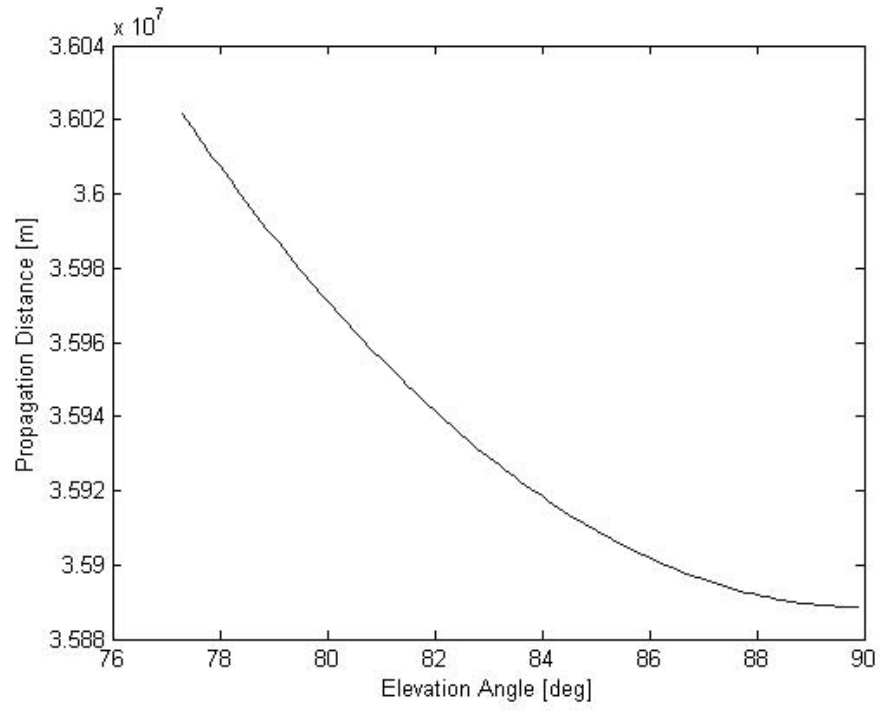


Figure D.1: Propagation Distance vs Elevation Angle

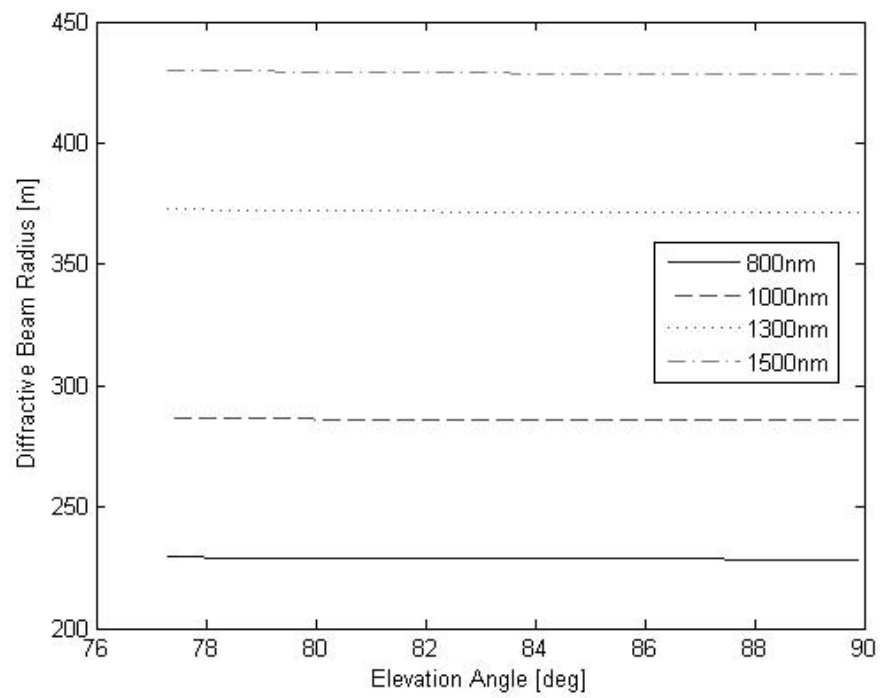


Figure D.2: Diffractive Beam Waist Radius vs Elevation Angle

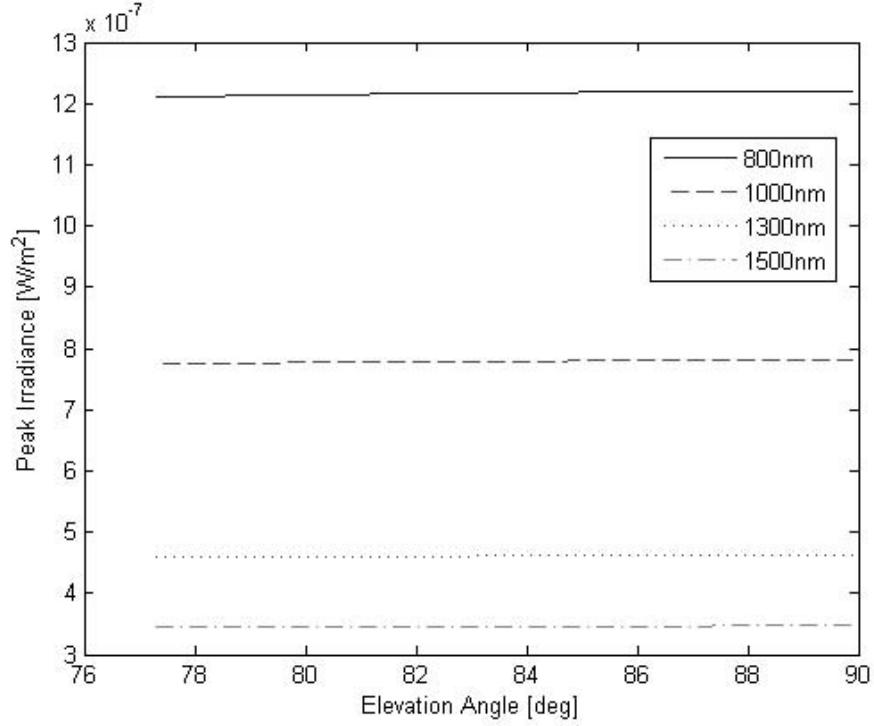


Figure D.3: Transmitted Peak Irradiance vs Elevation Angle

*D.1.2 Optical Modulation.* For the purposes of this study, binary amplitude shift keying (ASK), also known as on-off keying (OOK), is the bandpass digital modulation format. For RF systems, ASK is a continuous wave (CW) amplitude modulation technique: varies carrier wave amplitude as a linear function of the baseband waveform [12, page 114]. However, in optical communications the modulation variable is optical power, which is assumed to be linearly proportional to an input voltage [22, pages 149, 255]. Thus, the uncoded NRZ-L PCM baseband waveform, defined in Appendix A as a  $g(t)$  and shown in Figure D.4, pulses the laser either on or off transmitting an OOK modulated waveform,  $s(t)$ , derived from the optical field equation as [12, page 114]

$$s(t) = E_o \left[ 1 + \frac{g(t)}{V} \right] \cos(\omega_c t + \phi_c) \quad (\text{D.13})$$

Based on this waveform, we can assign a unique transmission symbol, which has a corresponding channel symbol meaning, to each modulation type. Hence, two

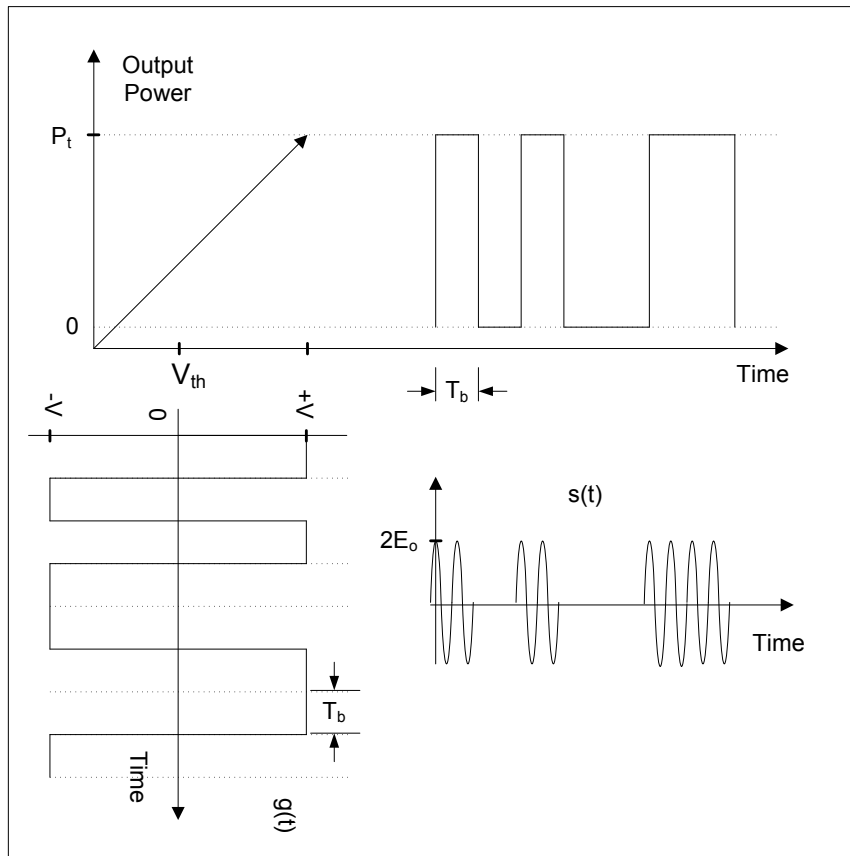


Figure D.4: OOK Digital Bandpass Modulation

possible unipolar signal waveforms are transmitted within the interval  $t \in [0, T_g]$ , denoted by

$$\begin{aligned} s_1(t) &= 2E_o \cos(\omega_c t + \phi_c) \implies \text{symbol 1} \\ s_2(t) &= 0 \implies \text{symbol 0} \end{aligned} \quad (\text{D.14})$$

Correlation of these two signals reveals

$$\int_0^{T_g} s_1(t) s_2(t) dt = \int_0^{T_g} [2E_o \cos(\omega_c t + \phi_c)] [0] dt = 0 \quad (\text{D.15})$$

Thus, the transmitted signal waveforms are orthogonal [29, page 129].

*D.1.2.1 Transmitted Optical Signal Statistics.* Since  $s(t)$  is a linear function of  $g(t)$ , assuming  $\phi_c$  is an independent uniform random variable distributed in the interval  $[0, 2\pi]$ , the mean is calculated as [10, page 232]

$$\begin{aligned} m_S(t) &= E \left\{ E_o \left[ 1 + \frac{G(t)}{V} \right] \cos(2\pi f_c t + \Phi_c) \right\} \\ &= E_o \left[ 1 + \frac{E[G(t)]}{V} \right] E [\cos(2\pi f_c t + \Phi_c)] \\ &= E_o [1 + 0] (0) = 0 \end{aligned} \quad (\text{D.16})$$

The autocorrelation of  $S(t)$  is determined as

$$\begin{aligned}
R_S(t_1, t_2) &= E[S(t_1)S(t_2)] \\
&= E \left\{ E_o \left[ 1 + \frac{G(t_1)}{V} \right] \cos(2\pi f_c t_1 + \Phi_c) \right. \\
&\quad \times \left. E_o \left[ 1 + \frac{G(t_2)}{V} \right] \cos(2\pi f_c t_2 + \Phi_c) \right\} \\
&= E_o^2 \left[ 1 + \frac{E[G(t_1)]}{V} + \frac{E[G(t_2)]}{V} + \frac{E[G(t_1)G(t_2)]}{V^2} \right] \\
&\quad \times E[\cos(2\pi f_c t_1 + \Phi_c) \cos(2\pi f_c t_2 + \Phi_c)] \\
&= E_o^2 \left[ 1 + \frac{R_G(\tau)}{V^2} \right] E \left[ \frac{1}{2} \cos(2\pi f_c t_1 + \Phi_c + 2\pi f_c t_2 + \Phi_c) \right. \\
&\quad \left. + \frac{1}{2} \cos(2\pi f_c t_1 + \Phi_c - 2\pi f_c t_2 - \Phi_c) \right] \\
&= E_o^2 \left[ 1 + \frac{R_G(\tau)}{V^2} \right] E \left[ \frac{1}{2} \cos(2\pi f_c(t_1 + t_2) + 2\Phi_c) \right. \\
&\quad \left. + \frac{1}{2} \cos(2\pi f_c(-\tau)) \right] \\
&= \left( \frac{E_o^2}{2} \right) \left[ 1 + \frac{R_G(\tau)}{V^2} \right] \{0 + E[\cos(2\pi f_c \tau)]\} \\
&= \left( \frac{E_o^2}{2} \right) \left[ 1 + \frac{R_G(\tau)}{V^2} \right] \cos(2\pi f_c \tau) = R_S(\tau) \tag{D.17}
\end{aligned}$$

The autocovariance of  $S(t)$  is defined as [10, page 335]

$$\begin{aligned}
C_S(t_1, t_2) &= E[\{S(t_1) - m_S(t_1)\}\{S(t_2) - m_S(t_2)\}] \\
&= E[\{S(t_1) - 0\}\{S(t_2) - 0\}] = E[S(t_1)S(t_2)] \\
&= R_S(t_1, t_2) = R_S(\tau) \tag{D.18}
\end{aligned}$$

Since the mean is constant and the autocovariance is a function of  $\tau = t_2 - t_1$ ,  $S(t)$  is a wide-sense stationary process (WSS) [10, page 359].

*D.1.2.2 Transmitted Optical Signal Power Spectral Density.* The power spectral density (PSD) is determined from the Fourier transform of  $R_S(\tau)$

as [10, page 404]

$$\begin{aligned}
S_S(f) &= (\epsilon c \pi W_o^2) \mathcal{F} \{R_S(\tau)\} = (\epsilon_o c \pi W_o^2) \int_{-\infty}^{\infty} R_S(\tau) \exp(-j2\pi f \tau) d\tau \\
&= \left[ \frac{(\epsilon c \pi W_o^2) E_o^2}{2} \right] \int_{-\infty}^{\infty} \left[ 1 + \frac{R_G(\tau)}{V^2} \right] \cos(2\pi f_c \tau) \exp(-j2\pi f \tau) d\tau \\
&= \left[ \frac{(\epsilon c E_o^2) (\pi W_o^2)}{2} \right] \left[ \left( \frac{1}{2} \right) [\delta(f - f_c) + \delta(f + f_c)] \right. \\
&\quad \left. + \left( \frac{1}{V^2} \right) S_G(f) * \left( \frac{1}{2} \right) [\delta(f - f_c) + \delta(f + f_c)] \right] \\
&= \left[ \frac{(2I_o) (\pi W_o^2)}{4} \right] \left[ \delta(f - f_c) + \delta(f + f_c) + \left( \frac{1}{V^2} \right) [S_G(f - f_c) + S_G(f + f_c)] \right] \\
&= \left[ \frac{I_o (\pi W_o^2)}{2} \right] \{ T_b \text{sinc}^2 [(f - f_c) T_b] + T_b \text{sinc}^2 [(f + f_c) T_b] \\
&\quad + \delta(f - f_c) + \delta(f + f_c) \} \\
&= P_t \{ T_b \text{sinc}^2 [(f - f_c) T_b] + T_b \text{sinc}^2 [(f + f_c) T_b] \\
&\quad + \delta(f - f_c) + \delta(f + f_c) \} \quad [\text{W/Hz}]
\end{aligned} \tag{D.19}$$

Based on the Chapter III defined operational parameters, an OOK modulated PSD for a 1510nm beam is shown in Figure D.5, accounting for positive frequencies and scaled to unit amplitude. The null-to-null bandwidth of  $s(t)$  is determined as [29, page 49]

$$BW_{NN} = \left[ \frac{1}{T_b} - \left( -\frac{1}{T_b} \right) \right] = \left( \frac{2}{T_b} \right) = 2R_b \quad [\text{Hz}] \tag{D.20}$$

The average power is determined by [1, page 63]

$$\begin{aligned}
R_S(0) &= (\epsilon c \pi W_o^2) \left( \frac{E_o^2}{2} \right) \left[ 1 + \frac{R_G(0)}{V^2} \right] \cos(0) \\
&= (\epsilon c \pi W_o^2) \left( \frac{I_o}{\epsilon c} \right) \left[ 1 + \frac{R_G(0)}{V^2} \right] \\
&= (\pi W_o^2) (I_o) \left[ 1 + \frac{R_G(0)}{V^2} \right] \\
&= P_t \left[ 1 + \frac{R_G(0)}{V^2} \right]
\end{aligned} \tag{D.21}$$

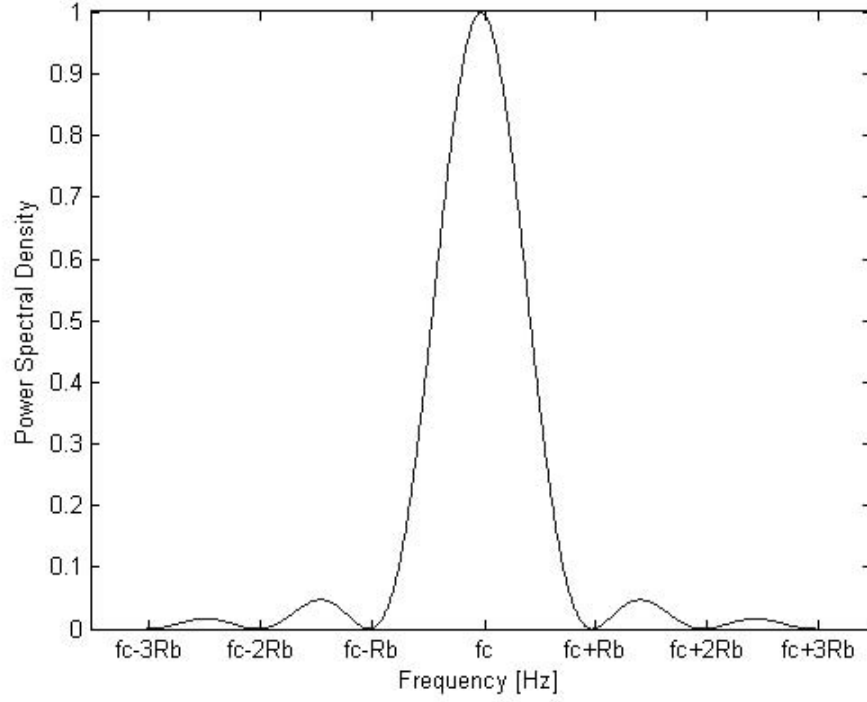


Figure D.5: Transmitted Signal PSD

Thus, for each transmitted binary symbol, the average power is either  $R_S(0) = 2P_t$  for symbol 1 or  $R_S(0) = 0$  for symbol 2. Assuming transmission of either symbol is equally likely, the average transmitted power is  $R_S(0) = P_t$  [24, page 472].

*D.1.3 Transmitter Antenna Gain.* As defined in Chapter 2, the transmitter antenna power gain for a Gaussian beam is denoted by [8, page 253]

$$G_t = \left[ \frac{2\pi W_o}{\lambda_c} \right]^2 \quad (\text{D.22})$$

Figure D.6 illustrates the theoretical relationship between antenna gain and near infrared (IR) wavelengths. Larger  $W_o$  yields a higher gain, however, shorter wavelengths achieve higher gain than longer wavelengths. On the other hand, as shown in Appendix E, a larger waist radius suffers increased atmospheric loss from optical turbulence.



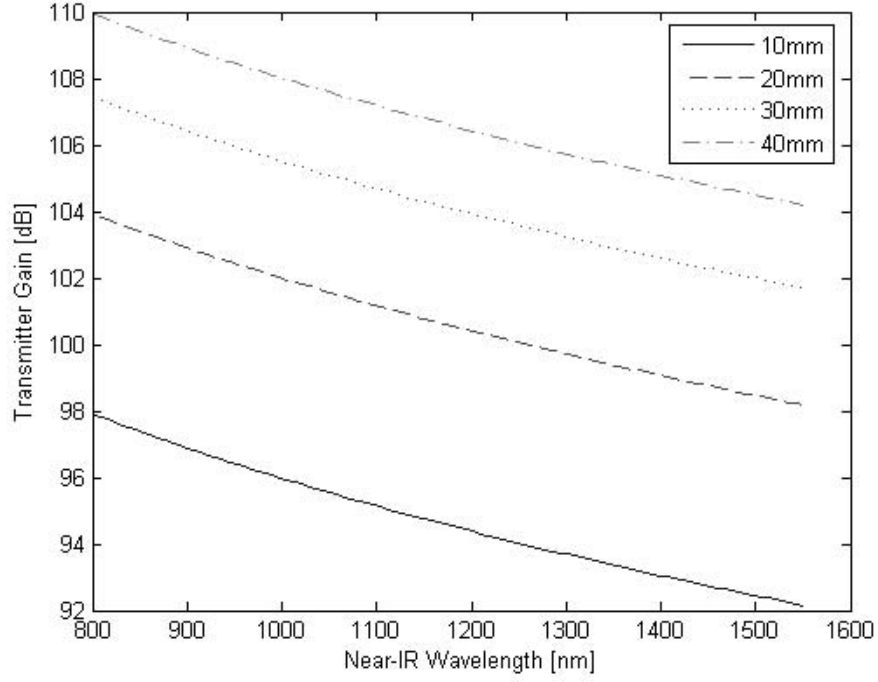


Figure D.6: Transmitter Antenna Gain vs Wavelength

## D.2 Receiver

### D.2.1 Optical Signal Processing.

*D.2.1.1 Cassegrain Telescope.* Based on telescope dimensions, the receiver FOV is determined from the effective focal length and primary mirror diameter,  $f_L$  and  $D_{pm}$  respectively, defined as [13, pages 171, 217]

$$FOV_R = 2 \tan^{-1} \left( \frac{D_{pm}}{2f_L} \right) \quad (D.23)$$

Focal length is determined from the telescope focal ratio,  $f/\#$ , which is determined as [13, page 174]

$$f/\# = \frac{f}{D} \quad (D.24)$$

Effective focal length and primary mirror focal length,  $f_{pm}$ , are related by the magnification ratio,  $M_f$ , which is denoted by [13, page 221]

$$f_L = M_f f_{pm} \quad (\text{D.25})$$

Thus, given the Chapter III defined telescope specifications, 300 mm aperture diameter, 15 focal ratio, and 10 magnification ratio, the remaining telescope parameters are calculated as [15, pages 118-122]

$$\begin{aligned} D_{pm} &= 300 \text{ mm} \\ f_L &= D_{pm} f / \# = 4500 \text{ mm} \\ f_{pm} &= f_L / M_f = 450 \text{ mm} \\ D_{sm} &= 0.25 D_{pm} = 75 \text{ mm} \\ L &= \frac{1}{3} f_{pm} = 150 \text{ mm} \end{aligned}$$

where,  $D_{sm}$  is the secondary mirror diameter and  $L$  is the length of the telescope. Thus, the receiver FOV is determined as

$$FOV_R = 3.818 \text{ deg } [0.066 \text{ rad}] \quad (\text{D.26})$$

The corresponding Earth coverage about the subsatellite point (SSP), defined as the Earth central angle, is determined as [16, page 111]

$$\lambda_r = 90^\circ - \eta_{ar} - \varepsilon_r \quad (\text{D.27})$$

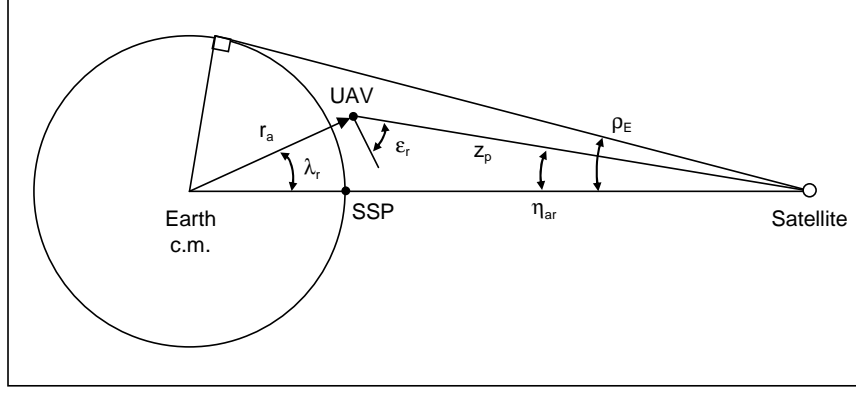


Figure D.7: Receiver Field of View Geometry

where  $\eta_{ar}$  is the nadir angle visible within  $FOV_R$ , and  $\varepsilon_r$  is corresponding minimum transmitter elevation angle, determined respectively as [16, page 111]

$$\eta_{ar} = \left(\frac{1}{2}\right) FOV_R = 1.909 \text{ deg } [0.033 \text{ rad}] \quad (\text{D.28})$$

$$\begin{aligned} \varepsilon_r &= \cos^{-1} \left[ \frac{\sin(\eta_{ar})}{\sin(\rho_E)} \right] \\ &= \cos^{-1} \left[ \frac{\sin(1.909)}{\sin(8.7)} \right] = 77.278 \text{ deg } [1.349 \text{ rad}] \end{aligned} \quad (\text{D.29})$$

where  $\rho_E = 8.7^\circ$ , which was determined in Appendix B, is the radial distance of Earth visible from the satellite orbit. Thus, as illustrated in Figure D.7, the Earth central angle is determined as

$$\lambda_r = 90^\circ - 1.909^\circ - 77.278^\circ = 10.813 \text{ deg } [0.189 \text{ rad}] \quad (\text{D.30})$$

The corresponding maximum aircraft-to-satellite range, also referred to as propagation distance, is determined as [16, page 111]

$$\begin{aligned} z_p(\text{max}) &= r_a \left[ \frac{\sin(\lambda_r)}{\sin(\eta_{ar})} \right] = (6378) \left[ \frac{\sin(10.813)}{\sin(1.909)} \right] \\ &= 36,022 \text{ km} \end{aligned} \quad (\text{D.31})$$

where  $r_a$ , determined in Appendix C, is the magnitude of the aircraft position vector.

*D.2.2 Receiver Antenna Gain.* As defined in Chapter 2, the receiver antenna power gain, calculated for each beam respectively, is determined as [8, page 253]

$$(G_r)_A = \left( \frac{\pi D_{pm}}{\lambda_c} \right)^2 = \left[ \frac{(\pi)(0.3)}{1510 \times 10^{-9}} \right]^2 = 3.8957 \times 10^{11} \text{ [W]} \quad (\text{D.32})$$

$$(G_r)_B = \left[ \frac{(\pi)(0.3)}{1550 \times 10^{-9}} \right]^2 = 3.6973 \times 10^{11} \text{ [W]} \quad (\text{D.33})$$

### *D.2.3 Optical Signal Detection.*

*D.2.3.1 Photodetector.* In order to determine the received power for demodulation into the communication signal, each incident beam is directed to a corresponding avalanche photodiode detector (APD). A photodiode detector, commonly referred to as a photodetector, detects and converts the received optical power,  $P_r$ , into an output dc current determined by [17, page 936]

$$i_{dc} = R_{ph} P_r \text{ [A]} \quad (\text{D.34})$$

where  $R_{ph}$  is the photodetector responsivity. Thus, in terms of the two transmitted unipolar signal waveforms, within the interval  $t \in [0, T_b]$ , the received current is determined respectively as

$$\begin{aligned} i_1 &= R_{ph} P_r + i_n \text{ [A]} \implies \text{symbol 1} \\ i_2 &= i_n \text{ [A]} \implies \text{symbol 0} \end{aligned} \quad (\text{D.35})$$

where  $i_n$  is the equivalent noise current. The photodetector responsivity,  $R_{ph}$ , is determined by [17, page 937]

$$R_{ph} = G_d \frac{\eta e q_e}{\hbar f_d} \text{ [A/W]} \quad (\text{D.36})$$

where

$$\begin{aligned}
G_d &= \text{detector gain} \\
\eta_e &= \text{quantum efficiency} \\
q_e &= \text{electronic charge} \\
&= 1.602 \times 10^{-19} \text{ coulombs} \\
\hbar &= \text{Plank's constant} \\
&= 6.626 \times 10^{-34} \text{ joules} \cdot \text{s} \\
f_d &= \text{detection frequency} \\
&= \frac{c}{\lambda_c}
\end{aligned}$$

Responsivity is constant while operating within the photodetector's linear dynamic range (DR): region between noise equivalent power (NEP) and saturation power,  $P_{sat}$ , denoted by [17, page 942]

$$DR = 10 \log \left( \frac{P_{sat}}{NEP} \right) \text{ [dB]} \quad (\text{D.37})$$

Photodetector noise equivalent power (NEP), defined as the minimum received power for a SNR of unity, is determined by [17, page 938]

$$NEP = \text{rms}(i_n) \left( \frac{\hbar f_d}{\eta_e q_e} \right) \text{ [W]} \quad (\text{D.38})$$

Quantum shot noise determines the maximum capable received SNR for an optical receiver, which defines the photodetector saturation limit as [1, page 64]

$$P_{sat} = \frac{i_{dc}^2}{i_{qsh}^2} \quad (\text{D.39})$$

where  $i_{qsh}^2$  is the quantum shot current noise power. Thus, based on the Chapter III defined operational parameters and assuming  $\eta_e = 0.8$ , the photodetector responsivity,

operating within the linear dynamic range, is calculated for each beam respectively as

$$\begin{aligned}
[R_{ph}]_A &= G_d(0) \left( \frac{\eta_e q_e}{\hbar f_d} \right) \\
&= 20 \left[ \frac{(0.8)(1.602 \times 10^{-19})}{(6.626 \times 10^{-34})(1.9868 \times 10^{14})} \right] \\
&= 20 [0.9735] = 19.4709 \text{ [A/W]}
\end{aligned} \tag{D.40}$$

$$\begin{aligned}
[R_{ph}]_B &= 20 \left[ \frac{(0.8)(1.602 \times 10^{-19})}{(6.626 \times 10^{-34})(1.9355 \times 10^{14})} \right] \\
&= 20 [0.9993] = 19.9867 \text{ [A/W]}
\end{aligned} \tag{D.41}$$

where  $G_d(0)$  is the dc multiplicative gain.

Additional photodetector response characteristics are rise time,  $t_r$ , fall time,  $t_f$ , and 3 dB cutoff frequency,  $f_{ph}$ . Rise time is the time response from 10 to 90% output peak value, while fall time is the decay interval from 90 to 10% peak value. Cutoff frequency, which defines the detection bandwidth  $BW_d$ , is related to rise time and signal bandwidth,  $BW_{NN}$ , respectively by [17, pages 943-944]

$$\begin{aligned}
f_{ph} = BW_d &\approx \frac{0.35}{t_r} \\
&\approx (0.886)BW_{NN} \text{ [Hz]}
\end{aligned} \tag{D.42}$$

Based on the Chapter III defined operational parameters, the photodetector gain frequency response is calculated for each beam respectively as [1, page 108]

$$\begin{aligned}
[G_d(\omega)]_A &= G_d(0) \left[ 1 + \left( \frac{\omega}{2\pi f_d} \right)^2 \right]^{-1/2} \\
&= 20 \left[ 1 + \left( \frac{\omega}{1.2483 \times 10^{15}} \right)^2 \right]^{-1/2}
\end{aligned} \tag{D.43}$$

$$[G_d(\omega)]_B = 20 \left[ 1 + \left( \frac{\omega}{1.2161 \times 10^{15}} \right)^2 \right]^{-1/2} \tag{D.44}$$

Thus, based on the operational parameters defined in Chapter III, assuming symbol 1 is sent within the detector bandwidth, the theoretical received optical power for each beam is shown in Figure D.8. Although, a larger wavelength is less susceptible to atmospheric loss, at higher elevation angles the shorter wavelength achieves slightly better power performance. After photodetection and conversion to a current signal, the theoretical received dc current for each beam is illustrated in Figure D.9. In particular, a longer wavelength achieves a higher dc current due to greater detector responsivity.

*D.2.3.2 Quadrant Cell Detector.* In order to determine the tracking error, each incident beam is directed to the corresponding quadrant cell detector (QD) field of view (FOV<sub>D</sub>). Similar to a photodetector, the QD detector absorbs incident power from an optical signal and produces a corresponding current, denoted by [17, page 936]

$$i_{qd} = R_{qd}P_r \quad [\text{A}] \quad (\text{D.45})$$

where  $R_{qd}$  is the quadrant cell detector responsivity. QD responsivity is determined by [17, page 937]

$$R_{qd} = G_d \frac{\eta_e q_e}{\hbar f_d} \quad [\text{A/W}] \quad (\text{D.46})$$

Divided into four equivalent quadrant cells, as shown in Figure D.10, current signals from each cell are used to determine azimuth and elevation signal errors. In the presence of random quadrant signal noise,  $n_i$ , assumed to have zero-mean Gaussian statistics, error signals are determined by [15, pages 180-181]

$$x_e = \text{Azimuth Error} = \frac{i_a + n_a + i_b + n_b - i_c - n_c - i_d - n_d}{i_a + n_a + i_b + n_b + i_c + n_c + i_d + n_d} \quad (\text{D.47})$$

$$y_e = \text{Elevation Error} = \frac{i_a + n_a + i_c + n_c - i_b - n_b - i_d - n_d}{i_a + n_a + i_b + n_b + i_c + n_c + i_d + n_d} \quad (\text{D.48})$$

Assuming quadrant signal noises are independent of each other, the mean errors are

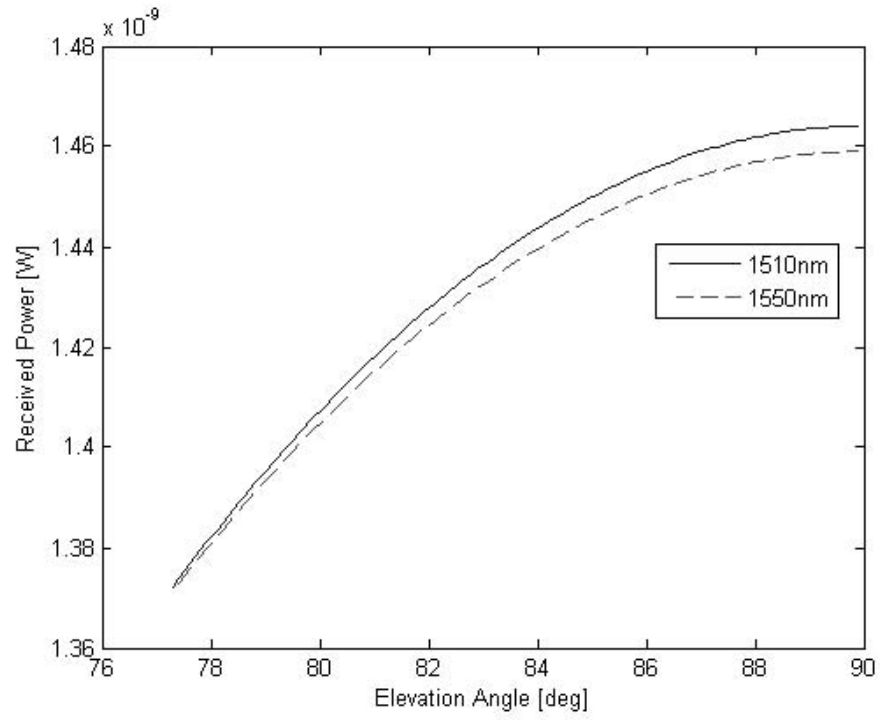


Figure D.8: Theoretical Received Optical Signal Power

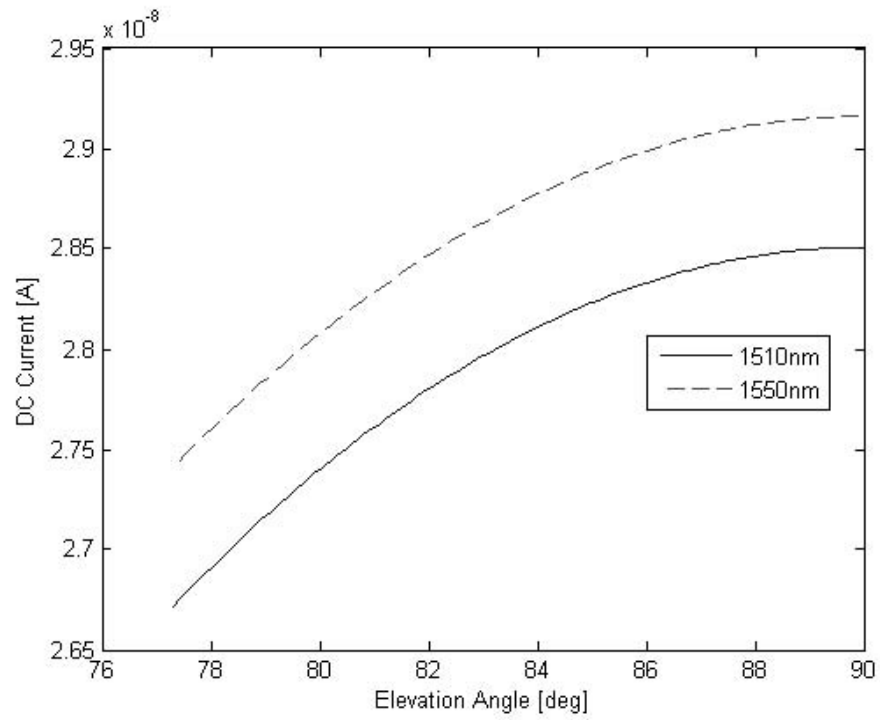


Figure D.9: Theoretical Received DC Current



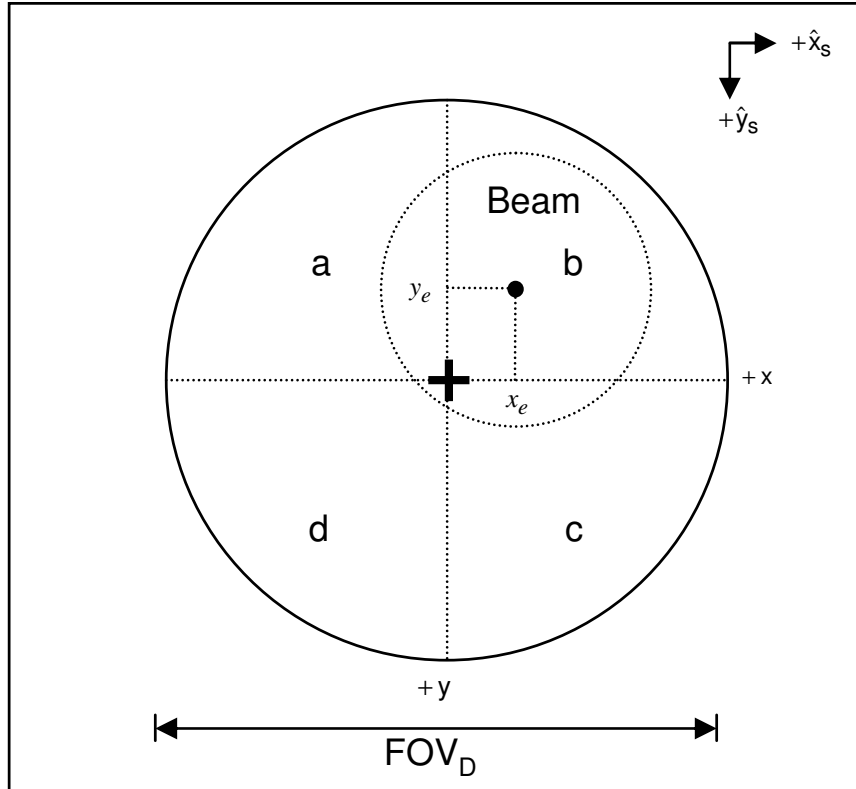


Figure D.10: Quadrant Cell Detector

determined by,

$$\begin{aligned}
E[x_e] &= \frac{E[i_a + n_a + i_b + n_b - i_c - n_c - i_d - n_d]}{E[i_a + n_a + i_b + n_b + i_c + n_c + i_d + n_d]} \\
&= \frac{i_a + i_b - i_c - i_d + E[n_a] + E[n_b] - E[n_c] - E[n_d]}{i_a + i_b + i_c + i_d + E[n_a] + E[n_b] + E[n_c] + E[n_d]} \\
&= \frac{i_a + i_b - i_c - i_d}{i_a + i_b + i_c + i_d} \tag{D.49}
\end{aligned}$$

$$E[y_e] = \frac{i_a + i_c - i_b - i_d}{i_a + i_b + i_c + i_d} \tag{D.50}$$

Assuming a large SNR and independent quadrant noises, azimuth and elevation variances are calculated as [15, pages 181-182]

$$\begin{aligned}
\sigma_x^2 &= E[x_e^2] - E[x_e]^2 \\
&= E\left[\frac{(i_a + n_a + i_b + n_b - i_c - n_c - i_d - n_d)^2}{(i_a + n_a + i_b + n_b + i_c + n_c + i_d + n_d)^2}\right] - \left(\frac{i_a + i_b - i_c - i_d}{i_a + i_b + i_c + i_d}\right)^2 \\
&= E\left[\left(\frac{(i_a + i_b - i_c - i_d) + (n_a + n_b - n_c - n_d)}{(i_a + i_b + i_c + i_d) + (n_a + n_b + n_c + n_d)}\right)^2\right] - \frac{(i_a + i_b - i_c - i_d)^2}{(i_a + i_b + i_c + i_d)^2} \\
&= \frac{(i_a + i_b - i_c - i_d)^2 + E[n_a^2] + E[n_b^2] - E[n_c^2] - E[n_d^2]}{(i_a + i_b + i_c + i_d)^2} - \frac{(i_a + i_b - i_c - i_d)^2}{(i_a + i_b + i_c + i_d)^2} \\
&= \frac{E[n_a^2] + E[n_b^2] + E[n_c^2] + E[n_d^2]}{(i_a + i_b + i_c + i_d)^2} \\
&= \frac{\sigma_a^2 + \sigma_b^2 + \sigma_c^2 + \sigma_d^2}{(i_a + i_b + i_c + i_d)^2} \\
&= \frac{i_{nq}^2}{i_{qd}^2} = \frac{1}{SNR_{qd}} \tag{D.51}
\end{aligned}$$

$$\sigma_y^2 = \frac{i_{nq}^2}{i_{qd}^2} = \frac{1}{SNR_{qd}} \tag{D.52}$$

where  $i_{qd}^2$  is the current signal power and  $i_{nq}^2$  is the current noise power, also referred to as current noise variance. Since azimuth and elevation error variances are equivalent, the root mean square (rms) error is defined by

$$\text{rms}(\sigma_x) = \text{rms}(\sigma_y) = \sigma_{rms} = \frac{1}{\sqrt{SNR_{qd}}} \tag{D.53}$$

In addition, quadrant detector noise imparts residual angular jitter, known as noise equivalent angle (NEA), defined as [15, page 71]

$$\text{NEA} = \frac{\sigma_{rms}}{\text{SF}} = \frac{1}{\text{SF}\sqrt{SNR_{qd}}} \quad (\text{D.54})$$

where SF is the slope factor. Thus, the accuracy of the QD sensor is inversely proportional to  $SNR_{qd}$ , which affects the ability of the tracking control system to reject platform and signal propagation disturbances [5, page 676].

*D.2.3.3 Photodetector Noise.* Three types of noise sources occur within a photodetector: thermal noise, dark current noise, and quantum shot noise. Thermal noise, also known as Johnson noise, arises from electron thermal motion within dissipative elements and is modeled as a zero-mean white Gaussian noise process [29, pages 30-31]. Thermal current noise power is denoted as [17, page 932]

$$\begin{aligned} \text{VAR}[i_{th}] &= i_{th}^2 \\ &= \frac{\sigma_{th}^2}{R_L} \text{ [A}^2\text{]} \end{aligned} \quad (\text{D.55})$$

where  $\sigma_{th}^2$  is the thermal noise power, and  $R_L$  is the load resistance. The thermal noise power is determined by [17, page 932]

$$\sigma_{th}^2 = 4(k_B T_s^o)BW_d \text{ [W]} \quad (\text{D.56})$$

where  $k_B = 1.38 \times 10^{-23}$  joules/ $^{\circ}\text{K}$  is the Boltzmann's constant, and  $T_s^o$  is the receiver noise temperature. Thus, based on the Chapter III defined operational parameters and assuming a 1000 Ohm load resistance, thermal current noise power is calculated as

$$\begin{aligned} i_{th}^2 &= \frac{4(1.38 \times 10^{-23})(400)(0.886)(200 \times 10^3)}{1000} \\ &= 3.9126 \times 10^{-18} \text{ [A}^2\text{]} \end{aligned} \quad (\text{D.57})$$

Due to the inherent nature of a photodetector, dark current is an additional current source present whether or not the detector is illuminated. Consisting of two components, dark current is modeled as [1, pages 146]

$$i_{dk} = i_{du} + G_d(0)i_{dm} \quad [\text{A}] \quad (\text{D.58})$$

where  $i_{du}$  is the unmultiplied dark current,  $i_{dm}$  is the multiplied dark current, and  $G_d(0)$  is the DC photodetector gain. For the purposes of this study, it is assumed both the unmultiplied and multiplied dark current within the APD are approximately 1 nA [1, page 116].

Quantum shot noise occurs within a photodetector due to quantum nature of incident photons and charge carriers, background radiation, and dark current. Incident photons arriving upon a photodetector exhibit Poisson statistics [17, page 929]. However, assuming a high photon counting capability, photodetection statistics can be approximated by a zero-mean white Gaussian distribution [1, page 240]. The variance, referred to as quantum shot noise current power, is determined as [17, page 931]

$$\begin{aligned} \text{VAR}[i_{qsh}] &= i_{qsh}^2 \\ &= (2q_e F_n)[i_{dc} + G_d(i_b + i_{dm})]BW_d \quad [\text{A}^2] \end{aligned} \quad (\text{D.59})$$

where  $F_n$  is the excess noise factor,  $i_b$  is the background current, and  $i_{dm}$  is the multiplied dark current. The excess noise factor can be approximated by [1, page 143]

$$F_n \approx G_d^{0.1} \quad (\text{D.60})$$

Background current arises from optical background radiation, which causes background current flow,  $i_b$ , determined as [5, page 679]

$$i_b = \left( \frac{\eta_e q_e}{\hbar f_d} \right) \sigma_b^2 \quad [\text{A}] \quad (\text{D.61})$$

where  $\sigma_b^2$  is the optical background noise power, defined in Appendix E. As such, based on the Chapter III defined operational parameters and assuming  $\eta_e = 0.8$ , the optical background current respectively for each beam, is calculated as

$$\begin{aligned}(i_b)_A &= \left[ \frac{(0.8)(1.602 \times 10^{-19})}{(6.626 \times 10^{-34})(1.9868 \times 10^{14})} \right] (1.3164 \times 10^{-14}) \\ &= 1.2816 \times 10^{-14} \text{ [A]}\end{aligned}\tag{D.62}$$

$$\begin{aligned}(i_b)_B &= \left[ \frac{(0.8)(1.602 \times 10^{-19})}{(6.626 \times 10^{-34})(1.9355 \times 10^{14})} \right] (1.2825 \times 10^{-14}) \\ &= 1.2816 \times 10^{-14} \text{ [A]}\end{aligned}\tag{D.63}$$

Thus, based on the operational parameters defined in Chapter III, previously defined dc current, dark current and background current, assuming symbol 1 is sent within the detector bandwidth, the maximum theoretical quantum shot noise power for each beam is illustrated in Figure D.11. In particular, as the elevation angle increases, which decreases the propagation distance, the noise power increases, due to the increased dc current. In addition, the quantum shot noise power is at least three orders of magnitude less than thermal noise power; hence, the detector is thermal noise limited [17, page 933].

During normal operations, the photodetector equivalent current noise power is determined as [1, page 154]

$$i_n^2 = i_{qsh}^2 + i_{th}^2 + 2q_e i_{du} BW_d \text{ [A}^2\text{]}\tag{D.64}$$

Based on the operational parameters defined in Chapter III and previously defined current noise sources, the theoretical maximum noise equivalent power, respectively for each beam, is shown in Figure D.12, which inherits the elevation angle versus power trend as quantum shot current noise power.

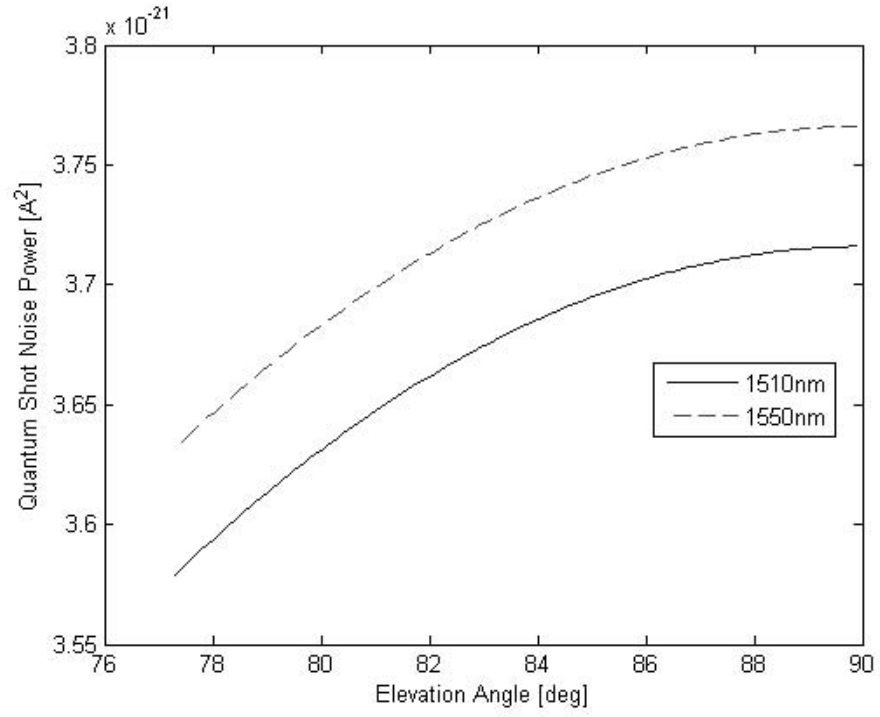


Figure D.11: Maximum Quantum Shot Noise Power

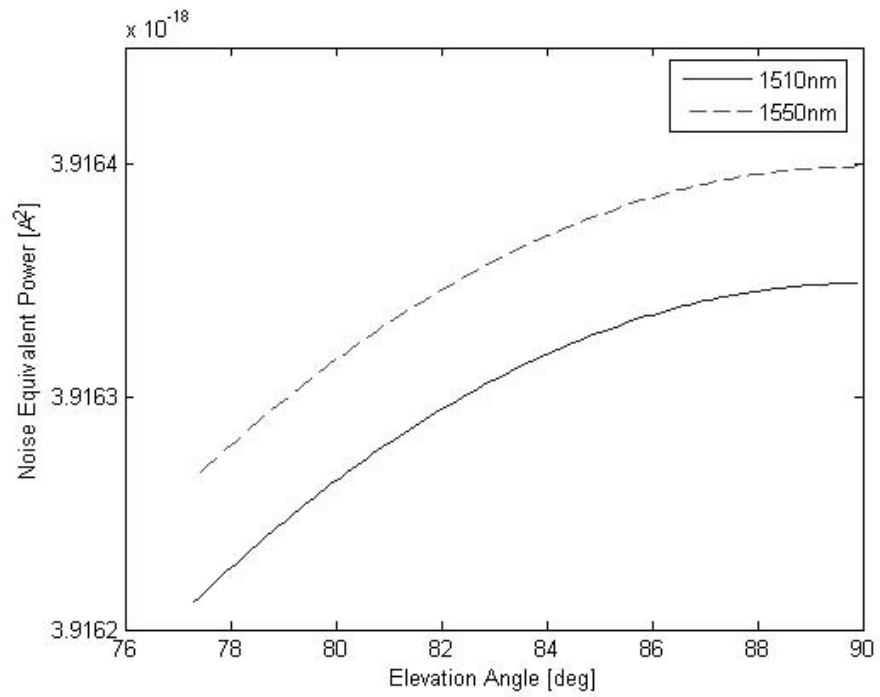


Figure D.12: Maximum Photodetector Noise Equivalent Current Power

### ***D.3 Summary***

This appendix presented the fundamental electromagnetic theory aspects, propagation characteristics, and optical components of the laser communication architecture. A near infrared (IR) on-off keying (OOK) modulated Gaussian beam is selected as the transmitter carrier wave, which is subject to channel propagation effects defined in Appendix E. Receiver optical components collect and detect each incident beam for tracking error and communication signal processing.

## Appendix E. Communication Channel

The communication channel, propagation medium between transmitter and receiver, consists of Earth's atmosphere and free space. Although a majority of optical disturbances occur within the atmosphere, most of the propagation path occurs in free space. Within free space, an optical signal is subject to free space diffraction, which is characterized by path loss. In addition, optical background radiation from extraneous sources attenuates the received signal power.

### E.1 Atmospheric Loss

The atmosphere is a nonhomogeneous medium, which affects laser beam propagation by absorption, scattering, and optical turbulence. These effects are found in four types of atmospheric conditions: clear-air, clouds, rain, and fog [4, page 480]. Based on the operational parameters defined in Chapter III, clear-air atmospheric condition is the primary concern for this study. For a direct detection system, clear-air atmosphere produces the following optical effects: attenuation, beam spreading, beam wander, and beam scintillation [2, page 22]. Attenuation, beam spreading and beam wander contribute to an atmospheric loss to the received optical signal power, while beam scintillation affects signal probability of fade.

*E.1.1 Attenuation.* Attenuation is caused by the interaction of a medium with an incident electromagnetic wave. In particular, atoms within the medium interact with an incoming wave, depending upon its wavelength, by either absorbing or scattering incident photons [13, page 67]. A majority of this interaction occurs up to 20 km above the Earth's surface, however, some optical turbulence exists up to 40 km [4, page 480]. Assuming absorption and scattering occur independently, attenuation loss is defined by the Beer Lambert Bouguer Law as [14, page 25]

$$L_{at} = \frac{I(\rho_z, z_p)}{I_o(z_p)} = \exp \left[ - \int_0^{z_p} \alpha(z) dz \right] \quad (\text{E.1})$$



where  $I(\rho_z, z_p)$  is the observed irradiance,  $I_o(z_p)$  is the peak irradiance,  $\rho_z$  is the radial distance from the propagation axis  $\vec{z}_p$ ,  $z_p$  is the propagation distance, and  $\alpha(z)$  is the extinction coefficient. If the extinction coefficient is assumed constant, for a given wavelength,  $\lambda_c$ , attenuation loss becomes

$$L_{at} = \exp[-\alpha(\lambda_c)z_p] \quad (\text{E.2})$$

Based on clear-air atmospheric conditions, which is a low attenuation environment, optical and infrared (IR) laser beam propagation is predominantly affected by optical turbulence [4, page 480]. Thus, for the purposes of this study, the attenuation loss is approximated as

$$L_{at} \approx 0.9 [-0.46 \text{ dB}] \quad (\text{E.3})$$

*E.1.2 Optical Turbulence.* Optical turbulence is defined as atmospheric refractive index fluctuations caused by temperature, which induces beam spreading, beam wander, and beam scintillation upon a propagating optical wave. For the purposes of this study, optical turbulence effects are based on the Kolmogorov power law spectrum [4, pages 490]. The strength of optical turbulence is determined by the refractive index structure constant,  $C_n^2$ , which is assumed to be constant along a horizontal path. However, for propagation along a vertical or slant path, the structure constant varies as a function of altitude, commonly defined by the Hufnagel-Valley (H-V<sub>5/7</sub>) profile model as [4, pages 480-481]

$$\begin{aligned} C_n^2(h) &= 0.00594(v/27)^2(10^{-5}h)^{10} \exp(-h/1000) \\ &+ 2.7 \times 10^{-16} \exp(-h/1500) + A_h \exp(-h/100) \end{aligned} \quad (\text{E.4})$$

where  $h$  is the altitude,  $v = 21$  m/s is the rms windspeed, and  $A_h = 1.7 \times 10^{-14} \text{ m}^{-2/3}$  is the nominal value of  $C_n^2(0)$  at the ground. Figure E.1 illustrates the structure constant profile based on the H-V<sub>5/7</sub> model. Due to operational parameters defined in Chapter III, the altitude range being considered,  $h \in [18.3 \text{ km}, 40 \text{ km}]$ , results

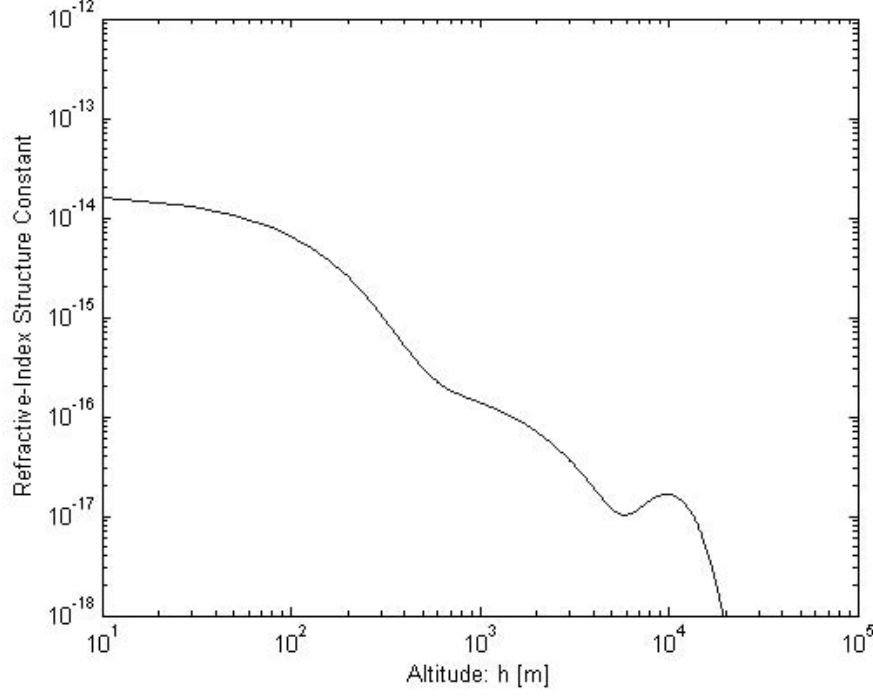


Figure E.1: Refractive Index Structure Constant Profile

in an extremely small structure constant, as illustrated in Figure E.2. For a communication uplink,  $C_n^2(h)$  is used to determine the following optical turbulence constants [4, pages 502,523]

$$\mu_0 = \int_{h_a}^{h_s} C_n^2(h) dh \quad (\text{E.5})$$

$$\mu_1 = \int_{h_a}^{h_s} C_n^2(h) \left[ \Theta - \bar{\Theta} \left( \frac{h - h_a}{h_s - h_a} \right) \right]^{5/3} dh \quad (\text{E.6})$$

$$\mu_2 = \int_{h_a}^{h_s} C_n^2(h) (\xi)^{5/3} dh \quad (\text{E.7})$$

$$\mu_3 = \text{Re} \int_{h_a}^{h_s} C_n^2(h) \left\{ \xi^{5/6} [\Lambda \xi + i(1 - \bar{\Theta} \xi)]^{5/6} - \Lambda^{5/6} \xi^{5/3} \right\}^{5/3} dh \quad (\text{E.8})$$

$$\xi = 1 - \left( \frac{h - h_a}{h_s - h_a} \right)$$

where  $h_a$  is the aircraft altitude, and  $h_s$  is the satellite altitude. Parameters  $\Theta$ ,  $\bar{\Theta}$ , and  $\Lambda$  are the output plane beam parameters, which were derived in Appendix D

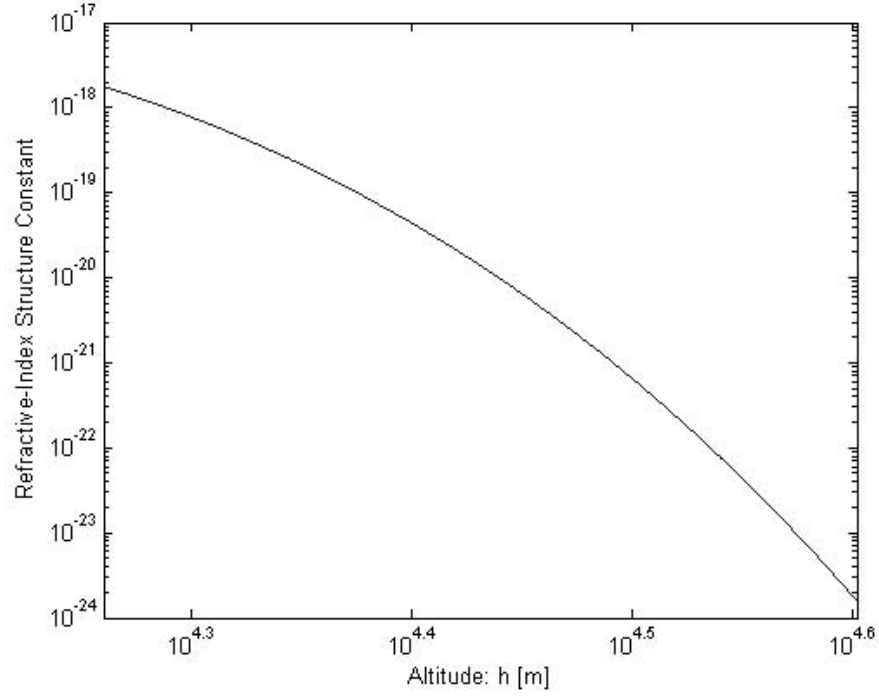


Figure E.2: Relative Refractive Index Structure Constant Profile

as [4, page 489]

$$\Theta = \frac{\Theta_o}{\Theta_o^2 + \Lambda_o^2} \quad (\text{E.9})$$

$$\bar{\Theta} = 1 - \Theta \quad (\text{E.10})$$

$$\Lambda = \frac{2z_p}{k_c W^2(z_p)} \quad (\text{E.11})$$

where  $z_p$  is the propagation distance,  $W(z_p)$  is the diffractive beam radius, and  $k_c$  is the wave number. Parameters  $\Theta_o$  and  $\Lambda_o$  are the input plane beam parameters, defined in Appendix D as [4, page 488]

$$\Theta_o = 1 \quad (\text{E.12})$$

$$\Lambda_o = \frac{2z_p}{k_c W_o^2} \quad (\text{E.13})$$

where  $W_o$  is the initial beam radius at transmission.

### E.1.2.1 Beam Spreading.

Optical turbulence produces additional beam spreading, beyond normal diffraction occurring within free-space propagation. Thus, for a Gaussian beam the effective beam radius is defined by [4, page 500]

$$W_e(z_p) = \begin{cases} W(z_p) [1 + (D_o/r_{at})^{5/3}]^{1/2}, & 0 \leq D_o/r_{at} < 1 \\ W(z_p) [1 + (D_o/r_{at})^{5/3}]^{3/5}, & 0 \leq D_o/r_{at} < \infty \end{cases} \quad (\text{E.14})$$

where  $D_o^2 = 8W_o^2$  and  $r_{at}$  is the atmospheric coherence width, defined as [4, page 492]

$$r_{at} = [0.42 \sec(\zeta_{as}) k_e^2 \mu_0]^{-3/5} \quad (\text{E.15})$$

where  $\zeta_{as}$  is the zenith angle, defined as the complement to the elevation angle. The first condition satisfies the condition for weak irradiance fluctuations theory, while the second condition satisfies strong irradiance fluctuation theory. As similarly derived in Appendix D, the expected Gaussian beam irradiance profile, subject to  $W_e(z_p)$ , is determined as [4, page 494]

$$E[I(\rho_z, z_p)] = \left[ \frac{W_o^2}{W_e^2(z_p)} \right] \exp \left[ -\frac{2\rho_z^2}{W_e^2(z_p)} \right] \quad (\text{E.16})$$

where  $\rho_z$  is the radial distance from the propagation axis. Comparison with free space peak irradiance, defined in Appendix D, the beam spreading power loss is defined as

$$L_{bs} = \frac{E[I(\rho_z, z_p)]}{I_o(z_p)} = \left[ \frac{W^2(z_p)}{W_e^2} \right] \exp \left[ 2\rho_z^2 \left( \frac{1}{W^2(z_p)} - \frac{1}{W_e^2} \right) \right] \quad (\text{E.17})$$

where the maximum power loss occurs on-axis,  $\rho_z = 0$ , denoted by

$$\begin{aligned} L_{bs}(max) &= \frac{E[I(0, z_p)]}{I_o(z_p)} = \left[ \frac{W^2(z_p)}{W_e^2} \right] \exp \left[ (0) \left( \frac{1}{W^2(z_p)} - \frac{1}{W_e^2} \right) \right] \\ &= \left[ \frac{W^2(z_p)}{W_e^2} \right] \end{aligned} \quad (\text{E.18})$$

Figure E.3 illustrates the theoretical irradiance fluctuation condition of beam spreading at the satellite receiver, for a collimated Gaussian beam based on Chapter III input

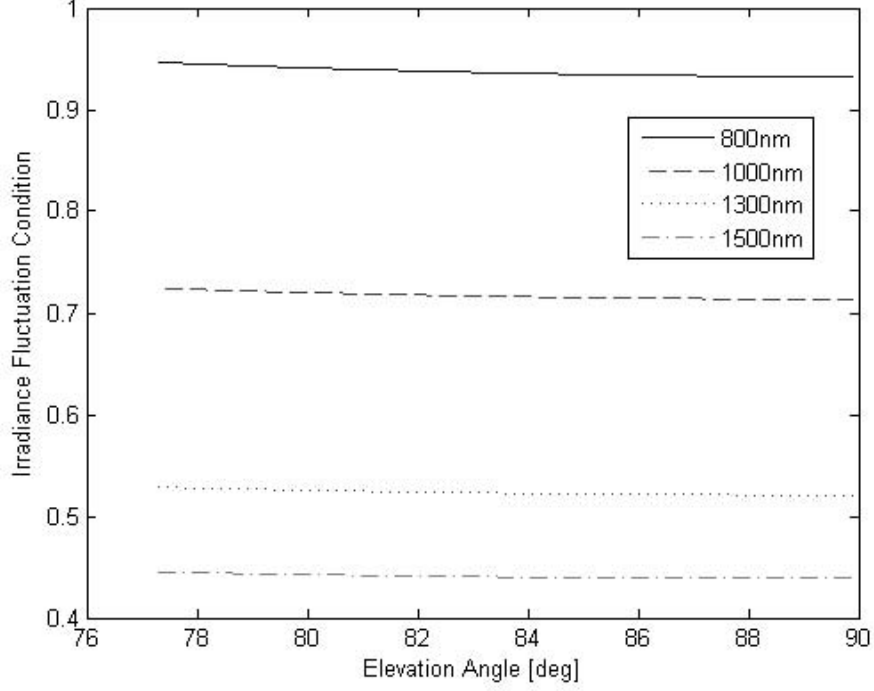


Figure E.3: Irradiance Fluctuation Condition

parameters  $P_t = 100$  mW,  $W_o = 40$  mm,  $\varepsilon_{sa} \in [77.3^\circ, 90^\circ]$ ,  $h \in [18.3 \text{ km}, 35786 \text{ km}]$ , and arbitrary Near IR carrier wavelengths,  $\lambda_c \in [800 \text{ nm}, 1100 \text{ nm}, 1300 \text{ nm}, 1500 \text{ nm}]$ . For a given initial beam radius, shorter wavelengths approach the strong irradiance fluctuation regime, while long wavelengths are less susceptible to optical turbulence. On the other hand, the corresponding beam spreading effects, shown in Figures E.4 thru E.6, share a similar trend with free-space diffraction effects revealed in Appendix D. Shorter wavelengths are less susceptible to beam spreading, which results in a higher mean peak irradiance.

*E.1.2.2 Beam Wander.* Optical turbulence induces random radial displacements, based on zero-mean Gaussian statistics, of the incident beam centroid within the receiver boresight, commonly referred to as beam wander. For zenith angles less than 60 degrees, optical turbulence is characterized by weak irradiance fluctuation theory based on Rytov approximation [4, page 478]. As such, based on the previously defined operational parameters, the beam wander displacement variance for an uplink

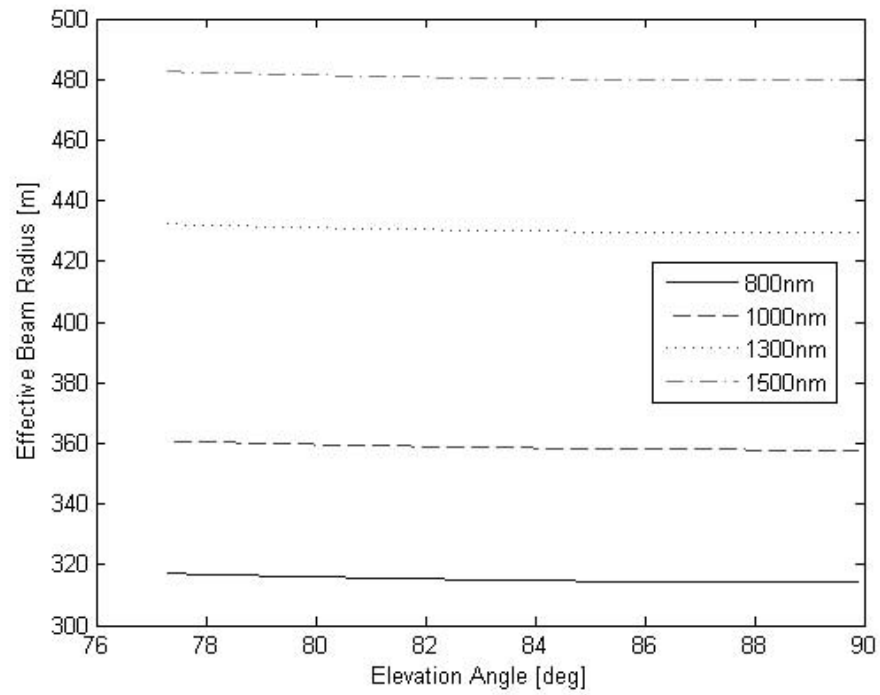


Figure E.4: Effective Beam Radius

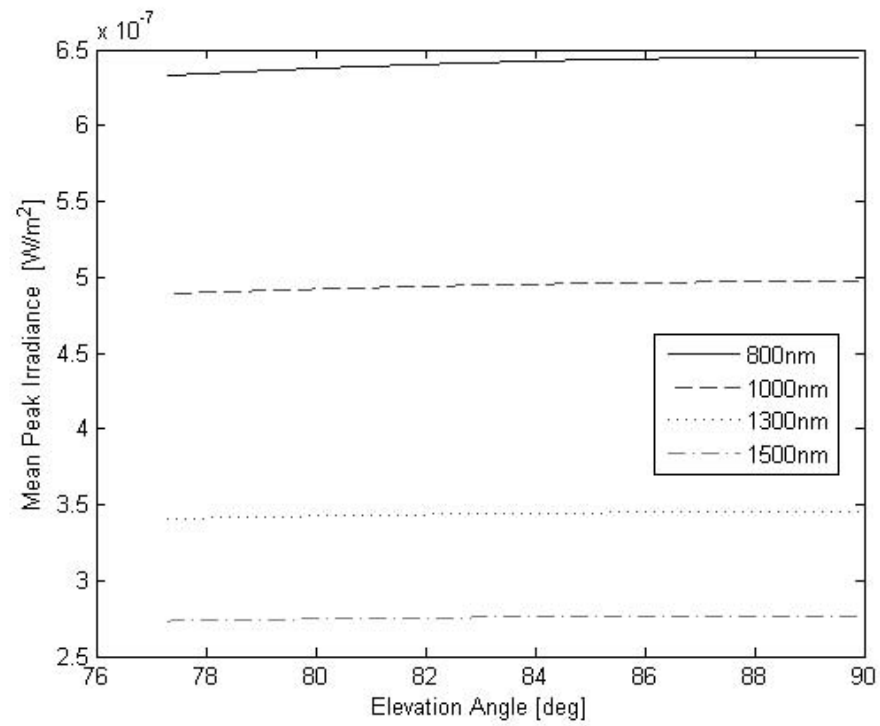


Figure E.5: Mean Peak Irradiance

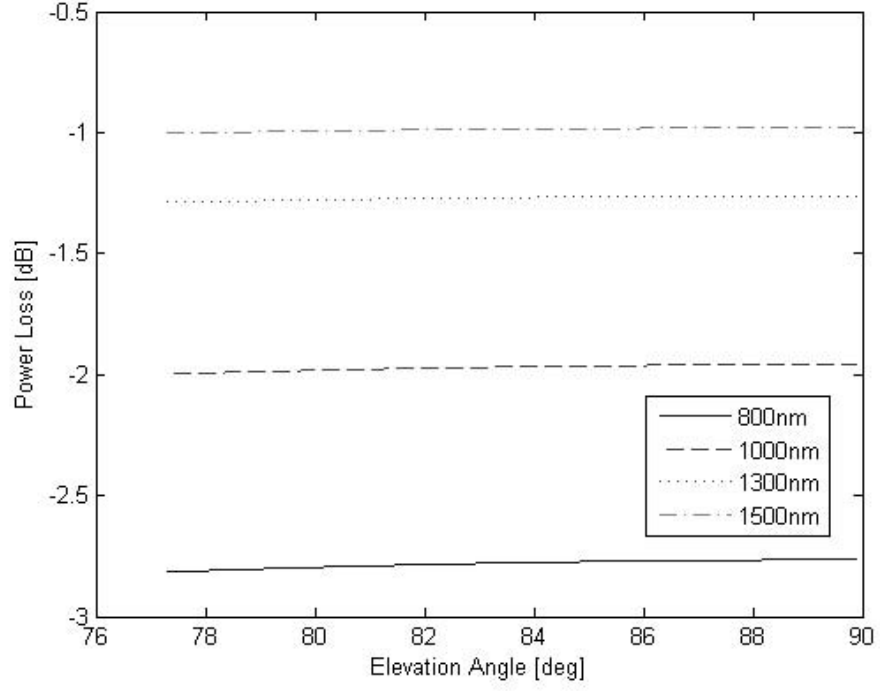


Figure E.6: Beam Spreading Loss

propagation path is defined as [4, page 502]

$$\begin{aligned} \text{VAR}[\rho_{bw}] &= [7.25\mu_o(h_s - h_a)^2 \sec^3(\zeta_{as})W_o^{-1/3}]^{\frac{1}{2}} \text{ [m}^2\text{]} \\ &= \sigma_{bw}^2 \end{aligned} \quad (\text{E.19})$$

After conversion to radians,  $\rho_{bw} = \sigma_{bw}/z_p$ , beam wander power loss can be interpreted as a pointing loss, determined by [8, page 253]

$$L_{bw} = \exp(-G_t \rho_{bw}^2) \quad (\text{E.20})$$

Figures E.7 and E.8 illustrate the observed theoretical beam wander effects. Although beam wander is independent of wavelength, a similar trend results for increasing elevation angle as previously shown for beam spreading. However, the power loss is affected by the signal gain, which is a function of wavelength as illustrated in Appendix D. Thus, shorter wavelengths suffer more power loss due to beam wander.

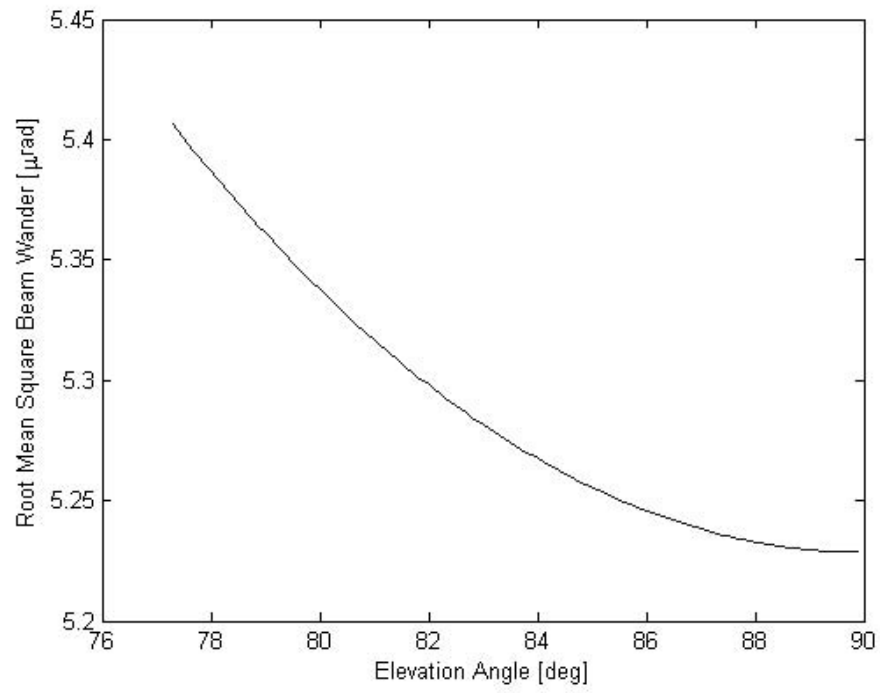


Figure E.7: Root Mean Square Beam Wander

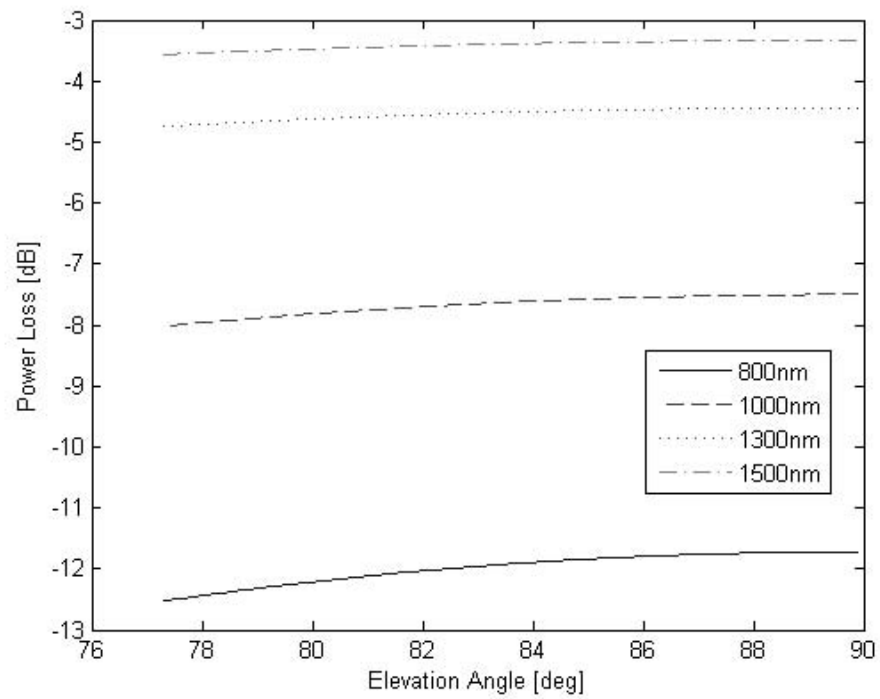


Figure E.8: Beam Wander Loss



*E.1.2.3 Beam Scintillation.* Random index of refraction fluctuations, caused by optical turbulence, produce corresponding irradiance fluctuations, known as beam scintillation. Classified as weak, medium, or strong, irradiance fluctuations are analyzed by the normalized variance of irradiance, commonly known as scintillation index, denoted by  $\sigma_I^2$  [4, page 261]. Based on the previously defined uplink communication operational parameters and ideal tracking, within the weak irradiance fluctuation regime,  $\sigma_I^2$  is defined by [4, page 504]

$$\begin{aligned} \sigma_I^2(\rho_r, z_p) &= 8.70(\mu_3) (k_c^{7/6}) (h_s - h_a)^{5/6} \sec^{11/6}(\zeta_{sa}) \\ &+ \left\{ 5.95 (h_s - h_a)^2 \sec^2(\zeta_{sa}) \left( \frac{2W_o}{r_{at}} \right)^{5/3} \right. \\ &\times \left. \left[ \frac{\rho_r - \rho_{bw}}{W_e(z_p)} \right]^2 U(\rho_r - \rho_{bw}) \right\} \end{aligned} \quad (\text{E.21})$$

where  $U(\rho_r - \rho_{bw})$  is the unit step function.

Ideally,  $\sigma_I^2 < 1$  satisfies the conditions for weak fluctuation theory [4, page 264]. Based on the previously defined parameters for the uplink beam, the tracked on-axis,  $\rho_r = 0$ , scintillation index is shown in Figure E.9. Sharing a similar trend for elevation angle as other optical turbulence effects, transmitting from an altitude of 18.3 km, results in a scintillation index roughly between an order of magnitude of  $10^{-4.38}$  and  $10^{-4.28}$ . Thus, optical turbulence induced beam scintillation effects can be considered negligible beyond an altitude of 20 km [4, page 504].

*E.1.3 Atmospheric Loss.* Atmospheric loss is comprised of power losses from attenuation, beam wander, and beam spreading, denoted by

$$L_a = L_{at} + L_{bs} + L_{bw} \text{ [dB]} \quad (\text{E.22})$$

Based on the precalculated values, the maximum theoretical atmospheric loss is shown Figure E.10. Retaining the trend in elevation angle and wavelength dependency, longer wavelengths are less susceptible to power loss induced by atmospheric effects.

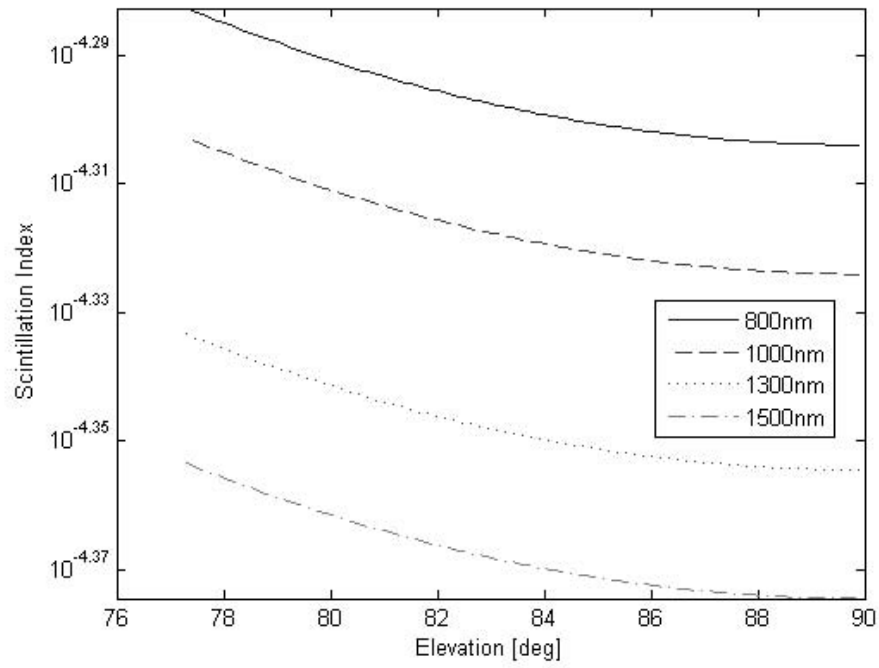


Figure E.9: Tracked On-Axis Scintillation Index

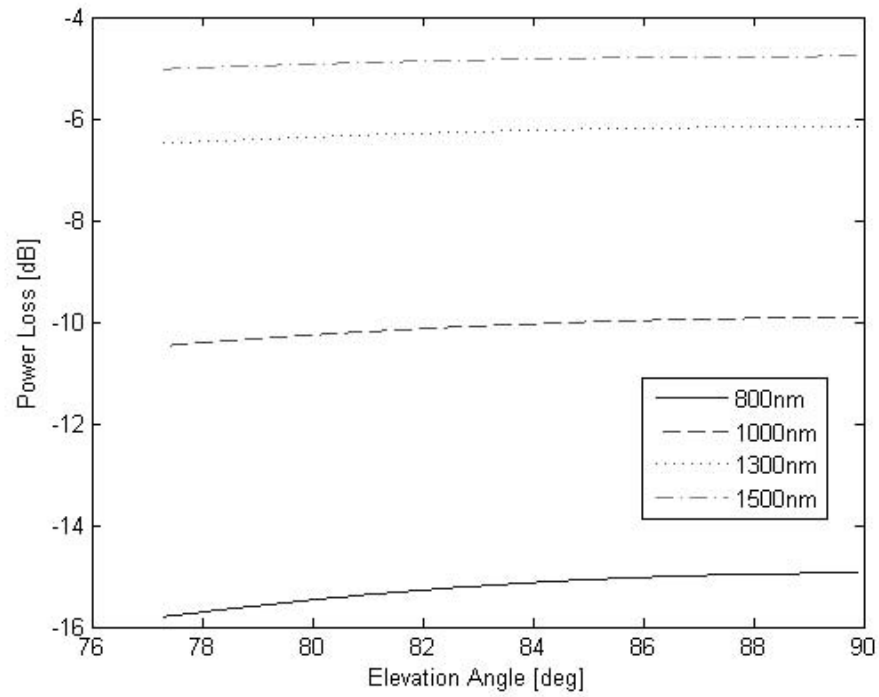


Figure E.10: Atmospheric Loss

### E.2 Path Loss

As shown in Appendix D, the decrease in irradiance of an electromagnetic wave, subject to free-space diffraction, is a function of propagation distance. As such, the effective transmitted power loss, commonly referred to as path loss, is defined by [29, page 254]

$$L_s = \left( \frac{\lambda_c}{4\pi z_p} \right)^2 \quad (\text{E.23})$$

Based on the previously defined parameters for the uplink beam, the path loss is shown in Figure E.11. Although wavelength dependent, clearly path loss is the largest contributor to attenuation of transmitted signal power.

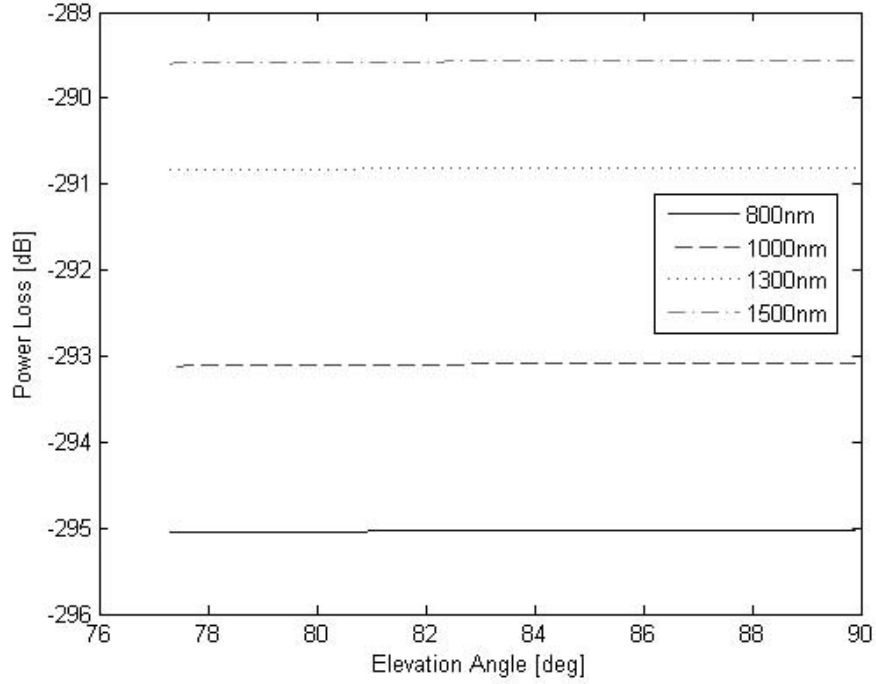


Figure E.11: Path Loss

### E.3 Optical Background Radiation

Extraneous optical sources, such as the sun, planets, stars, and blackbody radiation, are the main contributors of optical background radiation. Depending upon

wavelength and the satellite receiver field-of-view (FOV), these sources are modeled as additive white Gaussian noise (AWGN) for a direct detection optical receiver [4, page 444]. However, optical filtering can restrict background radiation to a manageable level, at the cost of signal attenuation. For an Earth observing satellite receiver in geosynchronous orbit (GEO), optical background radiation is approximately  $10^4$  photons per second per Angstrom of optical bandwidth [1, page 151]. Depending upon optical filter bandwidth, denoted as  $\Delta\lambda_F$ , the observed optical background radiation power is defined by [5, page 679]

$$\sigma_b^2 = (N_b)(\Delta\lambda_F) [\text{W}] \quad (\text{E.24})$$

where

$$\begin{aligned} N_b &= \left( \frac{10^4 \text{ photons/s}}{1 \times 10^{-10} \text{ m}} \right) \left( \frac{\text{photon energy}}{1 \text{ photon}} \right) \\ &= (1 \times 10^{14}) \left( \frac{\hbar c}{\lambda_c} \right) [\text{W/m}] \\ \hbar &= \text{Plank's constant} \\ &= 6.626 \times 10^{-34} \text{ joules} \cdot \text{s} \\ c &= \text{speed of light} \\ &\approx 3 \times 10^8 \text{ m/s} \\ \lambda_c &= \text{carrier signal wavelength} \end{aligned} \quad (\text{E.25})$$

Based on the operational parameters, defined in Chapter III, the optical background noise power, respectively for each beam, is calculated as

$$\begin{aligned} (\sigma_b^2)_A &= (1 \times 10^{14}) \left[ \frac{(6.626 \times 10^{-34})(3 \times 10^8)}{1510 \times 10^{-9}} \right] (1 \times 10^{-9}) \\ &= 1.3164 \times 10^{-14} \text{ [W]} \end{aligned} \quad (\text{E.26})$$

$$\begin{aligned} (\sigma_b^2)_B &= (1 \times 10^{14}) \left[ \frac{(6.626 \times 10^{-34})(3 \times 10^8)}{1550 \times 10^{-9}} \right] (1 \times 10^{-9}) \\ &= 1.2825 \times 10^{-14} \text{ [W]} \end{aligned} \quad (\text{E.27})$$

#### ***E.4 Summary***

This appendix presented the channel propagation effects encountered within the laser communication architecture. Assuming clear-air atmospheric conditions, path loss is the greatest contributor to signal attenuation. However, optical turbulence induces additional signal attenuation due to beam spreading and beam wander effects. Optical background radiation creates an additional noise source for signal detection processing.

## *Appendix F. Controller Characterization*

As determined in Chapter III, the control system is required to regulate radial tracking error within the error performance limit,  $1.68 \mu\text{rad}$  and  $1.74 \mu\text{rad}$  respectively for each beam, to ensure the communication system meets a bit error rate (BER) of  $10^{-6}$ . On the other hand, due to a single actuator limitation of one fast steering mirror (FSM), the controller must switch between state estimates for each beam. Thus, the controller characterized by the weighting matrices and switching time which yields the best performance.

Analysis of controller performance is based on applying Monte Carlo analysis, taking samples generated from multiple simulation runs, and computing an ensemble average of the outputs. In order to perform ensemble averaging, the system model is converted to a fixed-step system using the SIMULINK Runge-Kutta solver solution. After trial and error, a fixed time step of  $T_s = 5 \times 10^{-5}$  sec was used to ensure against SIMULINK processing errors. Only ten simulation runs were performed to ensure against creating memory overloads, due to the small fixed time step and final time selection, in processing the data in MATLAB.

In addition, a rate transition block, defaulted to act as a unit delay for continuous sample time, is used on all plant disturbance and measurement noise inputs to ensure proper timing of these inputs into the system. Correlation time for the bandlimited white noise blocks, due to SIMULINK requirements, is changed to an integer factor of the fixed time step as  $t_c = 20T_s = 0.001$  sec. The response signal means and standard deviation statistics are computed to produce outputs for evaluating the modeled fine tracking control system.

### ***F.1 Weighting Matrices***

Since each quadrant cell detector determines relative azimuth and elevation tracking error, an initial state weighting matrix based on this tracking error is given

by

$$\mathbf{Z} = \begin{bmatrix} 1 & 0 \\ 0 & 1 \end{bmatrix} \quad (\text{F.1})$$

As derived in Chapter III, the corresponding system state weighting matrix is denoted by

$$\begin{aligned} \mathbf{Q} &= [\mathbf{Cm}_G^T \mathbf{Z} \mathbf{Cm}_G] \\ &= \begin{bmatrix} -1 & 0 & 0 & 0 & 1 & 0 \\ 0 & 0 & -1 & 0 & 0 & 1 \end{bmatrix}^T \begin{bmatrix} 1 & 0 \\ 0 & 1 \end{bmatrix} \begin{bmatrix} -1 & 0 & 0 & 0 & 1 & 0 \\ 0 & 0 & -1 & 0 & 0 & 1 \end{bmatrix} \\ &= \begin{bmatrix} 1 & 0 & 0 & 0 & -1 & 0 \\ 0 & 0 & 0 & 0 & 0 & 0 \\ 0 & 0 & 1 & 0 & 0 & -1 \\ 0 & 0 & 0 & 0 & 0 & 0 \\ -1 & 0 & 0 & 0 & 1 & 0 \\ 0 & 0 & -1 & 0 & 0 & 1 \end{bmatrix} \end{aligned} \quad (\text{F.2})$$

The fast steering mirror (FSM) is modeled as an uncoupled second order SISO system for each axis, thus the control weighting matrix is defined by

$$\mathbf{R} = \begin{bmatrix} 1 & 0 \\ 0 & 1 \end{bmatrix} \quad (\text{F.3})$$

In order to determine the relative LQR weighting matrix affects on controller performance, the control system was implemented by varying  $\mathbf{Q}$  and  $\mathbf{R}$  independently and evaluated against the tracking error performance limit with the maximum plant disturbance due to maximum rms beam wander of  $5.406 \times 10^{-6} \mu\text{rad}$ . The implemented weighting matrices are shown in Table F.1, and the scalar coefficients of  $\mathbf{Q}$  and  $\mathbf{R}$  will be referred to as the *weighting scale factors*.

Table F.1: Weighting Matrix Variables

State Matrix	Q1	Q2	Q3	Q4
Scale Factor	1000	100	10	1
Control Matrix	R1	R2	R3	R4
Scale Factor	1	0.1	0.01	0.001

*F.1.1 State Weighting Matrix Response.* Based on simulation final time,  $T_f = 1$  second, and an arbitrary switching time based on the FSM 2% settling time,  $T_{sw} = 0.4$  seconds, tracking error and control input data was collected for each state weighting matrix, associated with the chosen tracking error weighting matrix, paired with a unit control weighting matrix. Figures F.1 thru F.3 show a magnified view of the time response ensemble average mean and standard deviation data. Based on the time interval illustrated, Beam B tracking error is regulated while the other beam is unregulated. In particular, the standard deviation transient peaks, during regulation of Beam B, are due to the noise correlation time. An initial comparison of the response for each state weighting scale factor response reveals relatively similar mean values. However, a larger state weighting matrix encounters more dispersion as seen in the standard deviation plots. In terms of control input response, which reveals similar behavior for each axis, a larger state weighting results in greater mean control authority, but at the cost of increased dispersion.

Taking a temporal average of the ensemble averaged mean and standard deviation data, illustrated in Figures F.4 thru F.6, reveals each state weighting matrix yields relatively similar temporal mean tracking error values, but higher order weighting has slightly greater dispersion. Analysis of the temporal standard deviation data shows an increasing temporal mean trend for lower order weighting, but the dispersion decreases. A larger control weighting results similar in temporal mean control and larger dispersion due to more regulation being applied. In addition, a decreasing mean and dispersion trend in control standard deviation is seen for decreased weight-



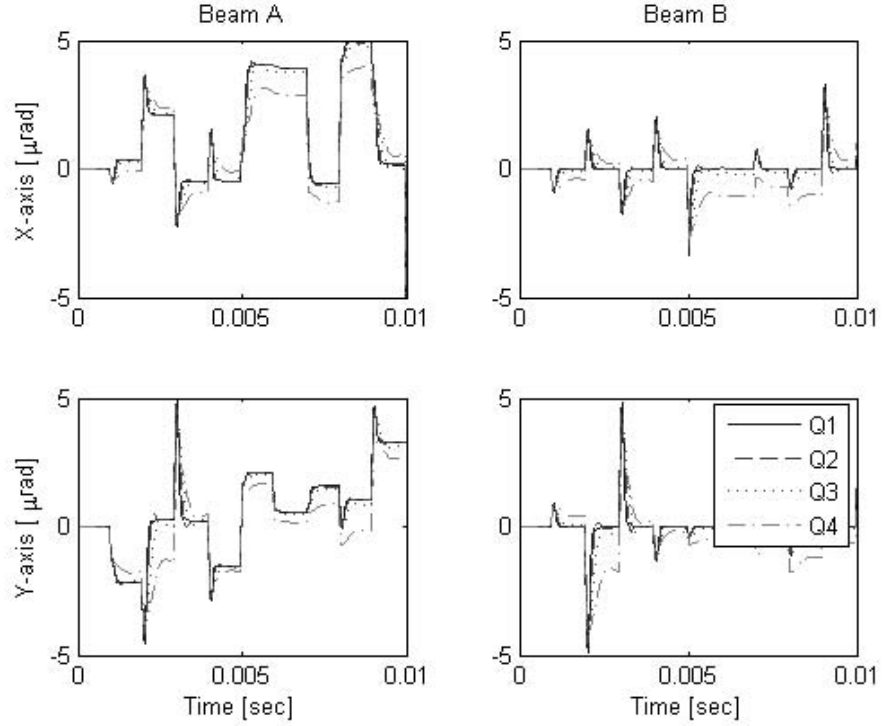


Figure F.1: State Weighting Matrix Ensemble Average Mean Tracking Error Response

ing. Based upon these results, the optimum state weighting matrix is Q3, due to better overall standard deviation performance.

*F.1.2 Control Weighting Matrix Response.* Applying the same method used for determining the state weighting matrix, tracking error and control input data was collected for for each control weighting matrix paired with a unit tracking error matrix. Figures F.7 thru F.9 show a magnified view of the time response ensemble average mean and standard deviation data. In particular, a greater tracking error trend is evident for decreased control weighting. Thus, lower control weighting increases control authority, at the cost of greater deviation. Temporal average of the ensemble averaged mean and standard deviation data, illustrated in Figures F.10 thru F.12, reveals each control weighting matrix yields a relatively similar temporal mean tracking error response. However, comparison of the standard deviation response shows a lower order control weighting has slightly less mean deviation at the cost of greater

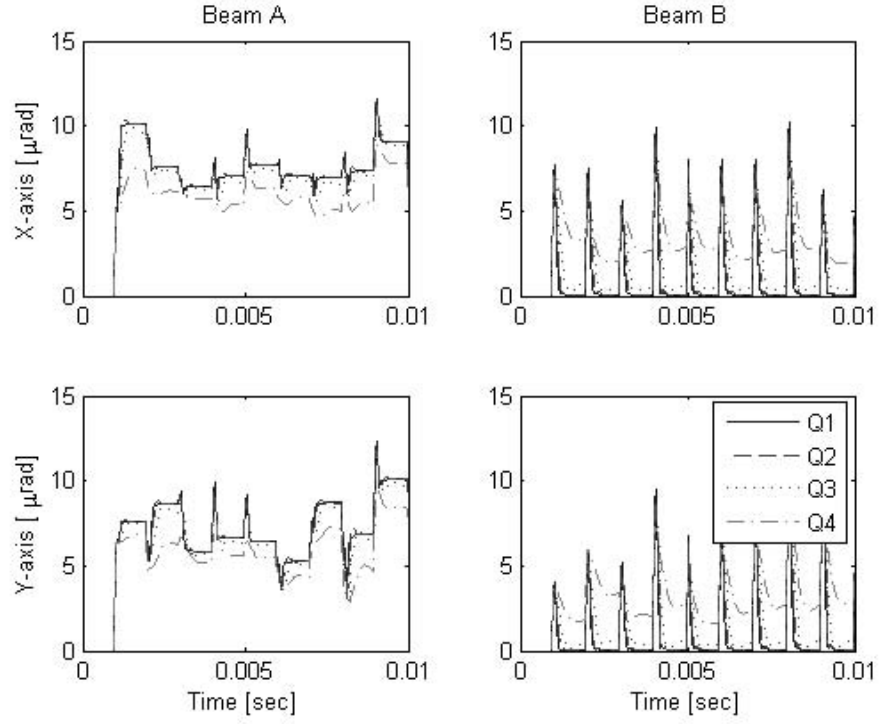


Figure F.2: State Weighting Matrix Ensemble Average Tracking Error Standard Deviation Response

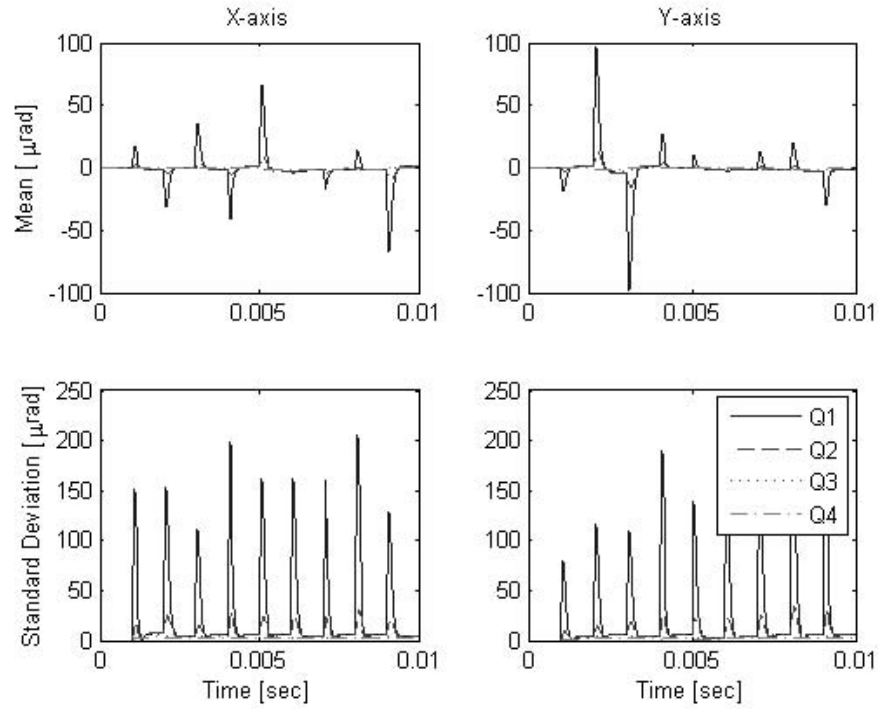


Figure F.3: State Weighting Matrix Ensemble Average Control Response

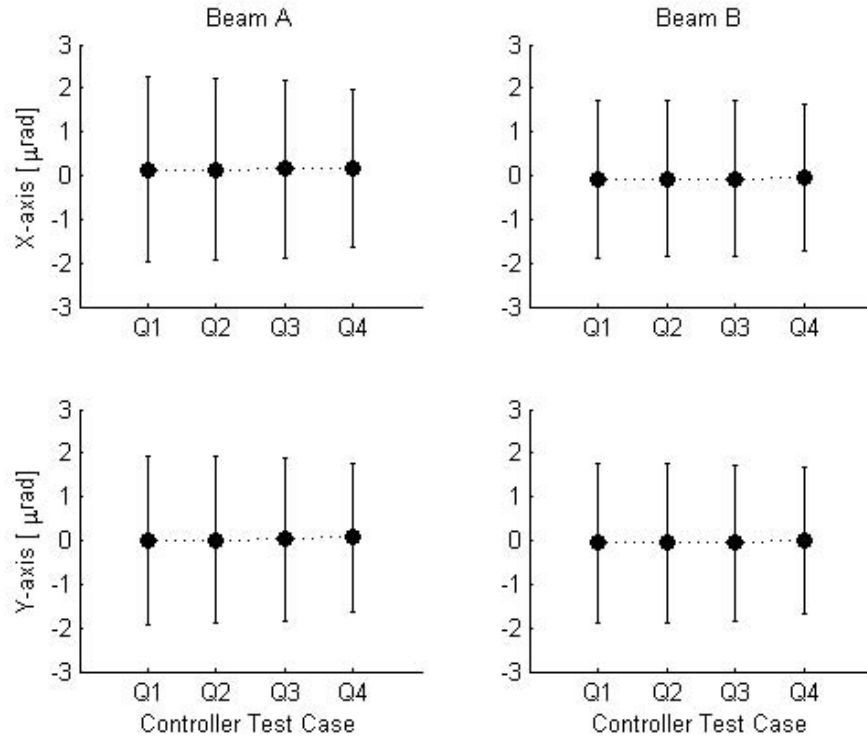


Figure F.4: State Weighting Matrix Temporal Mean Tracking Error Response

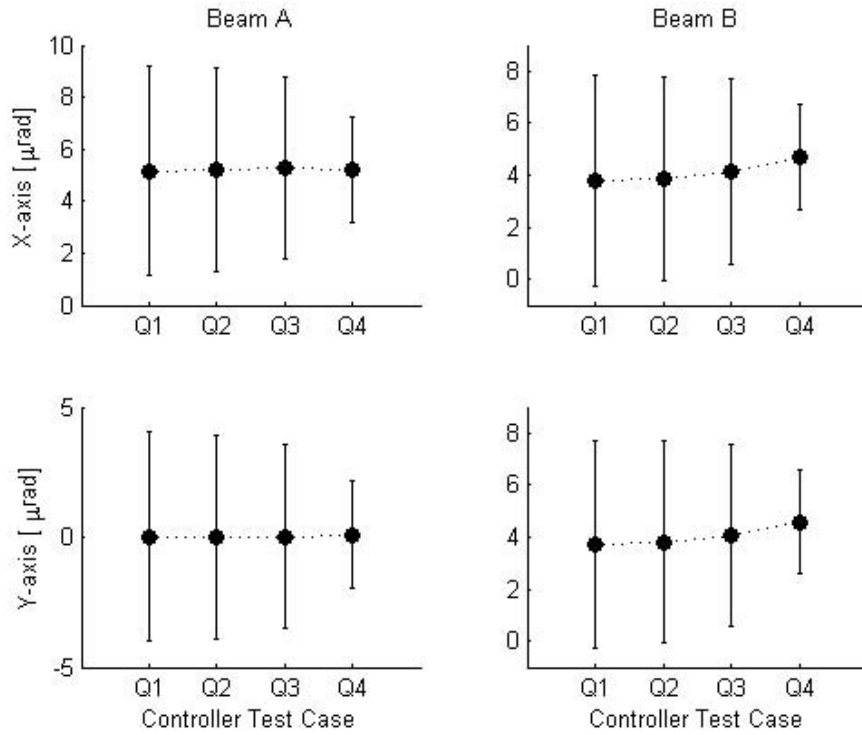


Figure F.5: State Weighting Matrix Temporal Standard Deviation Response

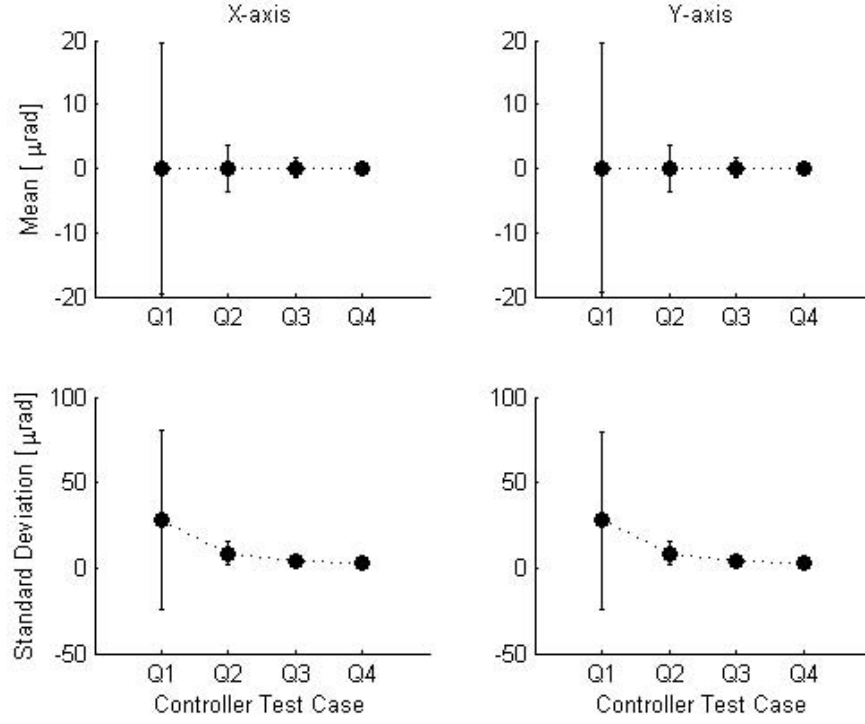


Figure F.6: State Weighting Matrix Temporal Control Response

dispersion. As seen with the state weighting matrix data, each control weighting case achieves a similar mean control input response, but smaller weighting results in larger deviation due to less regulation being applied. Based upon these results, the optimum control weighting matrix is R2, due to better overall standard deviation performance.

## F.2 Switching Time

Applying a similar simulation approach to characterize switching time effects, the control system was implemented, with the predetermined optimum weighting matrices and  $T_{sw}$  was varied and evaluated against the tracking error performance limit. The implemented switching times, based on multiples of the FSM 2% settling time of approximately 0.002 seconds, are shown in Table F.2. Applying the same method used for determining the weighting matrices, tracking error and control input data was collected for each switching time over a simulation time of 5 seconds.

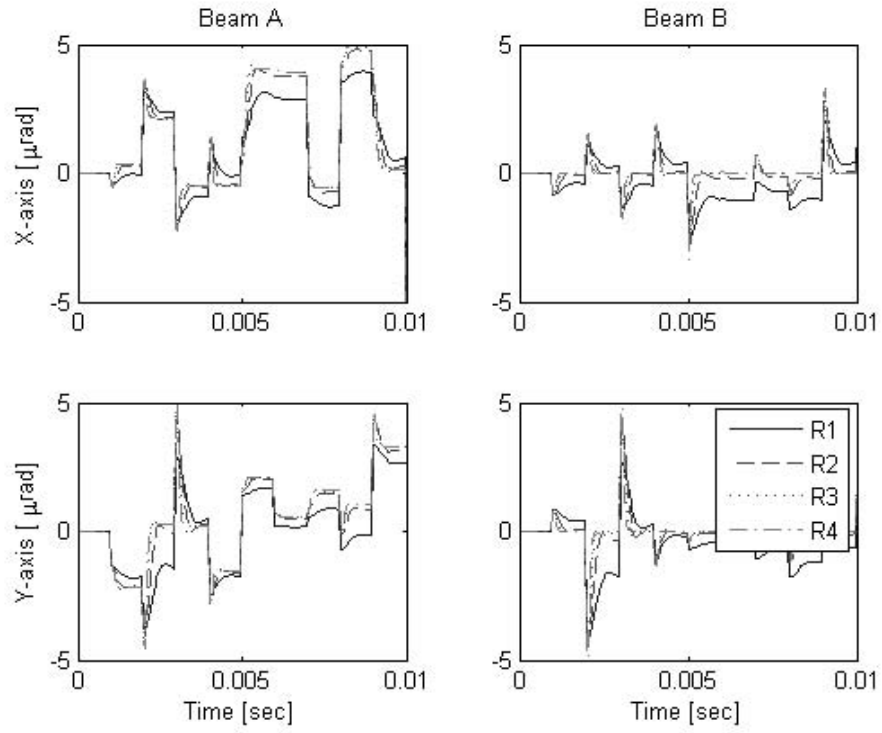


Figure F.7: Control Weighting Matrix Ensemble Average Mean Tracking Error Response

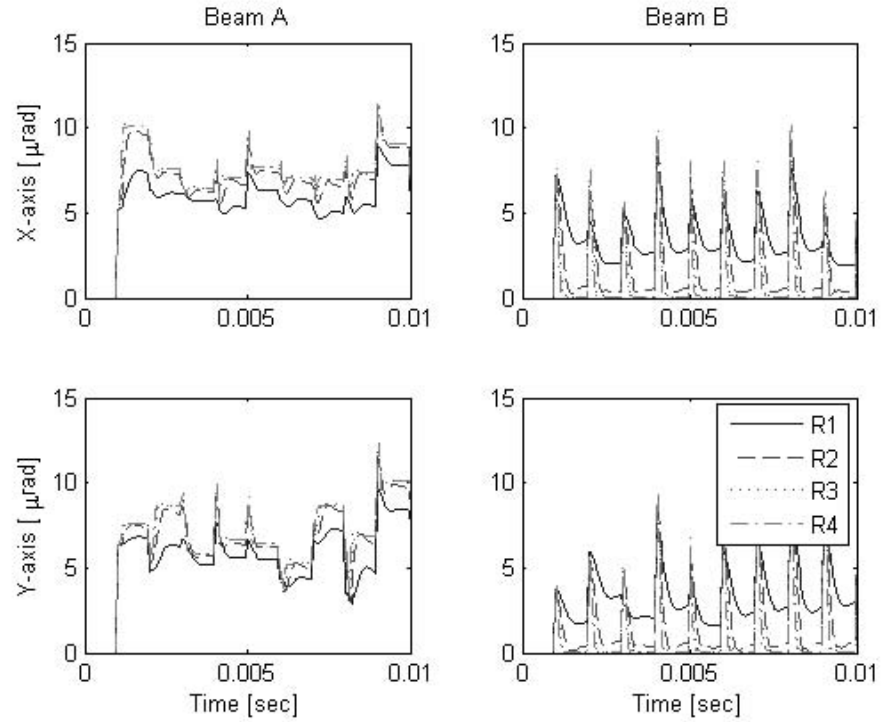


Figure F.8: Control Weighting Matrix Ensemble Average Tracking Error Standard Deviation Response

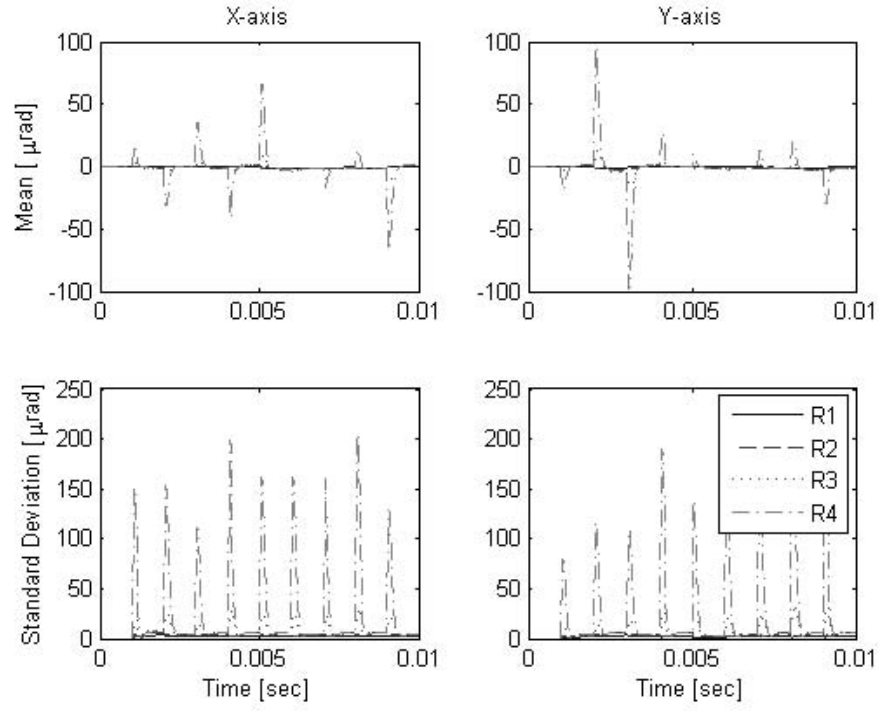


Figure F.9: Control Weighting Matrix Ensemble Average Control Response

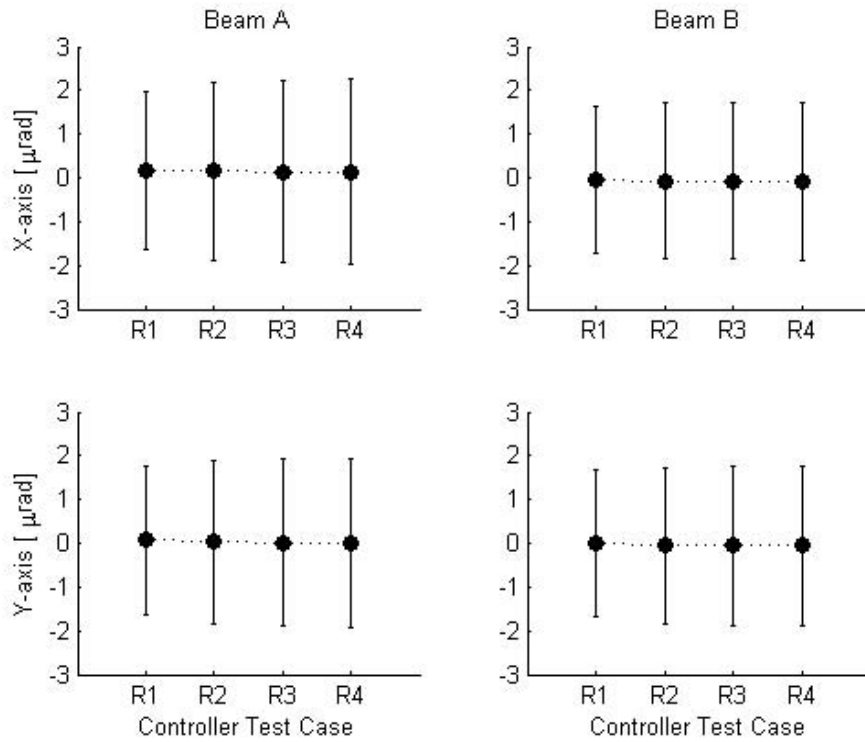


Figure F.10: Control Weighting Matrix Temporal Mean Tracking Error Response

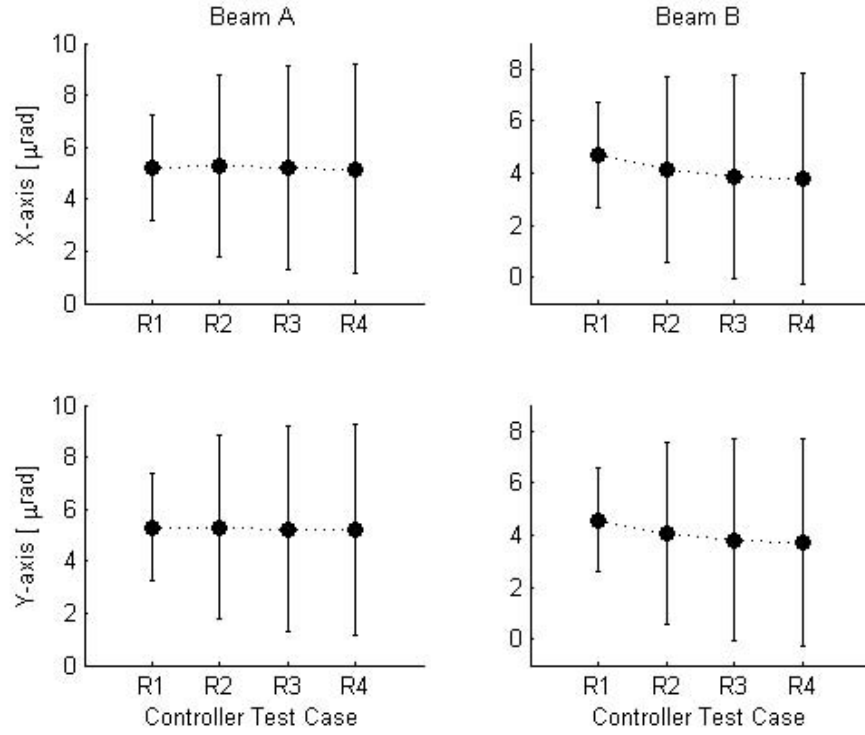


Figure F.11: Control Weighting Matrix Temporal Standard Deviation Response

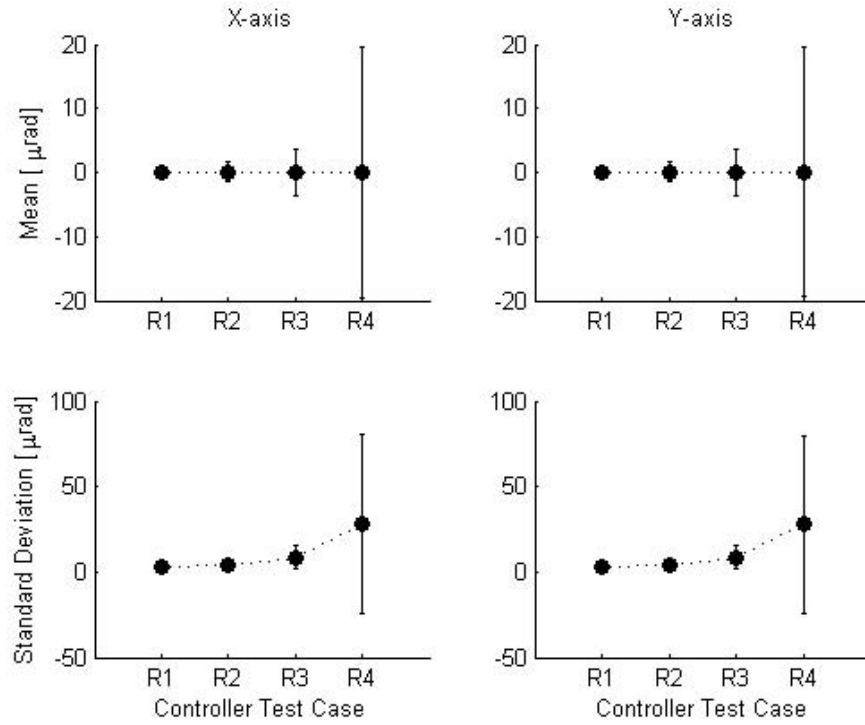


Figure F.12: Control Weighting Matrix Temporal Control Response

Table F.2: Candidate Switching Time Variables

Variable	T1	T2	T3	T4
$T_{sw}$	0.002 sec	0.02 sec	0.2 sec	1.0 sec

*F.2.1 Ensemble Average Tracking Error Response.* Since each FSM axis is modeled by the same SISO system, controlled independently, and yielded similar weighting performance, the tracking error time response results are only given for the X-axis, as illustrated in Figures F.13 thru F.16. Each figure shows the ensemble mean and standard deviation results for the time domain propagated through to each switching time. As time progresses, the controller switches tracking error regulation between Beam A and Beam B. In either case, at time of regulation for each switching time, an initial transient spike is seen in the mean response. In particular, each standard deviation time response exhibits initial transients occurring at intervals of the noise block correlation time. Based on these results, it is apparent that all of the switching times have similar performance.

*F.2.2 Ensemble Average Control Input Response.* Comparison of the ensemble mean and standard deviation of the control input, shown in Figures F.17 thru F.20, reveals that all switching times generate a similar time response. As the time domain propagates, regulation standard deviation is subject to the noise block correlation time interval, as seen in the tracking error response. However, none of the candidate switching times show noticeable benefits over other switching times.

*F.2.3 Temporal Average Response.* Temporal average of the ensemble averaged mean and standard deviation data, illustrated in Figures F.21 thru F.23, reveals each switching time case yields relatively similar temporal mean tracking error response. In addition the standard deviation share similar range of dispersion about the mean. The slight increase at T4 in Beam A mean deviation, while Beam B decreases, is due to more Beam B tracking error regulation occurring over the 5 second simulation. However, the range of dispersion about the mean deviation does not



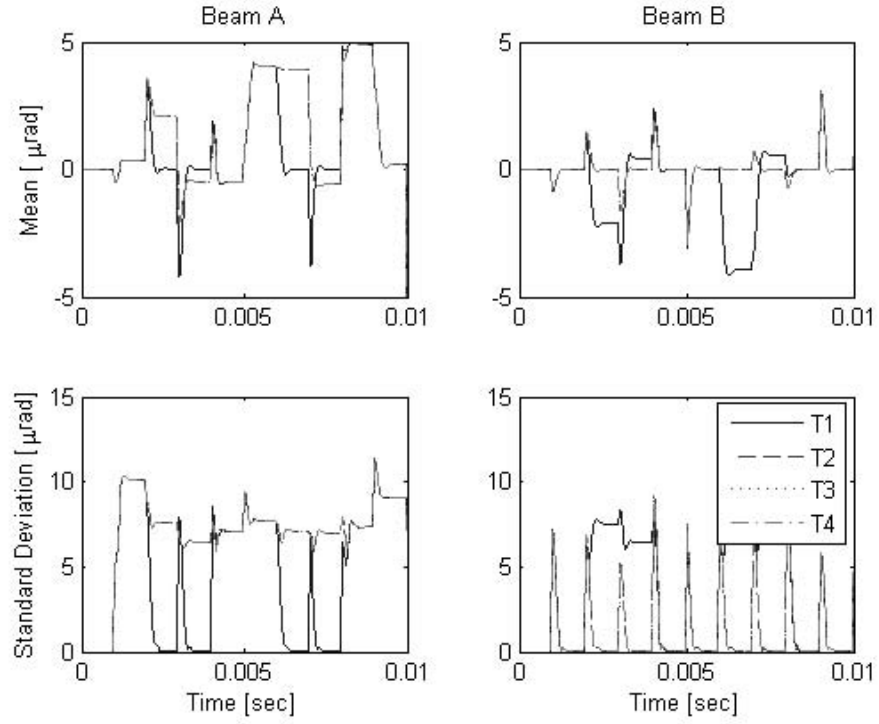


Figure F.13: Tracking Error Time Response,  $t \in (0, 0.01s)$

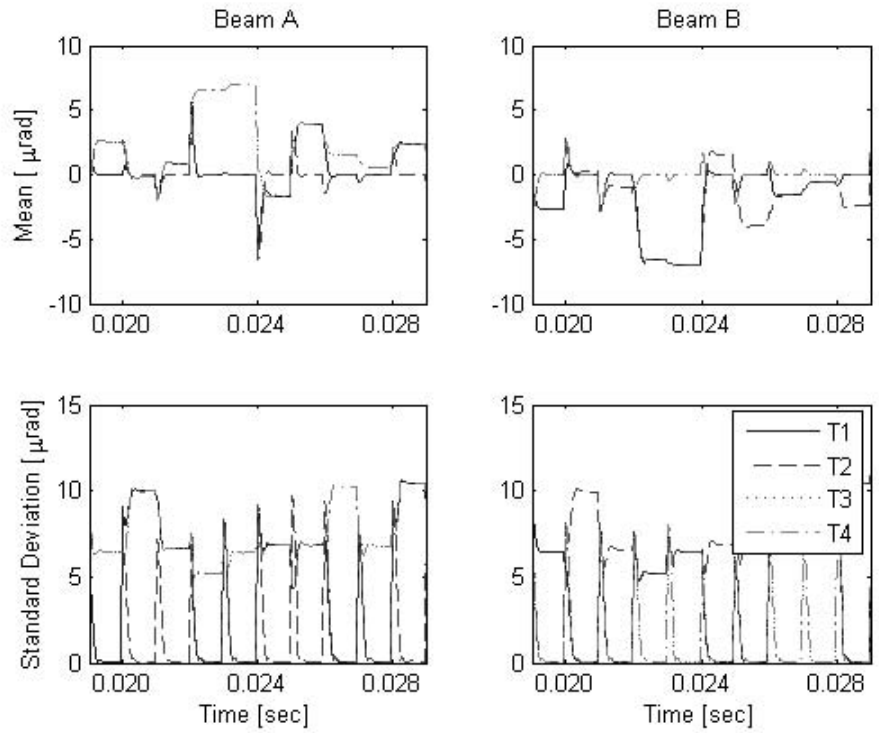


Figure F.14: Tracking Error Time Response,  $t \in (0.02, 0.03s)$

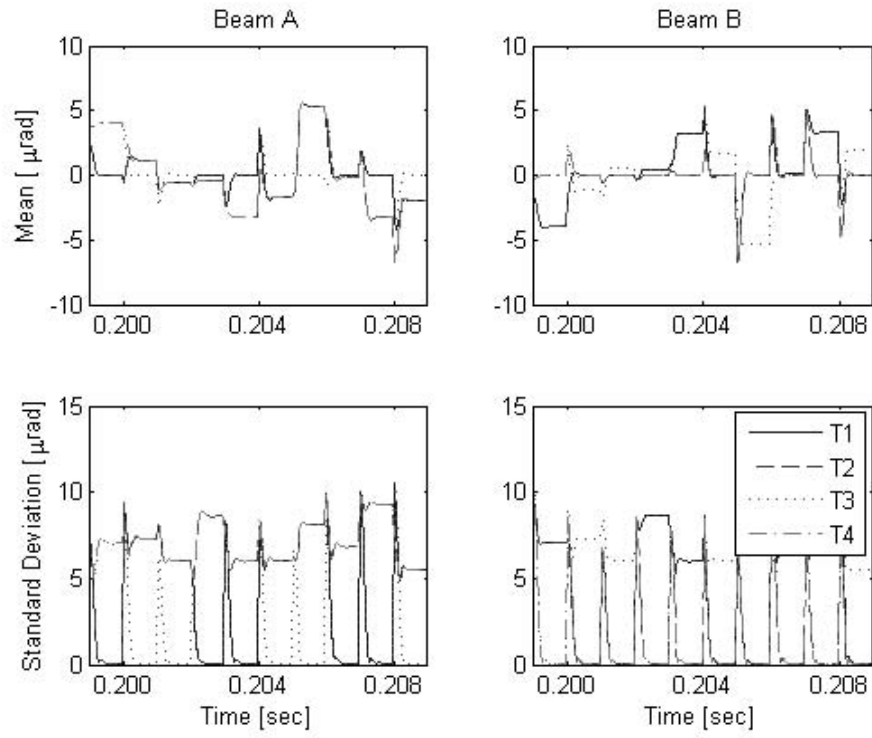


Figure F.15: Tracking Error Time Response,  $t \in (0.20, 0.21\text{s})$

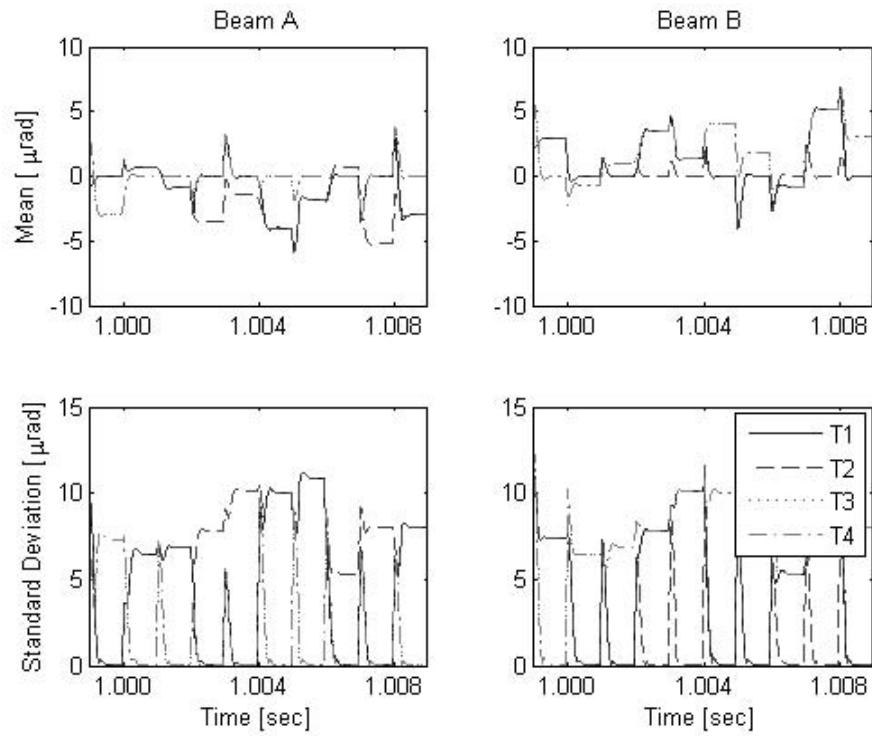


Figure F.16: Tracking Error Time Response,  $t \in (1.00, 1.01\text{s})$

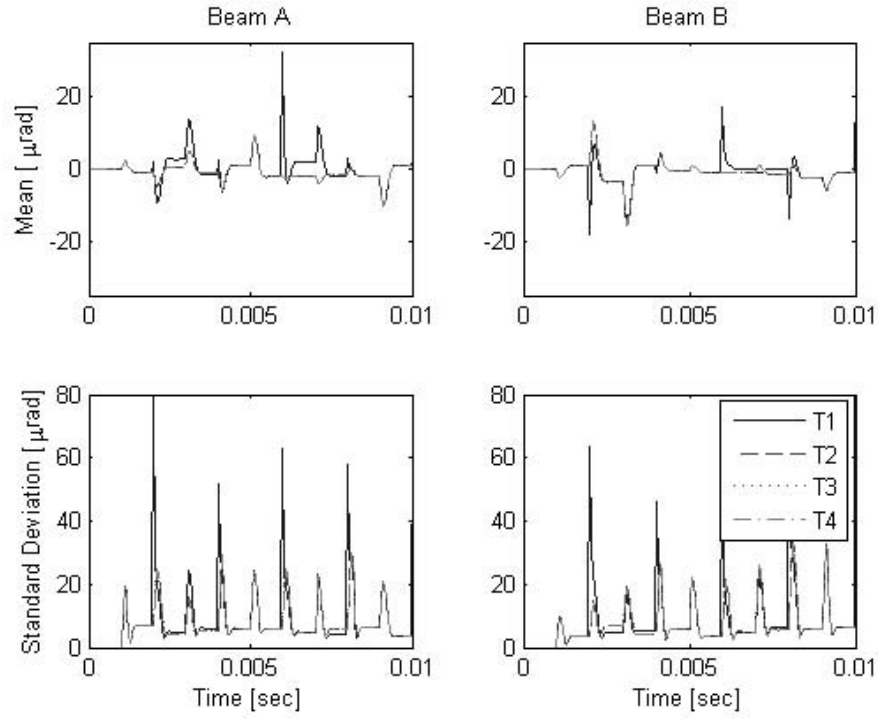


Figure F.17: Control Input Time Response,  $t \in (0, 0.01s)$

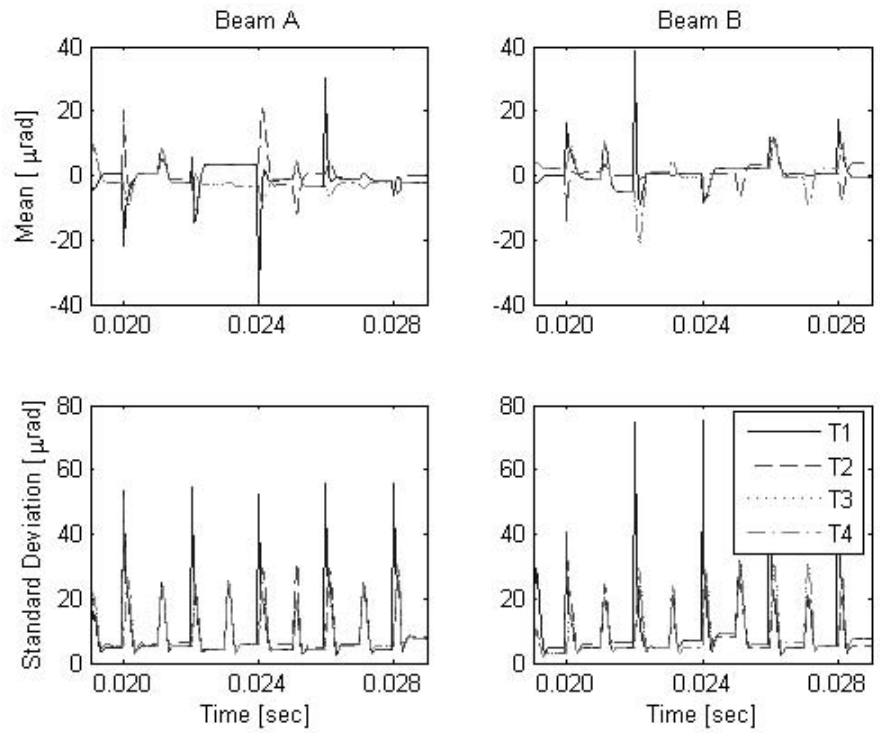


Figure F.18: Control Input Time Response,  $t \in (0.02, 0.03s)$

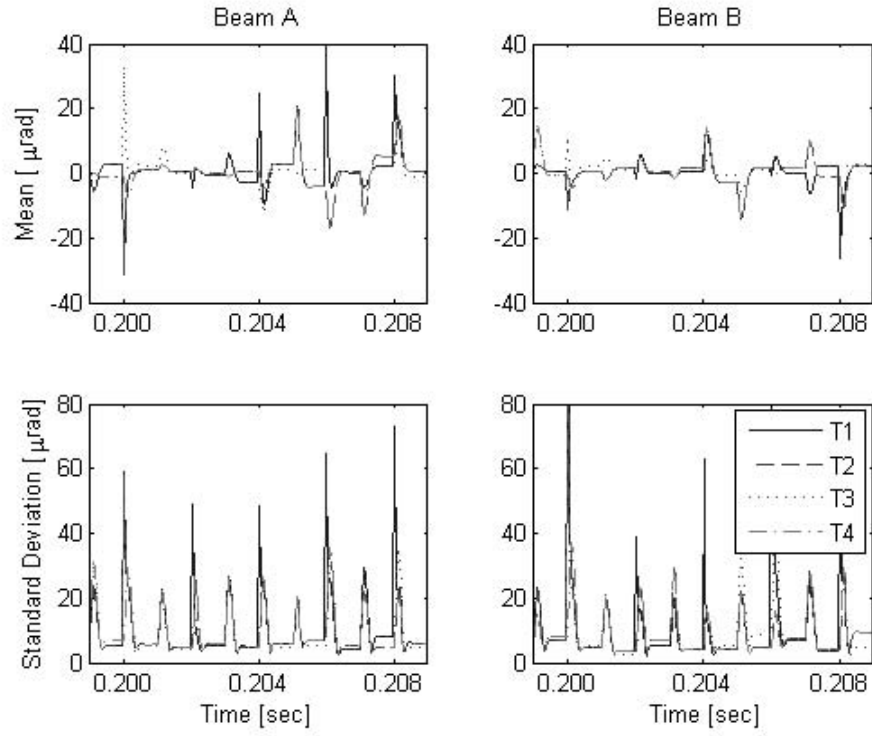


Figure F.19: Control Input Time Response,  $t \in (0.20, 0.21\text{s})$

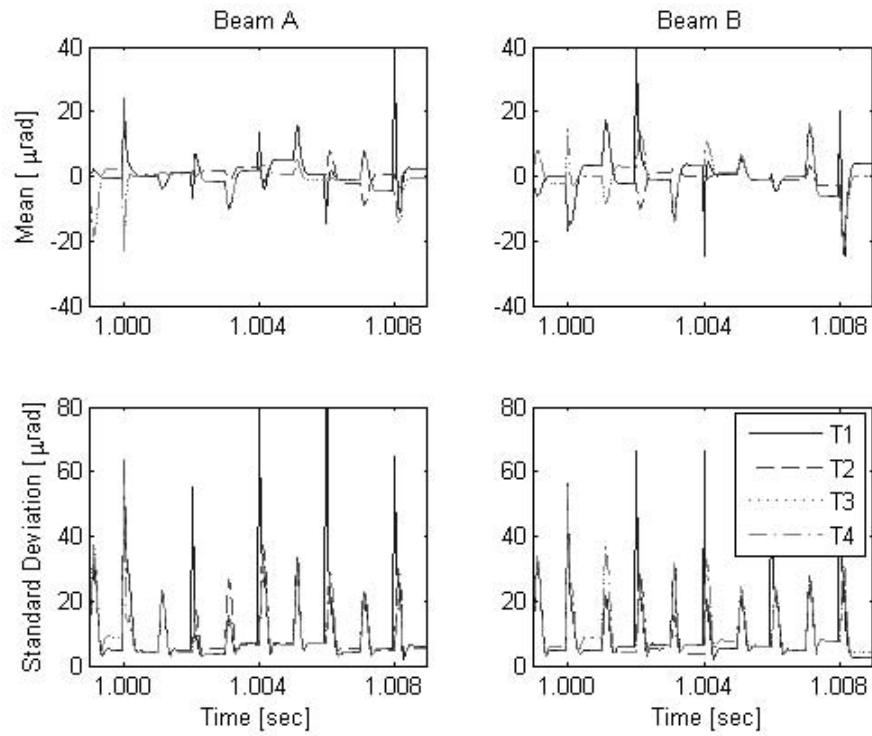


Figure F.20: Control Input Time Response,  $t \in (1.00, 1.01\text{s})$

change. In terms of the associated control input, all cases once again exhibit similar mean response. However, dispersion increases at shorter time cases for both the mean and standard deviation control input responses, which is due to more instants in time of control authority is being applied during the simulation duration.

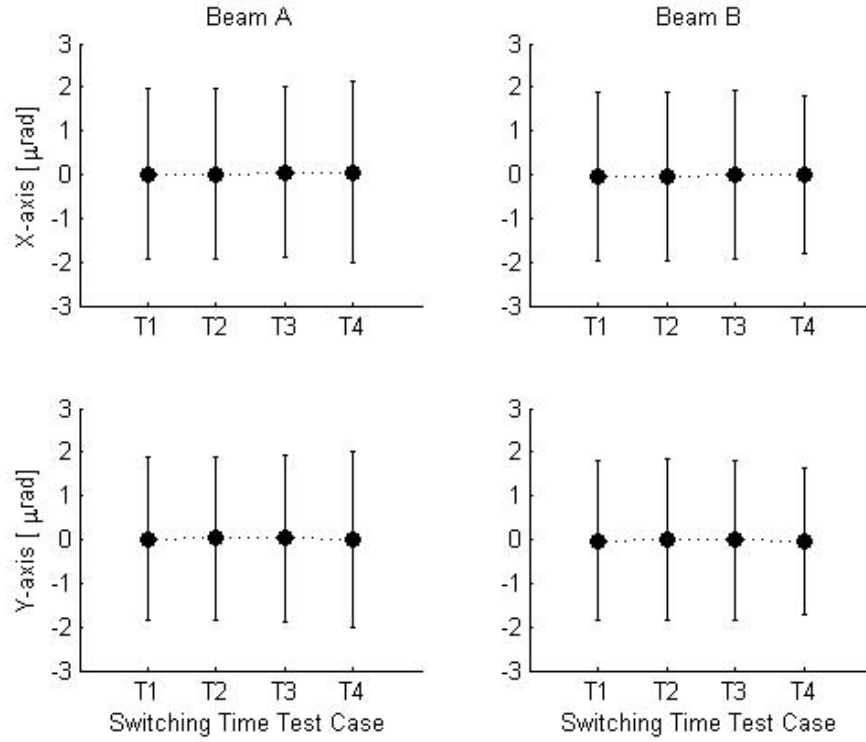


Figure F.21: Switching Time Temporal Average Mean Tracking Error

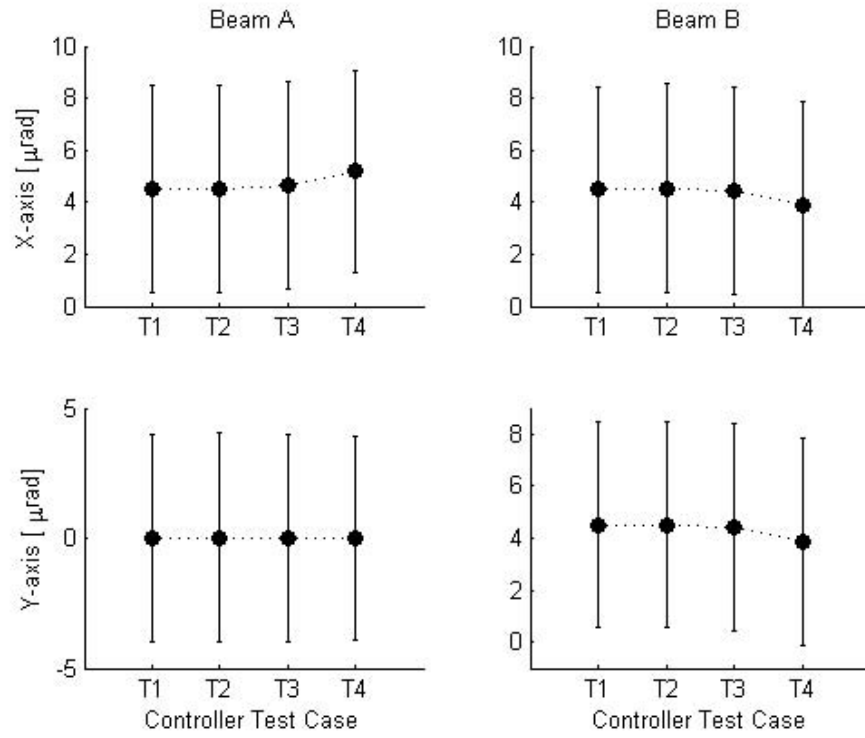


Figure F.22: Switching Time Temporal Average Tracking Error Standard Deviation

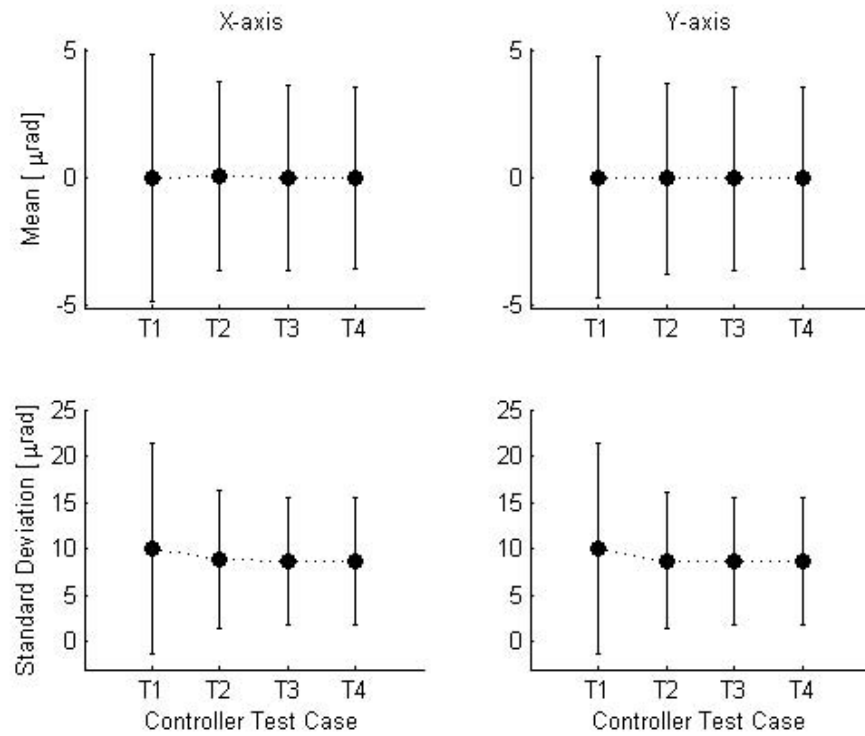


Figure F.23: Switching Time Temporal Average Control Input

### ***F.3 Summary***

Controller characterization, based on weighting matrix and switching time, has been examined using SIMULINK simulations. Simulation results show that an optimum regulator performance is achieved with a state weighting scale factor of 10 and control weighting scale factor of 0.1. In general, initial transients occurred approximately every 0.001s due to the correlation time for the bandlimited white noise blocks. On the other hand, neither switching time case positively or negatively affected controller performance. For each case, the controller adequately compensated for the disturbance. Hence, for the purposes of this study, the defined optimum regulator weighting parameters will be implemented with a switching time of 0.02s, which allows the noise correlation time to remain a significant order of magnitude faster.

## Appendix G. Dual Fine Tracking Control System Simulation Model

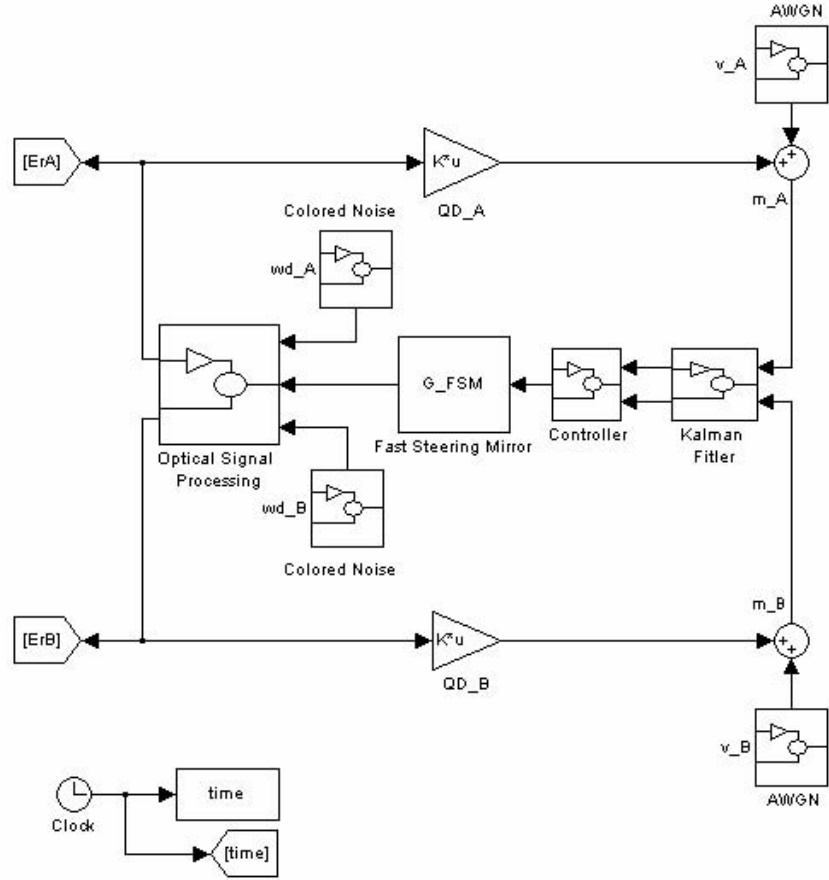


Figure G.1: Dual Fine Tracking Control System Simulation Model



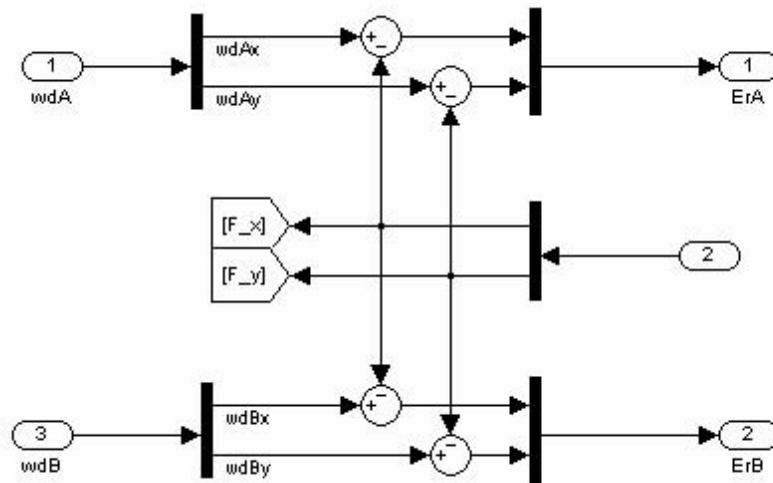


Figure G.2: Optical Signal Processing Block

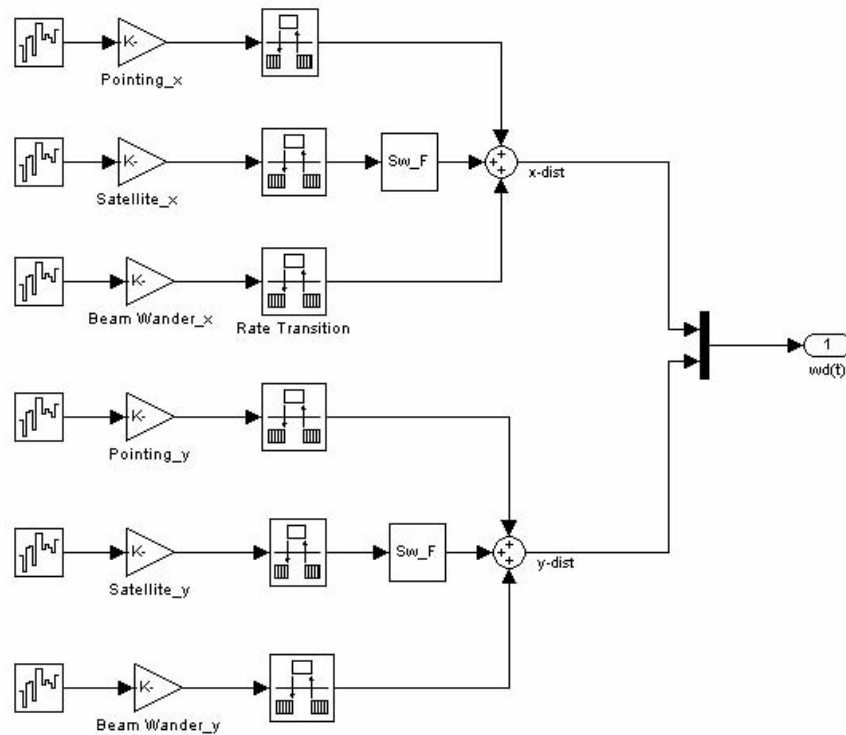


Figure G.3: Plant Disturbance Noise Block

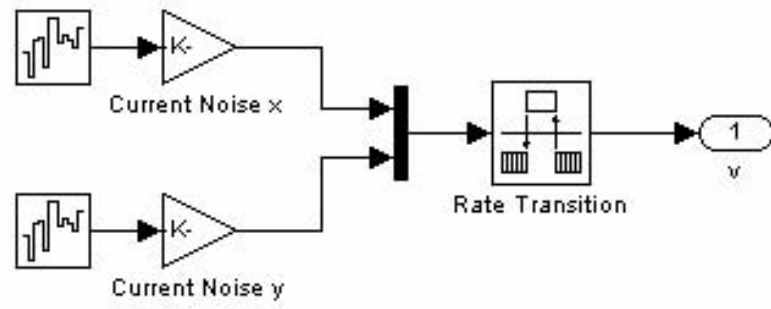


Figure G.4: Measurement Noise Block

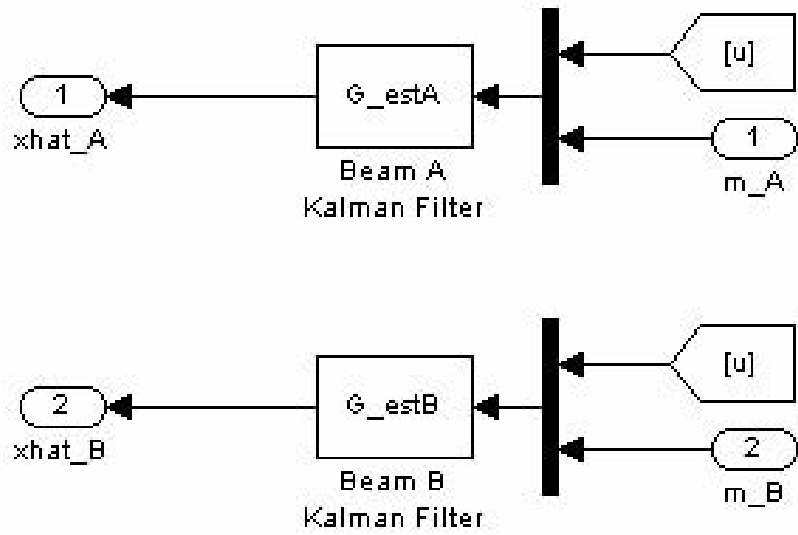


Figure G.5: Kalman Filter Block

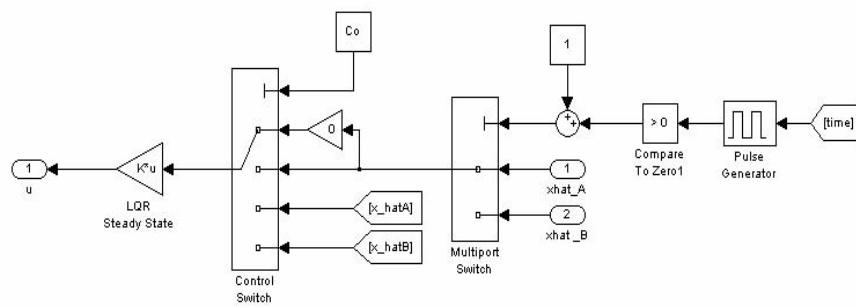


Figure G.6: Controller Block

## Bibliography

1. Alexander, Stephen B. *Optical Communication Receiver Design*. The International Society for Optical Engineering (SPIE) and The Institution of Electrical Engineers (IEE), Bellingham, WA and Stevenage, Hertfordshire UK, 1997.
2. Andrews, Larry C. *Field Guide to Atmospheric Optics*. SPIE, Bellingham, WA, 2004.
3. Andrews, Larry C. and Ronald L. Phillips. “Free Space Optical Communication Link and Atmospheric Effects: Single Aperture and Arrays”. *Proceedings of SPIE, Free-Space Laser Communication Technologies XVI*, volume 5338, 265–275. The International Society for Optical Engineering (SPIE), January 2004.
4. Andrews, Larry C. and Ronald L. Phillips. *Laser Beam Propagation Through Random Media*. SPIE, Bellingham, WA, 2nd edition, 2005.
5. Arnon, Shlomi, Stanley R. Rotman, and Norman S. Kopeika. “Bandwidth Maximization for Satellite Laser Communication”. *IEEE Transactions on Aerospace and Electronic Systems*, AES-35, No. 2:675–682, April 1999.
6. Barkat, Mourad. *Signal Detection and Estimation*. Artech House Inc., Norwood, MA, 2nd edition, 2005.
7. Burl, Jeffrey B. *Linear Optimal Control*. Addison-Wesley, Menlo Park, CA, 1999.
8. Chen, Chien-Chung and Chester S. Gardner. “Impact of Random Pointing and Tracking Errors on the Design of Coherent and Incoherent Optical Intersatellite Communication Links”. *IEEE Transactions on Communications*, COM-37, No. 3:252–260, March 1989.
9. Dudenzak, Alexander E., Alexander S. Kuzhelev, Daniel Gratton, Louis Hotte, and Yoshinori Arimoto. “High Bitrate Free-Space Communicator Using Automatic Nonlinear All-Optical Beam Tracking”. *Proceedings of SPIE, Free-Space Laser Communication Technologies XVII*, volume 5712, 72–80. The International Society for Optical Engineering (SPIE), April 2005.
10. Garcia, Alberto L. *Probability and Random Processes for Electrical Engineering*. Addison Wesley Longman Inc., Reading, MA, 2nd edition, 1994.
11. Griffin, Michael D. and James R. French. *Space Vehicle Design*. AIAA, Reston, VA, 2004.
12. Haykin, Simon. *Communication Systems*. John Wiley and Sons, New York, NY, 1983.
13. Hecht, Eugene. *Optics*. Addison Wesley, San Francisco, CA, 2002.

14. Henniger, Hennes, Dirk Giggenbach, Joachim Horwath, and Christoph Rapp. "Evaluation of Optical Up- and Downlinks from High Altitude Platforms Using IM/DD". *Proceedings of SPIE, Free-Space Laser Communication Technologies XVII*, volume 5712, 24–36. The International Society for Optical Engineering (SPIE), April 2005.
15. Lambert, Stephen G. and William L. Casey. *Laser Communications in Space*. Artech House, Boston, MA, 1995.
16. Larson, Wiley J. and James R. Wertz. *Space Mission Analysis and Design*. Microcosm, Torrance, CA, 2nd edition, 1992.
17. Liu, Jia-Ming. *Photonic Devices*. Cambridge University Press, Cambridge, MA, 2005.
18. Ludeman, Lonnie C. *Random Processes Filtering Estimation and Detection*. John Wiley and Sons Inc., Hoboken, NJ, 2003.
19. Nikulin, Vladimir V., Mounir Bouzoubaa, Victor A. Skormin, and Timothy E. Busch. "Modeling of an Acousto-Optic Laser Beam Steering System Intended for Satellite Communication". *Optical Engineering*, 40, No. 10:2208–2214, October 2001.
20. Nikulin, Vladimir V., Mounir Bouzoubaa, Victor A. Skormin, and Timothy E. Busch. "Modeling of the Tracking System Components of the Laser Satellite Communication Systems". *Proceedings of SPIE, Free-Space Laser Communication Technologies XIII*, volume 4272, 72–82. The International Society for Optical Engineering (SPIE), June 2001.
21. Ogata, Katsuhiko. *Modern Control Engineering*. Prentice Hall, Upper Saddle River, NJ, 2002.
22. Palais, Joseph C. *Fiber Optic Communications*. Prentice Hall, Upper Saddle River, NJ, 4th edition, 1998.
23. Pratt, Timothy and Charles W. Bostian. *Satellite Communications*. John Wiley and Sons, Inc., New York, NY, 1986.
24. Roden, Martin S. *Analog and Digital Communication Systems*. Prentice Hall, Upper Saddle River, NJ, 4th edition, 1996.
25. Saksonov, Avigdor, Shlomi Arnon, and Norman S. Kopeika. "Vibration Noise Control in Laser Satellite Communication". *Proceedings of SPIE, Acquisition, Tracking, and Pointing XV*, volume 4365, 188–194. The International Society for Optical Engineering (SPIE), August 2001.
26. Saleh, Bahaa E.A. and Malvin C. Teich. *Fundamentals of Photonics*. John Wiley and Sons, Inc., New York, NY, 1991.
27. Schodorf, Jeffrey B. "A Probabilistic Mispointing Analysis for Land Mobile Satellite Communications Systems with Directive Antennas". *IEEE Conference Proceedings, IEEE 54th Vehicular Technology Conference*, volume 1, 296–300. IEEE

- Vehicular Technology Society, Institute of Electrical and Electronics Engineers (IEEE), October 2001.
28. Sidi, Marcel J. *Spacecraft Dynamics and Control*. Cambridge University Press, New York, NY, 1997.
  29. Sklar, Bernard. *Digital Communications: Fundamentals and Applications*. Prentice Hall, Upper Saddle River, NJ, 2001.
  30. Skormin, Victor A., Carl R. Herman, Mark A. Tascillo, and Donald J. Nicholson. "Mathematical Modeling and Simulation Analysis of a Pointing, Acquisition, and Tracking System for Laser-Based Intersatellite Communication". *Optical Engineering*, 32, No. 11:2749–2763, November 1993.
  31. Skormin, Victor A., Mark A. Tascillo, and Donald J. Nicholson. "Demonstration of a Jitter Rejection Technique for Free-Space Laser Communication". *IEEE Transactions on Aerospace and Electronic Systems*, 33, No. 2:568–576, April 1997.
  32. Trolinger, James D. and William C. Rose. "Technique for Simulating and Evaluating Aero-Optical Effects in Optical Systems". *42nd AIAA Aerospace Sciences Meeting and Exhibit*, 1–11. American Institute of Aeronautics and Astronautics (AIAA), January 2004.
  33. Watkins, R. Joseph, Brij N. Agrawal, Young S. Shin, and Hong-Jen Chen. "Jitter Control of Space and Airborne Laser Beams". *22nd AIAA International Communications Satellite Systems Conference and Exhibit 2004 (ICSSC)*, 1–17. American Institute of Aeronautics and Astronautics (AIAA), May 2004.
  34. Wiesel, William E. *Spaceflight Dynamics*. Irwin McGraw Hill, Boston, MA, 2nd edition, 1997.
  35. Wijker, Jaap J. *Mechanical Vibrations in Spacecraft Design*. Springer-Verlag, New York, NY, 2004.
  36. Wittig, Manfred E., L. van Holtz, D.E.L. Tunbridge, and Herman C Vermeulen. "In-Orbit Measurements of Microaccelerations of ESA's Communication Satellite OLYMPUS". *Proceedings of SPIE, Free-Space Laser Communication Technologies II*, volume 1218, 205–214. The International Society for Optical Engineering (SPIE), July 1990.
  37. Xu, Xuping and Panos J. Antsaklis. "Optical Control of Switched Systems: New Results and Open Problems". *Proceedings of the American Control Conference*, volume 4489, 2683–2687. American Automatic Control Council (AACC), June 2000.
  38. Xu, Xuping and Panos J. Antsaklis. "Optimal Control of Switched Systems Based on Parameterization of the Switching Instants". *IEEE Transactions on Automatic Control*, 49, No. 1:2–16, January 2004.
  39. Zipfel, Peter H. *Modeling and Simulation of Aerospace Vehicle Dynamics*. American Institute of Aeronautics and Astronautics (AIAA), Reston, VA, 2000.

<b>REPORT DOCUMENTATION PAGE</b>				Form Approved OMB No. 0704-0188	
<small>The public reporting burden for this collection of information is estimated to average 1 hour per response, including the time for reviewing instructions, searching existing data sources, gathering and maintaining the data needed, and completing and reviewing the collection of information. Send comments regarding this burden estimate or any other aspect of this collection of information, including suggestions for reducing the burden, to Department of Defense, Washington Headquarters Services, Directorate for Information Operations and Reports (0704-0188), 1215 Jefferson Davis Highway, Suite 1204, Arlington, VA 22202-4302. Respondents should be aware that notwithstanding any other provision of law, no person shall be subject to any penalty for failing to comply with a collection of information if it does not display a currently valid OMB control number.</small> <b>PLEASE DO NOT RETURN YOUR FORM TO THE ABOVE ADDRESS.</b>					
1. REPORT DATE (DD-MM-YYYY) 14-09-2006		2. REPORT TYPE Master's Thesis		3. DATES COVERED (From - To) Aug 2005 - Aug 2006	
4. TITLE AND SUBTITLE  Dual Fine Tracking Control of a Satellite Laser Communication Uplink				5a. CONTRACT NUMBER	
				5b. GRANT NUMBER	
				5c. PROGRAM ELEMENT NUMBER	
				5d. PROJECT NUMBER	
6. AUTHOR(S)  Noble, Louis A. Maj				5e. TASK NUMBER	
				5f. WORK UNIT NUMBER	
7. PERFORMING ORGANIZATION NAME(S) AND ADDRESS(ES) Air Force Institute of Technology Graduate School of Engineering & Management Department of Electrical and Computer Engineering 2950 Hobson Way, Wright Patterson AFB, OH 45433-7765				8. PERFORMING ORGANIZATION REPORT NUMBER  AFIT/GSS/ENG/06-02	
9. SPONSORING/MONITORING AGENCY NAME(S) AND ADDRESS(ES)				10. SPONSOR/MONITOR'S ACRONYM(S)	
				11. SPONSOR/MONITOR'S REPORT NUMBER(S)	
12. DISTRIBUTION/AVAILABILITY STATEMENT  Approved for public release; Distribution unlimited.					
13. SUPPLEMENTARY NOTES					
14. ABSTRACT  A dual fine tracking control system (FTCS) is developed for a single aperture optical communication receiver to compensate for high frequency disturbances affecting tracking of two incident laser communication beams. The optical communication receiver resides within a payload module aboard a geosynchronous satellite, while each laser communication transmitter is housed within a module aboard a high altitude unmanned aerial vehicle (UAV). In addition to platform specific disturbances, the impact of atmospheric optical disturbances affecting tracking error are investigated. The system dynamics and FTCS are modeled and evaluated in MATLAB and SIMULINK. An optimal controller is developed to mitigate these disturbances and provide tracking errors commensurate with a bit error rate (BER) that does not exceed 1e-6.					
15. SUBJECT TERMS Laser Communication, Satellite Communication, Fine Tracking Control					
16. SECURITY CLASSIFICATION OF:			17. LIMITATION OF ABSTRACT		18. NUMBER OF PAGES
a. REPORT U	b. ABSTRACT U	c. THIS PAGE U	UU		19a. NAME OF RESPONSIBLE PERSON Vasquez, Juan R. Lt Col (juan.vasquez@afit.edu)
					19b. TELEPHONE NUMBER (Include area code) (937) 255-3636 ext. 7231